

The GlueX Experiment

A Search for QCD Exotics Using a Beam of Photons

GlueX-doc-346 — October 2004

The GlueX Collaboration

J. Pinfold

University of Alberta (Edmonton, Alberta, Canada)

D. Fassouliotis, P. Ioannou, Ch. Kourkouvelis

**University of Athens (Athens, Greece)*

G. B. Franklin, J. Kuhn, C. A. Meyer (Deputy Spokesperson), C. Morningstar, B. Quinn,

R. A. Schumacher, Z. Krahn, G. Wilkin

Carnegie Mellon University (Pittsburgh, PA)

H. Crannell, F. J. Klein, D. Sober

Catholic University of America (Washington, D. C.)

D. Doughty, D. Heddle

Christopher Newport University (Newport News, VA)

R. Jones, K. Joo

University of Connecticut (Storrs, CT)

W. Boeglin, L. Kramer, P. Markowitz, B. Raue, J. Reinhold

Florida International University (Miami, FL)

V. Crede, L. Dennis, P. Eugenio, A. Ostrovidov, G. Riccardi

Florida State University (Tallahassee, FL)

J. Annand, D. Ireland, J. Kellie, K. Livingston, G. Rosner, G. Yang

University of Glasgow (Glasgow, Scotland, UK)

A. Dzierba (Spokesperson), G. C. Fox, D. Heinz, J. T. Londergan, R. Mitchell, E. Scott,

P. Smith, T. Sulanke, M. Swat, A. Szczepaniak, S. Teige

Indiana University (Bloomington, IN)

S. Denisov, A. Klimenko, A. Gorokhov, I. Polezhaeva, V. Samoilenko, A. Schukin, M. Soldatov

Institute for High Energy Physics (Protvino, Russia)

D. Abbott, A. Afanasev, F. Barbosa, P. Brindza, R. Carlini, S. Chattopadhyay, H. Fenker,
G. Heyes, E. Jastrzembki, D. Lawrence, W. Melnitchouk, E. S. Smith (Hall D Group Leader),
E. Wolin, S. Wood
Jefferson Lab (Newport News, VA)

A. Klein
Los Alamos National Lab (Los Alamos, NM)

V. A. Bodyagin, A. M. Gribushin, N. A. Kruglov, V. L. Korotkikh, M. A. Kostin,
A. I. Demianov, O. L. Kodolova, L. I. Sarycheva, A. A. Yershov
Nuclear Physics Institute, Moscow State University, Moscow, Russia

E. Solodov
Budker Institute of Nuclear Physics (Novosibirsk, Russia)

P. Mueller
** Oak Ridge National Lab (Oak Ridge, TN)*

D. S. Carman, K. Hicks, S. Taylor
Ohio University (Athens, OH)

M. Barbi, E. J. Brash, G. M. Huber, V. Kovaltchouk, G. J. Lolos, Z. Papandreou
University of Regina (Regina, Saskatchewan, Canada)

T. Barnes, S. Spanier
** University of Tennessee (Knoxville, TN)*

T. Hatziantoniou, Ch. Kanellopoulos, Ch. Petridou, D. Sampsonidis
**University of Thessaloniki (Thessaloniki, Greece)*

GlueX Theory Group

D. B. Leinweber, A. G. Williams
CSSM, University of Adelaide, (Adelaide, Australia)

S. Godfrey
Carleton University (Ottawa, Ontario, Canada)

C. Morningstar
Carnegie Mellon University (Pittsburgh, PA)

R. Kaminski, L. Lesniak
H. Niewodniczanski Institute of Nuclear Physics (Cracow, Poland)

J. Goity
Hampton University (Hampton, VA)

J. T. Londergan, M. Swat, A. Szczepaniak
Indiana University (Bloomington, IN)

A. Afanasev, W. Melnitchouk, A. W. Thomas
Jefferson Lab (Newport News, VA)

M. Pichowsky
Kent State University (Kent, OH)

P. Page
Los Alamos National Lab (Los Alamos, NM)

E. Swanson
University of Pittsburgh (Pittsburgh, PA)

T. Barnes
*University of Tennessee (Knoxville, TN)
Oak Ridge National Lab (Oak Ridge, TN)*

Contents

1	Overview	1
1.1	Science of confinement	1
1.1.1	Light meson spectroscopy	1
1.1.2	Experimental Situation	2
1.1.3	Using Photons as Probes	2
1.2	The GlueX/Hall D Project	3
1.2.1	Photon Beam	3
1.2.2	Accelerator Upgrade	4
1.2.3	Detector	4
1.3	Plan for Analysis	5
1.4	Project history and collaboration	5
2	Photon Beam	9
2.1	Choice of Technique	9
2.1.1	Compton Back-scatter	10
2.1.2	Tagged Bremsstrahlung	12
2.1.3	Coherent Bremsstrahlung	12
2.2	Photon Source	13
2.2.1	Essential Features	14
2.2.2	Use of Collimation	15
2.2.3	Choice of Radiator	20
2.2.4	Crystal Quality	22
2.2.5	Crystal Thickness	24
2.2.6	Crystal Mount	27
2.2.7	Crystal Alignment and Monitoring	28
2.2.8	Crystal Lifetime	29
2.3	Electron Beam	31
2.3.1	Beam Polarization	31
2.3.2	Beam Emittance	32
2.3.3	Electron Beam Line Optics	34
2.3.4	Electron Beam Dump	34
2.3.5	Beam Containment and Shielding	34
2.4	Tagging Spectrometer	37
2.4.1	Specifications	37
2.4.2	Magnet	37
2.4.3	Spectrometer Optics	40
2.4.4	Tagger Detectors	42
2.4.5	Beam Dump Optics	44
2.5	Polarimetry Instrumentation	44
2.6	Operating Beam Intensity	46

3	The Superconducting Solenoid	47
3.1	Introduction	47
3.2	Brief Description	47
3.3	Solenoid Refurbishment Activities	48
3.3.1	Detailed Tests of The Coils	48
3.3.2	Refurbishment of Coils One and Two	50
3.3.3	Plans To Complete Coils Three and Four	50
3.3.4	Plans To Complete The Solenoid at JLab	50
3.4	The Magnetic Field of The Solenoid	51
3.4.1	Magnetic Modifications Needed	51
3.4.2	TOSCA Simulations	51
3.4.3	Compensation of the Upstream Plug	54
4	The GlueX Detector in Hall D	57
4.1	Overview	57
4.2	The Target	57
4.3	Calorimetry	60
4.3.1	Global Design	60
4.3.2	The Lead-Glass Calorimeter	60
4.3.3	Barrel Calorimetry	71
4.3.4	Upstream Photon Veto	85
4.4	Charged Particle Tracking	88
4.4.1	Design Considerations	88
4.4.2	Track Reconstruction	90
4.4.3	Straw-tube Drift Chamber	93
4.4.4	Forward Drift Chambers	101
4.4.5	The Start Counter	114
4.5	Particle Identification	114
4.5.1	Overview	114
4.5.2	The Time-of-flight System	119
4.5.3	Čerenkov Counter	124
4.5.4	Acceptance of The Particle Identification System	138
4.6	Detector Integration	144
4.6.1	Assembly and Mounting	146
4.6.2	Survey and Alignment	148
4.6.3	Access	148
4.6.4	Interaction Between Subsystems	149
4.6.5	Cabling	149
5	Readout Electronics	151
5.1	Overview	151
5.2	FADCs for Calorimetry	151
5.2.1	Prototype	153
5.2.2	Additional requirements for final version	154
5.3	FADCs for Tracking	154
5.4	TDCs	155
5.4.1	Jefferson Lab TDC	155
5.4.2	TDC Performance	157
5.4.3	Additional requirements for final version	158
5.5	Track Count	159
5.6	Clock Distribution and Pipeline Synchronization	159
5.7	Discriminators and Amplifiers	159
5.8	High Voltage	159
5.9	Packaging	159

CONTENTS

vii

5.10 Readout Bus	161
5.11 Construction	161
5.12 Review	162
A Report of the Hall D Electronics Review Committee	163

Chapter 1

Overview

The goal of the GLUEX/HALL D project at Jefferson Lab (JLab) is to address one of the outstanding and fundamental questions in physics – the quantitative understanding of the confinement of quarks and gluons in quantum chromodynamics (QCD). Confinement is a unique feature of QCD and understanding confinement requires an understanding of the soft gluonic field responsible for binding quarks in hadrons. Exotic hybrid mesons manifest gluonic degrees of freedom and their spectroscopy will provide the crucial data needed to test assumptions in lattice QCD and phenomenology leading to confinement. Photoproduction is expected to be particularly effective in producing exotic hybrids but there is little data on the photoproduction of light mesons. GLUEX will use the coherent bremsstrahlung technique to produce a linearly polarized photon beam. A solenoid-based hermetic detector will be used to collect data on meson production and decays with statistics that will exceed the current photoproduction data in hand by several orders of magnitude after the first year of running. In order to reach the ideal photon energy of 9 GeV for this mapping of the exotic spectra, the energy of the Jefferson Lab electron accelerator, CEBAF, will be doubled from its current maximum of 6 GeV to 12 GeV.

This document describes the GLUEX beam and detector – it is an upgrade of the relevant parts of version 4 of the GLUEX Design Report issued in November, 2002. By way of an introduction this section briefly reviews the science of GLUEX and the status of the collaboration.

1.1 Science of confinement

1.1.1 Light meson spectroscopy

The observation nearly four decades ago that mesons are grouped in nonets, each characterized by unique values of J^{PC} – spin (J), parity (P) and charge conjugation (C) quantum numbers – led to the development of the quark model. Within this picture, mesons are bound states of a quark (q) and antiquark (\bar{q}). The three light-quark flavors (*up*, *down* and *strange*) suffice to explain the spectroscopy of most – but not all – of the lighter-mass mesons (i.e. below $3 \text{ GeV}/c^2$) that do not explicitly carry heavy flavors (charm or beauty). Early observations yielded only those J^{PC} quantum numbers consistent with a fermion-antifermion bound state. The J^{PC} quantum numbers of a $q\bar{q}$ system with total quark spin, \vec{S} , and relative angular momentum, \vec{L} , are determined as follows: $\vec{J} = \vec{L} + \vec{S}$, $P = (-1)^{L+1}$ and $C = (-1)^{L+S}$. Thus J^{PC} quantum numbers such as 0^{--} , 0^{+-} , 1^{-+} and 2^{+-} are not allowed and are called *exotic* in this context.

Our understanding of how quarks form mesons has evolved within quantum chromodynamics (QCD) and we now expect a richer spectrum of mesons that takes into account not only the quark degrees of freedom but also the gluonic degrees of freedom. Gluonic mesons with no quarks (*glueballs*) are expected. These are bound states of gluons and since the quantum numbers of low-lying glueballs are not necessarily exotic, they should manifest themselves as extraneous states that cannot be accommodated within $q\bar{q}$ nonets. But their identification is complicated since they can mix with $q\bar{q}$. Excitations of the gluonic field binding the quarks can also give rise

to so-called *hybrid* mesons that can be viewed as bound states of a quark, anti-quark and valence gluon ($q\bar{q}g$). An alternative picture of hybrid mesons, one supported by lattice QCD [1], is one in which a gluonic flux tube forms between the quark and anti-quark and the excitations of this flux tube lead to so-called *hybrid* mesons. Actually the idea of flux tubes, or strings connecting the quarks, originated in the early 1970's [2] to explain the observed linear dependence of the mass-squared of hadrons on spin (Regge trajectories). Conventional $\bar{q}q$ mesons arise when the flux tube is in its ground state. Hybrid mesons arise when the flux tube is excited and some hybrid mesons can have a unique signature, exotic J^{PC} , and the spectroscopy of these exotic hybrid mesons is not complicated by possible mixing with conventional $\bar{q}q$ states.

The level splitting between the ground state flux tube and the first excited transverse modes is π/r , where r is the separation between the quarks, so the hybrid spectrum should lie about 1 GeV/ c^2 above the ground state spectrum. According to the flux-tube model [3] and lattice gauge calculations [4], one expects the lightest $J^{PC} = 1^{-+}$ exotic hybrid to have a mass of about 1.9 GeV/ c^2 .

In this discussion the motion of the quarks was ignored, but we know from general principles [3] that an approximation that ignores the impact of the flux tube excitation and quark motion on each other seems to work quite well.

In the coming years there will be significant computational resources [5], using lattice techniques, dedicated to understanding non-perturbative QCD including confinement. The prediction of the hybrid spectrum, including decays, will be part of this program but experimental data will be needed to validate assumptions. The spectroscopy of exotic mesons provides a clean and attractive starting point for the study of gluonic excitations.

1.1.2 Experimental Situation

After about two decades of experimental searches there have been reports of observations of states with $J^{PC} = 1^{-+}$ by the Brookhaven E852 collaboration. One of those was a state produced in the reaction $\pi^- p \rightarrow \pi^+ \pi^- \pi^- p$ using an 18 GeV/ c π^- beam. The state has a mass of (1593 ± 8) MeV/ c^2 and width of (168 ± 20) MeV/ c^2 and decays into $\rho^0 \pi^-$ [6]. A partial wave analysis (PWA) of the 3π system uncovered the exotic signal as a P wave between the ρ^0 and π^- with a line shape in the P wave amplitude and interference with the nearby $\pi_2(1670)$ ($J^{PC} = 2^{-+}$) characteristic of a Breit-Wigner resonance. The exotic state's contribution to the 3π spectrum is much smaller than the dominant $a_1(1260)$, $a_2(1320)$ and $\pi_2(1670)$ so uncovering the signal is a challenge.

1.1.3 Using Photons as Probes

The data to date are tantalizing and suggest that exotic hybrid mesons may exist but the extensive data collected to date with π probes have not uncovered the hybrid meson spectrum. Lattice QCD and phenomenology however indicate the photon is a probe that should be particularly effective in producing exotic hybrids but data on photoproduction of light mesons are sparse indeed.

The first excited transverse modes of the flux tube are degenerate and correspond to clockwise or counterclockwise rotations of the flux tube about the axis joining the quark and antiquark fixed in space with $J = 1$ [3]. Linear combinations of these two modes are eigenstates of parity and lead to $J^{PC} = 1^{+-}$ and $J^{PC} = 1^{-+}$ for the excited flux tube. When these quantum numbers are combined with those of the $q\bar{q}$ with $\vec{L} = 0$ and $\vec{S} = 1$ (quark spins aligned) three of the six possible J^{PC} have exotic combinations: 0^{+-} , 1^{-+} and 2^{+-} . A photon probe is a virtual $q\bar{q}$ with quark spins aligned. In contrast when the $q\bar{q}$ have $\vec{L} = 0$ and $\vec{S} = 0$ (spins anti-aligned), the resulting quantum numbers of the hybrid meson are not exotic. Pion probes are $q\bar{q}$ with quark spins anti-aligned. If we view one outcome of the scattering process as exciting the flux tube binding the quarks in the probe, the suppression of exotic hybrids in π -induced reactions is not surprising – a spin flip of one of the quarks is required followed by the excitation of the flux tube. In contrast the spins of the virtual quarks in the photon probe are properly aligned to

lead to exotic hybrids. Phenomenological studies quantitatively support this picture predicting that the photoproduction cross-sections for exotic mesons are comparable to those for copiously produced mesons such the $a_2(1320)$ [7, 8].

1.2 The GlueX/Hall D Project

Based on this guidance from theory and experiment, the GlueX/Hall D collaboration was formed to design a photon beam and detector to map the exotic hybrid spectrum [9]. The goal of the experiment is to reach meson masses up to about $3 \text{ GeV}/c^2$ and collect sufficient statistics on the production of mesons with a sensitivity to a wide variety of decay modes. In order to identify the quantum numbers, the PWA technique will be used. This requires a detector that has excellent resolution, is hermetic and has good rate capability. It is essential to kinematically identify exclusive reactions in order to apply PWA.

1.2.1 Photon Beam

The optimal photon energy for this study is around 9 GeV. The photon energy must be large enough to produce the higher mass states with sufficient boost in the laboratory so that their decay products will be detected and measured with sufficient resolution. It is also important that the energy be high enough to avoid line shape distortions that arise due to relatively large values of $|t|_{min}$ occurring near threshold – $|t|_{min}$ is the minimum momentum transfer squared from the incident photon beam to the produced meson.

As will be described below, a solenoid-based detector design will be used. This represents the optimal design for fixed-target photoproduction experiment as the intense photon beam produces large electromagnetic backgrounds (e^+e^- pairs) that can be trapped within a tight region along the beam by the axial field of the solenoid. However, with this geometry, the momentum resolution of two-body decays of lighter mesons degrades if the photon beam energy exceeds $9 \text{ GeV}/c^2$.

The photon beam must also be linearly polarized due to the PWA requirements. This is related to the fact that states of linear polarization, in contrast to states of circular polarization, are eigenstates of parity. The linear polarization of the photon beam can also be used as an exotics filter [10].

Coherent bremsstrahlung will be used to produce linearly polarized photons. Instead of using an amorphous radiator, a diamond crystal is used. At special settings for the orientation of the crystal with respect to the electron beam, the atoms of the crystal can be made to recoil together from the radiating electron leading to an enhanced emission at particular photon energies and yielding linearly polarized photons. The resulting spectrum of photons is a sum of incoherent bremsstrahlung, whose spectrum falls like $1/E_\gamma$, and the coherent spectrum. The correlation of emitted photon energy and angle also allows one to substantially collimate out the incoherent portion of the photon spectrum before the photons reach the detector. A collimator with a 3.4 mm diameter hole placed 80 m from the radiator will be used to greatly reduce the backgrounds from unwanted lower energy photons in the detector target. The collimation is also needed to increase the degree of linear polarization to 40% in the current design. The employment of coherent bremsstrahlung and collimation is made possible by the superb characteristics of the electron beam at Jefferson Lab including the continuous wave feature leading to a duty factor close to one, the small spot size and the emittance characteristics. In addition, recent advances in growing and thinning diamond wafers down to $20 \mu\text{m}$ result in negligible multiple scattering allowing collimation to be effective.

The diamond crystal in the electron beam will be immediately followed by a focal plane spectrometer (photon tagger) that will be used to measure the electron energy after the radiator thus allowing an energy determination of each photon into the detector with a resolution of 0.1%.

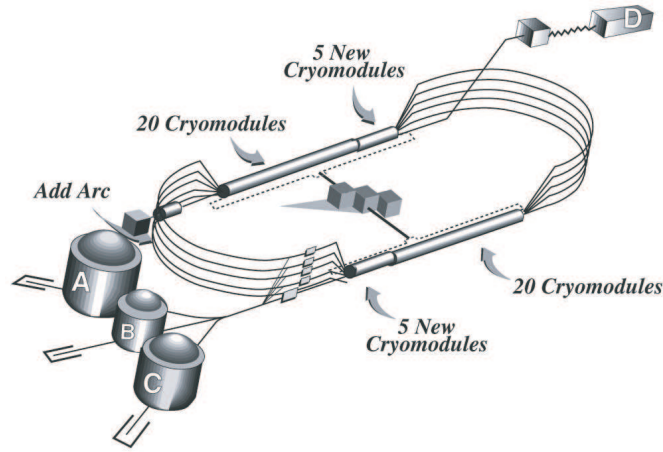


Figure 1.1: The proposed configuration for the 12 GeV upgrade of CEBAF at Jefferson Lab showing the additional new Hall D for the GlueX experiment. Details are given in the text.

1.2.2 Accelerator Upgrade

In order to produce 9 GeV photons with sufficient degree of linear polarization an electron energy of 12 GeV will suffice. For example, increasing the electron energy to 20 GeV will only double the degree of polarization of 9 GeV photons from 40% to 80% while requiring a major modification of the accelerating section and arcs. However, dropping from 12 GeV to 10 GeV electrons would reduce the degree of linear polarization of 9 GeV photons by nearly an order of magnitude.

Figure 1.1 shows the configuration of the proposed 12 GeV CEBAF upgrade at Jefferson Lab. The present CEBAF accelerator consists of two linear accelerating sections, each about 250 m long. Re-circulating arcs of magnets allow multiple-passes of the electrons through the accelerating regions. Currently beam is delivered to three existing experimental halls labeled A, B and C. The proposal calls for the construction of a fourth hall (D) preceded by the photon tagger to which 12 GeV electrons will be delivered. To accomplish the energy upgrade, 5 new accelerating superconducting cryomodules will be added to the 20 existing cryomodules in each of the two accelerating sections. The space for the additional modules already is available. A tenth added arc will allow for 11 full passes of the electrons before delivery to HALL D. More details of the accelerator upgrades along with the proposed GLUEX/HALL D project and the planned upgrades for the existing halls for the upgrade project are described in reference [11].

1.2.3 Detector

Figure 1.2 shows a schematic of the proposed detector for GLUEX. Central to the detector is a superconducting solenoid with a clear bore diameter of 73 in and a length of 183 in. The central field is 2.24 T. The magnet was originally constructed for the LASS experiment at SLAC and then moved to LANL where it was used for the MEGA experiment. It has been moved to IUCF where it is currently being refurbished. It will be shipped to Jefferson Lab for use in the GLUEX/HALL D experiment starting in 2005. The inside bore of the solenoid will be lined with an electromagnetic calorimeter surrounding the target and the central and forward particle tracker. That will be followed by an Cerenkov counter, a time-of-flight wall and then a 2500-element lead glass calorimeter. The latter was originally built and used in the E852 experiment and has since been moved to Jefferson Lab for the GlueX/Hall D experiment.

Initially the detector will run with an incident photon flux of 10^7 photons per second. With this flux and after the first year of data-taking, the collected sample will exceed current photoproduction data in the literature by several orders of magnitude and current π -induced data

by an order of magnitude. Later the beam flux will be increased by a factor of 5. Data will be recorded at the rate of 100 MB/s leading to roughly 1 PetaByte of stored data per year. This is comparable to the size of the data sets planned for the LHC experiments.

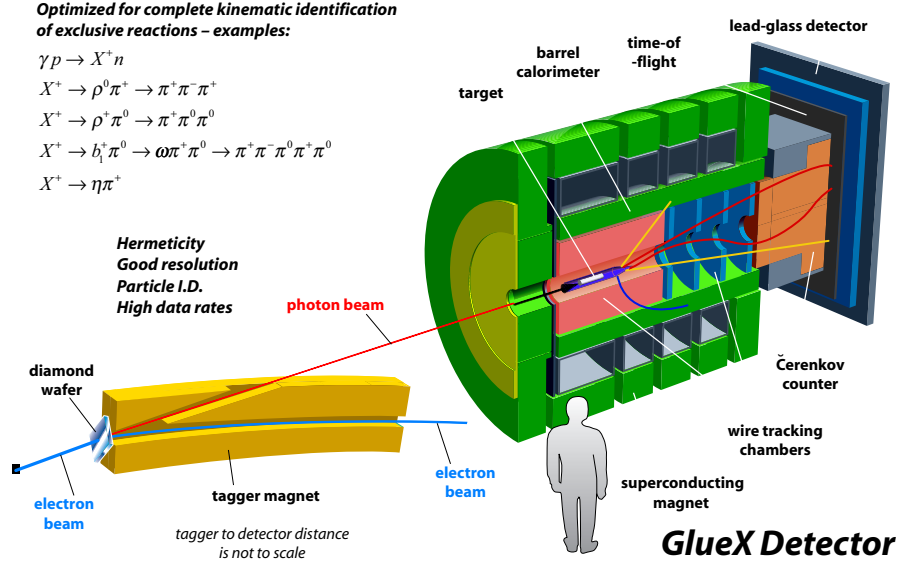


Figure 1.2: Schematic of the GLUEX/HALL D Detector.

1.3 Plan for Analysis

Extensive Monte Carlo studies have been carried out to evaluate the proposed detector design. The acceptance of the proposed detector over relevant kinematic variables including decay angles is high and uniform. Double-blind Monte Carlo studies have included exotic signals at low levels mixed with conventional mesons. Generated events have been smeared according to expected resolution and passed through acceptance simulations. The surviving sample has then been acceptance corrected, reconstructed and passed through PWA-fitting programs. Signals at the few percent level have been successfully recovered. Studies have also been carried out to study *leakage* in the PWA by introducing distortions in the Monte Carlo. It is extremely difficult to produce leakage. In addition to Monte Carlo studies, the fundamental assumptions behind the PWA are also under study including any model assumptions (e.g. the *isobar* assumption), mathematical ambiguities, and issues of analyticity. It is essential to minimize possible biases and uncertainties from the dynamical unknowns.

1.4 Project history and collaboration

The GLUEX Collaboration includes nearly 100 physicists from 25 institutions in six countries and it was officially formed in 1999. The current organization chart and management structure is shown in Figure 1.3. Beginning with the formation of the collaboration, the project has been presented by various members of the collaboration at international conferences and workshops, to the DOE, NSF and NSERC, to program committees at JLab and institutional plan reviews and reviews committees including NSAC, at colloquia and seminars and in articles in the *American Scientist* [12] and the *CERN Courier* [13].

Within the GLUEX collaboration there is a strong theory and phenomenology effort that is impacting the design of the experiment and the development of software tools.

The GLUEX/HALL D project was born at a workshop at Indiana University in July, 1997 when about 40 experimentalists and theorists met to explore the possibility of using photo-production to produce exotic hybrid mesons. There followed a number of workshops at JLab, North Carolina State University, Carnegie Mellon, Florida State University and the Rensselaer Polytechnic Institute.

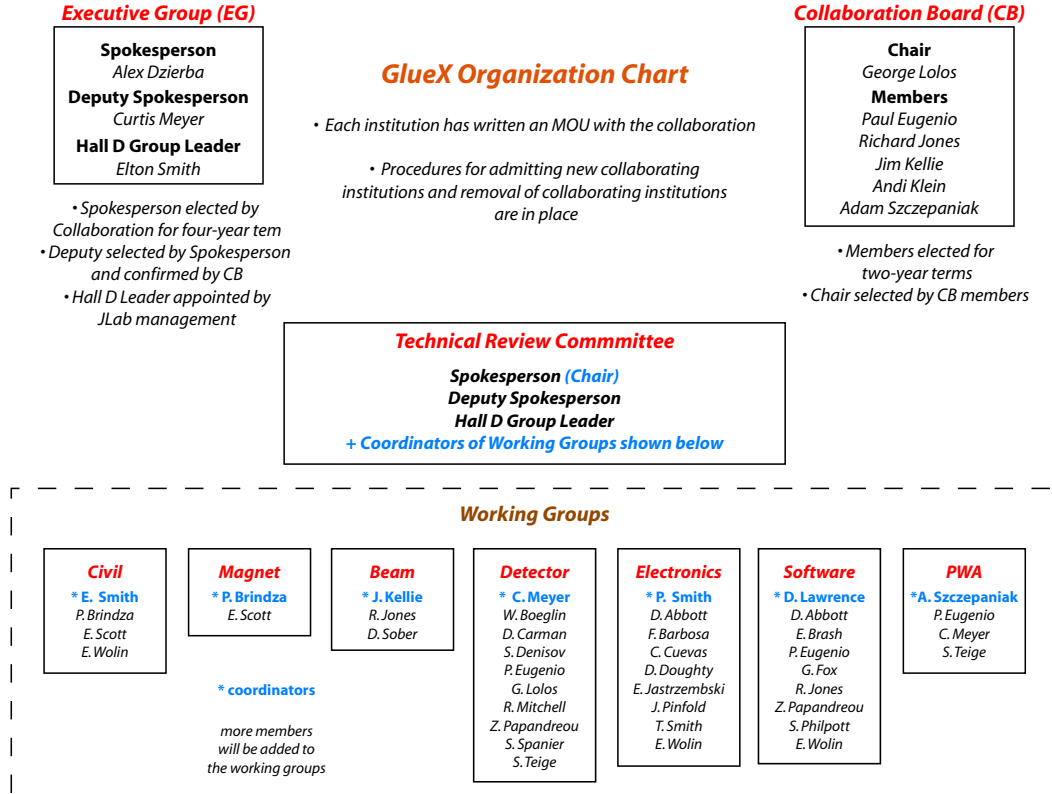


Figure 1.3: Organization chart and management plan for the GLUEX Collaboration. Working groups are now being formed.

In 1998 a preliminary plan for an experimental program and detector was presented to JLab Users' Group at its annual meeting in June, 1998 with Preliminary Design Report issued in September, 1998. The first formal presentation to the JLab Physics Advisory Committee was made in January, 1999. The collaboration was formally constituted in March, 1999 and version 2 of the HALL D Design Report was issued in August, 1999. The JLab management appointed an external review committee chaired by David Cassel of Cornell (other members included Frank Close, John Domingo, Bill Dunwoodie, Don Geesaman, David Hitlin, Martin Olsson and Glenn Young) to review the science goals and proposed realization of those goals. The review took place in December, 1999 and the committee issued its report in January, 2000. The report of the Cassel committee was very positive noting that "JLab was uniquely suited to carry out this program of searching for exotic states" and that "the basic approach advocated by the collaboration is sound." A modest R&D program was initiated motivated by the recommendations of the committee. More collaboration meetings followed and version 3 of the HALL D Design Report was issued in November, 2000. The project was presented at the APS Town Meeting at JLab in December, 2000 and to the NSAC Long Range Planning Meeting in April, 2001. The large superconducting MEGA/LASS magnet was moved from Los Alamos to the Indiana University Cyclotron Facility where work on refurbishing the magnet began. The NSAC Long Range Planning document [14] was released in April, 2002 endorsing the proposed JLab upgrade and the HALL D project. And version 4 of the HALL D Design Report was issued

in November, 2002.

In July, 2003 a committee including John Domingo, Andy Lankford and Glenn Young conducted a review of the GLUEX electronics preparation. That committee concluded that characteristics of the overall design (detector-mounted analog front-end electronics and pipelined data acquisition) were sound and appropriate choices. More detail are given in the full report which is included as an appendix to this document.

In November, 2003, in his speech at the National Press Club, Energy Secretary Spencer Abraham rolled out the 20-Year Facilities Plan prepared by Dr. Raymond Orbach, Director of the Office of Science at the DOE. The Jefferson Lab upgrade was included among the near-term priorities in that plan. Quoting from that report:

Specifically, the upgrade will enable scientists to address one of the great mysteries of modern physics the mechanism that confines quarks together. New supercomputing studies indicate that force fields called flux-tubes may be responsible, and that exciting these should lead to the creation of neverbefore-seen particles.

And in April, 2004 Kyle McSlarrow, Undersecretary for Energy, signed the CD-0 (Critical Decision Zero) for the JLab upgrade.

With the release of the 20-Year Plan and the signing of CD-0 the collaboration has redoubled its efforts to recruit new collaborators and with success. New groups from the US, Canada, Greece and Mexico have expressed interest in joining and taking on major equipment responsibilities. And these are groups that have not been previously involved in experiments at JLab but rather are groups that have worked at FNAL and SLAC or finishing hardware commitments for LHC.

During the last two years there has been substantial work on refurbishing the solenoid magnet coils, beam tagger magnet design, electronics development of FADC's and TDC's, use of robotics to construct PMT bases, techniques for constructing 4 m long lead/scintillator calorimeter modules, beam tests of time-of-flight modules, assessment elements from the lead glass calorimeter, tests of drift chambers, development of software tools including detector simulations and amplitude analysis techniques. More details are included in the following descriptions of the subsystems.

Chapter 2

Photon Beam

One of the unique opportunities presented by a CEBAF upgrade to energies of 12 GeV and beyond is the possibility of generating high-intensity continuous photon beams for high-energy photoproduction experiments. In this regime, photon beams represent an interesting extension to the meson spectroscopy program that has been actively pursued using beams of pseudoscalar mesons at hadron accelerator laboratories: with high energy photons one has essentially a beam of *vector* mesons. It is difficult, in fact, to conceive of any other way to obtain such a vector beam.

The requirements for photon beam energy and polarization were described in Chapter 1. This chapter describes a design for a real photon source that meets these requirements. Starting with a beam of monochromatic electrons, it provides an intense beam of high-energy photons with an energy spectrum that is dominated by a single peak. A significant fraction of the total power in the beam is concentrated inside this peak, which has a width of less than 10% f.w.h.m. At a fixed electron beam energy E_0 , the peak energy of the photon beam can be varied anywhere up to 90% E_0 simply by rotating a crystal. The photon spectrum inside the intensity peak has a large degree of linear polarization. The precise energy of an individual photon inside the peak is determined (“tagged”) from the momentum of the recoil electron measured in a dedicated “tagging” spectrometer. The design is formed around the expected parameters for the CEBAF beam following the energy upgrade to 12 GeV , although nothing prevents its operation at lower energies before the time that 12 GeV beams are available.

This chapter begins with a survey of the techniques for producing high-energy photons that were considered in the development of this design, and the reasons for the choice of coherent bremsstrahlung. The coherent bremsstrahlung source is then described in greater detail, followed by a discussion of the requirements that the design places on the electron beam that feeds the source. The tagging spectrometer design is described next, and the chapter concludes with a discussion of the considerations that govern the choice of beam intensity for particular measurements.

2.1 Choice of Technique

Two basic methods have been considered for producing photons of the highest possible energy, flux and polarization from electrons of $E_0 = 12 GeV$. The methods are bremsstrahlung and Compton scattering of light. Both are well-established methods of producing photon beams. Both techniques are actually described by the same Feynman diagrams, shown in Fig. 2.1. In the case of Compton scattering the incoming photon is real, whereas it is virtual for the case of bremsstrahlung.

Each of these techniques has its own limitations and advantages. In order to be suitable for GLUEX, the photon source must be capable of producing photons of energy at least 80% E_0 , (9 GeV). The photon beam should have linear polarization. The energy resolution for individual photons in the beam should be as high as possible, *i.e.* on the order of the energy

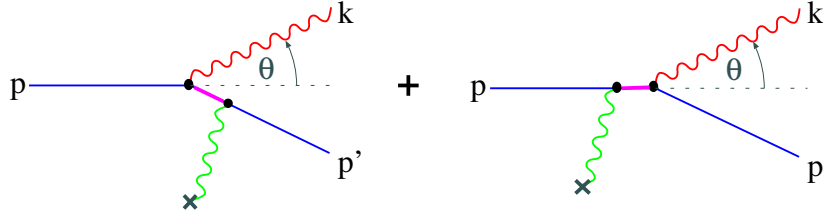


Figure 2.1: Generic diagrams for hard photon production from a high energy electron beam. The symbol \times represents either a static charge distribution, in the case of virtual photons in the initial state (i.e. bremsstrahlung), or an optical cavity, in the case of real photons in the initial state (i.e. Compton scattering).

spread of the electron beam itself. It should be capable of producing intensities up to 10^8 /s. The contamination of the beam with photons outside the desired energy band should be as low as possible. It is also important that the source be reliable and require a minimum of down-time for maintenance. The suitability of each approach is discussed below in the light of these criteria.

2.1.1 Compton Back-scatter

A Compton source begins with a beam of visible or ultraviolet light, typically from a laser that is aligned to intersect the incident electron beam at close to 180° . Some of the photons undergo Compton scattering with the beam electrons. In the lab frame, the scattered photons come out in a narrow cone about the incident electron direction and carry a significant fraction of the electron energy.

The basic design of the Compton back-scatter source for this study was put forward by C. Keppel and R. Ent [15]. The design entails the use of a four-mirror high-gain cavity pumped by a 10 kW argon-ion laser putting out 2 ps pulses at a frequency of 100 MHz. The pulses in the cavity are synchronized so that the light pulses intercept an electron bucket each time they pass through the beam. The total length of the cavity is 2 m with a crossing angle of 1° . Both cavity and electron beam are focused to a tiny spot of 10 μm r.m.s. radius at the crossing point. A small spot size is necessary in order to get as high a scattering rate as possible. The gain of the cavity is 10^4 , which is conservative in view of recent advances in mirror technology. The wavelength of the light is 514 nm. The rate spectrum of the back-scattered beam from this source is shown in Fig 2.2a for a 1 μA electron beam at 12 GeV.

From the point of view of flux, this source is marginal. With a few μA of beam and mirror improvements, it might produce 10^8 photons/s in the upper third of its energy spectrum. However, its maximum photon energy of 3.7 GeV is far short of the 80% E_0 needed for GLUEX. To remedy this one must decrease the wavelength of the laser beam. This can be done by the use of a frequency-doubling crystal that absorbs the green light from the laser and produces ultraviolet light at 257 nm. Storing this light in a cavity of similar design to that described above yields the back-scatter rate spectrum shown in Fig. 2.2b. The major reason for the drop in rate is the decrease in the cavity gain from 10000 to 250. This is imposed by the diminished reflectivities of mirrors in the UV. Other factors are the inefficiency of the doubling crystal, a factor of two in rate from the doubling itself, and the decreasing Compton cross section with energy. The maximum photon energy is still under 50% E_0 and the flux is three orders of magnitude below the desired rate.

In order to reach photon energies of 80% E_0 , initial photons of 20 eV are needed. The brightest source of these would be a synchrotron light source or a free electron laser (FEL). Mirrors that operate at these wavelengths typically have reflectivities around 70%. With these one could conceive of a scheme that uses a wiggler to extract energy from the 12 GeV beam before it enters the dump. This light would have the same time structure as incident beam, and so it could be reflected back and made to cross the incident beam at a small angle for a Compton back-scatter source. An indication of the level of flux that could be achieved with

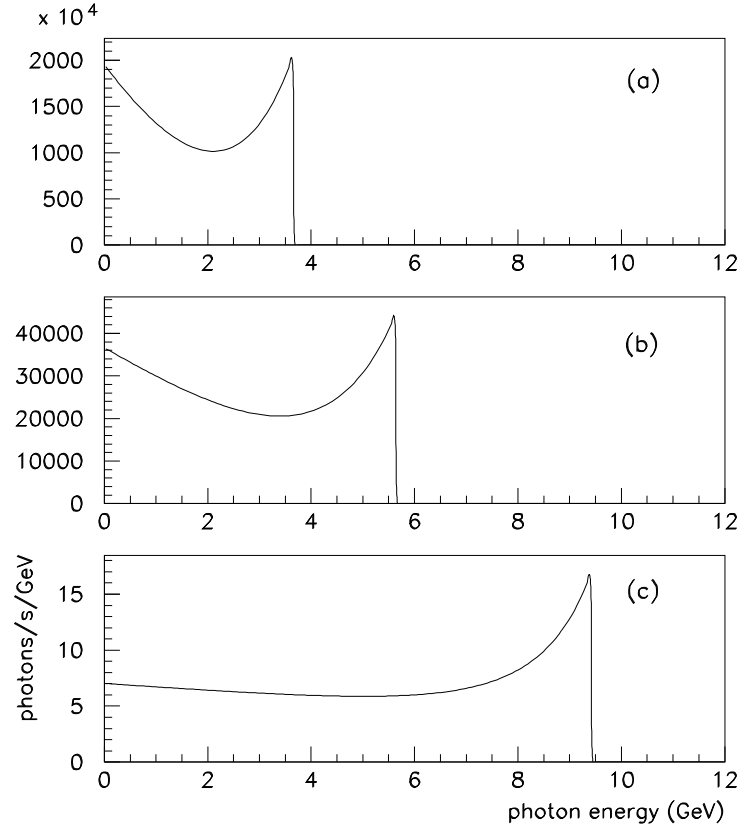


Figure 2.2: Photon energy spectrum from the Compton back-scatter source described in the text and a 12 GeV electron beam at 1 μA . (a) cavity of gain 10000 driven by a 10 kW Argon-ion laser (514 nm) at 100 MHz. (b) cavity of gain 250 driven by 3 kW frequency-doubler (257 nm) pulsed at 100 MHz. (c) cavity of gain 1 driven by a hypothetical FEL source operating at 20 eV with the same time structure as CEBAF beam, peak power 1 kW.

such a source can be obtained by using the laser cavity model described above, setting the gain to 1, the wavelength to 62 nm, and assuming 1 kW peak (1 W average) of synchrotron light. The back-scatter rate is shown in Fig 2.2c. This plot shows that even if the full power of a 1 μA on a 12 GeV beam were converted into 20 eV photons and back-scattered from the incoming beam, the rate would still fall far short of the requirements for GLUEX.

From the point of view of polarization, the Compton back-scatter source would be ideal. The polarization of the back-scattered beam is controlled by that of the laser, and can be essentially 100%. This source is also virtually background-free because the spectrum below any desired cutoff can be eliminated by collimation. The energy of the remaining beam can be measured to within the resolution of the electron beam by tagging. However the the combination of sufficient energy and sufficient flux for the purposes of the GLUEX experiment in HALL D cannot be achieved using this source.

2.1.2 Tagged Bremsstrahlung

A bremsstrahlung source consists of a thin piece of material (the radiator) that is placed in the electron beam and converts part of the energy of the beam into bremsstrahlung radiation. Bremsstrahlung offers the only practical way, starting with an electron beam at CEBAF energies, to produce a photon beam with a significant flux in the vicinity of the end point. It produces a naturally collimated photon beam with a characteristic angular spread of m/E_0 . This allows the low emittance of the CEBAF beam to be effectively transferred into the secondary photon beam.

Bremsstrahlung does not suffer from the kind of flux limitations that were encountered in the examination of Compton back-scatter sources. The radiator thickness must be kept below 1% of a radiation length in order to maintain good energy resolution in the tagger. Keeping the thickness below 10^{-3} radiation lengths ensures that multiple scattering in the radiator does not significantly broaden the divergence angle of the photon beam. A 10^{-3} radiator and 1 μA of electrons would produce much more than sufficient flux for GLUEX.

A bremsstrahlung source is, however, deficient in some other respects. Averaged over the bremsstrahlung cone, the photon beam has zero linear polarization. Circular polarization can be achieved by polarization transfer from a polarized electron beam, but for the purposes of GLUEX it is linear polarization that is desired. A bremsstrahlung source also suffers from a large low-energy flux in the beam. The power spectrum of a bremsstrahlung beam is approximately uniform from zero up to the energy of the incident electrons. This means that an experiment that uses the high-energy part of the beam must operate in a background of low-energy photons that are many times more frequent. The tagger is helpful in eliminating many of the false starts in the detector that arise from the background, but this technique becomes ineffective at rates above a few 10^7 tagged photons/s. For the typical experiment using tagged bremsstrahlung and open detector geometry, background from low-energy beam particles limits the rate at which the experiment can run to less than $5 \cdot 10^7$ tagged photons/s. The goal for GLUEX pushes that limit to 10^8 /s by employing tagged *coherent* bremsstrahlung.

2.1.3 Coherent Bremsstrahlung

The source described in the previous section meets most of the requirements for GLUEX, but is deficient in the areas of polarization and backgrounds. Both of these deficiencies can be remedied by replacing the conventional amorphous or polycrystalline radiator with a thin mono-crystalline wafer. At special settings for the orientation of the crystal, the atoms in the radiator can be made to recoil together from the radiating electron. When they do this they produce a coherent enhancement at particular energies in the radiation spectrum, which correspond to the reciprocal lattice vectors of the crystal. The kinematics are such that a randomly oriented lattice vector would make a tiny peak located up at the end point of the energy spectrum, where the coherent gain factor is negligible. By careful orientation of the crystal, however, one of the lattice vectors can be aligned with the favored kinematics for bremsstrahlung, at which point its coherent peak appears well below the end point, and its coherent gain can be large enough that it contributes a large fraction of the total radiated power.

This is illustrated in Fig. 2.3. This plot shows the intensity (dP/dE) or power spectrum of the coherent bremsstrahlung beam after collimation. The sequence of secondary peaks above the primary correspond to integral multiples of the fundamental reciprocal lattice vector and so they are always present. By careful choice of orientation angles it is possible to suppress all other vectors and isolate just one primary peak in the energy band of interest, as shown in the figure. By a small rotation of the crystal, the position of the peak can be moved from one end of the spectrum to the other. Note that the coherent peaks appear as enhancements on top of the incoherent bremsstrahlung continuum.

Unlike those from the incoherent process, coherent bremsstrahlung photons have significant net linear polarization in the plane given by the beam direction and the crystal lattice vector. This polarization is enhanced by collimating the photon beam below its intrinsic angular spread, as discussed in the next section. The loss in flux from collimation can be recovered by increasing

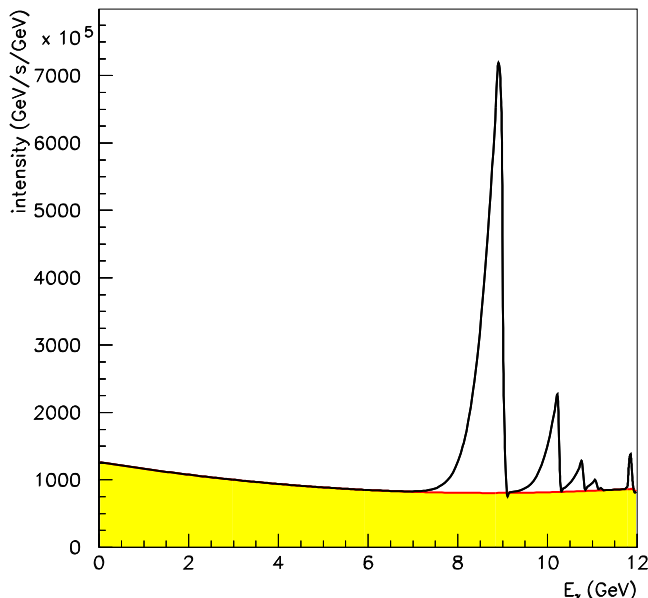


Figure 2.3: Photon power spectrum from an oriented diamond radiator. The y axis is dP/dE with power P expressed in GeV/s and E in GeV . The radiator thickness is 10^{-4} radiation lengths and the electron beam current is $1 \mu A$. Shown is what emerges after the photon beam passes through a collimator 3.4 mm in diameter located 80 m downstream from the radiator.

the electron beam current. As will be shown in the following section, even in the case of very thin crystals and severe collimation, quite modest electron beam currents are needed to produce the required photon flux.

The use of coherent bremsstrahlung improves the background conditions of the beam by enhancing the spectral intensity in the desired energy band relative to the incoherent continuum. For measurements that do not require polarization, a crystal radiator can be used without collimation to reduce the low-energy beam background for a given rate of tagged photons. Where polarization is required, coherent bremsstrahlung is indispensable.

2.2 Photon Source

A horizontal plan view of the photon beam line is shown in Fig. 2.4 with the major components labeled. The electron beam enters the figure from below ground at the left and is bent into the horizontal plane to enter the tagger building. There it passes through two small dipoles to impinge upon the bremsstrahlung radiator. After its exit from the radiator, the electron beam passes into the tagging spectrometer where the primary beam is bent in the direction of the electron beam dump. The radiator crystal is thin enough that the average energy loss by the electrons in traversing the radiator is less than the intrinsic energy spread of the incident beam. Those electrons which lose a significant fraction of their initial energy inside the radiator do so by emitting a single bremsstrahlung photon. These degraded electrons are bent out of the primary beam inside the tagger magnet and exit the vacuum through a thin window, passing through air for a short distance to strike the focal plane of the spectrometer. The primary electron beam is contained inside vacuum all the way to the dump.

The photons that are produced in the radiator pass through a small hole bored in the return

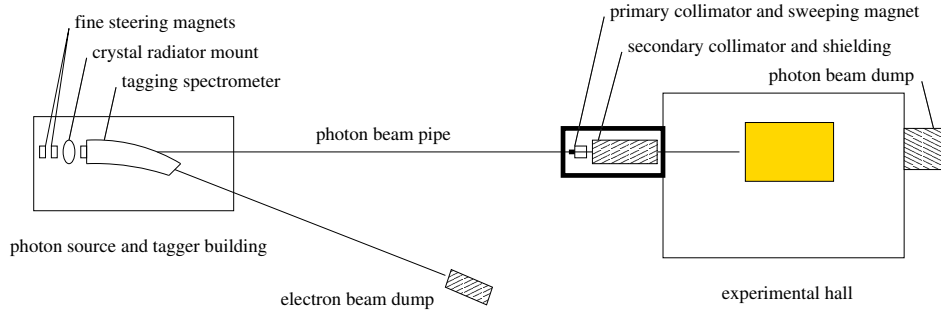


Figure 2.4: Schematic plan view of the photon beam line, shown in the horizontal plane as viewed from above. The objects in this figure are not drawn to scale.

yoke of the tagger magnet in the forward direction. They then pass into an evacuated photon beam pipe and travel to the experimental hall. Just before entering the hall the photon beam passes through a system of collimators and sweeping magnets. They are housed in a separate enclosure for shielding purposes. The primary collimator is first. It defines the part of the photon beam that is allowed to reach the target. Debris from interactions along the inside surface of the collimator bore forms a halo around the photon beam that exits the primary collimator. The charged component of the halo is deflected away from the beam axis by a dipole “sweeping” magnet just downstream of the collimator. A secondary collimator follows the sweeping magnet to stop the deflected shower particles and block the halo of secondary photons generated by the first collimator. The secondary collimator is of a larger diameter than the primary and so sees a reduced rate of secondary interactions on the inner surface of the hole. What new showers are generated there are cleaned up by a second sweeping magnet. The beam then passes through a block of shielding material into the experimental hall. This triple-collimation system is similar to the setup at the SLAC coherent bremsstrahlung beam line [16].

The collimated photon beam, now only a few mm in diameter, is delivered to the experimental target. After passing through of order 3% radiation lengths of target, the photon beam passes through the detector and into the photon beam dump at the back of the hall. Based upon a design upper limit of $60 kW$ ($5 \mu A$ at $12 GeV$) being delivered to the electron beam dump, the total power in the photon beam is not more than $1.5 W$ in the experimental hall and not more than $15 W$ in the collimator enclosure.

2.2.1 Essential Features

The adjective ‘coherent’ in coherent bremsstrahlung does not indicate that the photons in the beam are in a coherent state, as is light from a laser. Rather it refers to the coherent effect of multiple atoms in a crystal lattice in absorbing the recoil momentum from a high energy electron when it radiates a bremsstrahlung photon. In X-ray spectroscopy one encounters the same thing in the Mössbauer effect, except in that case the chief physical consequence is the disappearance of the recoil Doppler shift from the photoabsorption/emission spectrum. Here the chief consequence is the enhancement of bremsstrahlung at those particular kinematics for which the recoil momentum matches one of the reciprocal lattice vectors of the crystal.

Another useful way to view the process of coherent bremsstrahlung is as virtual Compton scattering. To the high energy electron, the atoms in the radiator appear as clouds of virtual photons. For a disordered radiator material, the virtual photon spectrum is given simply by the atomic form factor squared, averaged over the different species in the material. If the radiator is a single crystal, however, the atomic form factor gets multiplied by the form factor of the crystal, which in the ideal case looks like a series of delta-functions located at the sites of the reciprocal lattice. In effect, the crystal provides a set of virtual laser beams, each one a standing wave tuned to a specific reciprocal lattice vector. In this view the process of hard bremsstrahlung is seen to be the same as Compton back-scattering of laser light. For a more detailed discussion

of the physics of coherent bremsstrahlung there are a number of good references [16, 17, 18, 19].

The use of Compton back-scattering of laser light as a photon source was earlier noted as ruled out by the limitation of high-power lasers and cavities to wavelengths above $100 \mu m$. The characteristic wavelength of the crystal photons is a few Angstroms, three orders of magnitude shorter. In this case, 180° scattering would result in essentially 100% of the electron beam momentum being transferred to the photon in the lab frame. However, the Compton cross section contains a factor of $1/(\vec{q} \cdot \vec{p})^2$ where \vec{q} is the virtual photon momentum and \vec{p} is that of the electron, which strongly favors incident photons with \vec{q} nearly orthogonal to \vec{p} . With reciprocal lattice vectors pointing in almost every direction, only those nearly perpendicular to the beam contribute appreciably to the scattering rate. This fact applies equally to ordinary bremsstrahlung; in fact, to a first approximation the bremsstrahlung spectrum from a single crystal is the same as from a disordered radiator. The reason is that, if the sum over crystal momenta were replaced with a continuous integral, one would recover the ordinary bremsstrahlung result for isolated atoms. Beyond a few unit cells from the origin in reciprocal lattice space, the atomic form factor and kinematic factors become slowly varying on the scale of the lattice spacing, and the sum becomes indistinguishable from the integral. Besides that, the uncertainty principle requires that atoms localized at the sites in a crystal undergo fluctuations about their mean position. This has the effect of attenuating the discrete peaks in the crystal form factor at progressively higher-order crystal momenta, eventually washing them out and filling in the gaps between them, so that the sum deforms smoothly into the integral at high momentum transfer. Hence, the sum over crystal indices that yields the final photon spectrum can be separated into two parts: a discrete sum over a limited set of small crystal indices and an integral over the continuum of momentum transfer values beyond. The latter appears in the coherent bremsstrahlung beam as an ordinary $1/k$ bremsstrahlung spectrum, while the former appears as a set of peak structures superimposed upon it. The $1/k$ continuum, referred to as the incoherent component, is invariant as the crystal is rotated, whereas the coherent peaks change in position and intensity, depending on crystal orientation.

A typical coherent bremsstrahlung spectrum is shown in Fig. 2.5. The distinction between incoherent and coherent components in the figure is artificial; it is there to show the part of the spectrum that shifts as the crystal is rotated. The vertical scale in the figure gives the photon rate for the given beam current and crystal thickness. Note that the intensity of the incoherent background is less than what would be obtained with an amorphous carbon radiator of the same thickness, because a part of the momentum transfer integral in the Bethe-Heitler formula has been moved into the discrete sum and contributes to the coherent part. The radiation length of diamond is actually an average over all orientations of the crystal. In the calculation for Fig. 2.5 the leading 400 lattice sites were included in the discrete part of the calculation, although it can be seen that, at the chosen crystal orientation, only two or three of them contribute with sufficient intensity to be individually visible in the spectrum.

2.2.2 Use of Collimation

The presence of the large incoherent continuum in Fig. 2.5 presents a significant handicap to a photoproduction experiment. Not only do the continuum photons produce background in the detector, but they diminish the polarization of the beam. The entire beam polarization appears in the coherent component; the underlying incoherent flux only serves to dilute the polarization. There is another difference between the two components that allows them to be separated to some extent. The kinematics of bremsstrahlung confines most of the intensity of the photon beam to forward angles within m/E radians of the incident electron direction. This is true both for the incoherent and coherent components. In the lab this is a small angle, but in the rest frame of the electron-photon system it subtends all angles in the forward hemisphere. The difference lies in the fact that a peak in the coherent component corresponding to a single reciprocal lattice vector has two-body kinematics, so there is a well-defined relation between the emission angle and the energy of the emitted photon in the lab: emission at 0° yields a maximum energy photon, with energy decreasing with increasing angle. This accounts for the

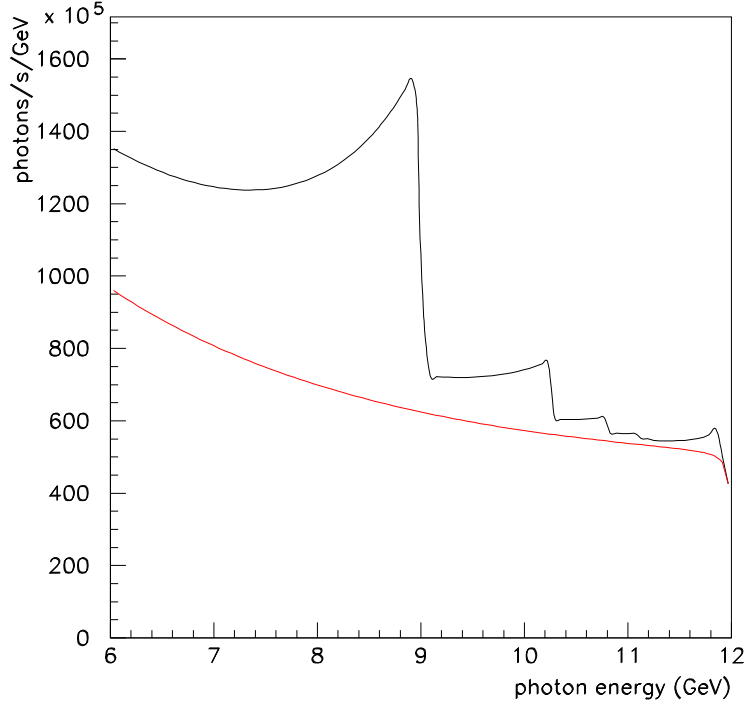


Figure 2.5: Uncollimated coherent bremsstrahlung spectrum, calculated for a diamond crystal radiator $15 \mu m$ thick and a $1 \mu A$ electron beam of $12 GeV$ energy. Typical values are used for beam emittance and crystal mosaic spread.

shape of the coherent peaks in Fig. 2.5, with the sharp right-hand edge corresponding to 0° emission and the tail to lower energies corresponding to emission at higher angles.

The incoherent component, because it comes from a sum over momentum transfers at all angles, has essentially no correlation between photon energy and emission angle. This means that collimating away all photons beyond some angle $\theta_{max} < m/E$ uniformly attenuates the incoherent spectrum at all energies, whereas it preserves all of the coherent photons from the maximum energy for the given peak down to some cutoff. The kinematic relations for coherent bremsstrahlung are as follows,

$$\theta^2 + 1 = \left(\frac{1-x}{x} \right) \left(\frac{x_{max}}{1-x_{max}} \right) \quad (2.1)$$

$$x_{max} = \frac{2\vec{p} \cdot \vec{q}}{2\vec{p} \cdot \vec{q} - m_e^2} \quad (2.2)$$

where x is the photon energy in units of the incident electron energy and θ is the lab emission angle of the photon relative to the incident electron momentum axis, in units of m/E .

The effects of collimation are demonstrated in the calculated spectra shown in Fig. 2.6. First, note that the collimation angles are very small, which requires a long flight path of order $100 m$ in order that the collimator can be larger than the intrinsic beam spot size, otherwise the collimator is cutting in transverse coordinate instead of in angle. This distance is, in fact, a sensitive function of the electron beam emittance from the machine, and must be increased in inverse proportion to the beam emittance if the effectiveness of collimation is held constant.

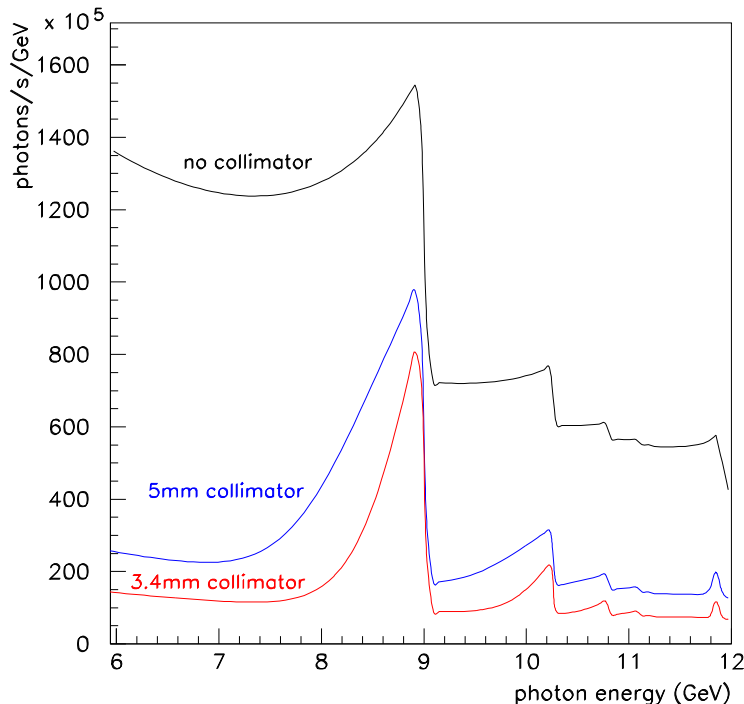


Figure 2.6: Coherent bremsstrahlung spectrum, calculated under the same conditions as in Fig. 2.5, after collimation. The upper curve is the uncollimated spectrum from Fig. 2.5. The middle curve corresponds to a 5 mm diameter collimator placed 80 m downstream of the radiator, or approximately $0.75 m/E$ in collimator half-angle. The lower curve corresponds to a 3.4 mm collimator in the same position, approximately $0.50 m/E$. For the 3.4 mm collimator there are approximately $3.3 \times 10^7 \gamma/s$ in the primary peak for a nominal electron beam current of $1 \mu A$ and crystal thickness of $15 \mu m$.

This issue, along with the associated demands placed on beam alignment and position stability, are taken up in more detail in the following section on the electron beam line.

Second, note that the cut imposed on the coherent peak by collimation does not produce a perfectly sharp edge as would be expected from two-body kinematics. This is because the collimator cuts on radius at some fixed distance which translates into a cut on emission angle only in an approximate way. Thus the curves in Fig. 2.6 are labeled by their collimator size and distance individually, rather than their ratio, which is the nominal collimation angle. Multiple scattering by the electron in the radiator prior to emission, and beam spot size and divergence are the major contributors to the error involved in translating a collimator radius into a cut on emission angle. All of these effects have been incorporated into the analytical calculation of the yields from a collimated coherent bremsstrahlung source that has been used in preparing this report. Crystal imperfections, which amount to an intrinsic spread in the direction of the incoming virtual photon, are also taken into account in the calculation.

Third, note that the relatively weak collimation at 5 mm reduces the incoherent background without significantly affecting the coherent flux near the maximum, and thereby almost doubling the polarization of the beam at the peak relative to the uncollimated case. Further reducing the collimator diameter continues to narrow the peak and reduce the incoherent flux relative to the peak, albeit at some cost in peak intensity.

The 3.4 mm collimator diameter has been chosen for this design because it provides for a maximum reduction in the incoherent flux while transmitting 95% of the coherent flux at the peak. Most of the total photon beam energy coming from the crystal is absorbed by the collimator. For this reason the collimator is located in a separate enclosure outside the experimental hall, and must be surrounded by a considerable amount of shielding. The peak in Fig. 2.6 for a 3.4 mm collimator contains 33M photons/s for an electron beam current of 1 μA , which will be increased by a factor of 3 for full-intensity running of the GLUEX experiment in HALL D.

Fourth, note that the rate seen in the focal plane of the tagging spectrometer corresponds to the upper curve in Fig. 2.6, regardless of the collimation. This means that collimating the bremsstrahlung beam increases the rate in the tagger focal plane relative to what is seen at the detector. For full-intensity running at 10^8 photons/s on target in the coherent peak, Fig. 2.6 implies a rate of 240 MHz in the focal plane within a 600 MeV window around the peak. Combining this rate with the beam pulse spacing of 2 ns leads to an accidental tagging rate of about 50% and to a fraction of ambiguous tags of 40%. Even with ideal electronics the per-second yield of single-tag events is close to saturation at this intensity. The detector and tagging spectrometer design are based upon a maximum rate of 10^8 photons/s on target and 400 MHz per GeV in the tagger. A novel focal plane design is currently under study, to be discussed below in section 2.4, which may enable the focal plane rate to be reduced by about a factor of two without any decrease in the collimated flux.

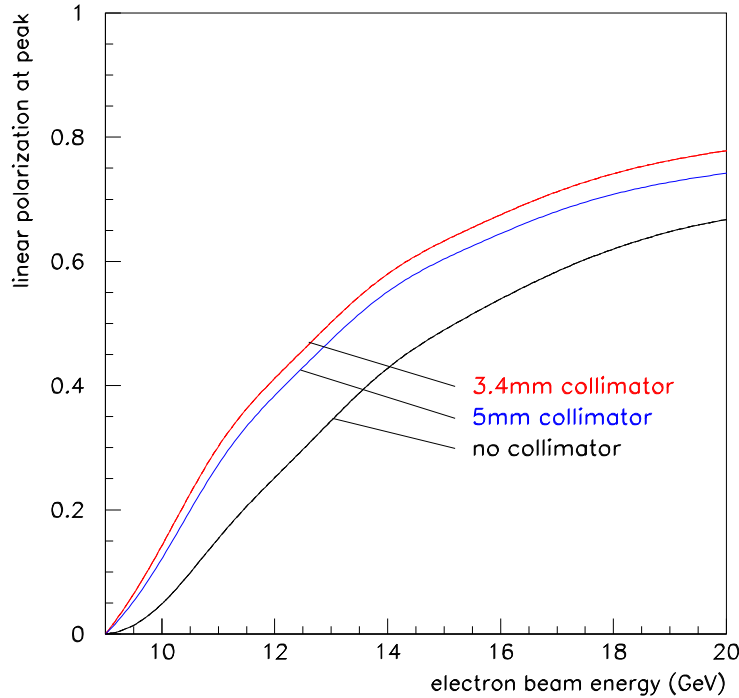


Figure 2.7: Linear polarization in the coherent bremsstrahlung peak as a function of electron beam energy keeping the energy of the coherent peak fixed at 9 GeV. The calculation is performed under the same conditions as in Fig. 2.6.

The linear polarization of the photons in the coherent peak is shown in Fig. 2.7 as a function of the energy of the electron beam. This figure demonstrates why it is essential to have electrons of as high energy as possible, even though photon energies of no more than 9 GeV are required.

The intensity of the coherent peak, not shown in the figure, has a similar dependence on the electron beam energy in this region.

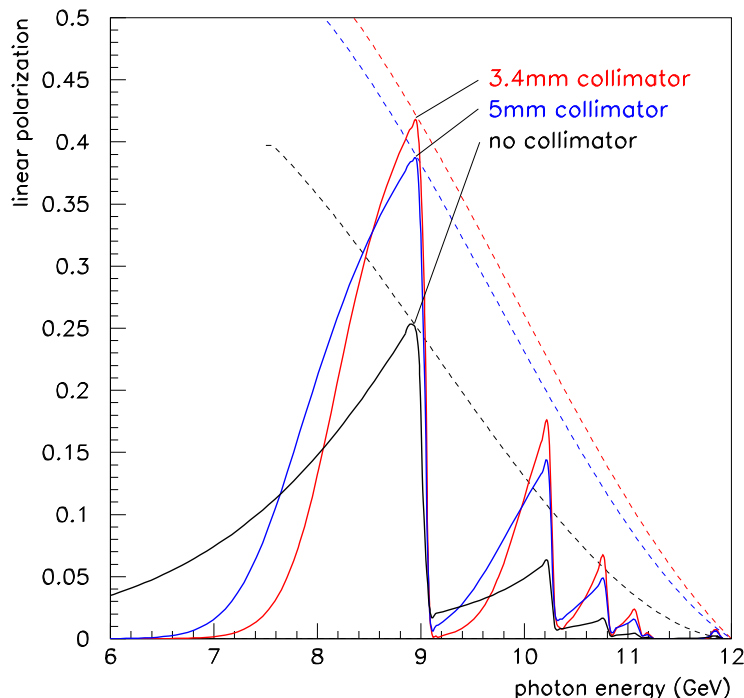


Figure 2.8: Linear polarization of the coherent bremsstrahlung beam for a fixed electron beam energy of 12 GeV , calculated under the same conditions as in Fig. 2.6. The dashed lines indicate the trajectory of the peak polarization as the peak energy is swept across the focal plane by rotating the crystal.

Shown in Fig. 2.8 is the linear polarization of the photon beam *vs* photon energy for fixed electron beam energy. The dashed curves show how the maximum polarization in the primary peak varies as the peak energy is changed by rotating the crystal. The polarization in all cases is zero at the end-point. Without collimation it rises as $(E_0 - k)^2$, one power coming from the intensity of the coherent peak relative to the incoherent component, and the other from the intrinsic polarization of the coherent photons. Collimation allows one to essentially isolate the coherent component, so that the polarization available to the experiment rises from zero at the end-point in a linear fashion. The dashed curves in Fig. 2.8 demonstrate this point.

In order to obtain the full polarization enhancement from collimation, it is necessary to have a distance between the radiator and collimator on the order of 100 m . This distance scale is set by the requirement that the collimator aperture must be large compared to the virtual electron beam spot on the collimator but small compared to the actual photon spot size. The virtual electron beam spot is defined as the profile that the electron beam would have at the entrance to the collimator if it were allowed to propagate freely instead of being bent into the beam dump.

The size of the virtual spot at the collimator is determined by the beam emittance combined with an upper limit of 20 μr on the angular spread of the electron beam at the radiator. The latter value was chosen to match the spread in the beam incidence angle to the mosaic spread of the crystal because it is the combination of the two that limits the definition of the coherent peak. Taking this value together with an emittance of $10^{-8} m \cdot r$, which has been projected for

the CEBAF beam at 12 GeV leads to a virtual spot size of 0.5 mm r.m.s. (1.2 mm f.w.h.m.). Note that this scale does not depend on the radiator-collimator distance. The size of the real photon spot is given by one characteristic angle m/E which defines a circle on the collimator containing approximately 50% of the total photon intensity. The real spot size is proportional to the radiator-collimator distance. At a distance of 80 m the ratio of spot sizes is 6, sufficient to allow collimator apertures that satisfy both of the above inequalities.

Fig. 2.9 shows the peak polarization of the beam as a function of radiator-collimator distance for a coherent peak at 9 GeV . In this calculation the collimator diameter is held constant at 3.4 mm to make sure that the virtual beam spot of 1.2 mm f.w.h.m. is well-contained within the aperture, which is the main condition for effective collimation. At zero distance the collimator has no effect except to attenuate the beam, and so the uncollimated polarization from coherent bremsstrahlung is obtained. At 100 m separation distance the polarization enhancement from collimation has saturated. The design for GLUEX calls for a radiator-collimator distance of approximately 80 m . However from the figure one can see that the performance of the photon source is not a very sensitive function of this variable.

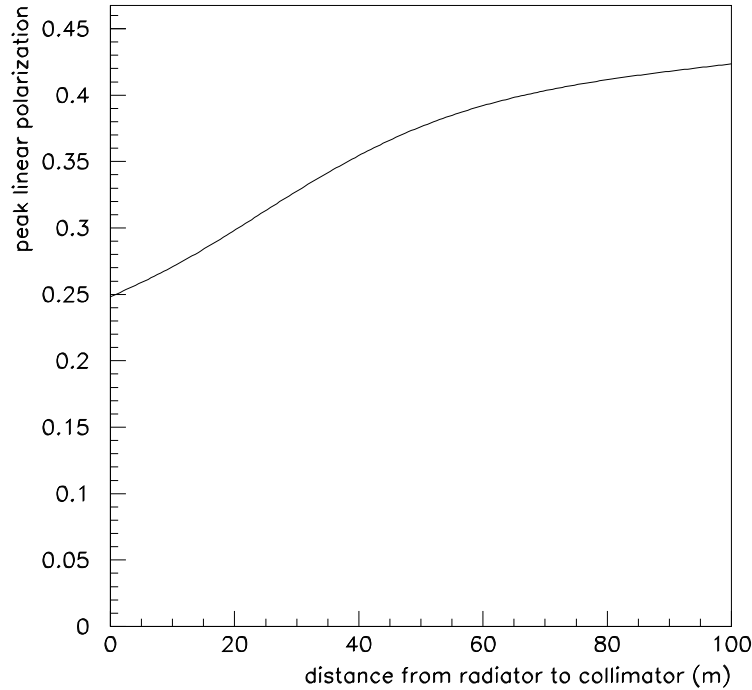


Figure 2.9: Maximum polarization *vs* radiator-collimator distance for a coherent peak at 9 GeV . The collimator diameter is held fixed in this calculation to keep a constant ratio between the sizes of the virtual electron spot and the collimator.

2.2.3 Choice of Radiator

The ideal radiator would be a layered structure with strong transverse fields that alternate between layers spaced about 50 nm apart, thus simulating the standing wave in a cavity driven by a 15 eV laser. While it is possible to construct ordered materials with unit cells as large as this, the self-shielding of atoms means that beyond the atomic length scale the residual

crystal	best reciprocal vector	P/P _{diamond}
diamond	2,-2,0	1.00
beryllium	0,0,2	0.86
boron	2,0,8	0.38
silicon	2,-2,0	0.19
Be ₂ C	2,2,0	1.10

Table 2.1: Figure of merit for various materials that might be used as a coherent bremsstrahlung radiator. This table is reproduced from Table 2 in Ref. [17].

fields are comparatively weak. Hence heterogeneous structures are not viable for use as a coherent radiator. Since the strong fields inside a solid are revealed at the atomic scale, the first requirement for a good radiator is that the unit cell be compact and closely packed. The best radiators are those with the smallest unit cells because these provide the best match between the atomic and the crystal form factors. This match is best for the light elements, and essentially prohibits the effectiveness of any materials heavier than carbon. An extensive survey of possible radiator materials is presented in Ref. [17]. In Table 2.1 is shown the figure of merit that those authors report for favored crystalline materials. The figure of merit is the product of the atomic times the crystal form factor evaluated at the leading peak, normalized to the value for diamond.

Table 2.1 shows that the list of viable materials for a crystal radiator is relatively short. Silicon would be an excellent choice from the point of view of price and fabrication, but unfortunately it is far inferior in terms of performance. Beryllium carbide is not a material that is familiar to the crystal growth industry, and nothing is known at present concerning its suitability for the growth of single crystals of large area. In general compound materials are more susceptible to radiation damage than are pure elements, which would argue in favor of diamond and beryllium metal. These two materials are comparable in terms of their performance.

Most of the experience to date with coherent bremsstrahlung has been with diamond radiators. Extensive expertise with large diamond crystals, such as would be required for the production of coherent bremsstrahlung radiators, already exists within the gem industry. However such capabilities are typically treated in that highly competitive business as sensitive corporate information, particularly as they pertain to the creation of large gem-quality synthetics. Researchers at the University of Glasgow have established contacts within the gem industry for procuring single-crystal diamonds of high quality and large surface area [20]. The techniques used for selecting and assessing the quality of the diamonds are discussed in the next section.

In general terms, diamonds are classified as type I or type II, where type II have been subjected to greater stresses during their formation than type I. Commonly, type II exhibit substantial plastic deformation. Diamonds are also classified according to the form in which nitrogen atoms are present in the crystal lattice. In type *a* the nitrogen is aggregated into clusters of atoms, whereas in type *b* the nitrogen is almost uniformly distributed throughout the crystal. For coherent bremsstrahlung radiators, type Ib diamonds are the most suitable. Unfortunately, type Ib natural diamonds are very rare and probably the most reliable source of Ib diamonds will be synthetics. At present synthetic diamond mono-crystals typically have nitrogen concentrations around 100 ppm.

Synthetic diamonds are made using either vapor deposition (CVD) or high pressure high temperature (HPHT) techniques. CVD diamonds have an extensive mosaic and are unsuitable for coherent bremsstrahlung. However HPHT synthetics look very promising, and the Glasgow group have recently acquired a 5×5 mm² synthetic diamond less than 18 μ m thick which has a [100] orientation. It produces a very good coherent bremsstrahlung spectrum and X-ray measurements show it has rocking curve widths of less than 10 μ r, quite close to the ideal value for diamond.

Beryllium is another material that might be used as a crystal radiator. Beryllium metal is

widely used in industry, being preferred for its high strength-to-weight ratio and robustness, in addition to its transparency to X-rays. Thin films of high-purity beryllium are routinely produced for vacuum window applications, which use some of the same vacuum deposition techniques that would be used for the growth of single crystals. As a radiator material, beryllium is distinguished as the metal with the highest Debye temperature, around 1400°K . The Debye temperature measures the temperature at which the thermal motion of the atoms in the lattice reaches the level of the zero-point motion due to their confinement in the lattice. A high Debye temperature indicates a stiff crystal lattice, in which the atoms have little liberty to move and so have large momentum fluctuations, as dictated by the uncertainty principle.

A high Debye temperature is important for a bremsstrahlung radiator material for three reasons. First, the cross section for coherent bremsstrahlung from a discrete crystal momentum vector \vec{q} contains a factor $e^{-q^2/4M\theta_D}$ which reflects the fact that position fluctuations of atoms in the lattice diminish the coherent effect. This factor is near unity for the low-order crystal momenta provided that the Debye temperature θ_D is sufficiently large. Second, the Debye temperature is, roughly speaking, a measure of the stability of the crystal structure and hence its capacity to survive significant doses of radiation. Third, the radiator material will inevitably be heated by the beam, and will normally operate in vacuum well above the ambient temperature. A high Debye temperature means that there is a large range of temperatures over which the material may operate without degraded performance as a crystal radiator. The Debye temperature of diamond is about 2200° K.

Past experience has shown that diamond meets all of the requirements for a good crystal radiator. Beryllium remains a second choice, to be investigated further in the case that affordable sources of large-area diamond crystals at some point are no longer available.

2.2.4 Crystal Quality

In the calculation of the coherent bremsstrahlung spectrum it is necessary to take into account the fact that even the very best crystals have some dislocations and other defects. Besides locally disrupting the regularity of the crystal, these defects impose stresses which produce small ripples in the crystal planes. If these ripples were amplified, the surface of a crystal would appear like a mosaic of planar regions with approximately parallel surfaces. The scale of deviations from planarity across the face of a single crystal is termed the *mosaic spread* of the crystal. The mosaic spread contributes in the same way as electron beam divergence to the blurring of the exact energy-angle relation for coherent photons.

Besides dislocations, there are other kinds of crystal defects. The presence of foreign atomic species during the crystal growth process can result in the substitution of impurities at some lattice sites, or the formation of voids where impurities tend to collect in clusters of several atoms. In the growth of diamond crystals under conditions of high pressure and temperature, the growth rate is greatly enhanced by the presence of a small amount of nitrogen. Thus it is normal that small amounts of nitrogen impurities should exist even in the best natural stones, as well as in the synthetics created by the HPHT process.

The ideal conditions for growth of a perfect synthetic crystal require pre-existing mono-crystalline diamond with clean planar facets cleaved along the major crystal planes, upon which new layers of carbon are deposited in succession. If conditions are right, the registry of the atoms with the original crystal is preserved over millions of deposited layers, starting from the original seed. In principle, the expansion of the regular lattice should continue to match up perfectly at the boundaries between the different growth surfaces that originated on the facets of the seed, but in practice the strains from small imperfections that occur during the growth process tend to accumulate there, forming recognizable patterns of concentrated defects known as *growth boundaries*. If the stresses grow too large then new strain regions may develop, leading to a more pronounced mosaic pattern in the subsequent layers.

Unfortunately the growth process has proved difficult to control in a reproducible fashion. As a result, out of several dozen stones examined, only one or two may be of sufficient quality for use as a coherent bremsstrahlung radiator for HALL D. The selection process described below

was formerly developed by the Glasgow group to supply crystals for the coherent bremsstrahlung source at Mainz, Germany and subsequently for the Hall B source at Jefferson Lab. The requirements for HALL D are very similar to those of Mainz and Hall B, except that the electron beam current will be higher by about an order of magnitude and the crystals will be cut much thinner.

The diamond ingots from the synthetic process are sliced into sections at the laboratory where they are produced. From these, thin wafers of about $100\ \mu\text{m}$ thickness are cleaved along the (1,0,0) axis and provided to the Glasgow group for assessment. The samples are first examined under a microscope with polarized light. Many of the stresses in the crystal lattice can be revealed in this way, particularly those which exhibit plastic deformation. If the diamond appears clear and featureless under polarized light then it is examined with X-rays. Two types of X-ray measurements are performed.

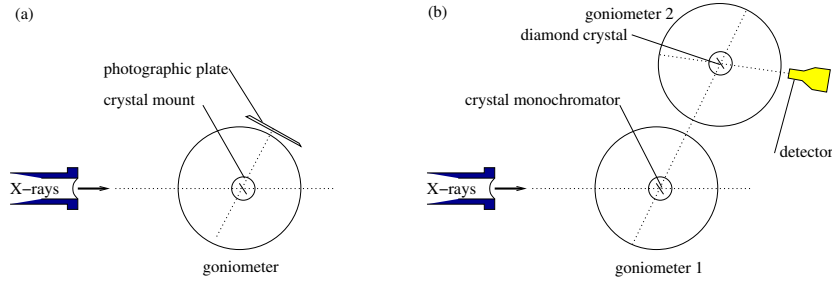


Figure 2.10: Experimental setup for assessment of diamond crystals at the Synchrotron Light Source beam line, configured for topograph measurements (a), and rocking curves (b).

1. Topographs

A topograph is a real-space image of a diamond formed from X-rays that Bragg-scatter from a particular set of planes in the crystal, as shown in Fig. 2.10a. Using the highly-parallel X-ray beam from the Synchrotron Light Source (SRS) and setting the detector at twice the Bragg angle for a known set of planes for diamond, X-rays of the appropriate wavelength to satisfy the Bragg condition are scattered at a precise angle θ into the detector. The X-ray image formed on the plane of the detector is a simple real-space projection of the crystal, called a *projection topograph*. If the vertical slits defining the X-ray beam are narrowed forming the incident beam into a thin ribbon a few μm wide, then the image at the detector reveals a slice through the crystal, called a *section topograph*. Projection topographs reveal any large-scale imperfections in the crystal. Section topographs can be used to examine the depth profile of imperfections. Topographs sample the whole volume of the crystal. Hence, by measuring projection and section topographs, a 3-dimensional picture of the diamond can be obtained. It is also possible to differentiate between screw and edge dislocations. The topograph image reveals dislocations, growth boundaries and any feature which suppresses or enhances Bragg scattering at the selected angle. In principle, topographs taken at different angles provide independent views of the crystal structure. In practice, however, the imperfections that are revealed with one set of planes appear in a similar fashion when viewed from other orientations.

2. Rocking curves

A rocking curve is a plot of Bragg-scattering intensity *vs* angle between the incident X-ray beam and the normal to the crystal planes. A diagram of the setup is shown in Fig. 2.10b. First the broad-band X-ray beam from the SRS is monochromated by scattering at a known fixed angle from a reference crystal, in this case silicon. This beam is then directed at the diamond crystal under study, from which it scatters a second time and is detected. The scattering is appreciable only when the diamond is at just the right angle with respect to the incident beam such that the Bragg condition is satisfied at both crystals. The

variation in the scattering intensity with angle as the diamond wafer is rotated through the resonance is called the *rocking curve* for that diamond. A perfect crystal exhibits a rocking curve consisting of a single peak whose width is called the *natural width* and depends on the material. The natural width for diamond is about $5 \mu r$. Instead of a single peak, for actual crystals one typically sees a number of peaks spread out over a region in angle over known as the rocking curve width. Rocking curves widths, for a selected set of crystal planes, measure quantitatively how any defects or dislocations distort the crystal lattice. By adjusting the slits it is possible to examine the rocking curve of a region of the crystal or to examine the entire crystal at once. Using rocking curves it is possible to measure how close to ideal is the lattice structure of the diamond being investigated.

Figs. 2.11-2.12 show some of the results that were obtained at the SRS laboratory in Daresbury, England in January, 2002. At the left of the figures is shown a projection topograph taken using the (0,4,0) planes, the second harmonic of the (0,2,0) planes used for coherent bremsstrahlung. At the right is shown the corresponding rocking curve taken in combination with a silicon crystal set to reflect from the (3,3,3) planes at a wavelength of 1 Å. The two diamond wafers had been cut from the same original type Ib stone, with Fig. 2.11 coming from the end close to the seed, and Fig. 2.12 coming from near the middle of the ingot. The topographs are negatives, meaning that the image is dark in regions where the X-ray intensity was largest.

The first thing to notice from the topographs is that both wafers are mono-crystalline; there are no regions where X-rays do not scatter. Even so, there are important differences between the two samples. The growth boundaries (the picture-frame pattern) which are visible in Fig. 2.11 spread out and become less pronounced in slice 2 which was taken further from the seed. It is interesting that the strain pattern appears mostly as dark regions rather than light, which indicates stronger scattering in the defects than in the ordered regions, the opposite from what one might naively expect. It should be recalled that both crystals appeared clear and featureless under polarized light at visible wavelengths. The requirement for a diamond radiator useful for HALL D is that the rocking curve width be of the same order of magnitude as the divergence of the electron beam at the radiator, which when folded with multiple-scattering is about $25 \mu r$ r.m.s. The conclusion is that slice 2 is a good candidate for use in the GLUEX experiment, and that slice 3 is not. Having confirmed the quality of slice 2, it should now be possible for the manufacturer to cut a dozen or more wafers of similar quality from that region of the original stone.

2.2.5 Crystal Thickness

The range of permissible thicknesses for a crystal radiator is bounded both from above and below. It is bounded from above by multiple scattering of the electron beam as it passes through the radiator, which causes the divergence of the incident beam to grow, thereby enlarging the photon beam spot on the collimator face and degrading the degree to which collimation discriminates against the incoherent component in favor of the coherent part. It is bounded from below by the fact that the crystal must have some minimum thickness in order to achieve the full coherent gain. In the calculation of the coherent bremsstrahlung process one begins by assuming an infinite crystal, although practically it is presumed to mean only that the crystal is large compared to some characteristic scale. It is important to identify what the characteristic scale is in this problem in order to know how thin one can make the crystal without hurting performance. In the analogous case of the Mössbauer effect, one can estimate the number of atoms participating in the collective absorption by looking at the emission time of the photon (lifetime of the radiating transition) and asking how many nuclei lie within the envelope of the photon wave packet. In the coherent bremsstrahlung process, the lifetime of the radiating system is given in the lab system by the uncertainty principle and by how far the electron energy deviates from its on-shell value between absorbing the virtual photon and emitting the real one. The latter quantity is almost exactly given by q_z , the virtual photon momentum component along the incident electron axis, which means that the electron travels a distance $\lambda = \hbar c/q_z$ during the interaction. For a given

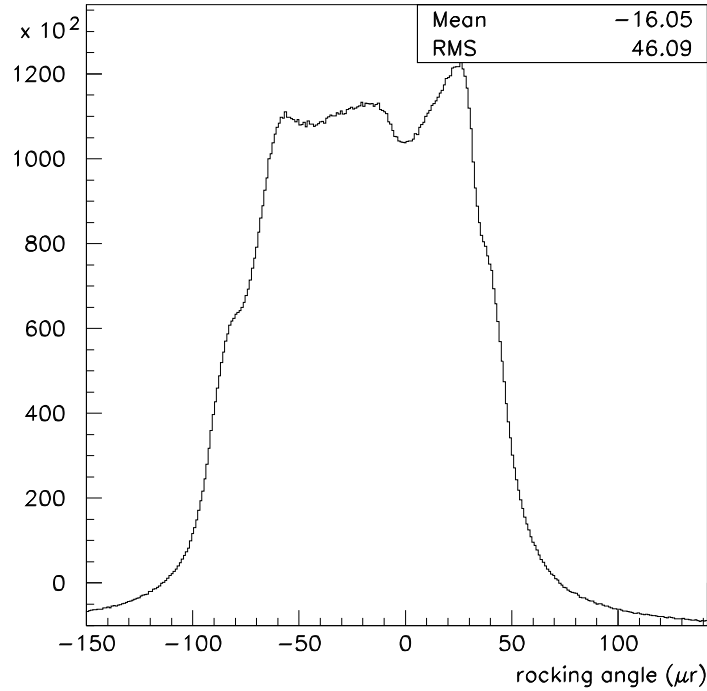
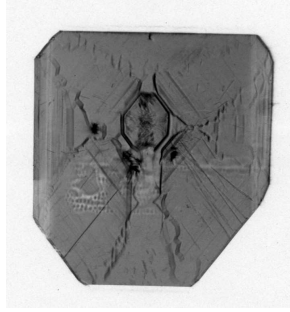


Figure 2.11: Experimental data collected using highly-parallel X-rays from the SRS light source for stone 1482A slice 3 (close to the seed). At the top is shown a projection topograph of the wafer taken using the broad-band X-ray beam and a Polaroid film placed at the angle for reflection from the (0,4,0) planes. The image is a magnified by a factor of 5. The graph shows the rocking curve for the same set of planes, taken using a NaI counter and 1 Å X-rays monochromated by a silicon crystal.

coherent peak at normalized energy x in the photon spectrum, the coherence length is given by

$$\lambda = \frac{2E(1-x)}{xm^2} \quad (2.3)$$

in units of $\hbar c$. From this simple argument one sees that the coherent gain goes linearly to zero at the end-point, a result that is borne out by the full QED calculation. One also sees that the lower limit on crystal thickness imposed by the coherence length depends upon both the electron beam energy and the photon energy. For a 12 GeV beam energy and a 6 GeV coherent photon the coherence length is 18 nm, or about 50 unit cells for diamond. This shows that the coherence length does not impose a practical limit on how thin the radiator should be.

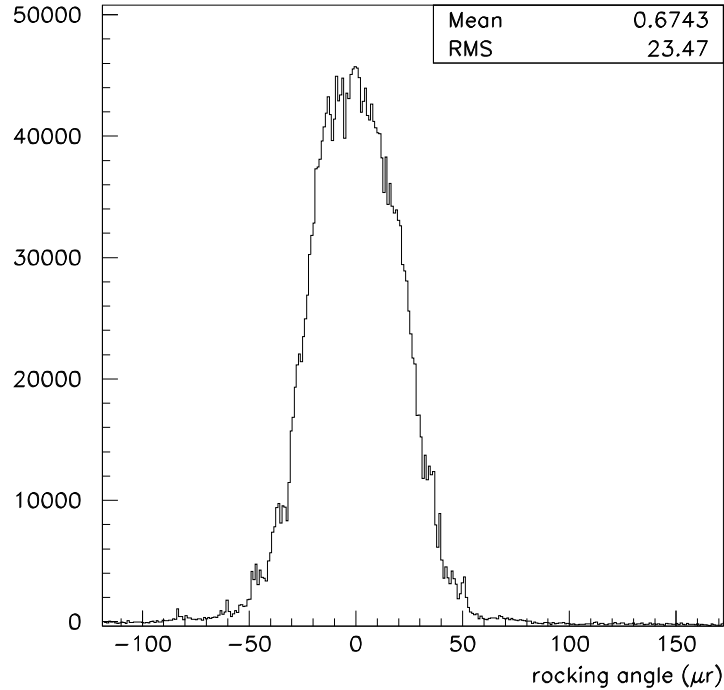
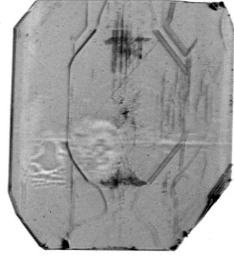


Figure 2.12: Experimental data collected using highly-parallel X-rays from the SRS light source for stone 1482A slice 2 (further from the seed). At the top is shown a projection topograph of the wafer taken using the broad-band X-ray beam and a Polaroid film placed at the angle for reflection from the (0,4,0) planes. The image is magnified by a factor of 5. The graph shows the the rocking curve for the same set of planes, taken using a NaI counter and 1 Å X-rays monochromated by a silicon crystal.

The effects of multiple scattering are best presented by showing the calculated spectra for various radiator thicknesses. In Fig. 2.13 is shown the photon spectrum for a 10^{-4} and a 10^{-3} radiation-lengths radiator to demonstrate the effect. The 10^{-3} radiator spectrum is scaled down by a factor of 10 to facilitate the comparison. The calculation assumes a 3.4 mm collimator located 80 m downstream of the radiator. The loss in normalized intensity with the thicker radiator, as well as the broadening of the left edge of the peak, is due to the enlarging of the photon beam spot on the collimator face from multiple scattering of the electron beam in the crystal prior to radiation. A 10^{-4} diamond radiator is 15 μm thick. The goal for GLUEX is to

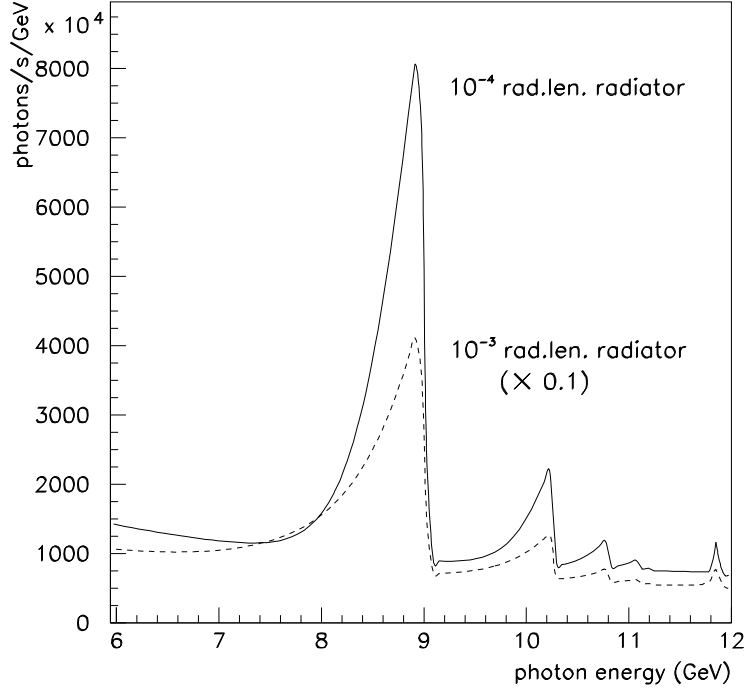


Figure 2.13: Collimated coherent bremsstrahlung spectrum from a $1\mu\text{A}$ electron beam at 12 GeV using diamond radiators of two different thicknesses. The calculation assumes a 3.4 mm collimator located 80 m from the radiator, and typical values for beam emittance and crystal quality.

run with crystals of thickness in the range $10\ \mu\text{m}$ to $20\ \mu\text{m}$.

2.2.6 Crystal Mount

It has already been shown that in order to achieve appreciable coherent gain the crystal must be oriented so that the coherent peaks appear well below the end point. Equation 2.2 then implies that the orientation must be such that the crystal momentum dotted with the beam momentum be of order m^2 . Given a p of 12 GeV and q of 10 keV , this requires that the two vectors must be within $100\ \mu\text{r}$ of perpendicular to each other and that, within a range of angles of that order, the coherent peak sweeps out nearly the full range in x from 0 to 1.

Hence, to have a stable photon beam with the coherent peak positioned at the right energy, the angle between the incident electron beam and the crystal radiator must be adjustable in steps of a few μr and remain stable at this level. Since the angle of the incident beam is fixed by the beamline optics and the position of the photon collimator, all adjustments must be made by changing the orientation of the crystal. This is achieved with a precision goniometer (shown schematically in Fig. 2.14) which should provide motion on at least 5 axes. Rotation about the azimuthal axis ϕ sets the orientation of the polarization plane, rotations about the θ_v, θ_h axes set the angle of the crystal relative to the beam, and x, y translations select the position of the beam spot on the crystal. Estimates of the approximate range and step size for each of the axes are given in Table 2.2.

In practice several targets need to be mounted in the goniometer. The minimum requirement

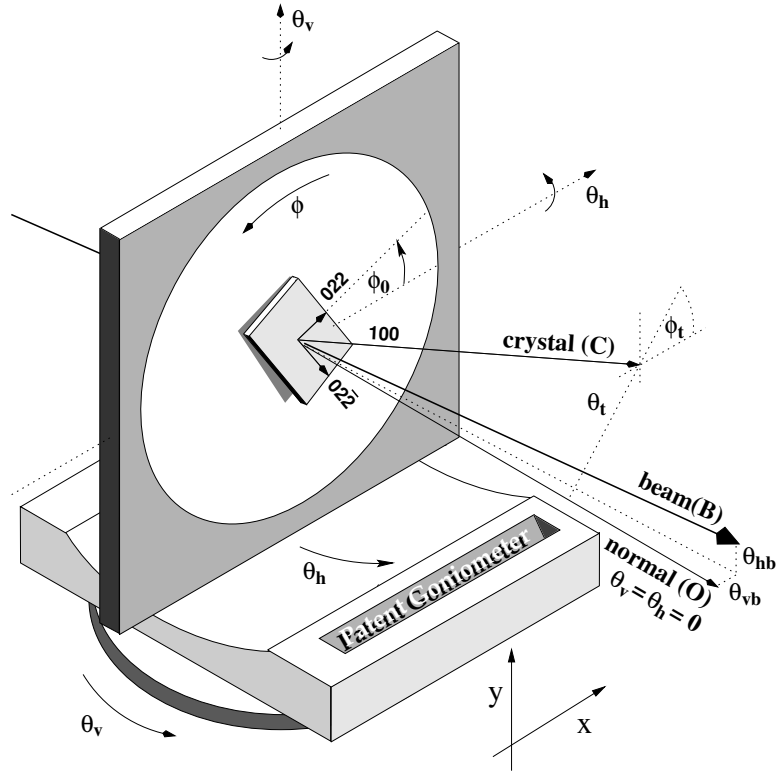


Figure 2.14: Schematic illustration of crystal mounted in goniometer

Axis	Motion	Range	Step size
x	horizontal translation	-50 mm - +50 mm	0.01 mm
y	vertical translation	-20 mm - +20 mm	0.01 mm
θ_v	vertical rotation	-100 mr - +100 mr	10 μ r
θ_h	horizontal rotation	-100 mr - +100 mr	10 μ r
ϕ	azimuthal rotation	-100 $^\circ$ - +100 $^\circ$	0.01 $^\circ$

Table 2.2: Requirements for goniometer axes

is a diamond crystal, an amorphous radiator, and a blank. It is also desirable to have a screen to show the position of the beam spot and a spare diamond. This means either mounting some targets off-axis on the azimuthal plate (as in the Mainz setup), or having a sixth axis to allow a target ladder to sit inside the azimuthal plate (as in the Jlab Hall B setup). A goniometer with the required precision can be obtained commercially, and would be controlled with the slow controls system.

2.2.7 Crystal Alignment and Monitoring

As can be seen in Fig. 2.14 the goniometer setting θ_v, θ_h defines the direction of the normal to its inner plate (O). Ideally at its zero setting $\theta_v = \theta_h = 0$ this would coincide with the electron beam direction (B), but in practice there are small offsets θ_{vb}, θ_{hb} which may vary according to the stability of the electron beam. There will also be a misalignment of the crystal lattice with respect to the inner plate due to imperfections in the mounting and in the cutting from the original stone. The 100 axis (C) will be tilted with respect to the inner plate at an angle θ_t with

this maximum tilt occurring at an azimuthal angle ϕ_t . In addition, the 022 vector will be offset by ϕ_0 with respect to the horizontal. Any motion about the azimuthal axis ϕ changes the angle of the 100 axis (C) relative to the beam. The angle of the polarization plane is set by adjusting the azimuthal angle of the crystal ϕ . Hence when a new crystal is installed, the default value ϕ_0 needs to be measured. Furthermore, to position the coherent peak at the required photon energy, the angle (or *offsets*) between the beam and 100 crystal axis (C) at the chosen value of ϕ must also be established.

Feedback on the relative angle between the crystal and the beam is obtained from a photon energy spectrum derived from the tagger focal plane counters, either via scalers or a TDC hit pattern. The scaler spectrum does not show the effect of collimation (unless the scalers are gated with a downstream photon detector), but can be obtained very quickly since it does not require a triggered data acquisition system. The scaler readout is essential for the alignment process, where the offsets are measured by carrying out a series of scans in which 2d histograms of photon energy vs. crystal angle are built up by moving the goniometer in a sequence of small angular steps and reading the tagger scalers. In addition to providing the feedback required for alignment, the focal plane counters provide essential online diagnostics to monitor drifts in angles caused by the beam tuning, or thermal effects in the crystal mount. If necessary a feedback system could be implemented via the slow control system, where any drift in the position of the coherent peak could be corrected by periodically adjusting the goniometer within predefined limits.

The spectrum obtained from the tagger focal plane can also provide online monitoring of the photon polarization to within 5% by fitting with an analytic bremsstrahlung code. A more detailed discussion of polarimetry appears in the following sections.

2.2.8 Crystal Lifetime

The best information regarding crystal degradation comes from X-ray studies performed by the Glasgow group of a diamond which had been used in the MAMI coherent bremsstrahlung source at Mainz for several years. The electron beam on the Mainz crystal had a diameter of about $100 \mu m$ and it was estimated that around 10^{20} electrons had passed through the diamond during its use in the source. There was a small greenish black spot where the beam had hit the diamond.

The X-ray rocking curve measurements showed that considerable damage had occurred to the integrity of the crystal structure in the center of the beam spot. However $2 mm$ away from the damage center the width of the diffraction peak was the same as it had been for the pristine crystal, which indicates that the lifetime of the crystal could be extended by occasionally moving the beam spot on the face of the crystal.

The area of the MAMI beam spot on the radiator is two orders of magnitude smaller than what is being planned for GLUEX in HALL D. A larger spot means a longer crystal lifetime before radiation damage substantially degrades its crystal properties. Appropriately scaled, the exposure of the Mainz crystal would correspond to 15 years of running in HALL D at the full intensity of $3 \mu A$ without a spot move. Plans for the HALL D source are to keep the exposure about three orders of magnitude less than this. At the SLAC coherent bremsstrahlung beam line it was found that the performance of their diamond radiators had degraded noticeably after a total charge of 3 Coulombs had been accumulated over a spot of size roughly $2 mm$ r.m.s., leading to a limit of about $0.25 \text{ Coulomb}/mm^2$ [21]. Taking this as a conservative estimate for the allowed exposure, the source can run at a full intensity of $3 \mu A$ for 60 hours before it is necessary to move the spot on the crystal. If it had no bad zones, a square crystal of $5 \times 5 mm^2$ would accommodate 5 spot moves before the crystal would need to be replaced. SLAC researchers were able to recover a good performance for the damaged crystals by putting them through an annealing process. Further research and development will be required to determine whether crystal recovery through annealing is an effective way to reduce the operating costs of the HALL D source.

Another issue related to crystal degradation is that of heat dissipation for very thin crystals.

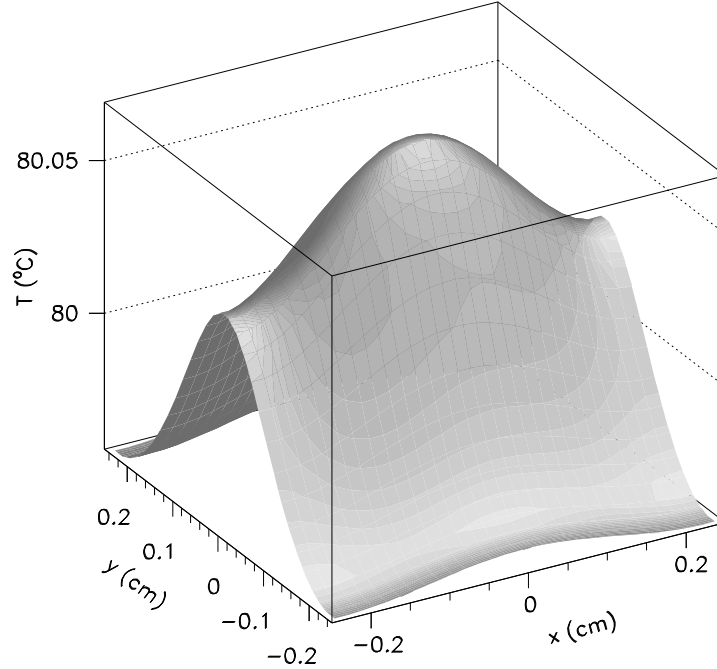


Figure 2.15: Calculated temperature profile of diamond crystal with a 12 GeV beam at 3 μA . The crystal dimensions are 5 mm \times 5 mm \times 15 μm . The ambient room temperature was taken to be 27° C (300 K). The x-y asymmetry is caused by the elliptical shape of the electron beam spot on the radiator.

The heat comes from the ionization energy loss of the beam as it passes through the crystal. Although this is small compared to the bremsstrahlung energy loss, it is not entirely negligible at these beam currents. It can be calculated using the restricted energy loss formula, which yields 21 mW for a 15 μm (10^{-4} radiation lengths) crystal at a current of 3 μA . This is not much power, but the crystal is very thin. Heat dissipation is through radiation and conduction. Diamond has a very high melting point; at low pressures it sublimates at about 4027° C. However at normal pressures it begins to transform into graphite above 707° C, at a rate that depends on temperature. It is therefore important that the crystal at the center of the beam spot stay well below this limit.

The diffusion equation including a heating term and one for radiative cooling can be written as

$$C_P a \frac{dT}{dt} = h(x, y) - 2\sigma (T^4 - T_0^4) + \kappa a \nabla^2 T$$

where the heating term $h(x, y)$ has units of power/area, σ is the Stefan-Boltzmann constant, C_P is the heat capacity and κ the coefficient of conduction for diamond, and a is the thickness of the crystal. T_0 is the ambient temperature of the environment and T is the local crystal temperature, a function of space and time coordinates. After a certain time, T converges to the steady-state solution shown in Fig. 2.15. The calculation used a crystal of dimensions $5 \times 5 \times 15 \mu m^2$ and a beam current of 3 μA . This calculation shows that the conductivity of diamond is sufficient to prevent significant temperature gradients across the crystal even for very thin wafers, and that radiative cooling alone is sufficient to dissipate the heat being generated by the beam passing

parameter	design goals	design results
energy	12 <i>GeV</i>	12 <i>GeV</i>
electron polarization	not required	available
minimum useful current	100 pA	100 pA
maximum useful current	3 μ A	5 μ A
r.m.s. energy spread	< 10 <i>MeV</i>	7 <i>MeV</i>
transverse <i>x</i> emittance	10 <i>mm</i> $\cdot\mu$ r	10 <i>mm</i> $\cdot\mu$ r
transverse <i>y</i> emittance	2.5 <i>mm</i> $\cdot\mu$ r	2.3 <i>mm</i> $\cdot\mu$ r
<i>x</i> -dispersion at radiator	none	negligible
<i>y</i> -dispersion at radiator	none	< 1 cm
<i>x</i> spot size at radiator	1.7 <i>mm</i> r.m.s.	1.55 <i>mm</i> r.m.s.
<i>y</i> spot size at radiator	0.7 <i>mm</i> r.m.s.	0.55 <i>mm</i> r.m.s.
<i>x</i> image size at collimator	0.5 <i>mm</i> r.m.s.	0.54 <i>mm</i> r.m.s.
<i>y</i> image size at collimator	0.5 <i>mm</i> r.m.s.	0.52 <i>mm</i> r.m.s.
distance radiator to collimator	80 m	75 m
position stability	± 200 μ m	

Table 2.3: Electron beam properties that were asked for (column 2) and obtained (column 3) in a preliminary optics design for the transport line connecting the accelerator to the HALL D photon source.

through the crystal so that the crystal mount does not need to act as a heat sink.

2.3 Electron Beam

The performance of the photon source is dependent upon the parameters of the electron beam in several important areas. These parameters are listed in Table 2.3. The first column of numbers gives the set of parameters that have been adopted as the design goals for the source. These are the values that have been taken as input in calculating the characteristics of the coherent bremsstrahlung source. The second column of numbers was obtained from a concrete design of the HALL D beam line [22] that was carried out by members of the Jefferson Lab Accelerator Division. The exact choice of the final parameters has not yet been made, but the preliminary design shows that all of the design goals can be met within the available real estate. The reduction of the radiator-collimator distance from 80 to 75 *m* does not significantly affect the performance of the source.

The following sections highlight the particular properties of the electron beam which have a special impact on the performance of the source.

2.3.1 Beam Polarization

It has already been stated that to generate bremsstrahlung photons with linear polarization it is necessary to use an oriented crystal radiator. However photons with circular polarization are produced by ordinary incoherent bremsstrahlung any time the incident electrons are longitudinally polarized. In fact for 9 *GeV* photons produced by 12 *GeV* electrons, the transfer from electron beam longitudinal polarization to photon beam circular polarization is greater than 80%. This raises the question of what happens when one has longitudinally-polarized electrons incident on an oriented crystal radiator. What happens in this case is that the photon beam is elliptically polarized; it carries both circular and linear polarization. There is a sum rule that limits the sum of the squares of the linear plus circular polarizations to be no greater than 1. Hence one sees the linear polarization in coherent bremsstrahlung going to zero as one approaches the end-point energy (see Fig. 2.8) while at the same time the circular polarization goes to 1 at the end-point (assuming electrons of 100% longitudinal polarization).

The statement in Table 2.3 that electron beam polarization is not required for the GLUEX experiment in HALL D is correct, but it is not correct to assume that the photon source is independent of the state of polarization of the electron beam. The presence of a non-zero circular polarization in the HALL D photon beam will, in principle, produce observable effects in the angular distributions measured in photoproduction reactions. This means that there will be an important coupling between the GLUEX program and the other experimental halls whose programs sometimes require them to have control over the beam polarization. This coupling can be eliminated by setting up the tune of the electron beam line to HALL D such that the longitudinal component of the electron beam polarization is rotated to zero at the crystal radiator. Whether the decision is made to rotate it away or simply to measure its value periodically, this consideration underlines the importance of having a means to measure photon beam polarization in a way that does not rely on *a priori* knowledge of the properties of the electron beam.

Although the ability of the source to produce photon beams with both circular and linear polarization complicates operation when one of them is desired without the other, it does increase the versatility of the source. The two kinds of polarization are controlled independently of one other, and together they give access to a more complete set of polarization observables than would be possible with only one or the other.

2.3.2 Beam Emittance

The values for the electron beam emittances shown in Table 2.3 are estimates based upon the parameters of the current machine projected to 12 GeV[22]. The definition of emittance used here is the product of the r.m.s. widths of the beam in transverse position and divergence angle. Because synchrotron radiation inside the accelerator occurs mainly in the horizontal plane, the emittance values in x are generally larger than those for y . The two vertical bends required for bringing the 12 GeV beam from the level of the accelerator up to beam height in HALL D do increase the vertical emittance a small amount over its value inside the machine; this effect has been included in computing the vertical emittance shown in Table 2.3.

The longitudinal emittance of the beam is important as it is the limiting factor in determining the ultimate energy resolution of the tagger. The design goal of 0.1% photon energy resolution is well matched to the energy spread expected for the CEBAF beam at 12 GeV.

The place where transverse emittance plays a critical role is at the photon collimator. For optimum effectiveness in collimation it is important that the virtual electron beam spot at the collimator position be as small as possible. The electron beam does not actually reach the photon collimator, being bent into the dump by the tagger magnet shortly after the radiator. But considering the optics of the electron beam as if the tagger dipole were switched off, the electron beam at the radiator can be projected forward to form a virtual image on the collimator entrance plane. The position and size of this virtual spot determines the definition of 0° emission angle for the photons. If this spot is small compared to the collimator aperture and is correctly centered then the bremsstrahlung photons of a given emission angle α intersect the entrance plane of the collimator in a well-defined ring of radius $D\alpha$ concentric with the collimator aperture, where D is the distance between the radiator and the collimator entrance plane. In this way a collimator of diameter d passes only those photons of emission angle $\alpha \leq d/2D$. If however the size of the virtual spot is comparable to or larger than the collimator aperture then the ring image of photons of a given emission angle α is smeared out, so that the effect of collimation is simply to reduce the intensity of the beam but not to enhance the coherent component.

Note that this analysis does not place any specific limits on the size of the beam at the radiator. The beam spot can and should be larger there to increase the lifetime of the crystal between spot moves. For the SLAC coherent bremsstrahlung source the beam spot at the radiator was about 2 mm r.m.s., focused down to a 1 mm r.m.s. virtual spot at the primary collimator positioned 91 m downstream of the radiator.

The superior emittance characteristics of the CEBAF beam allow the transverse dimensions to be somewhat smaller than this for the HALL D source, more so in the vertical than the horizontal

dimension. The difference between the horizontal and vertical emittance of the CEBAF beam implies that making the spot round at the radiator implies an elliptical virtual spot at the collimator, and *vice versa*. It is difficult to construct a collimator with an elliptical aperture, so the choice was made to make the virtual spot round. This is why the beam spot on the radiator is asymmetric.

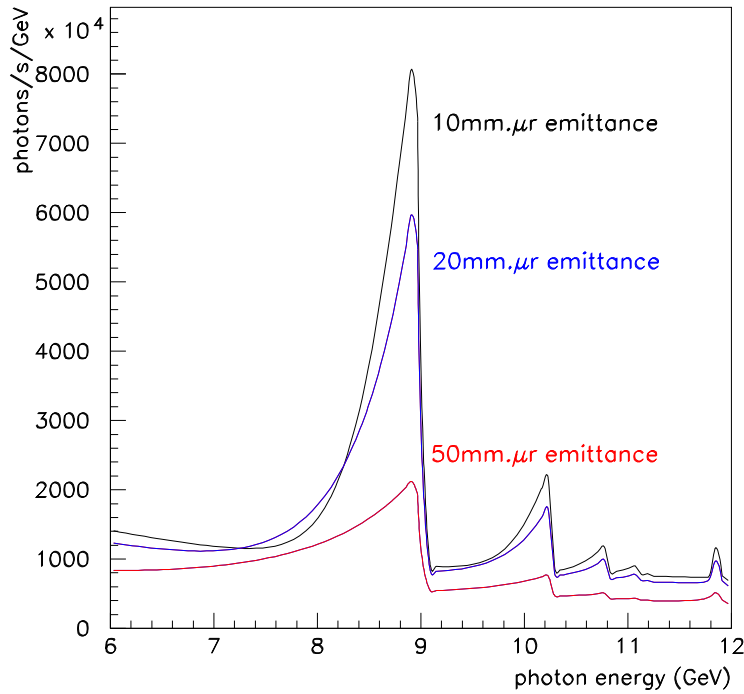


Figure 2.16: Coherent photon spectrum for three different values of the electron beam transverse emittance. The horizontal (shown on the plot) and vertical emittances are assumed to scale together. A 3.4 mm collimator located 80 m from the radiator was used for this calculation.

Figure 2.16 shows how the collimated photon spectrum depends upon the transverse emittance of the electron beam. To generate this plot the increases in emittance were simply translated into an increased virtual spot size on the collimator. This was done because it was assumed that the spot size of the electron beam on the radiator, already close to 2 mm r.m.s., cannot be further inflated and stay contained within the limits of the crystal. When the virtual spot size becomes comparable with the collimator aperture then the collimation is rendered ineffective, and the photon spectrum and polarization revert to their uncollimated values. There is another connection between focal spot size and beam emittance that is connected with the requirement that all electrons enter the radiator at the same incidence angle with respect to the planes of the crystal. Practically, the divergence does not broaden the coherent peak provided that it is kept below the mosaic spread of the crystal. A conservative value for the allowable angular divergence δ in the electron beam at the radiator would then be $20 \mu r$. Taken together with a $500 \mu m$ r.m.s. spot size at the focus, this leads to an emittance of $10 \text{ mm}\cdot\mu r$ at 12 GeV. This corresponds to the upper curve in Fig. 2.16.

2.3.3 Electron Beam Line Optics

Translating the beam emittance into r.m.s. values for the beam radius and divergence requires the knowledge of the β function of the transport line between the accelerator and the radiator, defined as the ratio of the beam size to its angular divergence.

The preliminary optics design [22] of the HALL D beam line (see Table 2.3) is shown in Fig. 2.17. The horizontal and vertical beta functions are shown in the upper and lower panels, respectively. Between the two panels is shown a schematic of the transport lattice. The design begins at the exit of the beam from the end of the linac and ends at HALL D. The z coordinate is measured along the axis of the linac, with its origin at the mid-point of the accelerator. Fig. 2.18 shows the beta functions translated into r.m.s. beam size and shifted to place the radiator at the origin. The design allows the ratio of the spot sizes at the radiator and collimator to be adjusted over about an order of magnitude simply by changing the current in the beam line elements. In this way it will be possible to optimize the optics for a given size of crystal and collimator after beams are delivered to the hall, and more precise values for the emittances are in hand.

Not only must the virtual electron spot be small enough to fit within the collimator aperture, but it must also be centered on the aperture and stable. In order to maintain a stable beam position on the collimator, the SLAC experiment [16] instrumented the collimator with a secondary-emission detector. The detector was of the “pin-cushion” design and was installed between segments of the collimator near the position of the shower maximum. The readout was divided into four quadrants, which read equal currents when the beam was properly aligned on the collimator. The readout was connected via a feedback loop to the last steering elements on the electron beam line prior to the radiator. Over that distance a bend of only $10 \mu r$ results in a shift of 1 mm at the collimator position. The small deflections that are necessary to keep the beam centered on the collimator do not produce appreciable walk in the beam-crystal angle. This means that an active feedback system can be set up between the instrumented collimator and deflection coils just upstream of the radiator, that can operate independent of the crystal alignment system to keep the electron beam aimed at the center of the collimator.

The experimental program in parity violation at Jefferson Lab has already demonstrated a position stabilization circuit that is able to keep the beam position steady to within $20 \mu m$ over a 20 m lever arm. A less sophisticated version of this circuit will meet the position stability requirements for the HALL D photon source.

2.3.4 Electron Beam Dump

The electron beam is dumped in the horizontal plane, as shown in figure 2.4. The horizontal bend offers several advantages over dumping the beam into the ground. The tagger magnet is easier to support if it sits in the horizontal position. It is also easier to mount and service the focal plane instrumentation in this position. The dump itself is also more accessible in case it needs to be serviced. An above-ground dump also affords the possibility of running parasitic beam dump experiments that do not interfere with the operation of the experimental hall.

The primary design requirement for the electron beam dump is that it has a sufficiently high capacity to handle beams of the highest intensities foreseen for the GLUEX experiment in HALL D. A 60 kW design would provide a healthy margin for operation of a 12 GeV beam at $3 \mu A$ and sufficient capacity to handle $3 \mu A$ at 20 GeV in the case of a further upgrade.

2.3.5 Beam Containment and Shielding

There are three factors that must be taken into account in the design of the shielding for the HALL D beam line. The first is the constraint on the background radiation level that is allowed outside the beam enclosure. The second factor is the level of radiation in the experimental hall which can generate background in the detector during normal running. The third factor is the control of hazards which may occur in the event of a failure of one or more of the beam delivery systems. The first issue has been studied by the Jefferson Laboratory Radiation Controls Group, and will be discussed further in the chapter on Civil Construction. The latter two

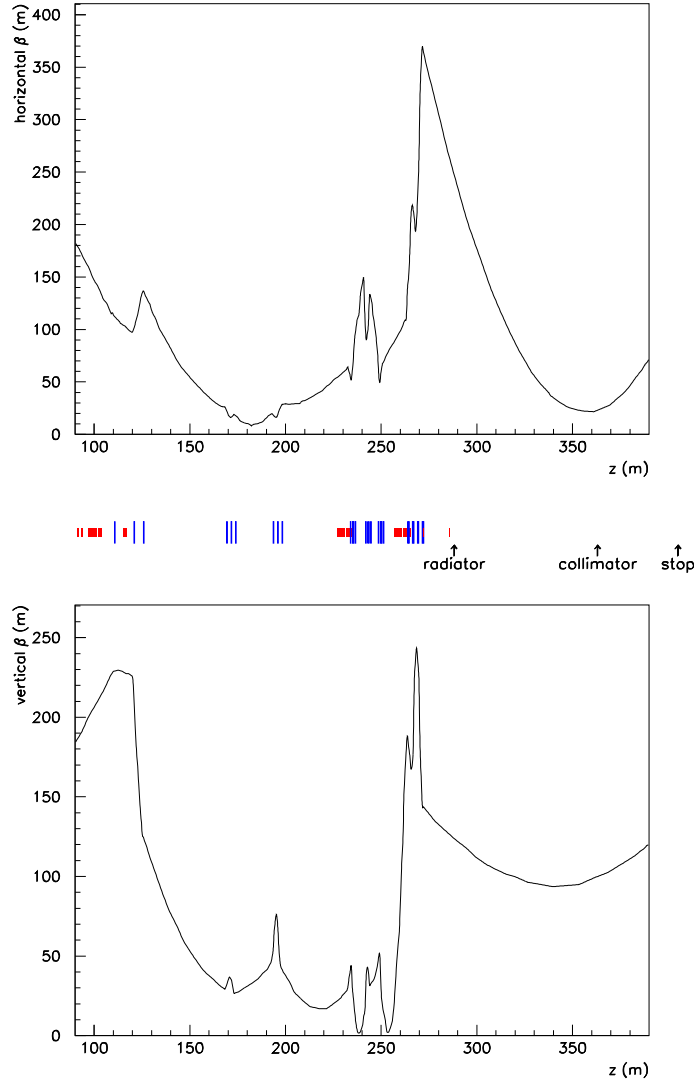


Figure 2.17: Horizontal (upper panel) and vertical (lower panel) beta functions from the preliminary optics design for the transport line from the accelerator to the HALL D photon source. The beam line lattice is shown schematically between the two panels, with dipole magnets represented by the short boxes and quadrupoles by the taller lines. The z coordinate is equal to the flight path length of the electrons starting at the center of the linac, up to an error of a few cm from the vertical motion of the beam.

considerations have been studied by a working group headed by L. Keller (SLAC). A summary of their recommendations [23] follows.

Assuming that the electron beam dump is shielded to the requirements of radiation safety, the next source of background radiation in the experimental hall is the photon collimator. The most penetrating forms of radiation from the collimator are muons and neutrons. A Monte Carlo simulation, assuming a 13 radiation lengths tungsten collimator followed by a sweeping magnet and 5 m of iron shielding, predicted a flux of $1.4 \times 10^3 \mu^\pm/s$ incident on the detector at full operating beam intensity. This is a negligible rate compared with the trigger rate from photon interactions in the target. The flux of neutrons from the collimator is more difficult to calculate, but some fraction of 1 m of concrete shielding will be needed surrounding the collimator enclosure to shield the hall from energetic neutrons.

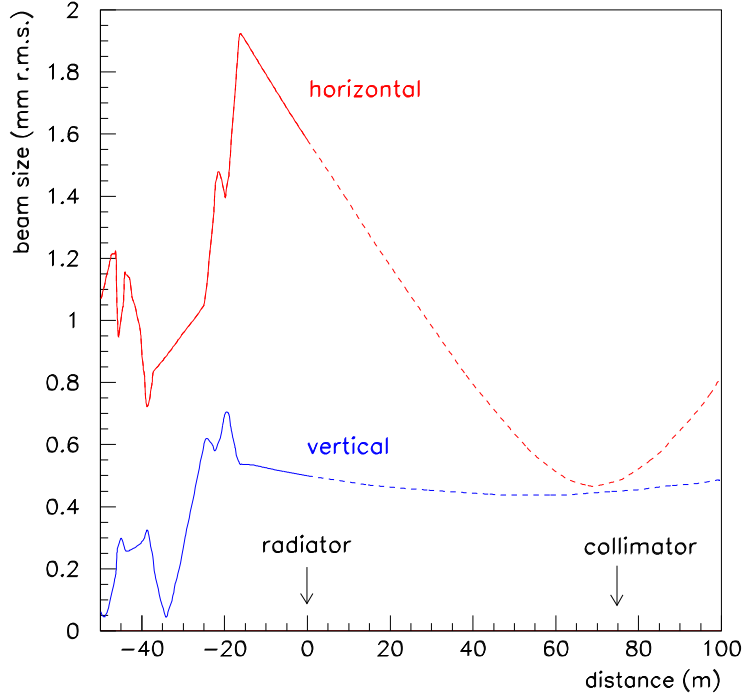


Figure 2.18: Horizontal and vertical r.m.s. envelopes for the electron beam in the region of the photon source, as derived from the beam emittance and beta functions of Fig. 2.17. The origin of the z coordinate has been placed at the radiator. In the region between the radiator and the collimator the envelope refers to the projected image of the electron beam, and does not describe the size of a physical beam that exists in that region.

With regard to hazards associated with the accidental failure of beam line elements or controls, the following measures were recommended in the Keller study [23] and have been incorporated into the HALL D design. The dipole string that bends the electron beam up towards the surface from the below ground and then bends it back horizontal will be connected in series so that failure of a magnet supply or current control electronics cannot result in the beam being steered into the ceiling of the tagger building. The power supply feeding this string of magnets will be protected by a meter relay that shuts off if the current varies from its desired value outside a predefined tolerance. A similar meter relay will also be used on the power supply of the tagger magnet. An electron beam collimator with a burn-through monitor will be located just upstream of the radiator to prevent a mis-steered beam from using radiator support structures as a bremsstrahlung target. Permanent magnets will be located in the upstream region of the photon beam line to bend an errant electron beam into the ground in the case that beam is present while the tagger magnet is off. An emergency beam stop will be installed in the bottom of the photon beam line to catch the errant beam deflected by the permanent magnets. It will be equipped with a current monitor to shut down the primary beam any time electrons are sensed in the photon beam line. Ion chambers located upstream of the photon collimator, and also at the entrance to the photon beam dump behind the experiment, will monitor the total flux in the photon beam and shut off the beam if the flux exceeds a safe value.

2.4 Tagging Spectrometer

2.4.1 Specifications

To satisfy the needs of the GLUEX physics program, the tagged photon spectrometer should meet the following specifications:

1. Photon energy detection from 70% to 75% of E_0 with energy resolution of about 0.1% r.m.s. Percentages refer to the primary beam energy E_0 , i.e. “0.1%” means 12 MeV energy resolution for a 12 GeV beam.
2. A detector system which allows a counting rate of at least 5×10^6 electrons per second per 0.1% over this range of photon energies.
3. An additional capability for photon energy detection from 25% to 90% of E_0 , with less stringent resolution and count rate requirements .
4. A quadrupole magnet between the radiator and dipole spectrometer which images the beam spot on the radiator onto a line on the focal plane. This feature makes it possible to envision the use of focal plane counters with two-dimensional readout, with which one could enhance the tagging efficiency of the source. Focal plane detectors with two-dimensional readout are considered as a possible upgrade beyond the baseline design presented in this chapter. Any improvements obtained using this technique would be over and above the performance figures presented in this report.

The system described below, based on a room-temperature design, meets all of these criteria. The option of a superconducting design was also studied. With a superconducting magnet, the spectrometer could operate at much higher fields, offering the possibility of some space savings in the size of the tagger focal plane array and larger head-room for future possible energy upgrades beyond 12 GeV. An iron yoke design was found which would clamp the 5 T field sufficiently to make it possible to operate normal phototubes on the nearby tagger focal plane. However, as shown below, rate considerations require a degree of segmentation in the tagging counters such that it is impractical to increase the dispersion along the focal plane above what is provided by a 1.5 T room temperature magnet. That being the case, it was decided that considerations of upgrade margin and electrical power alone do not justify the additional cost and complexity of a superconducting magnet.

2.4.2 Magnet

The original design of the tagger spectrometer, which incorporated a single, long dipole magnet ~ 6.1 m in length weighing about 100 tons, has been changed to replace the single dipole with a configuration consisting of two identical dipoles in series with each other.

The main reasons for this change are:

1. It will be difficult to find a supplier of ~ 6.5 m lengths of high quality magnetic iron at a reasonable cost.
2. Since the weight of the top and bottom yoke pieces for a single dipole tagger will weigh more than 20 tons, either a crane with a capacity of more than 20 tons or heavy duty lifting equipment will be necessary to install the magnet or undertake any future repairs or modifications.
3. The long structure of a single dipole tagger will be difficult to install.
4. Since the energy degraded bremsstrahlung electrons exit a tagger along the whole of its length, it is necessary to have the exit completely open. Due to the attractive magnetic force between the poles, the aperture along the exit will distort when the field is present.

The effect of this distortion will probably be less for two smaller dipoles than for a single long dipole.

5. The smaller magnets can be made by more manufacturers and will probably be cheaper.
6. Building costs will be less for the two dipole option - cheaper crane, smaller access doors etc.

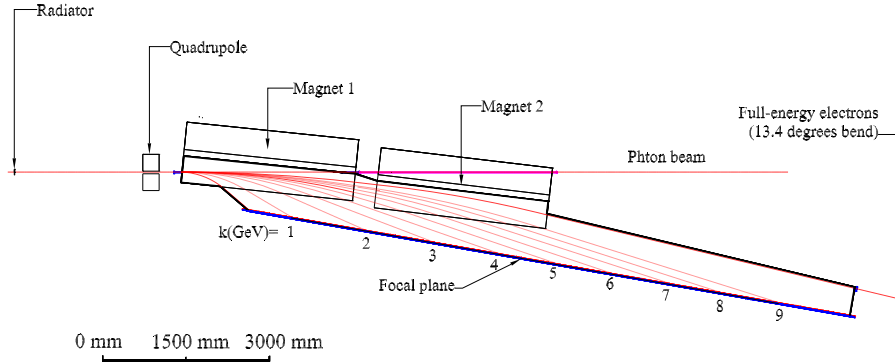


Figure 2.19: A plan view of the tagging spectrometer from above, showing the path of the primary beam and the trajectory of post-bremsstrahlung electrons of various recoil momenta.

The parameters of the two dipole tagger are shown in Table 2.4. The object distance is listed explicitly since it has been increased from 1.5 *m* to 3.0 *m*. This improves the resolution by around 30% and gives more room for the goniometer vacuum chamber, the quadrupole and monitoring devices. A plan view of the layout of the spectrometer is shown in Figure 2.19.

Radius of curvature	26.7 m
Full-energy deflection	13.4°
Object distance	3 m
Field at 12 <i>GeV</i>	1.5 Tesla
Gap width	3.0 cm
Length of each pole	3.1 m
Weight of each dipole	38 tons
Length of focal plane (25% to 90% of E_0)	~ 9.0 m
Coil power	30 kW

Table 2.4: Design parameters for the two dipole tagging spectrometer.

The coils for the two dipole tagger will be run in series from a single power supply.

The first dipole magnet analyzes electrons from 1 to 4.3 *GeV* corresponding to photon energies of 7.7 to 11 *GeV*, and the second magnet analysis electrons from 4.3 to 9 *GeV*, corresponding to photon energies of 3 to 7.7 *GeV*. This is ideally matched to GlueX which requires photons in the energy range covered by the first dipole. It is also clear that a two dipole magnet system is optimum, since with more magnets, the energy range required by GlueX would probably have to be shared between different dipoles.

The pole gap has been increased from 2.0 to 3.0 *cm*. The larger gap is more accessible, and is less susceptible to any changes to the pole gap caused by the magnetic field. Furthermore since only ~ 30 *kW* are required for the 3.0 *cm* gap -compared to ~ 17.6 *kW* for the 2.0 *cm* gap - the coil power consumption remains modest.

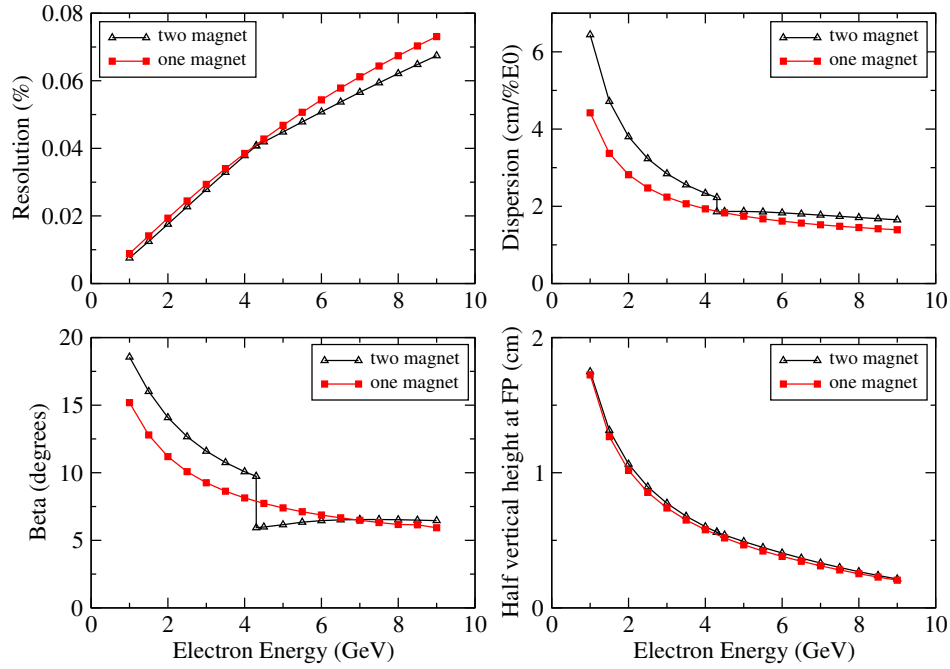


Figure 2.20: Comparison of optics properties between the one dipole and the two dipole tagger.

The two dipole magnet configuration was only adopted after extensive investigations into the magnetic optics confirmed it is possible to design such a system with a continuous focal plane. First order TRANSPORT calculations of the dispersion, resolution and vertical height along the focal plane, as well as beta, the angle at which the analyzed electrons cross the focal plane, are compared for the single and two dipole magnet systems in Figure 2.20.

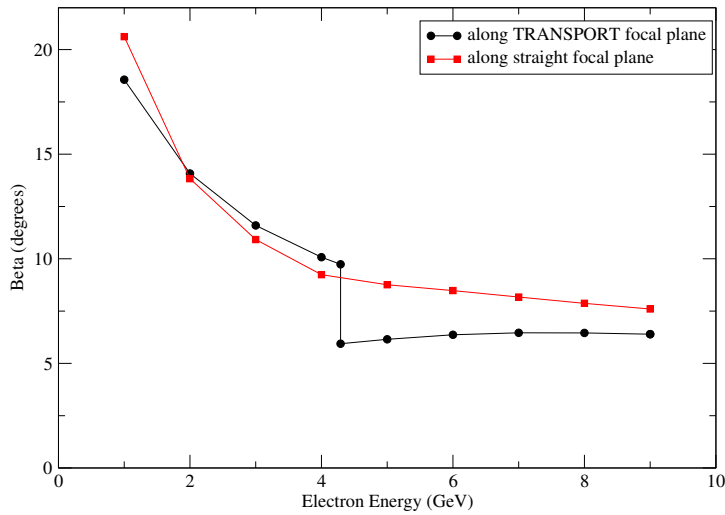


Figure 2.21: Comparison between the beta for the focal plane calculated using TRANSPORT and the beta for the straight focal plane determined according to the TOSCA results.

The resolution and vertical height are essentially unaltered. Although the dispersion shows a small discontinuity at an electron energy ~ 4.3 GeV, which is where the focal planes from the dipoles join, along the whole extent of the focal plane the dispersion from the two dipole tagger is slightly larger. However, beta shows a significant discontinuity at the join of the focal planes. This apparent effect was examined in more detail by ray tracing electron trajectories through a 3-D magnetic field obtained from TOSCA. The ray tracing calculations were also used to find an acceptable location for a straight focal plane which is displaced slightly from the curved TRANSPORT focal plane. Figure 2.21 compares the variation of beta along the straight focal plane obtained using TOSCA, and along the first order TRANSPORT focal plane. It shows that the realistic field computed by TOSCA leads to a smooth variation for beta and also shows that beta is larger for the higher energy section of the focal plane. The magnetic optics parameters, calculated by TRANSPORT along the straight focal plane, are shown in section 2.4.3.

Several designs have been considered for the vacuum system. The most promising approach is to use the magnet poles as part of the vacuum chamber. Either the poles could be welded to a stainless steel vacuum chamber, or the seals between the vacuum chamber and the poles could be made by compressing a viton O-ring between the top and bottom lids of the vacuum chamber and a lip machined round the pole shoes.

A reasonably detailed design for a two dipole magnet tagger, which incorporates a vacuum chamber using O-ring seals, has been completed. The design has been sent to Russian groups within the GlueX collaboration who will examine the technical feasibility of the design and investigate if ISTC funding can be obtained to construct the tagging spectrometer. It should be possible to assemble and test the complete spectrometer in Russia since a feature of the design which uses O-ring seals is that the spectrometer can be fully assembled and tested in the factory where it is built, and then be taken apart and subsequently re-assembled in Jefferson Lab.

The detector package is divided into two parts: a set of 141 fixed scintillation counters spanning the full energy range from 25% to 95%, and a movable “microscope” of more finely-segmented counters designed to span the region of the coherent peak.

The fixed array provides access to the full tagged photon spectrum, albeit at a modest energy resolution of 0.5% and reduced photon spectral intensity. These detectors are well suited for running with a broadband incoherent bremsstrahlung source. They enable experiments to be performed with the highest photon energies possible with the source. When running with a coherent source they play an essential role in the crystal alignment procedure, and provide a continuous monitor of the performance of the source. The microscope is needed in order to run the source in coherent mode at the highest polarization and intensities, and whenever energy resolution better than 0.5% is required. Using the microscope, the source is capable of producing photon spectral intensities in excess of 2×10^8 photons/GeV, although accidental tagging rates will limit normal operation to somewhat less than this.

2.4.3 Spectrometer Optics

Table 2.5 and Table 2.6 give some of the tagger optics parameters as functions of the photon energy. They were calculated for the one-magnet spectrometer option, but the differences between the optics of the two-magnet and one-magnet designs are not very significant, as shown in Figs. 2.20-2.21. The energy resolution and transverse position resolution were calculated assuming the beam properties listed in Table 2.3. The intrinsic energy resolution (i.e. the energy resolution independent of detector size) is limited in most cases by the 0.08% energy spread of the primary electron beam.

At the focal plane, the characteristic bremsstrahlung angle corresponds to a few millimeters of transverse displacement. The vertical beam spot size at the radiator (0.5 mm r.m.s.) contributes a comparable amount because of the large transverse magnification in the dipole transport matrix. However, placing a quadrupole magnet between the radiator and the tagger dipole magnet reduces this magnification nearly to zero over a substantial range of photon energies without substantially changing the other optical properties. Including the quadrupole in the design makes possible a future upgrade of the photon source to employ tagging detectors with

k	Bend	Drift	Angle	cm/% E_0	cm/% E_0
(GeV)	(deg)	(m)	(deg)	perp.to ray	along FP
6	17.270	3.7790	6.035	1.467	13.956
7	17.664	3.2039	6.428	1.568	14.008
8	18.28	2.6276	6.992	1.716	14.096
9	19.108	2.0485	7.872	1.954	14.264
10	20.695	1.4626	9.459	2.407	14.644
11	24.608	0.8560	13.372	3.668	15.860

Table 2.5: Geometrical parameters of the tagging spectrometer for $E_0 = 12$ GeV: Bend = deflection angle; Drift = distance from exit edge to focal plane; Angle = angle between electron path and focal plane; $cm/\%E_0$ = dispersion in units of cm per percent of the incident energy

k	(x x)	(y y)	(y y')	Δk_{beam}	Δk_{spot}	Δk_{tot}	Δy_{tot}	y_{char}
(GeV)	(mm/mm)	(mm/mm)	(mm/mr)	(% E_0)	(% E_0)	(% E_0)	(mm)	(mm)
Without quadrupole:								
6	-0.701	2.737	18.882	0.080	0.081	0.114	1.372	0.804
7	-0.667	2.708	16.538	0.080	0.072	0.108	1.357	0.986
8	-0.625	2.670	14.178	0.080	0.062	0.101	1.337	1.207
9	-0.569	2.617	11.788	0.080	0.050	0.094	1.310	1.506
10	-0.494	2.539	9.341	0.080	0.035	0.087	1.270	1.989
11	-0.389	2.402	6.745	0.080	0.018	0.082	1.201	3.159
With quadrupole: (length = 50 cm, gradient = -0.4 kGauss/cm)								
6	-0.628	0.451	17.622	0.080	0.073	0.108	0.242	0.750
7	-0.583	0.348	15.121	0.080	0.063	0.102	0.190	0.901
8	-0.526	0.202	12.535	0.080	0.052	0.095	0.119	1.068
9	-0.449	-0.024	9.792	0.080	0.039	0.089	0.050	1.251
10	-0.338	-0.427	6.699	0.080	0.024	0.083	0.216	1.426
11	-0.162	-0.416	2.474	0.080	0.008	0.080	0.708	1.159

Table 2.6: Optical properties and resolutions of the tagging spectrometer at the focal plane, for $E_0 = 12$ GeV: (x x),(y y),(y y') = first-order transport matrix elements where x and y are radial and transverse coordinates respectively; the focal plane is defined by (x x')=0.; Δk_{beam} = r.m.s. energy resolution due to beam energy uncertainty; Δk_{spot} = r.m.s. energy resolution due to spot size on radiator; Δk_{tot} = total r.m.s. energy resolution excluding detector size; Δy_{tot} = transverse r.m.s. position resolution due to spot size on radiator; y_{char} = transverse size corresponding to one characteristic electron angle $\theta_{Ce} = (m/E_0)(k/(E_0 - k))$.

two-dimensional readout.

2.4.4 Tagger Detectors

Fixed Focal Plane Array

Tagging of photons over the full range from 25% to 95% of E_0 is not required as part of the physics program here proposed for GLUEX, but is desirable for two separate reasons. First, it will increase the flexibility of the source by providing a broad-band incoherent bremsstrahlung tagging mode, enabling access to photons of the highest energy possible at Jefferson Lab. Second, the process of aligning the crystal radiator for coherent bremsstrahlung requires rotation about several axes and rapid observation of the resulting energy spectra, as described in section 2.2.7. The low-energy portion of the spectrum, between about 25% and 50% of E_0 , is most sensitive to these rotations, and experience with the coherent bremsstrahlung beam at Mainz [24, 25] indicates that the alignment process would be severely compromised if photon energies below $0.5 E_0$ were not measurable.

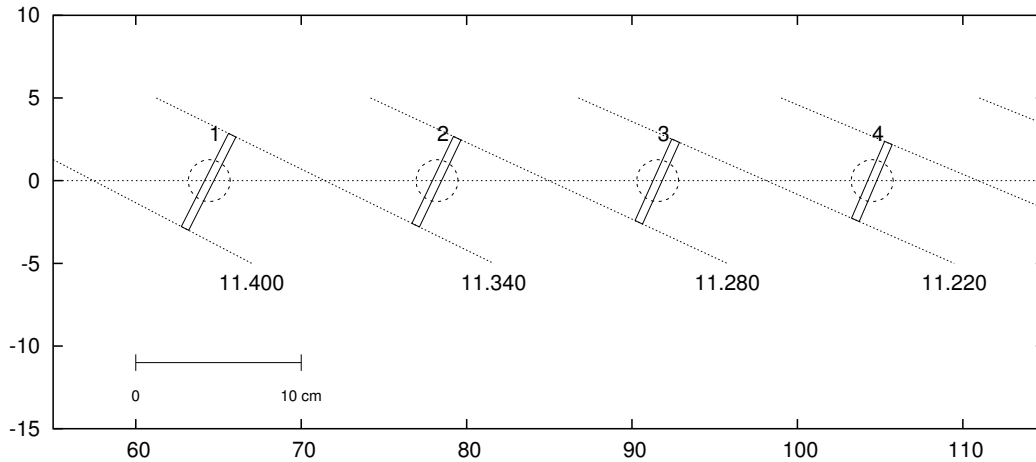


Figure 2.22: Layout of the tagging counters on the high-energy end of the tagger focal plane, corresponding to the lowest-energy electrons from the spectrometer. The view is from above.

The design for the fixed tagger focal plane array consists of 141 non-overlapping scintillation counters. The scintillators are 0.5 cm thick and 4 cm high and are read out by 1-inch phototubes located below the mid-plane of the spectrometer. The scintillator paddles are oriented perpendicular to the scattered electron rays and are distributed along the focal plane to give essentially 100% coverage of the range from 25% to 95% of E_0 . The size and spacing of the counters varies along the focal plane, according to the dispersion and crossing angle listed in Table 2.5. The high-energy end of the array is shown in Fig. 2.22, which corresponds to the lowest-energy electrons from the spectrometer.

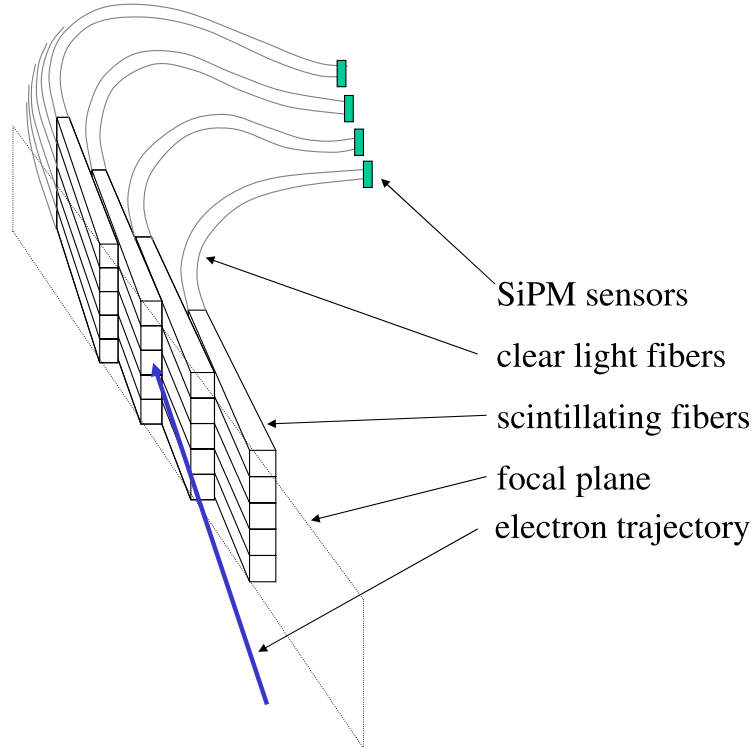


Figure 2.23: Conceptual design of a segment of the tagger microscope, showing the two-dimensional array of scintillating fibers and the clear fiber light guides that couple the light to the silicon photomultipliers.

Focal Plane Microscope Detectors

The design energy resolution of 0.1% r.m.s. (see Table 2.6) is met by non-overlapping detectors which span an energy range of 0.1% each. The principal limitation on detector size is imposed by the design goal of tagging collimated photons at rates up to 100 MHz over the coherent peak. The nominal collimated coherent peak has its highest intensity between about 8.5 and 9 GeV (see Fig. 2.6). However, the the tagger sees both collimated and uncollimated photons, and the total tagging rate in this region is more than twice the collimated rate (see Fig. 2.6), about 250 MHz. The nominal position of the microscope on the focal plane is spanning the region 70% - 75% of E_0 . Dividing this range into 80 bins of equal size limits all channels to less than 5 MHz, which is well within the operating range of the silicon photomultiplier (SiPM) devices foreseen to be used for this detector.

The detector is composed of a two-dimensional array of square scintillating fibers of cross section 1 mm^2 , as shown in Fig. 2.23. Electrons from the spectrometer follow a path approximately parallel to the axis of the fibers, creating a large light yield which effectively suppresses omnidirectional background in the hall and permits the operation of the SiPM detectors with a high discriminator threshold where their dark rate is low. Multiple scattering of electrons in the fiber material effectively produces some degree of overlap between the channels, but does not appreciably degrade the energy resolution of the device. Clear fibers attached to the back end of the scintillating fibers transport the light out of the spectrometer mid-plane to a region with low radiation where the SiPM detectors are located, each with an active area of 1 mm^2 . The microscope will be located immediately in front of the fixed array.

In the baseline operating mode, all five fibers in a column shown in Fig. 2.23 will be summed into one electronics channel. The vertical segmentation of the device also permits its operation in an enhanced mode, where only one fiber in each column is active. In the enhanced mode with the tagger quadrupole switched on, the detector counts only a narrow band of scattered electrons that lies close to the spectrometer mid-plane. This has the advantage that the tagger is blind to those electrons which scatter at large vertical angles in the radiator, whose corresponding photon will be lost on the photon collimator. This can be accomplished efficiently by delivering the power to the SiPM devices independently by row. Simply by selectively powering the individual rows of the array, the readout can be switched from tagging the full vertical range of the beam to counting only a central stripe which corresponds to the size of the photon collimator.

2.4.5 Beam Dump Optics

Although the full-energy beam leaving the tagger magnet is diverging in both directions, the range of angles is small enough that the beam does not blow up rapidly. For a dump distance of 30 *m* the r.m.s. beam size is 6.3 *mm* horizontal (dominated by the 0.08% beam energy spread) and 0.7 *mm* vertical (combination of vertical spot size and multiple scattering in a 10^{-4} radiation length radiator.)

These values scale approximately linearly with distance from the magnet to the dump, and are not very sensitive either to the quadrupole or to small rotations of the exit edge of the tagger magnet. Thus the beam dump design is quite insensitive to the beam optics, and depends only on the lateral and longitudinal spread of the shower in the absorber.

2.5 Polarimetry Instrumentation

The majority of bremsstrahlung photons produced in the radiator are absorbed in the collimator system. If the radiator and collimator system are well aligned, the photon spectrum behind the collimators is dominated by the coherent peak. The beam parameters can be determined by using the intensity spectra from the tagger.

Nevertheless, in order to monitor the polarization parameters – degree (P_γ) and direction (ϵ_γ) – of the collimated photon beam it is crucial to have an independent method, either a photon polarimeter detecting the asymmetry of a process that is well understood within theory (QED) or a well known hadronic process so that the measured beam asymmetry can be compared with theoretical (or experimental) expectations. At photon energies above 5 *GeV*, the forward production of vector mesons is described by vector meson dominance (VMD), resulting in a $\sin^2\theta_{hel}\cos(2\psi)$ dependence of the vector meson’s decay distribution where θ_{hel}, ϕ_{hel} are the polar and azimuthal decay angles in the helicity frame and $\psi = \phi_{hel} - \epsilon_\gamma$. With ρ^0 production accounting for about 10% of all hadronic triggers in the detector, this method suffers no lack of statistics. It is limited only by the accuracy of the VMD approximation, roughly 5 – 10% at these energies.

The other method, measuring the photon polarization by means of a polarimeter, can be realized by a pair polarimeter or a triplet polarimeter. It involves additional hardware components on the beamline between the collimator system and the spectrometer magnet. Both types of polarimeter require a thin radiator and a detector in a field free area followed by a dipole magnet and counters for the trigger. Space is available upstream of the spectrometer in HALL D for the insertion of a polarimeter.

QED based calculations for the latter process show that the angle and energy of the soft (triplet) electron is almost independent of the energy of the incident photon ($\bar{E}_{triplet} \approx 0.7 - 0.9 MeV$). The low rate of this process and the technical challenge for a counter device measuring accurately the angular distribution of low energy electrons do not favor this type of polarimeter.

For pair production, on the other hand, the opening angle between the produced electron and positron decreases with increasing energy making the measurement more complicated at higher energies. A magnetic separation is not desirable because the deflection cannot be determined

very accurately. The proposed polarimeter consists of a thin scintillator ($d = 50 \mu m$) as an active target, 1.5 m in front of a silicon microstrip detector arrangement, followed by a dipole magnet and two scintillators 10 cm apart from the beamline for triggering on symmetric e^+e^- pairs. The microstrip detector consists of four layers having 512 channels each of silicon wafers with a spatial width for a single channel of $25 \mu m$. The second and third layer are oriented at $\pm 60^\circ$ with respect to the first layer, the fourth perpendicular to one of the previous layers, thus allowing to measure the full angular range of produced e^+e^- -pairs without any gap in the acceptance. A Monte Carlo simulation of this device including multiple scattering in the target, the microstrip detector, and foils in the vacuum system (using GEANT) shows that an analyzing power of 25% is achievable (cf. fig 2.24). QED calculations predict an angular distribution for pair production proportional to $(1 + P_\gamma \alpha \cos 2(\phi - \epsilon_\gamma))$ with an analyzing power of $\alpha = 0.28$ for incident photons in the range of 6-10 GeV. Because of the thickness of the microstrip layers ($300 \mu m$) it is convenient to measure the beam polarization for fifteen minutes every time the orientation of the crystal radiator or the electron beam parameters have changed. The scintillator target as well as the detector device have to be mounted on motor driven stages so that they can be removed from the beamline.

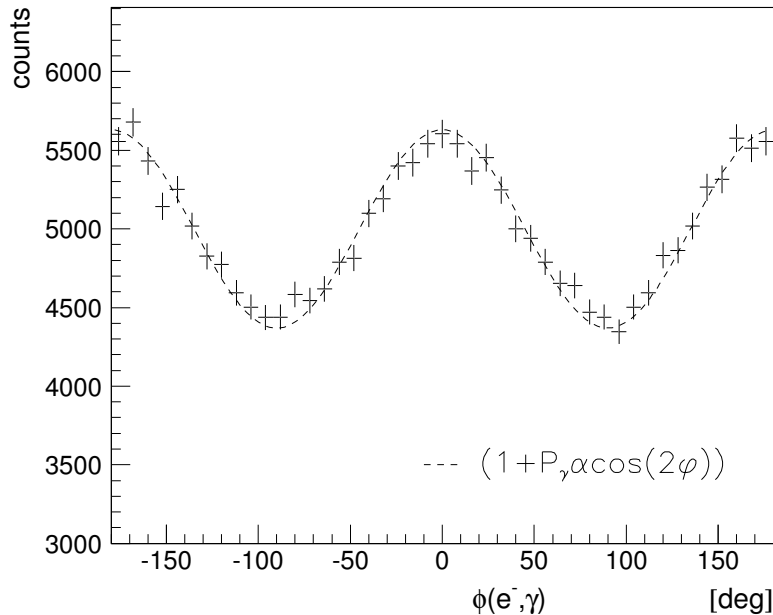


Figure 2.24: Angular distribution for pair production by linearly polarized photons as measured by a polarimeter in comparison with theoretical prediction (*dashed line*). The count rate corresponds to 15 minutes of data taking.

A research and development program is underway at the Yerevan Physics Institute to test these ideas using the 2 GeV coherent bremsstrahlung beam line at YerPhi (Yerevan, Armenia). This 2-year program is funded by the U.S. Civilian Research and Development Fund, and supports a collaboration of Armenian and U.S. collaborators from the University of Connecticut. One of the primary goals of this project is to show the accuracy with which the polarization of a coherent bremsstrahlung beam can be calculated based upon QED and the measured shape of the intensity spectrum.

E of peak	8 GeV	9 GeV	10 GeV	11 GeV
N_γ in peak	185 M/s	100 M/s	45 M/s	15 M/s
peak polarization	0.54	0.41	0.27	0.11
(f.w.h.m.)	(1140 MeV)	(900 MeV)	(600 MeV)	(240 MeV)
peak tagging efficiency	0.55	0.50	0.45	0.29
(f.w.h.m.)	(720 MeV)	(600 MeV)	(420 MeV)	(300 MeV)
power on collimator	5.3 W	4.7 W	4.2 W	3.8 W
power on target	810 mW	690 mW	600 mW	540 mW
total hadronic rate	385 K/s	365 K/s	350 K/s	345 K/s
tagged hadronic rate	26 K/s	14 K/s	6.3 K/s	2.1 K/s

Table 2.7: Operating parameters for an experiment using the coherent bremsstrahlung beam. The calculation assumes a 12 GeV electron beam energy and a 3.4 mm collimator 80 m downstream from a radiator of thickness 10^{-4} radiation lengths. The electron beam current is taken to be 3 μA . The rates in the detector (last two rows) are calculated for a 30 cm liquid hydrogen target and an open hadronic trigger.

2.6 Operating Beam Intensity

Table 2.7 brings together the diverse set of parameters that must be considered in evaluating the optimum beam intensity at which an experiment using the coherent bremsstrahlung beam should operate. All four columns of numbers were obtained for the same beam conditions, except that the crystal orientation was adjusted to align the coherent intensity peak at the energy listed in row one. The second row, labeled N_γ , gives the integrated rate of beam photons in the coherent peak downstream of the collimator. Note the sharp decrease in the intensity of the coherent peak as the energy approaches the end point. By contrast, the incoherent bremsstrahlung flux is approximately constant over this range of energies. The third and fourth row show the height and width of the peak in the polarization spectrum of the beam. Rows five and six report the height and width of the peak in the tagging efficiency spectrum. The tagging efficiency is defined as the number of beam photons of a particular energy reaching the target divided by the corresponding rate in the tagging focal plane. Large tagging efficiencies are required in order to make effective use of tagging. The width of the peak in the tagging efficiency spectrum determines the width of the focal plane that would be active when running with collimation. The peak integral reported in row two is summed within the f.w.h.m. tagging efficiency window. Rows seven and eight give the photon beam power that is incident on the experimental target (and photon beam dump) and the photon collimator, respectively.

The last two rows in Table 2.7 give the inclusive and tagged rates for hadronic triggers from a 30 cm liquid hydrogen target placed in the beam following the collimator. Note that the total hadronic rate is dominated by background (*i.e.* non-tagged) events associated with the low-energy component of the beam. This is why the total trigger rate is essentially constant while the flux in the coherent peak varies with peak energy over an order of magnitude. This table illustrates the value of having an electron beam energy well above the photon energy needed for the experiment.

Chapter 3

The Superconducting Solenoid

3.1 Introduction

Momentum analysis in GLUEX will be provided by a 2.24 T superconducting solenoid magnet. This solenoid was built at SLAC ca. 1970 for the LASS spectrometer and was subsequently moved to LAMPF in 1985 for inclusion in the MEGA spectrometer. The MEGA experiment and the solenoid were decommissioned in place in 1995. The MEGA experimental equipment was dismantled and preparations for shipment started in the spring and summer of 2002. The solenoid was shipped from LANL to the Indiana University Cyclotron Facility (IUCF) for coil refurbishment and testing in October 2002. Currently all four coils have been extensively tested and coils one and two have been completely refurbished. Refurbishment efforts on coils three and four will start in the fall of 2004.

The magnet employs a cryostatically stable design and uses cryostats that were designed to be easily opened for service with hand tools. The inspection of the magnet performed at LANL in 2000 concluded that the solenoid was still in excellent condition and worthy the time and cost involved in relocation and refurbishment. Nevertheless, the magnet support systems are now 30 years old. Even though the magnet is in good condition, it still requires repairs, maintenance, updating, and modifications for use as part of the GLUEX experiment.

3.2 Brief Description

The magnet is described in a technical note [26] and some relevant portions of that description are quoted below. Table 3.1 summarizes important magnet parameters. The refrigeration units are not currently available and new ones are required.

The LASS solenoid magnet provides a 22.4 kG magnetic field parallel to the beam direction. The clear bore inside diameter of the magnet is 73 *inches* and its final - as modified overall length - is 195 *inches*. Within the clear bore region the field homogeneity is $\pm 3\%$. Along the beam axis the field homogeneity improves to $\pm 1\%$. The solenoid is constructed of four separate superconducting solenoidal coil-cryostat units [27] and uses a segmented 232 *ton* iron flux return path that surrounds and supports the coil assemblies. A common liquid helium reservoir is located on top of the solenoid providing the gravity feed of the liquid to the coils.

The liquid helium vessel is surrounded by a liquid nitrogen cooled radiation shield and this assembly is centered in the vacuum tank by a circumferential series of tie bolts designed for minimum conductive heat flux to the helium bath. Radial centering and support are achieved by four low conductance hangers arranged in a spiral pattern. Various tie rods and hangers are instrumented with stress bolts to measure the tremendous forces on the assembly caused by the magnetic fields.

The inductance of the coil is 22 *Henries*, and the magnet is run at 1800 *Amperes*. The liquid helium volume is ≈ 5000 *liters* and the heat load is ≈ 50 *watts*. Refrigeration at Hall D

Inside winding diameter of SC coils	80 <i>inches</i>
Clear bore diameter	73 <i>inches</i>
Overall length (iron)	195 <i>inches</i>
Inside iron diameter	116 <i>inches</i>
Outside iron diameter	148 <i>inches</i>
Coil-to-coil separation	11 <i>inches</i>
Total iron weight	232 <i>tons</i>
Central field	22 <i>kG</i>
Conductor current	1800 <i>A</i>
Total stored energy	36 <i>MJ</i>
Inductance	22 <i>H</i>
Total helium volume (including reservoir)	5000 <i>liters</i>
Operating heat load (liquid He)	30 <i>liters/hour</i>
Operating heat load (liquid nitrogen)	30 <i>liters/hour</i>
Cool-down time	2 <i>weeks</i>
Copper to superconductor ratio	20 : 1 (grade A) 28 : 1 (grade B)
Total conductor length	117,600 <i>feet</i>
Total conductor weight	29,000 <i>lbs</i>
Turn on time	20 <i>minutes</i>
Turn off time (normal)	20 <i>minutes</i>
Axial load per coil due to magnetic forces	280 <i>tons</i>

Table 3.1: Summary of characteristics of the solenoid as used in the LASS configuration.

will be supplied by a small local refrigerator of 200 watt capacity. This over-engineered nature of the design of the magnet, cryostat and the superconductor itself, has produced a stable, reliable and safe superconducting magnet.

3.3 Solenoid Refurbishment Activities

The LASS/MEGA solenoid was inspected in April 2000 by a team from the GLUEX collaboration, JLab staff and two of the original designers of the magnet. This team met at Los Alamos with the MEGA staff and inspected the MEGA magnet installation and the fourth coil. The fourth coil was found sealed in its original shipping crate. The fourth coil iron yoke ring, yoke stand and coil insertion tool were all found in storage. Magnet documentation and spare parts were also found. Jefferson Lab subsequently entered into negotiation with Los Alamos and the DOE to transfer ownership of the magnet to Jefferson Lab. The solenoid was next dismantled by a heavy rigging contract crew and shipped to IUCF in October 2002.

Currently, two coils have been refurbished and the other two are expected to be completed in early 2005. The first two are expected to be moved to JLab in early 2005. After the all coils are completely refurbished at IUCF, the remainder of the solenoid will be moved to JLab for addition of new support systems including the DC system, control system and cryogenic interface. Testing of individual coils at 4.5 Kelvin and a full solenoid recommissioning test are planned prior to installation in HALL D.

3.3.1 Detailed Tests of The Coils

The detailed examination of the solenoid's four coils began in May 2003. The goal of this detailed testing was to accurately determine the leak rates, verify pressure ratings and verify operation of all internal instrumentation. The solenoid has had a 30 year history of large internal leaks which complicated operations and raised the cryogenic heat load. The internal instrumentation

Coil	N2 shield 10 ⁻⁵ torr-liter/s	He Vessel 10 ⁻⁵ torr-liter/s	External Vessel	Over Pressure
1	5	ok	12in bellows	ok
2	ok	0.2	12in bellows	ok
3	4	ok	12in bellows	ok
4	0.4	ok	12in bellows	ok

Table 3.2: Status of leak and pressure testing. To date, coils one and two have been tested and show no leaks. The status of “ok” indicates a leak rate of less than 10⁻⁹torr-liter/s

was known to have deteriorated and accurate checks of coil electrical properties needed to be confirmed.

Coil	Resistance Across coil (Ω)	Resistance LH Lead-Ground (Ω)	Resistance RH Lead-Ground (Ω)	Inductance (mH)
1	4.9	2.2	6.4	372
2	3.2	open	open	244
3	2.7	2.6	0.2	172
4	5.2	open	open	763

Table 3.3: Measured electrical properties of the four coils.

One of the goals of this effort was to carefully perform calibrated leak rate measurements of the four coils’ helium spaces, nitrogen spaces and vacuum spaces. This was necessary to quantify the leaks to guide the decision to repair. A decision was reached early on - when good leak detection sensitivity could not be achieved - to install 8 conflat on each of the four coils. This resulted in achieving leak detection sensitivity of 1×10^{-9} torr-liter per second. At this sensitivity the leaks were quickly identified and quantified. The complication due to 18 inch bellows failure was corrected by replacing the bellows. Coil four, which was not part of the MEGA experiment at LANL, had a non-standard vacuum pump-out flange that required replacing. The coil electrical properties and internal instrumentation were measured during this time also. The instrumentation operability was confirmed and the wiring was verified and documented. The results of the testing are summarized in Tables 3.2, 3.3 and 3.4.

The work at IUCF to test the four coils in detail and to perform such repairs as to permit the testing was concluded in February 2004. At the conclusion of this work all four coils had been extensively tested, and the leak position had been determined in coils one and two.

Coil	Voltage Taps	Carbon Resistance Thermometer (4 to 300K)	Thermocouple (80 to 300K)	Platinum Resistance (40 to 300K)	Strain Gauge (new)
1	ok	7 of 8 ok	removed	30 new	6 new
2	ok	ok	removed	30 new	6 new
3	ok	ok	TBD	TBD	TBD
4	ok	4 of 7 ok	TBD	TBD	TBD

Table 3.4: Table of internal instrumentation and voltage taps. Each coil has voltage taps (VT) and Carbon Resistance Thermometers (CRT) in the Helium vessel and Thermocouples (TC) on the N2 shield and strain gauges (SG) on the support posts.

3.3.2 Refurbishment of Coils One and Two

Following the conclusion of the initial investigations, a contract was negotiated with IUCF to perform all repairs and proof testing on coils one and two. The scope of work of this effort included localizing and repairing all leaks. Replacement of all strain gauges as most had failed. To replace the thermal couples shield thermometers with Platinum resistance thermometers (PT100). The replacement of all wiring, and finally to replace the aluminized mylar multi layer insulation(MLI). A decision was made to retain the original Liquid Nitrogen shields due to their good state of repairs and functionality. The new PT100 thermometers were installed in small copper blocks soldered to the copper shield panels for good thermal contact and reliable mounting. The new strain gauges were installed on the outermost of the three nested cylinders of the cold to warm supports.

Coil one was previously determined to have a shield leak only. The most difficult part of completing coils one and two was reconnecting the shields and plumbing due to the out of sequence reassembly. This necessitated replacing the simple joints with more complex junctions that had only forward facing welds. This technique was used extensively on a magnet in JLab's Hall C namely the HMS Dipole. Both coils were cooled to approximately 120 Kelvin and no leaks were found. A side benefit of this testing was the confirmation of proper operation of the new shield PT100 thermometers and the wiring correctness. Both coils were pressure tested to 100 psi successfully. This concluded the testing and internal repair phase of coils one and two. The next step was to replace all the shield MLI insulation and perform a final evacuation as preparation for placing the coils in storage. Both coils one and two achieved vacuum in the range of 1×10^{-5} , passed a final leak check and were subsequently backfilled with N₂ gas, sealed and moved to an inside storage location at IUCF.

3.3.3 Plans To Complete Coils Three and Four

As of September 2004, coils three and four have been moved into the working area at IUCF and contract negotiations for their refurbishment are underway. This work is expected to begin in the fall of 2004 and be completed before summer 2005.

3.3.4 Plans To Complete The Solenoid at JLab

The remaining work to upgrade and re-assemble and test the solenoid is planned to occur at JLab. Activities during 2005 include securing a test and assembly space in the Test Lab at JLab, moving coils one and two to the space in the test lab and preparing the coils for cool-down to 4.5 Kelvin. This testing effort requires equipping and staffing the solenoid test area in the test lab and designing and fabricating a new single coil test interface. The original SLAC-designed test interface was never found so a replacement is required to support testing. The replacement will have connections matching JLab standards. A set of temporary cryogenic connection lines for use in the Test Lab will also need to be designed and fabricated. These two design and fabricate items will become the highest priority of the JLab HALL D design and engineering staff in FY 2005. This is to support the cool-down and test of one single coil by the end of FY 2005. This test would consist of cool down and fill at 4.5 Kelvin with helium, LN₂ shield cool down and fill and only limited low current operation of the coil.

The solenoid also requires an entirely new control system. The original solenoid had only manual controls and instrument data were recorded in paper log books. The cryogenic control of the solenoid was completely absent and all cooling was achieved by manipulating a small Helium refrigerator. The replacement of the controls on the HMS SC magnets at JLAB at this time and the similarity of many systems and identical nature of others leads to common solutions. The prototype for the solenoid new controls is being tested as this is written. A full system of the prototype is planned for January and February 2005. Following debugging and commissioning of the HMS Dipole prototype system a clone will be prepared for the Hall D solenoid. The current plan calls for a more complete test of coil two using the new solenoid controls, new power supply

(already on site) and would operate a single coil at full current. Test and re-assembly of the entire solenoid are pending and depend significantly on the year of availability of HALL D.

3.4 The Magnetic Field of The Solenoid

3.4.1 Magnetic Modifications Needed

The original SLAC configuration of the solenoid allowed for gaps in the return yoke so that wire chambers could be inserted from the outside. Further, in the LASS and MEGA installations the Cerenkov detector had to be located at large radius due to the presence of high magnetic fields near the downstream end of the solenoid. The source of these high fields has been investigated using a 3D TOSCA model of the yoke and coil and various methods to reduce these “stray” fields have been explored.

The following yoke modifications will reduce the saturation in the pole cap and lower the stray field in the region where the GLUEX Cerenkov will be located:

1. Replace the air gaps with iron rings. This lowers the required operating current to achieve the same central field. The lowering of the local fields especially around coil seventeen helps reduce pole cap saturation.
2. Increase the distance in “Z” between the seventeenth coil and the downstream pole cap. This lowers the local field near the pole cap and thus lowers the saturation.
3. Increase the thickness of the pole cap by adding an iron disk to dilute the pole cap field and reduce saturation.

These yoke modifications will reduce the stray field levels in the Cerenkov region from ~ 700 gauss down to ~ 50 gauss, low enough to be shielded by thin iron and Mu-metal shields.

3.4.2 TOSCA Simulations

The original solenoid magnet was designed without the benefit of modern 3D magnetic modeling, yet the magnet has worked long and well in two experiments. But there has been a persistent difficulty with downstream stray fields, as noted above. Thus we have created a 3D TOSCA model of the solenoids fields to study the problem in detail and design a remedy.

TOSCA Model

The yoke and coils have been modeled using the TOSCA 3D magnetic analysis software. This model was prepared with geometry that allowed simulating the effect of closing the yoke gaps or creating new gaps, or opening or closing the ends by simply changing materials definitions.

The solenoid magnetic field as currently modeled is based on the actual distribution of current within the four coil cryostats and the actual details of the yoke construction. The yoke modifications for the benefit of the GLUEX experiment have also been included. The current distribution of the solenoid can not be modified and therefore the details must be included to accurately model the magnetic fields for experiment simulation taken and to test the effect of various modifications. The TOSCA model also provides valuable design information about the magnetic environment as seen by each detector system. The modifications to the yoke are a mix of requirements from GLUEX physics, the need to lower external fields, and modifications to provide better access for the GLUEX detectors. The TOSCA model is designed to evaluate the yoke modifications needed to lower the external fields. The TOSCA modeled internal fields have already been valuable as the source of magnetic fields for the Geant simulations. Further magnetic simulation work will be performed to study more carefully the effect of all the above changes on the exact B vs I excitation curve, the inductance and stored energy and the forces on the coils. Generally filling in the yoke gaps will lower all of these quantities but the exact values remain to be confirmed.

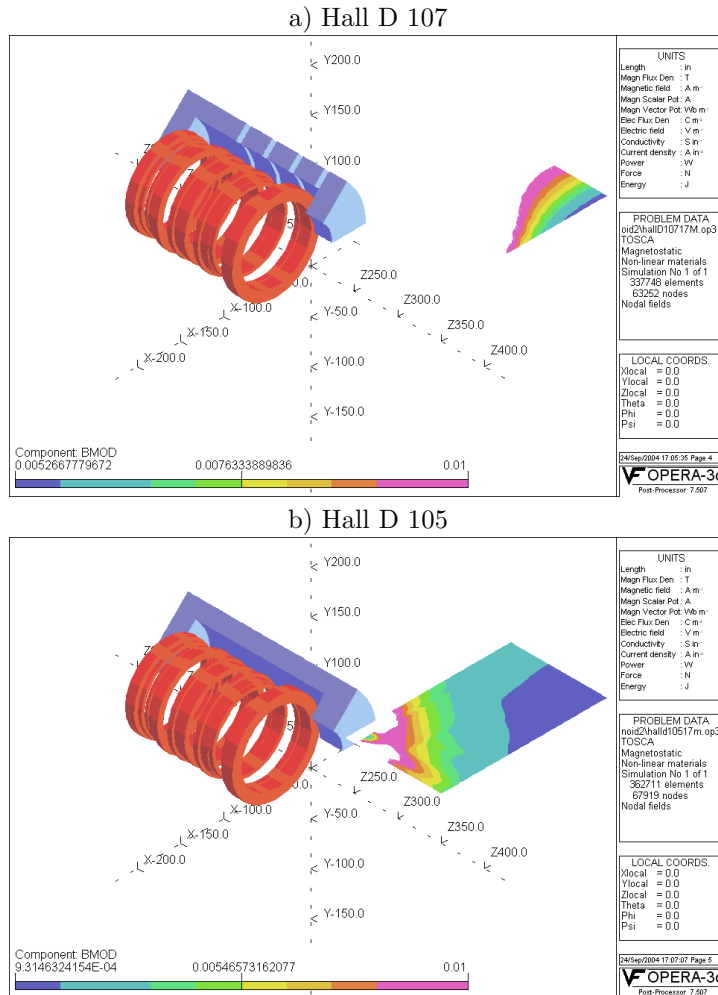


Figure 3.1: TOSCA models for a) the original magnet configuration and b) configuration that fills the gaps with iron, extends the fourth gap and thickens the pole. Both figures show the model for the coils (solenoid and 13th coil ring) and a 45 degree pie slice of the yoke iron. Also shown is a contour plot of fields which are less than 100 G in the region of 50 to 240 in radially and 190 to 300 in along the axis. This is a region that could be considered acceptable for placing photomultiplier tubes. Note that in the bottom configuration the region of low field begins at the iron, allowing detectors to be mounted near the solenoid. The magnetic field scale is in Tesla.

Preliminary Results

Four GLUEX models were investigated. The original and last configurations are shown in Figure 3.1. All four models use identical coil models and identical current densities. The integral field increases by 2.6 % as a result of filling the gaps. The other modifications have no significant effect on the total field. This effect can be easily understood since most of the flux must return through the original gaps. Thus filling them with iron must have a large effect on the field integral while only some of the flux is effected by the other changes, and thus a minimal effect on field integral is seen.

Model Number	Max Field (G)	Min Field (G)	Low-Field Area (%)	$\int B \cdot dl$ (T·Inches)
Hall D 107	1067	523.0	none	302.8
Hall D 106	351	82.5	none	311.0
Hall D 103	241	56.7	17	311.3
Hall D 105	158	45.7	50	310.8

Table 3.5: Field parameters for the region between 50 and 80 in radially, where Cerenkov photomultiplier tubes might be placed. The entries correspond to the maximum and minimum B fields, and fractional area with field below 75 Gauss. Also given is the on-axis field integral for each TOSCA model.

We briefly describe each configuration:

Hall D 107 has the iron yoke and coil configuration of the original LASS solenoid as it was used at SLAC. This model is to provide a baseline for comparison and to compare with historical calculations and measurements. The model has the original segmented yoke with the four original 6 inch air gaps. *This model should be used to measure the effectiveness of the yoke changes which are the subject of the other three models.*

Hall D 106 has the SLAC yoke but with the four 6 inch gaps filled with the same iron as the rest of the yoke. This was a requested change and it has the effect of lowering the external fields. You can clearly see that the external fields are in general lower, especially in the regions where it would be desirable to locate photo tubes.

Hall D 103 has the four gaps filled with steel and gap four extended from 6 inches to 12 inches. This modification was selected because of the extreme saturation in the yoke that was observed around the 13th coil. Fields as high as 3 Tesla are observed near the 13th coil. Moving the yoke further away from the 13th coil will lower the yoke saturation and thus make the yoke more effective in collecting external flux and channeling it back within the yoke iron.

Hall D 105 has the down stream “pole cap” thickened from 20 inches to 26 inches. This is in addition to filling the gaps and extending the fourth gap. This modification was selected to further reduce saturation levels in the yoke and thus reduce further the external fields.

We studied the external fields in the region where Cerenkov photomultiplier tubes may be located. The region extends in z for 20 inches and in R from 50 to 80 inches. The model Hall D 105 has a substantial volume ($\sim 50\%$) with fields between 46 and 74 gauss (see Table 3.5). These fields can be shielded by a combination of soft iron and Mu-Metal tubes. As this region extends from 65 to 80 inches in radius, the photomultiplier tubes for the Cerenkov could be located much closer to the detection volume. A maximum distance of about 2 meters (~ 80 inches) is certainly possible. Figure 3.2 plots the computed fields for the four models as a function of radial distance in the area where we expect to place sensitive detectors, and Table 3.5 summarizes the characteristics for each case. Clearly there are large regions close to the detection volume where tubes could be located. It is also obvious that simply moving further

out can have the same effect. Indeed the original solution chosen at SLAC was to locate the tubes at 4 meters where the fields are ~ 75 gauss for the original SLAC /LASS geometry. The modifications computed above can achieve these field levels in a much more efficient manner.

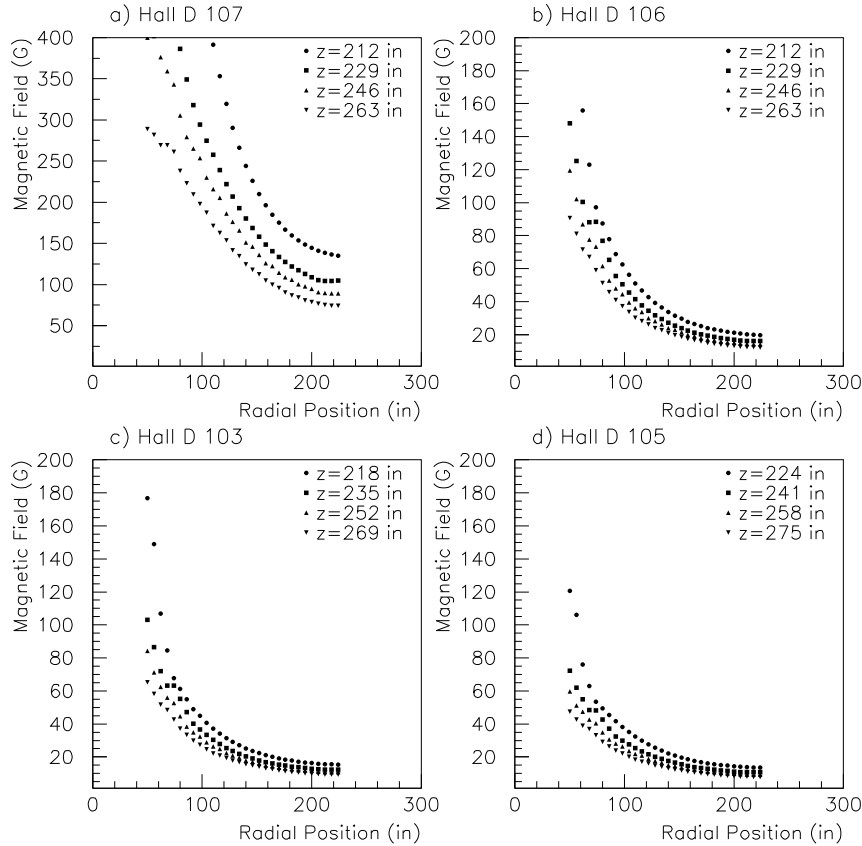


Figure 3.2: Magnetic field as a function of radial distance at constant distance along the z axis for the four different configurations of the solenoid. Note the scale change for plot a).

3.4.3 Compensation of the Upstream Plug

The collaboration desires a matching full aperture hole (73 inch diameter) in the upstream yoke to provide access to the detector volume for service, installation and support, and also to provide a route for cables to exit the upstream end of the magnetic volume. This upstream hole has the same effect on the internal field quality as the downstream hole and thus must be studied carefully. The downstream hole in the yoke is the same diameter as the cryostat inner diameter, 73 inches. This opening is equivalent in magnetic effect to boring a large hole in the center of the pole of a dipole magnet because the end yoke pieces for the solenoid are in fact the poles. The designers of the solenoid compensated for this large hole by increasing the current density in coil # 4, which has four times the average number of Amp-turns of the other 16 coils. This compensates for the missing iron and also contributes to the nearby yoke saturation and stray fields that we dealt with in the previous sections.

We examined four options to deal with the loss of field integral and flatness caused by the new opening: a) no action, b) creating a gap in the upstream yoke and c) increasing the current by 15% in all the coils of cryostat # 1 Figure 3.3 and show the on-axis magnitude of

the field through the solenoid for the various options discussed above. The first is the nominal configuration with the upstream plug in place and the second is with the new upstream hole. All other modifications mentioned earlier are included. The loss of field integral in the backward direction is not a significant problem, but the reduction of flatness has the effect of increasing the computation requirements for analysis. Clearly, an improvement in the upstream field flatness is desirable. We detail the three options considered.

New upstream yoke gap

Creating a new upstream yoke gap was examined in the first round of magnetic simulations and the conclusion was that this creates more of a problem than it solves. The new gaps make a lot of exterior field that can get into phototubes and it adds the complication to the assembly that cables, the yoke and detectors are now linked. The new gaps do not cause a loss of good field region but it does reduce the integral on axis.

Increase current in cryostat # 1

Increasing the current in the 7 coils inside cryostat # 1 by approximately 15% has the effect of increasing the local Amp-turns to boost the field back up and replace the flux lost by enlarging the upstream yoke hole. This can easily be accomplished by stacking a floating DC power supply across cryostat # 1 to enhance the current relative to the main current. The main current power supply provides 1800 A to all 4 cryostats in series. In this way all 17 internal coils are in series and have the same charging and discharging. The small biasing DC power supply that floats across cryostat # 1 permits a local current increase and is adjustable. This method if selected requires that a low amperage (≈ 300 A) current lead be added to the new cryo-reservoir during the solenoid refurbishment. The new DC biasing supply is simply connected between one of the main current leads and the low current biasing current lead. This is an adjustable, low cost, and reliable method to boost the field back up and is identical in principal to the method used to boost the downstream field. Instead of adding turns, which is difficult, one just adds some extra current to the existing turns. The magnet control and quench protection stems are marginally more complex as a result of this solution. Precautions must be taken to guarantee that there can never be a current path through the biasing lead and power supply that conducts the main 1800 A solenoid current. Figure 3.3 is a graph of the central field with extra current in the 7 coils of cryostat #1.

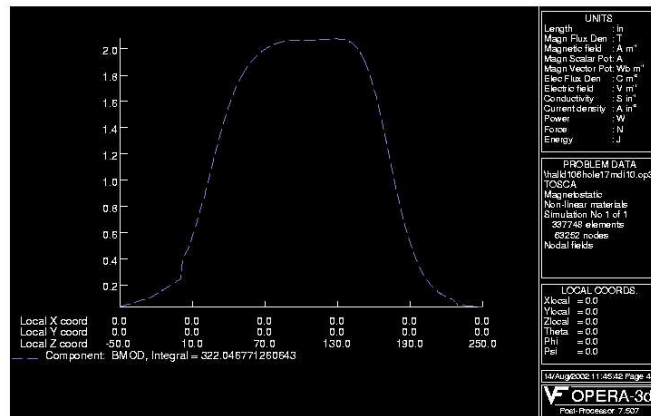
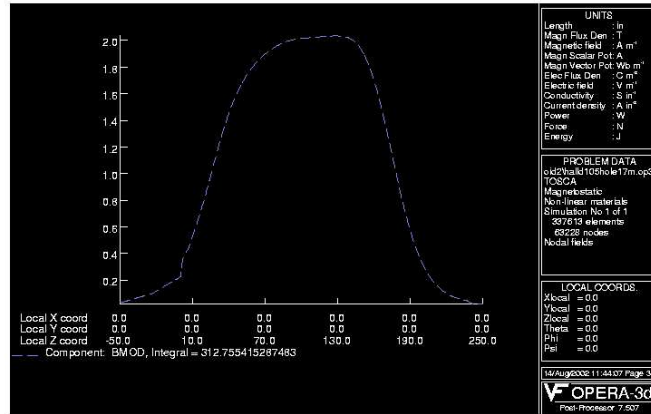
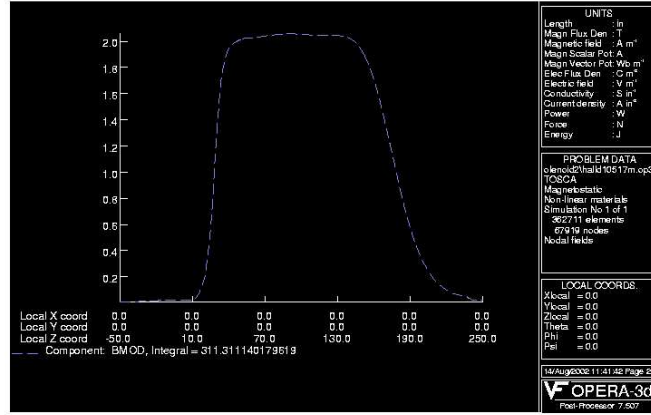


Figure 3.3: Upper) Standard configuration. Middle) Standard configuration without upstream plug. Lower) No upstream plug, nominal current in coils 2-4 (14000 A/in²), but current in coils

Chapter 4

The GlueX Detector in Hall D

4.1 Overview

The goal of the GLUEX experiment is to search for gluonic excitations with masses up to $2.5 \text{ GeV}/c^2$. The identification of such states requires knowledge about their production mechanism, the identification of their quantum numbers J^{PC} and their decay modes. The production mechanism and J^{PC} determination require a partial wave analysis which in turn depends on the kinematic identification of exclusive reactions. The decay products of produced mesons must be identified and measured with good resolution and with full acceptance in decay angles. In many cases the decays of mesons involve a chain of particle decays. The GLUEX detector (see Figure 4.1) must therefore be hermetic with 4π coverage and have the capability of measuring directions and energies of photons and momenta of charged particles with good resolution. Particle identification is also required.

The partial wave analysis technique depends on high statistics and in the case of incident photons, also requires linear polarization. The latter is needed to identify the production mechanism. The linear polarization is achieved by the coherent bremsstrahlung technique. The degree of linear polarization and flux of photons in the coherent peak fall dramatically as the photon energy approaches the endpoint energy. On the other hand, it is desirable to have photon energies high enough to produce the required masses with sufficient cross section and with sufficient forward boost for good acceptance. For a fixed incident momentum and a fixed resonance mass, it is also desirable to have a fairly constant $|t|_{min}$ over the natural width of the resonance. This also requires sufficiently high incident photon energy.

An operating photon energy 9.0 GeV produced from a 12.0 GeV electron beam represents an optimization of beam flux, cross-section and degree of polarization. The GLUEX detector is therefore optimized for this energy range. Figure 4.1 is a schematic representation of the proposed GLUEX detector. The individual subsystems are discussed in more detail below.

4.2 The Target

The main physics program for the GlueX experiment will be conducted with a low-power liquid hydrogen or liquid deuterium target. We propose a design which is very similar to the cryogenic target presently in use in Hall B. This target should fit comfortably into the detector geometry. Solid targets, required for various calibrations, can easily be incorporated into this design.

The maximum power deposited in the target by the beam is 100mW. In such low-power targets, natural convection is sufficient to remove heat from the target cell and a circulation pump is not required. These targets frequently employ mylar target cells. The mylar cell is often mounted on a metal base to provide for liquid entry ports and a reliable means of positioning the cell. The beam enters through a thin window mounted on a reentrant tube at the base of the cell. The diameter of this entrance window must be sufficiently large to allow

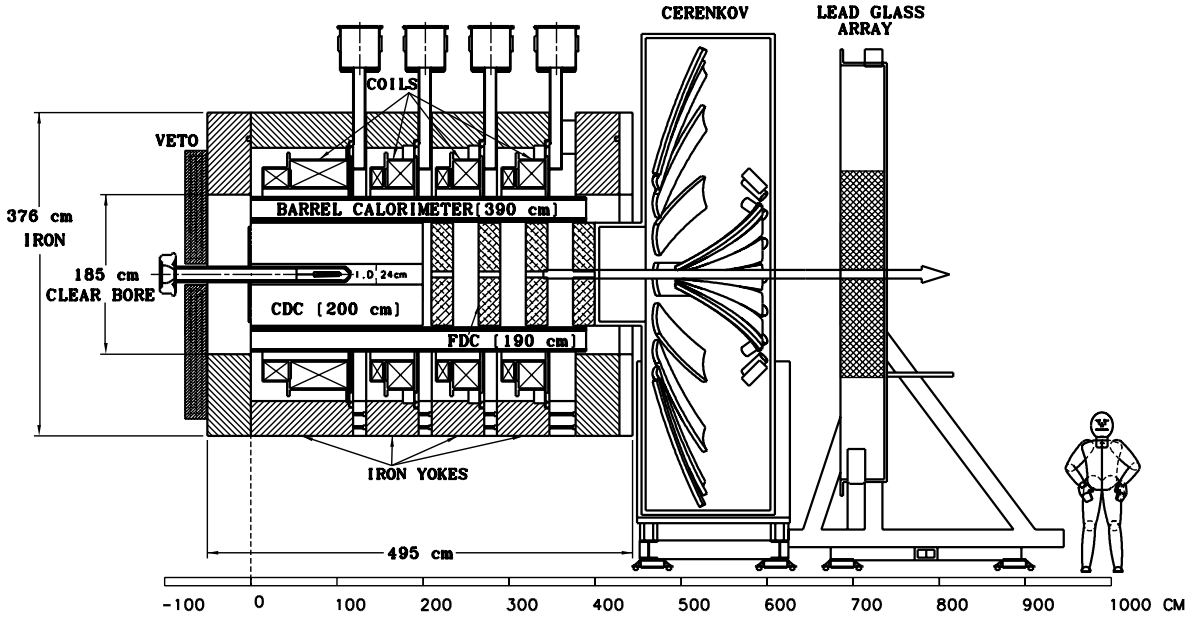


Figure 4.1: An overview of the GLUEX detector. The major subsystems are labeled and are discussed individually in the text.

the beam to enter the cell without scraping; taking into consideration the uncertainties that will be present in aligning the cell. The area between the reentrant window and the outer wall of the cell must be sufficiently large to allow for convection and to prevent bubbles from being trapped. A target cell diameter of three to six centimeters would seem reasonable. A smaller diameter cell would be possible with more stringent alignment requirements. A system such as this, containing a few hundred cm^3 of liquid hydrogen, would be considered “small” by Jefferson laboratory standards and the safety requirements would not place any significant constraints on the target design or operation.

The target cell is connected to a condenser located upstream of the cell. In the Hall B target the condenser is formed by concentric cylindrical shells with the axis of the cylinders lying along the beam line. The heat exchanger should be sized to allow the target to be condensed in a reasonable period of time (a few hours). In some target systems the condenser is cooled by a separate refrigerator. In other systems liquid helium at 4.5K is used as the refrigerant. Because the magnet in Hall D will require liquid helium there seems little reason to operate a separate refrigerator for the target. The standard CEBAF delivery system supplies 5K 3 atmosphere fluid through a 1-3/8” diameter bayonet. This gas is expanded through a JT valve to produce liquid. This system is somewhat cumbersome for small loads. It would be much more convenient to supply the target with low-pressure 4.5K liquid through a small transfer line. It would be possible to draw liquid from the magnet if a port is available. In Hall B it was found convenient to draw liquid helium for the target from a buffer dewar which is filled by a JT valve. To allow for a similar arrangement in Hall D, a 4.5K supply bayonet and a 5K cold return bayonet should be provided.

The extent to which target components shadow the veto counter must be considered. Some shadowing of the veto counter will be unavoidable, since the cell must be supported. As we are relying on convection to remove heat from the target cell it would be favorable to locate the heat exchanger as close to the target cell as possible. This would result in increased shadowing of the veto counter. It is not clear that convection alone would be sufficient if the condenser were located outside the veto detector. This design could easily be tested using the Hall B test cryostat.

The hydrogen cell is located inside of a scattering chamber to provide an isolation vacuum.

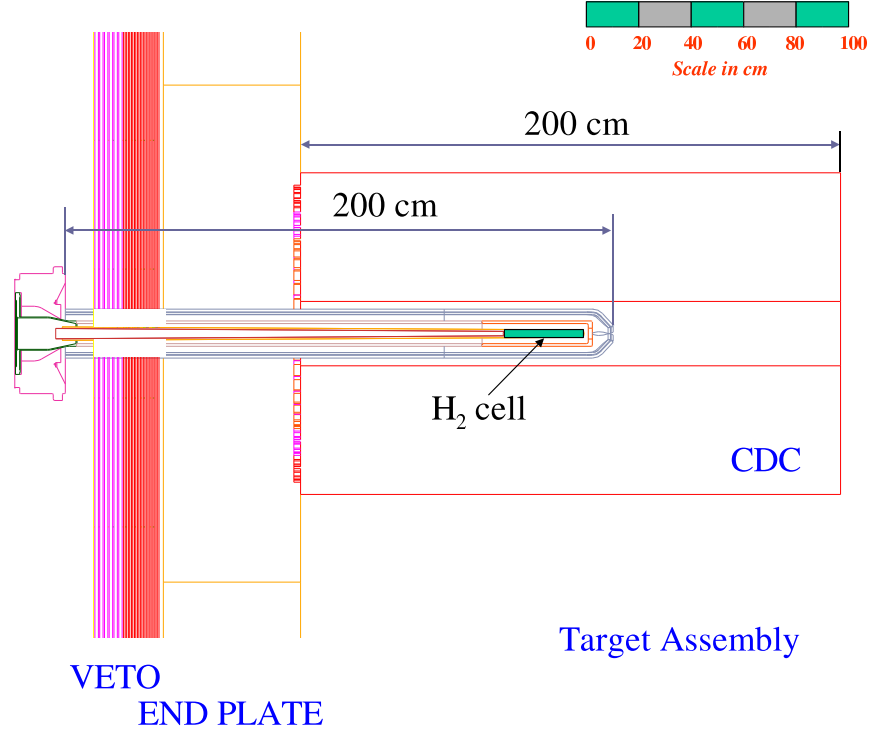


Figure 4.2: Target region including target cell, vacuum scattering chamber, start counter. Sufficient room exists for a vertex detector. Also shown for reference are the CDC and thickness of the magnet iron and upstream veto.

The walls of this chamber should be kept as thin as possible. In Hall B, plastic foam chambers have been used successfully. The target vacuum is likely to be shared with the upstream and downstream beam-lines. The target vacuum chamber would include a service port for the refrigerant, target gas and instrumentation connections.

Solid targets are required for purposes of calibration and studying detector response. It may be desirable to replace the target cell with a multi-foil “optics target” from time to time. Installing the target and bringing it into operation will probably require two days. A mechanism to introduce solid targets either upstream or downstream of the hydrogen cell would be possible. Consideration should be given to the number of different targets required and to their placement.

Attaching the vertex detector and veto counter to the target vacuum chamber will locate those detectors accurately with respect to the vacuum chamber, but may complicate target assembly and disassembly. The cool-down and vacuum motion of the target cell relative to the vacuum chamber will remain major sources of uncertainty in the target cell position. The alignment requirements for this are not severe but should be considered early in the design stage. It is likely that a rail system would be used to position the target inside the magnet, as the insertion cart is used to position the cryogenic target in Hall B. Figure 4.2 illustrates a target cell similar to one which has been used in Hall B positioned inside the GlueX detector. In this design the cell incorporates an extended reentrant window to place all metallic components upstream of the veto detector.

4.3 Calorimetry

4.3.1 Global Design

The electromagnetic (EM) calorimetry for the GLUEX experiment is divided in three parts, each handled by a different detector sub-system.

The very forward angles ($\theta < 14^\circ$) of the HALL D detector will be covered by an existing lead glass detector (LGD) used in the E852 experiment at BNL and re-stacked to meet the geometrical acceptance criteria for HALL D. The approximate polar angular range $14^\circ < \theta < 138^\circ$ will be subtended by the barrel calorimeter. Finally, the upstream, large-polar angle region ($\theta > 138^\circ$) will be the domain of the upstream photon veto.

Each of these three sub-systems is treated individually in a dedicated subsection within this chapter.

4.3.2 The Lead-Glass Calorimeter

The most downstream subsystem of the GLUEX experiment is the lead glass detector (LGD), an electromagnetic calorimeter consisting of nearly 2500 lead glass blocks. The purpose of the LGD is to detect and measure forward-going photons from the decays of π^0 , η and other mesons. The LGD will also provide a fast energy sum to be used in the level-1 trigger.

Each block has dimensions of $4 \times 4 \times 45 \text{ cm}^3$ and they are arranged in a nearly circular stack. The radius ($\approx 1 \text{ m}$) is matched to the aperture of the GLUEX solenoid magnet. The type of glass used in E852 and RADPHI and proposed for use in GLUEX was produced in Russia and is called type F8-00. Its chemical composition is 45% PbO, 42.8% SiO₂, 10.4% K₂O and 1.8% Na₂O. This glass has an index of refraction of 1.62, a density of 3.6 gm/cm^3 , a radiation length of 3.1 cm and a nuclear collision length of 22.5 cm. The blocks were machined to a precision of about 25 microns in transverse dimensions and flatness so stacking the array does not result in gaps. The Cerenkov light from each block is viewed by a FEU-84-3 Russian PMT. The PMT bases are of a Cockcroft-Walton (CW) design [28]. The PMT's will be registered with respect to the glass using a cellular wall that includes soft-iron and μ -metal shielding. The signal from each block will be digitized with an 8-bit 250 MHz FADC. A schematic of the calorimeter is shown in Figure 4.3.

Several of the GLUEX collaborating institutions have been involved in the design, construction and operation of calorimeters of a design similar to that presented here and in the analyses of data from those calorimeters. The first of these calorimeters was a 3000-block calorimeter used in the E852 experiment at Brookhaven Lab (BNL) which used an $18 \text{ GeV}/c \pi^-$ beam and the multiparticle spectrometer (MPS). Details of the design and operation of prototype calorimeters and the one used in E852 have been published [29, 30]. Several physics results based on measurements with the E852 LGD will be discussed here.

An LGD was also used in the RADPHI experiment [31, 32] at JLab that was located downstream of the CLAS detector in HALL B and used in a bremsstrahlung photon beam produced with 5.4 GeV electrons. The goal of RADPHI was a measurement of the radiative decay modes of the ϕ meson resulting in five-photon final states. The experience gained with the RADPHI LGD is extremely valuable for GLUEX. As will be discussed below, the π^0 and η mass resolutions based on measurements from the LGD improve as the distance from the production point of photons (the target) to the LGD increases. The resolutions also improve as the mean photon energy increases and thus as the beam energy increases. Photons produced in RADPHI resulted from interactions of beam photons of energies distributed almost uniformly in the range from 3 to 5.4 GeV and the target to LGD distance was $\approx 1 \text{ m}$. For GLUEX the photon energy is 9 GeV and the target to LGD distance is $\approx 5 \text{ m}$.

Based on the experience with the LGD's used in E852 and RADPHI we expect the GLUEX LGD to provide the granularity and resolution required to carry out the amplitude analysis needed to map the spectrum of gluonic excitations, the goal of this experiment.

In what follows we also address several technical issues regarding the GLUEX LGD including issues of the assessment of the E852 and RADPHI glass and PMT's that will be used in GLUEX,

curing of radiation-damaged glass, electromagnetic backgrounds in the beam region, shielding PMT's from the fringe field of the solenoid, calibration and monitoring.

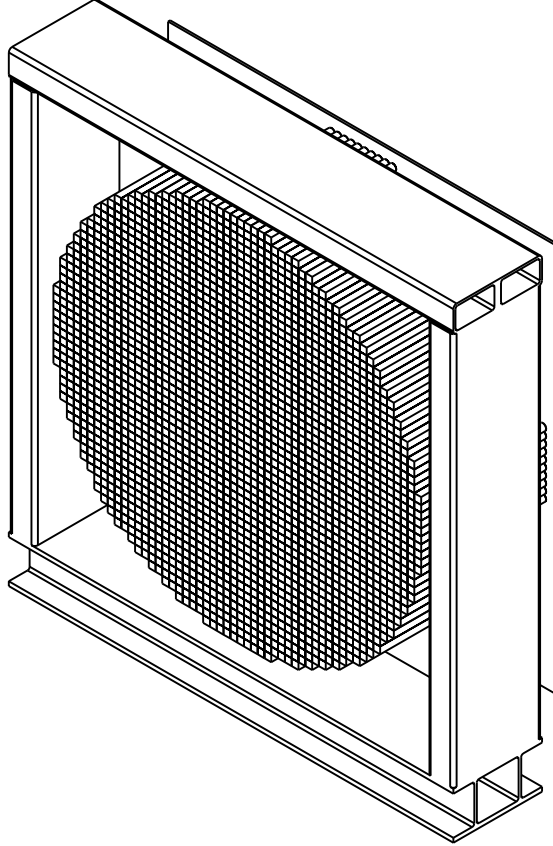


Figure 4.3: The lead glass detector as modified for GlueX . 2500 lead glass blocks will be arranged in a nearly circular stack of radius ≈ 1 m.

The E852 Experience

The goal of E852 was a search for mesons with unusual quantum numbers using the MPS at BNL with a Lead-Glass Calorimeter. The E852 LGD was located 5.4 m from a liquid H_2 target located mid-way inside a large dipole spectrometer magnet. E852 detected and measured both charged particles as well as photons from π^0 and η mesons. The measured mass resolution for π^0 and η mesons was 10 and 25 MeV/c^2 respectively.

Several physics results from amplitude analyses based solely on data from the LGD have been published. Events in which four photons were identified in the all-neutral final state $4\gamma n$ led to analyses of the $\pi^0\pi^0$ [33, 34] and $\pi^0\eta$ systems [35, 36, 37]. Figure 4.4 shows a scatterplot of one $\gamma\gamma$ effective mass combination versus the other $\gamma\gamma$ effective mass from the reaction $\pi^-p \rightarrow 4\gamma n$. Clusters associated with the $\pi^0\pi^0 n$ and $\pi^0\eta n$ final states are clearly observed.

The $\pi^0\pi^0$ effective mass spectrum for the $\pi^-p \rightarrow \pi^0\pi^0 n$ reaction is shown in Figure 4.5. The prominent feature in this spectrum is the $f_2(1275)$ tensor meson. The spectrum also shows a sharp dip at $\approx 1 GeV/c^2$ that is understood as evidence for the scalar meson $f_0(980)$ interfering with the S -wave background. A partial wave analysis (PWA) of these data set was performed [33, 34] for events in various ranges in momentum transferred from the target proton to the recoil neutron and some of the results for the lowest momentum transfer range are shown in Figure 4.6. Plots show open and filled circles corresponding to mathematically ambiguous solutions with

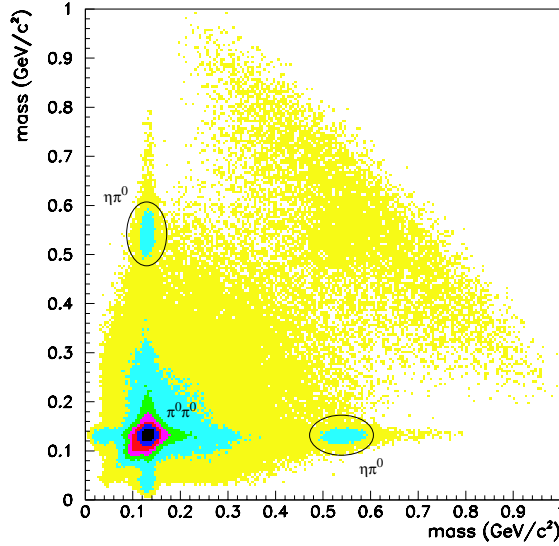


Figure 4.4: Scatterplot of one $\gamma\gamma$ effective mass combination versus the other $\gamma\gamma$ effective mass from the reaction $\pi^-p \rightarrow 4\gamma n$. These measurements were made using the E852 LGD.

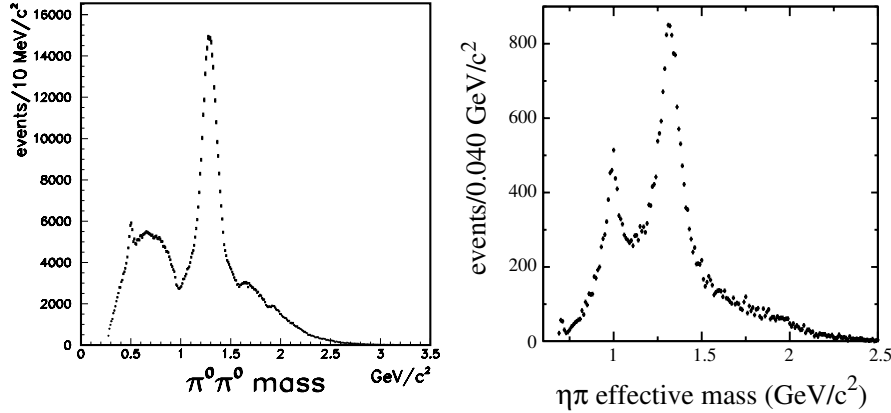


Figure 4.5: left: Distribution of the $\pi^0\pi^0$ effective mass in the E852 reaction $\pi^-p \rightarrow \pi^0\pi^0 n$. right: Distribution of the $\eta\pi^0$ effective mass in the E852 reaction $\pi^-p \rightarrow \eta\pi^0 n$.

the filled circles indicating the physical solutions based on other criteria. The S -wave shows evidence for the $f_0(980)$ scalar meson via its interference with a broad background, the D_0 -wave shows the $f_2(1275)$ and the phase difference between the S -wave and D_0 -waves show the classic motion expected of a resonance.

Figure 4.5 also shows the $\eta\pi^0$ effective mass spectrum for the $\pi^-p \rightarrow \eta\pi^0 n$ reaction. This spectrum features both the scalar $a_0(980)$ and the tensor $a_2(1320)$. A partial wave analysis of this system has also been performed [35, 36, 37].

Figure 4.7 shows the $\eta\pi^+\pi^-$ and $\eta\pi^0\pi^0$ effective mass distributions where well known meson states are clearly observed. The $\eta\pi^0\pi^0$ system requires the reconstruction of six-photons in the LGD. Other analyses involving photons and charged particles have also been published including a study of the $a_0(980)$ in the $\eta\pi^+\pi^-$ and $\eta\pi^0$ spectra [38] and a partial wave analyses of the $\eta\pi^+\pi^-$ [39], $\omega\eta$ [40], $\omega\pi^-$ [41] and $\eta\pi^+\pi^-\pi^-$ [42] systems.

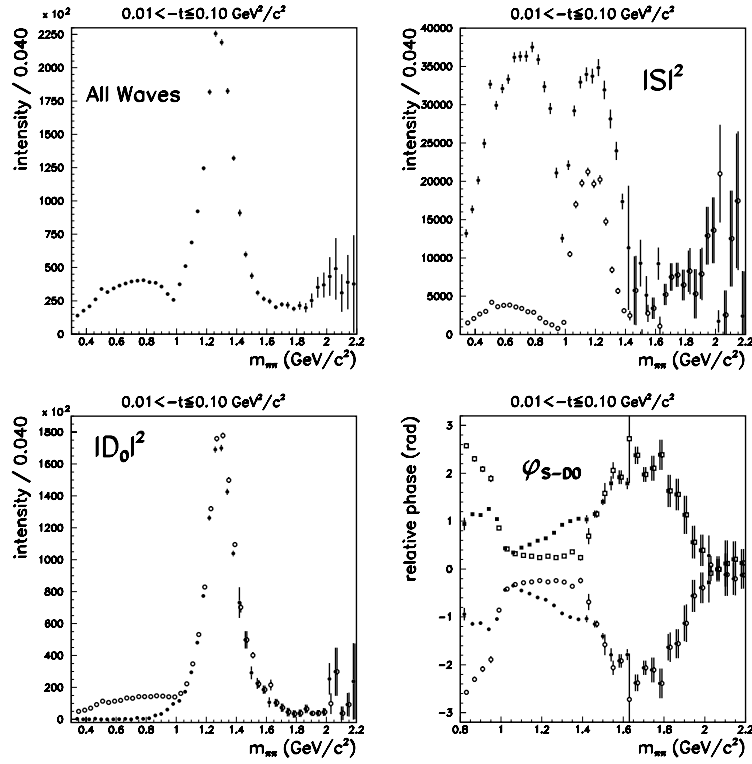


Figure 4.6: Results of a partial wave analysis of the $\pi^0\pi^0$ system in the E852 reaction $\pi^-p \rightarrow \pi^0\pi^0n$ for low momentum transfer events. The sum of all waves (upper left), the S -wave (upper right), the D_0 -wave (lower left) and the phase between the S -wave and D_0 -wave (lower right) are shown. Plots show open and filled circles corresponding to mathematically ambiguous solutions with the filled circles indicating the physical solutions based on other criteria.

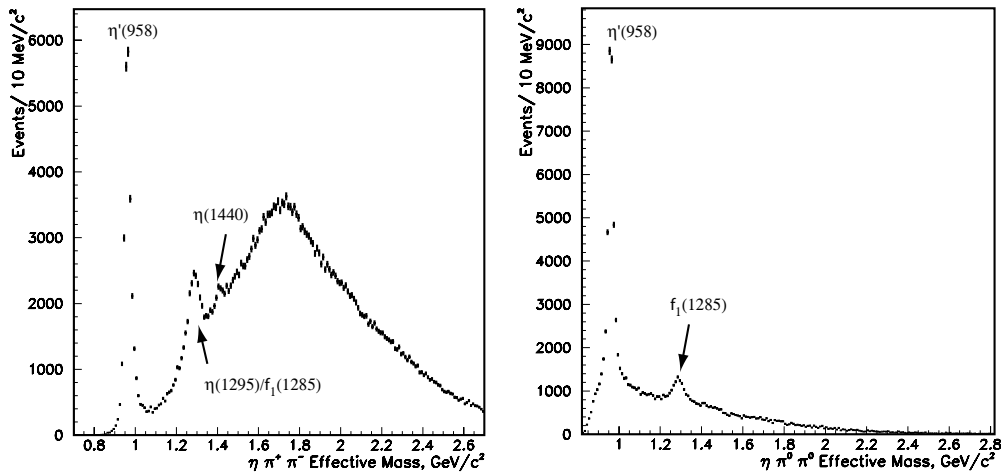


Figure 4.7: left: Distribution of the $\eta\pi^+\pi^-$ and right: $\eta\pi^0\pi^0$ mass distributions observed in E852.

The Radphi Experience

The RADPHI detector is shown schematically in Fig. 4.8. This detector was operated downstream of the CLAS detector in HALL B. The beam was incident on a 2.66-cm diameter, 2.54-cm long

beryllium target. Surrounding the target and extending forward to 30° from the beam axis was a cylindrical scintillator detector (BSD) which provided nearly full angular coverage for recoil protons. Surrounding the BSD was a cylindrical lead-scintillating fiber photon detector (BGD) which served to reject events (off-line) with large angle photons. The primary detector component was a 620-channel lead-glass wall (LGD) assembled to approximate a circle around the beam line with a $8 \times 8\text{cm}^2$ central hole for the passage of the beam. The lead-glass detector was positioned 1.07 m downstream of the target and subtended an angle of approximately 27° from the beam line.

The RADPHI experiment provides an opportunity to understand the operation of a lead glass calorimeter in a bremsstrahlung photon beam. Two important issues are understanding the energy and spatial resolution of the detector (relevant for the reconstruction of π^0 and η mesons) and electromagnetic backgrounds.

Lacking a source of electron or photon showers of a well-defined energy, the RADPHI experiment had to rely on the observed width of known mesons to deduce the energy resolution of the lead-glass calorimeter. The observed width of narrow mesons such as the π^0 and η that undergo 2γ decay is determined by the single-shower energy and position resolutions of the LGD. In cases where the spatial contribution can be neglected, the single shower energy resolution was extracted by selecting pairs with one of the two showers in a narrow energy window and examining the energy spectrum of the other, for a given cluster-separation angle. This energy spectrum shows peaks that correspond to the masses of the π^0 and η and whose line-shapes are convolutions of the energy response functions for the two showers plus contributions from uncertainties on the shower centroid positions. The contribution from spatial resolution to the width of the peaks was minimized by focusing first on the η , which is associated with pairs of showers that are well separated on the face of the calorimeter. By analyzing the dependence of the peak width on the energies of the individual showers, the convolution was inverted to obtain the r.m.s. resolution for single showers as a function of shower energy without introducing a model for the energy dependence. Once the energy resolution had been determined in this way, the spatial resolution was then examined by looking at the excess width of the π^0 peak over what was expected based upon energy resolution alone. In the end, a unified analysis including both energy and spatial resolution effects was able to reproduce both the π^0 and η profiles.

Assuming that the spatial resolution is not important for $\eta \rightarrow 2\gamma$ decays, the r.m.s. shower energy resolution can be extracted without assuming any functional form for its dependence on shower energy. This model-independent solution was then compared with the standard parametrization [43] of the lead glass energy resolution given in Eq. 4.1.

$$\frac{\sigma_E}{E} = \frac{B}{\sqrt{E}} + A. \quad (4.1)$$

The first term on the right contains the effects of photoelectron statistics, while the second term wraps up all of the systematic block-to-block differences and calibration errors which prevent the width of the response function from collapsing to a delta function in the high-energy limit. In order to describe the π^0 peak with the same parameters it is necessary to introduce a model for the shower spatial resolution, which itself depends upon shower energy. The energy dependence is proportional to $1/\sqrt{E}$ with a proportionality constant that depends on the size of the LGD block [44]. Eq. 4.2 is adopted for showers at normal incidence, with the constant C expected to be around $7 \text{ mm}\cdot\text{GeV}^{-\frac{1}{2}}$.

$$\sigma_x = \frac{C}{\sqrt{E}}. \quad (4.2)$$

In the RADPHI geometry many of the showers are far from normal incidence and so the shower depth fluctuations of roughly one radiation length also contribute to the centroid position resolution along one of the spatial axes. This was taken into account in the analysis by projecting one radiation length from along the shower axis onto the transverse plane and adding it in quadrature to the base term in Eq. 4.2. The final values for all parameters were determined by simultaneous analysis of the η and π^0 data where all of the above effects are included for both.

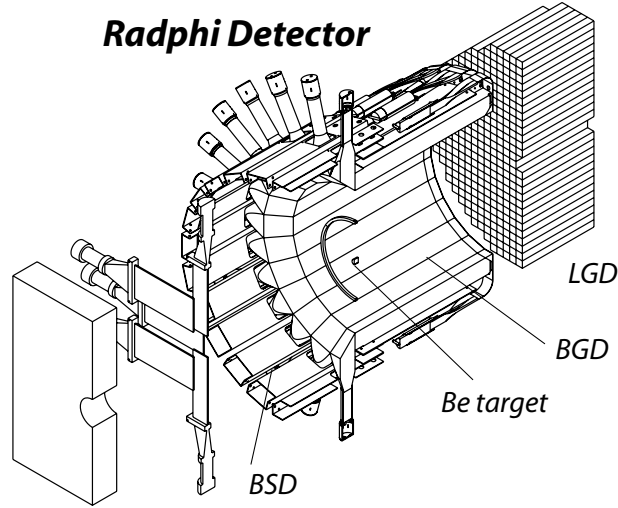


Figure 4.8: The RADPHI detector.

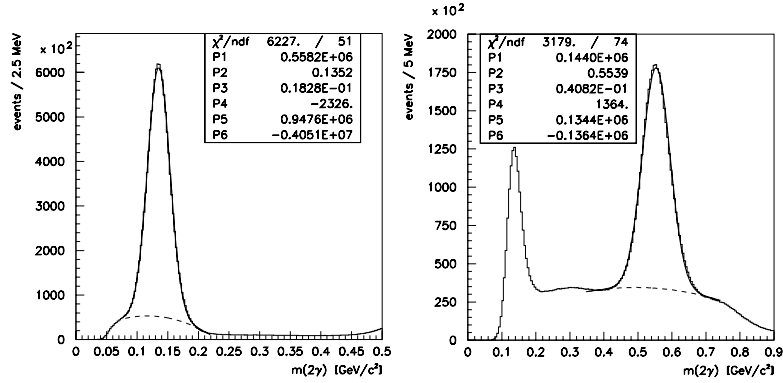


Figure 4.9: Invariant mass distribution of $\pi^0 \rightarrow 2\gamma$ (left) and $\eta \rightarrow 2\gamma$ (right). The parameters shown are the height (P1), mean (P2) and sigma (P3) of the Gaussian peak fitted to the data over a polynomial background described by parameters P4-P6.

Estimating the GlueX π^0 and η Mass Resolutions

The experience with the E852 and RADPHI detectors allows us to reasonably interpolate to expected GLUEX performance. Based on the discussion above and that of reference [45] we assume the energy resolution given by:

$$\frac{\sigma_E}{E} = 0.036 + \frac{0.073}{\sqrt{E}} \quad (4.3)$$

and the spatial resolution is given by:

$$\sigma_\rho = \sqrt{\left(\frac{7.1}{\sqrt{E}}\right)^2 + (X_0 \sin \theta)^2} \text{ mm} \quad (4.4)$$

where ρ locates the shower position in the plane of the LGD measured from the center of the LGD, θ is measured from the normal to the LGD plane, X_0 is the radiation length of glass (31 mm in this case) and E is the photon energy in GeV.

A Monte Carlo simulation of forward π^0 and η production for RADPHI, E852 and GLUEX assumed:

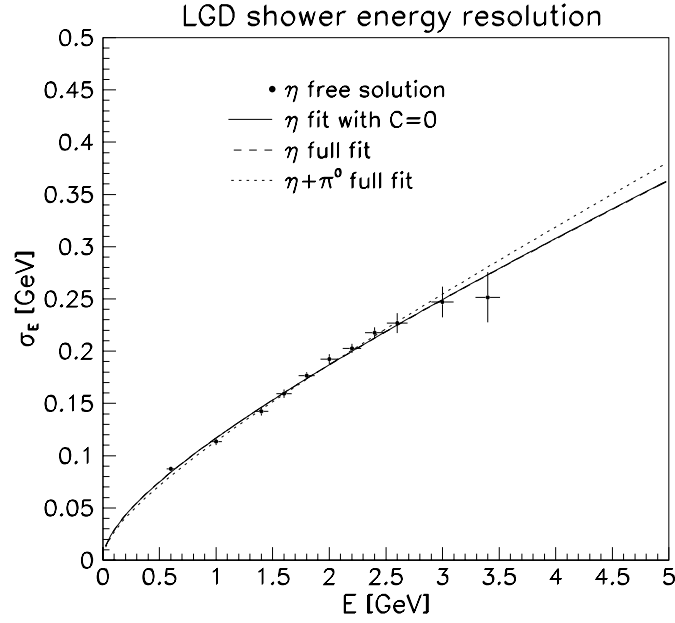


Figure 4.10: Energy resolution of showers in the LGD obtained from analysis of the 2γ sample.

1. A uniform photon beam between 3.0 and 5.4 GeV for RADPHI, 18.0 GeV for E852 and 9 GeV for GlueX;
2. A target to LGD distance of 1.0 m, 5.4 m and 5.0 m for the three experiments respectively.
3. Transverse LGD dimensions characterized by circular stacks of radii 0.5 m for RADPHI and 1.0 m for GLUEX and a 1.68 by 2.8 m rectangular stack for E852.
4. A minimum photon energy of 150 MeV and a minimum photon separation of 8 cm.

Simulation results are shown in the plots of Figure 4.11. We obtain π^0 mass resolutions of 16 MeV for RADPHI and 8 MeV for E852 compared to measured resolutions of 18 and 10 MeV. For GLUEX we predict 9 MeV. For the η we obtain mass resolutions of 40 MeV for RADPHI and 27 MeV for E852 compared to measured resolutions of 40 and 25 MeV. For GLUEX we predict 30 MeV.

Electromagnetic Backgrounds

The experience with the RADPHI LGD also allows us to compare estimates of electromagnetic backgrounds as calculated using GEANT with measured rates. Such a comparison is shown in Figure 4.12. The histogram in the figure is the Monte Carlo estimate for the LGD rates arising only from electromagnetic background. Note that for individual blocks, the expected hadronic rate is negligible on this scale. The simulation includes the principal components of the Hall B photon beam line starting at the radiator and including the (empty) CLAS target and downstream yoke aperture. Note that in Figure 4.12 a marked depression appears at small radius, relative to the observed rates. These blocks are in the vicinity of the beam hole and, in addition to suffering from the highest rates, these blocks also suffered from radiation damage. The eight blocks closest to the beam axis (first data point) are the most affected, but some effects can be seen at neighboring points.

Radiation Damage

Online monitoring of the LGD during the RADPHI experiment indicated that the 8 blocks immediately adjacent to the beam hole were becoming progressively reduced in gain as the run

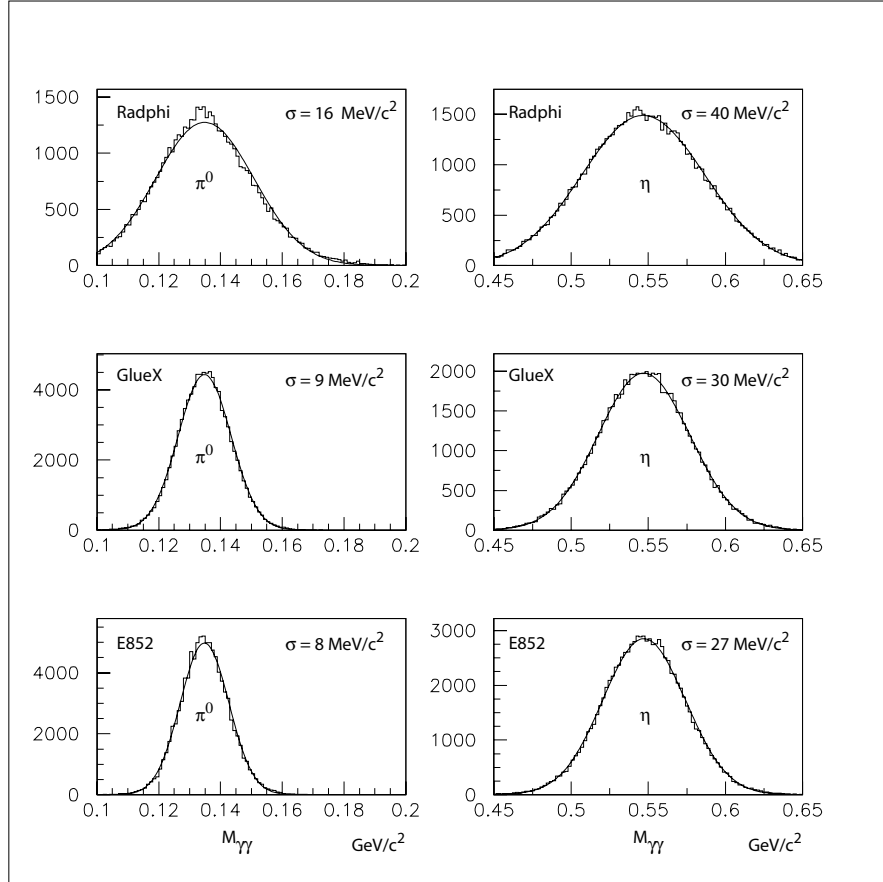


Figure 4.11: Simulated diphoton mass for the π^0 and η using the Radphi, GlueX and E8652 geometry.

progressed. This observation was based upon the laser monitor system, the raw pulse-height distributions, and the channel gains which were periodically recalibrated during the run. A similar effect was seen, but to a lesser degree, for the next layer of blocks once removed from the beam hole. During a pause in the experiment, visual inspection of the blocks indicated that the glass was darkening, a well-known effect of radiation damage on lead glass. Figure 4.13 illustrates the gain reduction with beam time (roughly proportional to integrated radiation dose) for a typical block adjacent to the beam hole. It is apparent that the gain change is a gradual, cumulative effect rather than a sudden change which might be characteristic of a beam mis-steering event.

The magnitude of the gain loss (order 40%) was such that it could be compensated by adjustments of the PMT high voltages. This was done periodically during the experiment. The last datum in Figure 4.13 shows the result of one adjustment. However, this is only a partial solution, since the module suffers a loss of photoelectrons due to the radiation damage, and thus a degraded resolution. Thus it was desirable to ‘heal’ the radiation damage as much as possible.

Radiation damage in lead glass is known to be temporary, and to largely heal itself on the time scale of a few months. The healing can be accelerated by the use of ultraviolet (UV) light. This approach was adopted for the most affected blocks. During an extended down-time in the run, the PMT and base for selected modules were removed and a UV light guide attached to a quartz envelope Mercury vapor lamp was inserted. The output of the lamp was 5 W/cm² in the range 300 to 480 nm, with a peak intensity at 365 nm. The affected blocks were each illuminated for periods of 6-8 hours. These blocks showed a gain increase of 30% following this treatment, nearly recovering their initial gains.

It should be noted that the change in the response of the modules due to radiation damage

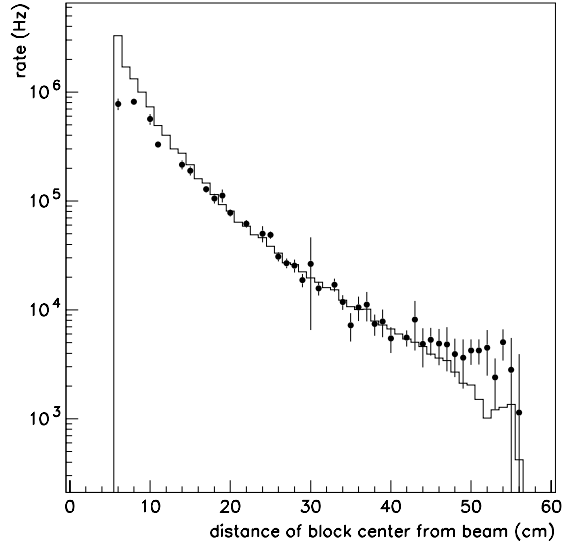


Figure 4.12: Characteristics of unbiased flux observed in individual blocks in the LGD as a function of distance from the beam. The points are derived from data and the histograms from a Monte Carlo simulation of the electromagnetic background coming from the beam and target. All hits over 15 MeV are recorded.

and the gain recovery following UV treatment was even more dramatic in the data from the laser monitoring system (typically a factor of two change). The difference between the shift in the pulser response and that seen in the gain constants from the calibration can be qualitatively understood by noting that the laser illuminates the front of the block and thus measures the transmission of the entire block, while the showers seen in the calibration data create Cerenkov light throughout the volume of the block, and are therefore less sensitive to attenuation effects in the upstream region of the block. The radiation damage is now known, from measurements, to be within 11 *cm* of the front surface of the detector, and this was confirmed by visual inspection, in qualitative agreement with the difference between the laser monitor data and the calibration data.

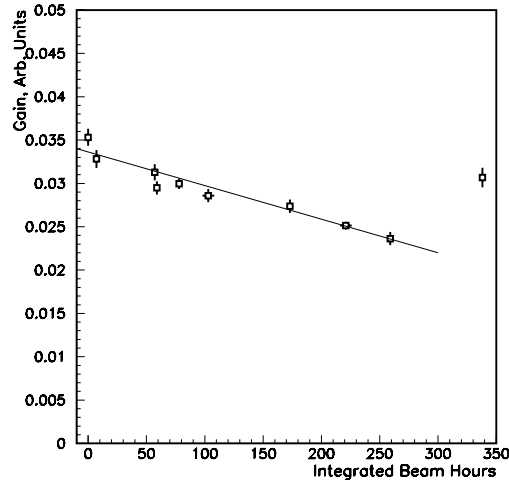


Figure 4.13: The effect of radiation damage on the central part of the detector. The last point shows the gain after an adjustment of the PMT high voltage.

Heat Curing of Damaged Blocks As part of the program to assess the glass used in E852 and RADPHI for use in GLUEX a spectrophotometer (Shimadzu UV-160) was modified to allow a lead glass bar to be automatically moved along its long axis to measure transmission through the 4 cm thickness. Based on the transmission dependence on wavelength, the transmission of the bar as a function of length was measured at 410 nm. Figure 4.14 shows the dependence of transmission as a function of length along the block for a block that visibly shows radiation damage. An alternative to UV curing, heating blocks in an oven has also been studied. The plot also shows the transmission curve for the same block after heating the block for several hours in an oven at 260 °C.

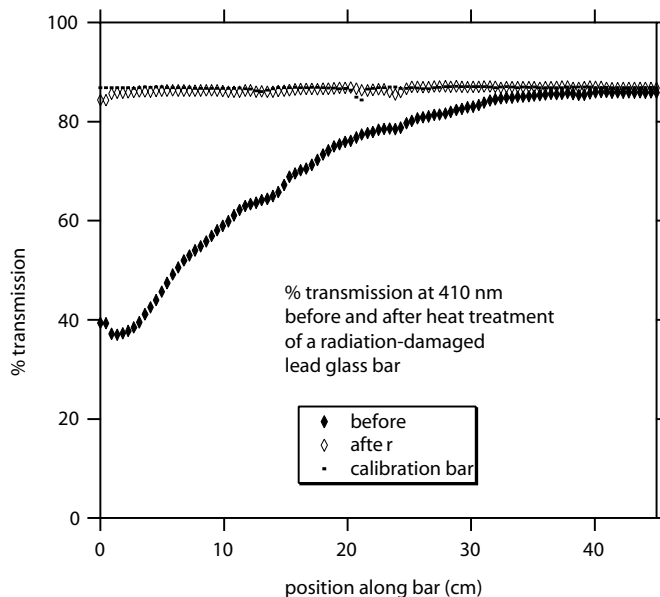


Figure 4.14: The effect of heat curing.

Assessing Lead Glass Blocks and PMT's

Lead glass block evaluation Some of the lead glass blocks used in the E852 experiment were used in the RADPHI experiment. All of the blocks are being examined for mechanical and radiation damage – the latter being assessed using the spectrophotometer described above.

The transmission at a wavelength of 410 nm as a function of length along the block will be measured and recorded for each block. The reason for measuring the transmission at this wavelength can be understood from the data presented in Figure 4.15 where the transmission as a function of wavelength is measured for a block that suffered radiation damage and a block with no damage. The measurement was made approximately 2.5 cm from the upstream end of block where *upstream* refers to the orientation of the damaged block in the beam. At about 410 nm the undamaged glass reaches a transmission plateau.

PMT Evaluation The PMT's available for GLUEX were used in E852 starting in 1994. There is some concern about the aging of the PMT's so a program of testing the 3200 PMT's (including spares) has already started. A similar process was used prior to constructing the E852 LGD for rating PMT's and is described in reference [29]. For the current test a light-tight box will accommodate 25 PMT's at a time. The tubes will view a diffusing plate that is illuminated by two blue LEDs that will be pulsed. Under computer control the gain as a function of high-voltage will be recorded and random noise and correlated noise rate will be measured. The correlated noise rate will be measured within a fixed gate delayed by a few hundred nanoseconds after the

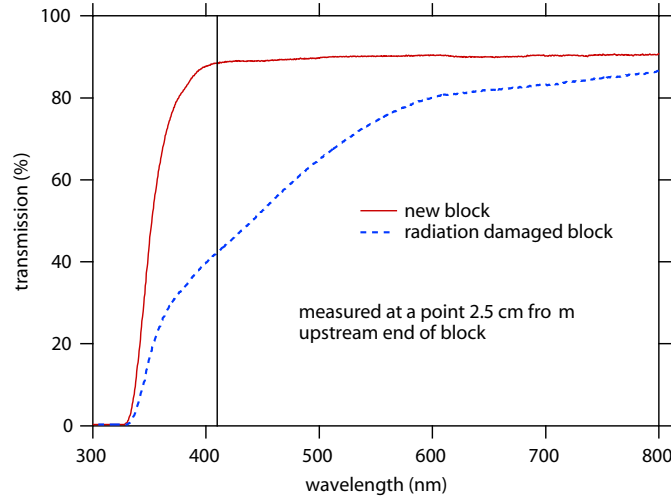


Figure 4.15: Transmission as a function of wavelength for radiation-damaged lead glass and undamaged glass. At about 410 nm the undamaged glass reaches a transmission plateau.

LED's are pulsed. Preliminary measurements with a random selection of PMT's indicate that the PMT's performance has not degraded.

Other Issues

Electromagnetic Rates in the LGD The RADPHI experience has forced us to deal with the issue of high rates in the central part of the detector and also how to use GEANT to estimate those rates. Those studies are currently underway for the GLUEX arrangement. We are also exploring the option of using another medium in the central region of the LGD, such a radiation hard lead glass, lead tungstate or another material. This will of course impact on shower reconstruction – especially for those showers that cross the boundary between media. Another option under investigation is to place a thin sheet of lead in front of the LGD blocks in danger of damage. The impact this has on resolution is also being studied.

Magnetic Shielding In E852 a cellular wall was used to register the PMT's to the glass wall. That cellular wall consisted of two aluminum plates with holes into which cylindrical soft iron tubes were squeezed (the tubes were sandwiched between the plates). Epoxy was injected the space between the tubes and between the plates through small holes in the plates. Additional μ -metal shields surrounded individual PMT's before insertion into the soft iron tubes. The PMT's were positioned against the glass blocks with an air gap in between. This entire cellular wall structure was surrounded by a thick iron frame to provide further shielding. The structure is described in reference [30]. A similar wall was used for RADPHI. In E852 the PMT's were shielded from the fringe field of the BNL MPS dipole magnet.

Simulations of the fringe field of the GLUEX solenoid are currently underway for various assumptions about the structure and material in the vicinity of the LGD. More details about magnetic shielding are also discussed in the section on the TOF – the forward time-of-flight system.

For the LGD we plan to have the PMT photocathode recessed inside the iron shielding tube by about the diameter of the photocathode and we plan to study the use of short cylindrical glass segments to couple the lead glass to the PMT with proper index of refraction matching.

Monitoring The E852 and RADPHI LGD's were monitored [30, 31] by using light from a nitrogen laser illuminating a block of scintillator. The scintillator light was transported by several optical fibers coupled to the sides of a Plexiglass sheet large enough to cover the front face of

the glass stack. This system was used for initial gain setting and to monitor gains throughout the run.

Calibration GLUEX will base its LGD calibration system on the extensive experience gained with calibrating the E852 and RADPHI LGD's that is described in references [30] and [31].

Triggering An energy sum trigger was provided by the E852 and RADPHI LGD's [30, 31]. In addition the E852 LGD had a trigger processor that provided an estimate of the total effective mass of photons striking the LGD and this was used in the trigger.

4.3.3 Barrel Calorimetry

The barrel calorimeter (BCAL) will be positioned immediately inside the solenoid, which constrains the outer radius to be 90 *cm* and results in an outer surface area of approximately 23 *m*². This leaves a 2.7 *cm* space radially for supports and installation. This device is a key component of a hermetic system, and is crucial for both fully reconstructing all the photons in many physics reactions and providing accurate time-of-flight measurements for charged particles. In addition, it may be possible to get some *dE* information on charged particles as well. The large size of this device implies that it will be a challenge to build and instrument it at reasonable cost. The main parameters of the BCAL are given in Table 4.1.

A principle goal of GLUEX calorimetry is to detect and to measure photons from the decays of π^0 's and η 's which, in turn, can come from the decays of produced mesons or possibly from excited baryons (N^* or Δ). The positions and energies of the photons must be determined to sufficient accuracy to allow for a complete kinematic reconstruction of the event. Detailed Monte Carlo studies [46] [47] indicate that the BCAL should be sensitive down to as close to 20 *MeV* as possible and up to a few *GeV* in energy. The BCAL is also required to provide timing information for charged particles. The BCAL, in conjunction with *dE/dx* measurements in the CDC, will be the primary PID device for most of the protons detected in GLUEX. Monte Carlo studies [48] [49] show that in order to carry out this function, the BCAL needs to have close to 200 *ps* timing resolution. For events with only charged particles, it is essential to be able to veto on neutral missing energy. Here, nearly hermetic coverage is critical. For selected triggers, neutral energy requirements (or vetoes) are relatively easy to implement. A secondary function for this device is to be able to provide *dE* information to further aid the central tracking system in particle identification.

Table 4.1: Main parameters of the Barrel Calorimeter.

Parameter	Size
Length	390 <i>cm</i>
Inner radius	65 <i>cm</i>
Outer radius	90 <i>cm</i>
Fiber diameter	1 <i>mm</i>
Lead Sheet thickness	0.5 <i>mm</i>
Number of Fibers	1,000,000
Number of Readout Channels	~1000-5000
Weight	35 metric tons

Design Considerations

For the tracking elements inside the magnet to perform optimally, the BCAL must be thin, no more than 25 *cm*. This and the 4.5 *m* length of the solenoid lead to a long, narrow, tube-like design. In this geometry, readout is easiest at the ends where space exists. The choice of readout device must bear in mind the considerable magnetic field (22.4 *kG*) inside the bore

and the rapidly varying fringe field at the ends. Conventional photo-multiplier tubes (PMTs) will work only outside of the solenoid and even there considerable attention must be paid to shielding.

While the collaboration initially looked at several potential designs, it was quickly realized that the only viable, cost-effective solution is one which utilizes scintillating fibers embedded in a lead matrix. The Pb/SciFi is used to make a relatively high-resolution sampling calorimeter. This solution is based on proven technology from other experiments.

Unfortunately, the very strong magnetic field in the immediate vicinity of the SciFi ends make the options for readout less clear. We initially looked at hybrid PMT (HPMT) which have been developed for CERN applications. These devices are immune to magnetic fields up to 2 T and their power supplies are very compact due to the fact that they draw virtually no current even under maximum bias. The HPMT's have a fast rise time of 6 ns or less, very good energy resolution, modest timing resolution, but low gain and as such require amplification. An additional drawback is their high cost. After careful study [50], these were rejected as an option because no suitable circuit could be devised to provide adequate pulse amplification and good timing simultaneously.

The option that is currently under investigation involves Silicon photo-multipliers (SiPM's). These devices offer gain and timing resolution comparable to that of a PMT, superior energy resolution, require a simple electronic circuit and are not sensitive to magnetic fields. These are discussed later in this report.

A more conventional option is to use magnetic field resistant PMTs coupled to fiber optic light guides to place the PMTs in regions of reduced field and with an appropriate orientation to further minimize signal loss. This option has the drawback that there is a loss of light associated with the long (probably fiber) light guides, as well as an increased mechanical complexity due to their placement. While this option would certainly work, it is being reserved as a backup.

Pb/SciFi Barrel Calorimeter

Scintillating fibers embedded in a matrix of lead (Pb/SciFi) or other high- Z materials have been used in calorimeter design and operation for more than a decade. The ratio of the active scintillator to the passive high- Z material, as well as the diameter of the fibers, can be tuned to enhance resolution, to determine the radiation length, and to achieve uniformity in the electromagnetic to hadronic response (the e/h ratio).

For high-resolution EM performance, the Jetset detector used such a calorimeter which was developed at Illinois [51]. This was the first detector designed specifically to optimize EM resolution. The recipe produced a detector comparable to lead glass at a considerably lower cost and with approximately half the radiation length. It utilized 1 mm fibers spaced uniformly (close packed) on specially grooved plates of lead. The lead was alloyed with 3 – 6% antimony to provide mechanical stiffness.

Of more relevance to the GLUEX experiment is the calorimeter built for the KLOE experiment at DAΦNE. The KLOE collaboration has taken the development of Pb/SciFi a step further than JetSet. They developed better tooling for the production of long grooved plates, have pushed the technology for excellent fibers with long attenuation lengths [52] and have built a device with larger radius than needed in GLUEX and 4.3 m in length. This device is currently operating and results on its actual performance are available. Like Jetset, the KLOE design utilizes 1 mm diameter scintillating fibers embedded in a lead matrix with a fiber to lead to glue ratio of approximately 48 : 42 : 10.

Both the JetSet and the KLOE calorimeter exhibit similar energy resolutions. An array of JetSet prototypes subjected to electrons in the range 0.3 – 1.5 GeV was represented by the function

$$\sigma/E = 6.3\%/\sqrt{E}$$

with E in GeV. The constant term was negligible. In the Jetset Forward Calorimeter, the beam entered nearly parallel to the fiber direction. The energy resolution was also measured with tagged photons below 0.1 GeV and improved to $\approx 5\%/\sqrt{E}$; the detector gave a resolvable

signal all the way down to 0.02 GeV . A KLOE prototype modules, 2 m in length was produced with conventional PMT readout at both ends. Such readout was possible due to the lower field and more favorable field gradient of KLOE compared to GLUEX. An excellent energy resolution parametrization of

$$\sigma/E \approx 4.4\%/\sqrt{E}$$

was extracted. The final energy resolution for KLOE [53] was

$$\frac{\sigma(E)}{E} = \frac{5.4\%}{\sqrt{E(\text{GeV})}} + 0.7\%,$$

and this number serves as a benchmark for the GLUEX Barrel Calorimeter.

Because of the $\sim 4 \text{ m}$ module length in KLOE, special efforts needed to be made to develop and test scintillating fibers with very long attenuation lengths. Tested fibers had attenuation lengths in the range from $2.3 < \lambda < 3.2 \text{ m}$ which is far superior to the average λ of 1 m for the JetSet fibers. This aspect of the design is critical because there exists a significant coupling between the position of impact (essentially the polar angle, θ) and the interpreted energy. Light collected at each end must be corrected for attenuation length before conversion to energy units.

Another important feature of scintillating fibers is the signal rise time and overall duration. Because fast plastic scintillator is used (Decay times are $2.0\text{--}2.5 \text{ ns}$), integrated signal time can be kept below 100 ns , with shorter times possible if deemed necessary for rate considerations. No problems are anticipated at the expected maximum luminosity of GLUEX. With rise times of a few ns , excellent timing can be expected for each of the devices involved in collecting the light from a shower. The time difference from the two ends produces the z coordinate of the hit.

Because we will use an array of such devices on each end (segmented in azimuth and depth), redundant measurements are made of the z coordinate. These measurements of z correspond to different average radii and therefore help to establish the angle of the incoming photon.

The fractional volume of scintillator in the detector naturally makes it efficient for detecting charged hadrons. The mean light collection time of the two readout ends can be used to determine the particle time-of-flight (TOF). TOF coupled with the track length and momentum then yields particle mass. Therefore, this design for a Barrel Calorimeter is expected to play an important role in the overall barrel PID scheme. KLOE achieved an operational time resolution of

$$\sigma_t = \frac{56 \text{ ps}}{\sqrt{E(\text{GeV})}} \oplus 133 \text{ ps},$$

which yields a nearly constant $\sigma_t \approx 180 \text{ ps}$ for photon energies above 150 MeV , and a diverging time resolution for $E_\gamma < 75 \text{ MeV}$. The first term is the sampling fluctuation term, and can be reduced by improving the calorimeter light collection. The constant term is mostly due to the intrinsic time spread due to the finite length in the z direction of the luminous point. Improvements on this are possible. A similar figure can be expected for GLUEX as long as readout devices and discriminator chains are selected carefully.

The GlueX BCAL

Pb/SciFi calorimeters have been built that satisfy the physics requirements of GLUEX. By using the knowledge gained in the KLOE construction, members of the GLUEX collaboration expect to improve on this for the GLUEX experiment.

For GLUEX, we expect to build 48 modules each $\sim 4 \text{ m}$ in length and $20\text{--}25 \text{ cm}$ deep. The readout scheme takes advantage of the fact that all fibers run parallel to the axis of symmetry of the solenoid and therefore all light piped to the ends of the modules retains its azimuthal and radial information. The polished ends of the detectors will be coupled with multiple independent light guides.

Because the EM showers spread across these azimuthal boundaries, algorithms for finer positioning of the shower are employed. In JetSet, one finds a typical weighted position resolution of $\delta x \approx 5 \text{ mm} / \sqrt{E}$. For the GLUEX design, this would lead to an azimuthal resolution of

≈ 8.5 mrad. Using the z position resolution of approximately 4 cm obtained from the time difference leads to a polar angular resolution at 45° of ≈ 7 mrad. As the design of the BCAL is further refined, it will be important to keep these numbers balanced.

The transverse size of each of the 48 modules is approximately 8.5 cm at impact. A further subdivision of the readout can reduce this number by half or more. In Figure 4.16, ten (two in width times five in depth) segments per azimuthal slice are shown as a minimal example of the readout subdivision. Each such segment would contain approximately 1200 fibers. In effect, this subdivision could be made smaller whether PMT's or SIPM's are used. The former would require a (clear) fiber-to-fiber mask to carry the light outside the magnetic field, whereas the latter would need a Winston cone with a light mixer or a diffuser, and wavelength shifting fibers (WLSF's) or ordinary fibers to further guide the light to the small surface of each SIPM. The investigation into the optimal readout scheme is now underway and will couple Monte Carlo simulations of the expected light produced to R&D trials in the lab with different geometries using SIPM's and PMT's.

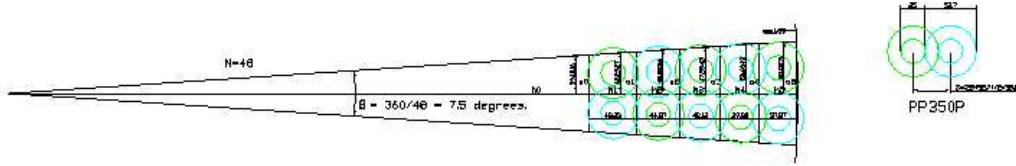


Figure 4.16: Sketch of Barrel Calorimeter readout ends. The subtended angle of each module corresponds to two azimuthal slices. Each slice has five readout devices on either end. As an example, the dimensions of DEP PP00350G HPMTs were used. The outer circles represent the boundary of the devices, assuming a 5.27 cm outer diameter. The devices have been closely packed so as to not shield each other's active area, which is indicated by the smaller circles (diameter of 2.5 cm). The readouts have been staggered axially to allow the closest packing.

Each channel requires high voltage, a flash ADC, discriminator, TDC and cabling. A calibration system is critical and can be based in part on the use of Nichia blue (or green) LEDs glued directly to a short light guide stub at the end of each module. An LED driver system is also required. The choice of ADC and TDC systems depends on the overall readout coordination for GLUEX.

Construction of Prototype Modules

In order to form grooved plates and construct modules 4 m long, we have studied and used the KLOE tooling techniques. GLUEX physicists visited Frascati and Pisa and were trained in the use of the KLOE 15 cm-wide lead swaging machine (a.k.a. *Francesca*). In May 2002, the GLUEX physicists successfully swaged 0.5 mm thick lead sheets, and glued 10 layers of lead and 1 mm optical fibers together, producing the first Pb/SciFi test module with dimensions 100 cm x 14 cm x 1.25 cm at LNF/Frascati. Francesca (total weight of 200 kg) was then moved to Canada on a two-year loan from Frascati, where four prototypes have been built:

1. 1 m x 13 cm x 5.0 cm, *Baby-0 Module*
2. 2 m x 13 cm x 17.0 cm, *Module-0*
3. 4 m x 13 cm x 23.7 cm, *Module-1*
4. 1 m x 13 cm x 5.0 cm, *Baby-1 Module*

As is reported below, the construction of all modules was met with success, with only minor faults resulting in the uniformity of each of the three matrices. The construction method has

been adjusted to avoid these in the production phase. Francesca has been returned to LNF; we will design and build a similar machine for our production phase.

Production of Lead Sheets The initial stages of construction for the 4m module calorimeter took place in February-April 2004 at the University of Regina. The main focus was to produce the needed lead rolls for the first full-length module (Module-1) of the Barrel Calorimeter at Hall D. A total of 240 rolls were cut, swaged and shipped to the Centre for Subatomic Research (CSR) at the University of Alberta where this module would be constructed.

The lead came from the manufacturer¹ on a giant roll, 27" wide. Five sheets (width-wise) could be extracted from each length of lead. The quality of lead used for this module was superior to that used for the 2 m module. The lead used for Module-1 had a lower percentage of copper than the roll used in the 2 m module (Module-0) and was consequently softer and easier to ply. *Bananas* (curved sheets resulting from uneven pressure of the rollers during the swaging process, or from impurities in the lead itself) were a continuous problem for Module-0. Bananas rarely occurred for the lead used in Module-1: out of 240 sheets there were only three irreversible bananas.

The wide lead sheets were placed under a special cutter that consists of two parallel blades, separated by 12.93 cm, attached to a roller on tracks. This cutter greatly reduced the cutting time over the mask and box cutters used in the previous modules. A few improvements in the design (easier exchange of blades, smoother insertion/extraction of lead sheets) are planned for the production phase, as well as a multi-track enhancement to allow cutting of 4-5 sheets at the same time. The lead was then swaged with Francesca to have 96 lengthwise grooves on both sides and trimmed to 404 cm.

The time required to cut and swage a sheet of lead, where one sheet contains 4-5 rolls of lead, changed with experience. Once a rhythm was established, on a good day with four workers, the time had reduced to approximately 9 min/roll with a daily total of about 30 rolls. After several trials of methods to lay the fibers in the lead grooves, a detailed method was developed [54]. This led to the successful construction of Module-1.

Module Construction During the summer of 2004 the University of Regina sent a team of undergraduates to Edmonton to build a 4m calorimeter module. Composed of 210 alternating layers of lead and scintillating fiber the module measured 4.04 m in length, 12 cm in width and 24 cm high. Over 80 km of fibers and 12 kg of epoxy was used in the four weeks of construction. The process itself was a learning experience, as much of the facility was custom built for the occasion.

The first stage of construction included the machining, assembly and installation of an electro-pneumatic press, used to press the matrix as it is being stacked with alternating layers of lead sheets and fibers. It consisted of steel bed, two tilting pistons that raised/lowered a group of 20 pistons to the top surface of the matrix, and the associated electronics and pneumatics.

The second stage of construction consisted of building the clean room where the module would be constructed. This was a 7 m x 5 m x 3 m room lined with Tyvek sheathing and black polyethylene sheets along its walls, and clear poly and UV filters as its ceiling. The room was ventilated with a variable speed fan and was equipped with an air exhaust. An airlock provided access to the room. The third stage of construction was the building of the 4 m module. A five member crew built this module working two three-hour shifts each day. This resulted in module growth of two centimeters each day. The fourth and final stage of the production was the construction of a one-meter Baby-1 module that was only 5 cm thick. This module is to be used for testing various readout systems.

Most tasks in the construction process are simple ones that are repeated each layer. A comprehensive report (how-to manual) and training video were prepared to simplify the training of personnel during the production phase and to document the methods employed [55].

¹Vulcan Lead Inc, <http://www.vulcanlead.com/>

The optimum size of the construction team turned out to be five people. Accurate documentation of all stages of the construction over a five week period show that just over 300 man hours are needed for each module, or a total of almost 15 thousand man hours for the construction of 48 modules. The construction of a second press and operations with two crews would allow the completion of the production phase in well under 24 months.

The Summer 2004 construction was a successful practice of full scale production. There were unanticipated problems and useful discoveries. The full set of recommendations for improving the construction technique is described in [55]. The GLUEX Collaboration believes that all R&D issues on the Pb/SciFi matrix construction have been resolved and that we are ready to proceed to the production phase.

Following the completion of the construction, Module-1 was craned out of the clean area and its ends machined and polished to final dimensions of $400\text{ cm} \times 13\text{ cm} \times 23.7\text{ cm}$ and was moved to Regina. A picture of one end of the module is shown in Fig. 4.17. A jump in the tracks of a single fiber layer is visible only on this end; the fibers are sitting properly at the other end. This was a result of having to lift the lead to realign it, something that had to be done several times and only once is resulted in misaligned fibers. This mishap has no effect on the light collection and integration of the module and will be tested for potential delamination. The testing of Module-1 with cosmic rays is underway at Regina and in 2005 the module will be tested in beam conditions at Serpukhov and latter at Jefferson Lab (Hall-B). Baby-1 will be cut into two equal length pieces that will be shipped to CERN and Athens for front end readout tests.

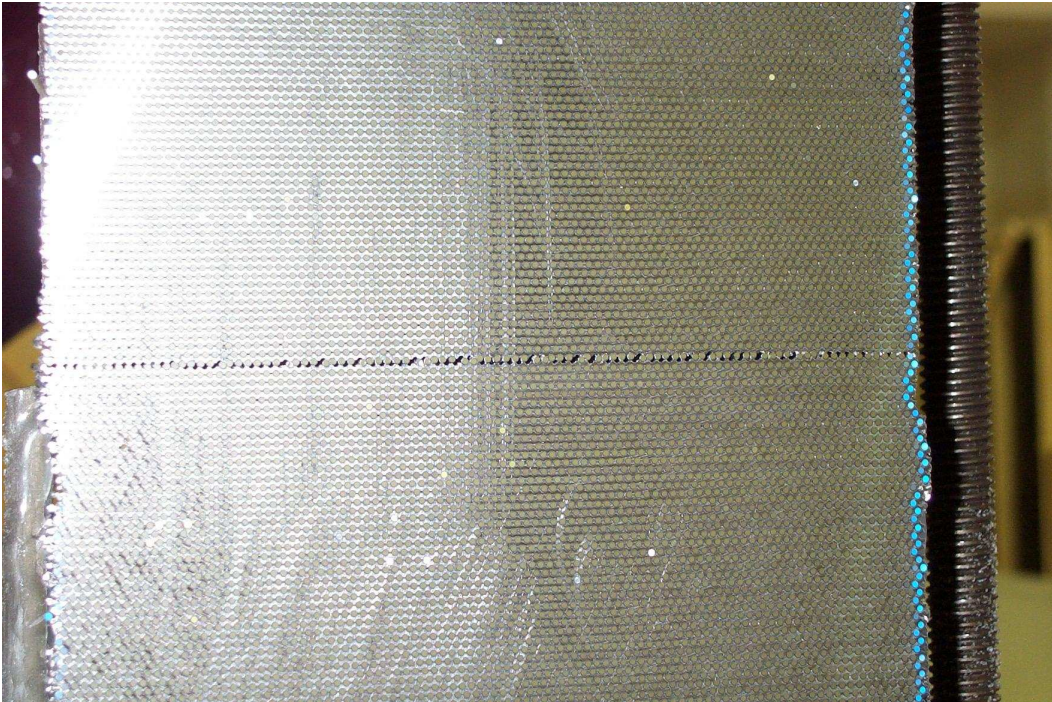


Figure 4.17: Module-1 end. Note the layer that has jumped its tracks. See text for a detailed description.

Scintillating Fiber Tests

Clearly, the inherent properties of scintillating fibers play a crucial role for the Barrel Calorimeter function. The criteria which must be evaluated include:

- Light collection efficiency (cladding),

- Amount of scintillation light produced (doping), and
- Loss of the light as it travels down the fiber (attenuation length) and decomposition of intensity as a function of wavelength.
- UV damage of fibers when exposed to sunlight or fluorescent lights.

To address the first three points, different types of fibers from two different manufacturers were procured and tested first with cosmics and then a pion beam at TRIUMF, Vancouver, in connection to their light attenuation and timing resolution. Specifically, the tested fibers were Kuraray SCSF-81 single-clad², Pol.Hi.Tech.0046 single- and multi-clad³. All fibers were 1 mm in diameter and were procured in the summer of 2000. In addition, a second bundle of single-clad Kuraray fibers was procured in 2001. Beam tests of these fibers are reported in reference [56], whereas tests of newer (2002 batch) Kuraray multi-clad and Pol.Hi.Tech. multi-clad fibers have been conducted using a spectrophotometer and the light output has been analyzed as a function of wavelength.

To evaluate the attenuation length of the various fibers tested, it is necessary to evaluate first the ratio of the means of the left and right PMT ADC values at each position along the beam. To understand this, consider that the attenuation of light as it travels along the fiber is given by

$$I(z) = I_0(z)e^{-z/\lambda} \quad (4.5)$$

where z is the distance from the point of impact of the beam along the fiber to the appropriate PMT, λ is the attenuation length, and $I_0(z)$ is the amount of light produced at the interaction point.

In practice, it is found that the amount of light produced at the interaction point is a function of z . Consequently, the ADC values for the two PMT's in question may be expressed as

$$ADC_{left} = f(z)e^{-z/\lambda} \quad \text{and} \quad ADC_{right} = f(z)e^{z/\lambda}, \quad (4.6)$$

where $f(z)$ is the geometric mean calculated from

$$f(z) = \sqrt{(ADC_{left}ADC_{right})}. \quad (4.7)$$

Thus, a reliable method to extract the attenuation length value is to take the ratio between the two ADC values above:

$$\ln(ADC_{left}/ADC_{right}) = -2z/\lambda. \quad (4.8)$$

Plotting the ADC ratio values at different positions on a semi-log scale results in a straight line with a slope of $-2/\lambda$. This is what is shown in Fig. 4.18 for all fiber bundles, where the curves have been shifted along the y-axis for clarity.

It is evident that the attenuation lengths of the Kuraray fibers are quite reproducible between different fiber samples, as well as different geometrical configurations. The Pol.Hi.Tech. multi-clad fibers had an attenuation length of $\lambda = (234 \pm 3)$ cm, considerably shorter than the Kuraray fibers. All the results are in broad agreement with those of KLOE and are presented in Table 4.2. It should be mentioned that the KLOE Collaboration also tested BICRON⁴ scintillating fibers, but recent price quotes from BICRON revealed that these are too costly for the HALL D project and so were excluded from testing for this reason.

To determine the timing resolution of the fiber bundles, the software mean time and the left-right timing difference must be computed. These quantities should have constant values at any given point along the fiber. However, there are some uncertainties associated with these values, which arise from inherent timing resolution of PMTs involved and photon statistics.

The timing resolution was determined with two methods that yielded consistent results. Statistically it appears that Kuraray fibers have superior timing resolution to the Pol.Hi.Tech.

²Kuraray Co., Ltd., 3-1-6, Nihonbashi, Chuo-ku, Tokyo 103-8254, Japan.

³Pol.Hi.Tech. s.r.l.0, Carsoli, Italy.

⁴BICRON Corporation, Newbury, Ohio, USA.

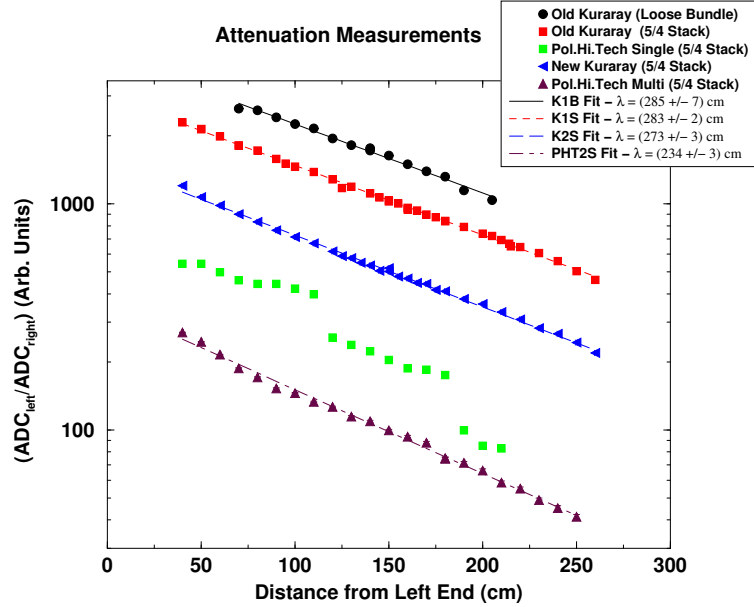


Figure 4.18: Attenuation length measurements for various fibers. The Pol.Hi.Tech. single-clad fibers appear to have been broken or stressed at the locations where the discontinuities appear in their curve (unconnected squares).

fibers which implies that the former fibers have better light production and light collection capabilities. All fiber bundles gave $\sigma = 550 - 700$ ps. This is consistent with the KLOE results which had $\sigma = 300$ ps for the Pol.Hi.Tech. and Kuraray fibers and 400 ps for the Bicon fibers, when the number of photo-electrons collected was $N(p.e.) = 30$. These numbers rise to 500-800 ps for $N(p.e.) \leq 10$. From the TRIUMF measurements, fitting of the ADC spectra yielded $N(p.e.) \leq 4$. Thus, the TRIUMF results are consistent, at least qualitatively, with those from KLOE. Additional details can be found in reference [56].

The Kuraray fibers showed a consistently better performance as per the light attenuation coefficient and timing resolution. However, the Pol.Hi.Tech. multi-clad fibers performed better in terms of light yield, based simply on the observation that for the same bias and gain the mean of the ADC spectra for these fibers was higher. These fibers had more than adequate performance for the requirements of the GLUEX experiment and are considerably cheaper (by a factor of 2) than the Kuraray fibers. For this reason, Pol.Hi.Tech. multi-clad fibers have been used in the construction of all prototype modules, except Baby-0.

Fiber Light Transmission Tests

Light-transmission tests of the scintillating fibers have been conducted using a dedicated optical testing system that employs LED light sources with different wavelengths, transport light guide fibers, optical filters, and is coupled to a dual-channel spectrophotometer and ADC. The system is sensitive to wavelengths from 350 nm to 1000 nm, is connected to the USB port of a laptop, and is read out by means of commercial software.

Preliminary tests had indicated that exposing scintillating fibers to UV light caused degradation in transmission intensity. This agreed with test results from KLOE [52]. The next step was to understand the reason for this decrease in light emission. One possibility was that UV exposure created cloudiness in the fiber, causing a decrease in attenuation length. Another theory was that after exposure, the fibers were absorbing light in different regions, shifting the output spectrum away from the PMT's peak efficiency. Using an Ocean Optics Inc.

Batch	Fiber Type (mode)	Attenuation Length (cm)		
		Cosmics	TRIUMF	KLOE
1992	Bicron BCF-12			226 ± 3
1993	Bicron BCF-12			286 ± 8
N/A	Kuraray SCSF-81 single-clad			321 ± 5
1992	Pol.Hi.Tech.0046 single-clad			284 ± 5
1993	Pol.Hi.Tech.0046 single-clad			267 ± 6
2000	Kur.SCSF-81 single-clad (loose)	321 ± 22	285 ± 7	
2000	Kur.SCSF-81 single-clad (5/4)		283 ± 2	
2001	Kur.SCSF-81 single-clad (5/4)		273 ± 3	
2000	P.H.T.0046 single-clad (loose)	259 ± 20		
2000	P.H.T.0046 multi-clad (loose)	247 ± 47		
2000	P.H.T.0046 single-clad (5/4)		Broken	
2000	P.H.T.0046 multi-clad (5/4)		234 ± 3	

Table 4.2: Attenuation length determined using 2" PMT's following the cosmics runs and the TRIUMF beam tests. The results are compared to those from the KLOE Collaboration [52, 57].

(OOI) ⁵ SD2000 spectrometer coupled successively to UV (380 *nm*), Blue (470 *nm*) and Tungsten ($\lambda = 350 - 1100$ *nm*) diodes, scintillating fibers were exposed to UV light emitted from normal fluorescent room lights while periodically measuring the fibers' output spectra.

Light from the diodes was divided into two channels. The master channel passed through a clear reference fiber that allowed us to monitor the stability of the diode. The sample scintillating fibers were placed into the slave channel. Five scintillating fibers and one Bicron (clear) light-guiding fiber were chosen at random to be tested. The six fibers were placed parallel to each other on a table and irradiated by leaving the room lights on for long periods of time. During the measurement of the output spectra of the fibers, all room lights were turned off and only lamps with UV filters were on.

Data reproducibility was a major concern for our experiment. If the fibers were not coupled into the OOI system in a consistent fashion, it would be impossible to compare recorded spectra from one hour to the next. Furthermore, it had been discovered that small rotations in the reference fiber at the connection point to the spectrometer could change the intensity of the reference spectrum by up to fifty percent.

A method that eliminated coupling as a contributing factor was sought. It was decided to perform the experiment one fiber at a time, leaving it connected to the OOI system even during exposure. One fiber was placed into the system and left unexposed over night. When re-tested in the morning, the results were found to be nearly identical. This gave a degree of confidence in the data to be collected. The light source used was the 470 *nm* LED. The results are shown in Fig. 4.19. A key observation in this figure is the effective "shift" of the spectra to higher values of λ . This is a result of a significant reduction of spectral strength in the blue region, precisely where PMT's are the most sensitive.

An additional interesting feature of these fibers can be gleaned from measurements of their light output as a function of length. These measurements are shown in Fig. 4.20. The reader is directed to notice the $\lambda=400-480$ *nm* region. Clearly, a reduction in intensity is observed with increasing fiber length. It should be mentioned that these measurements were done on a single fiber, starting with a 410 *cm* fiber that was successively trimmed to shorter lengths with its cut end being polished each time. As it turns out, such a light response is more suited for collection by SIPM's whose overall efficiency peaks in the yellow-green region. However, this renders yellow-green WLSF's useless when coupled to SIPM's; red WLSF's would have to be used instead and these suffer from poor timing resolution. The effect is pronounced enough to be visible by eye, as displayed in Fig. 4.20.

These measurements were repeated using a UV diode (380 *nm*) and the results are being an-

⁵<http://www.oceanoptics.com/>

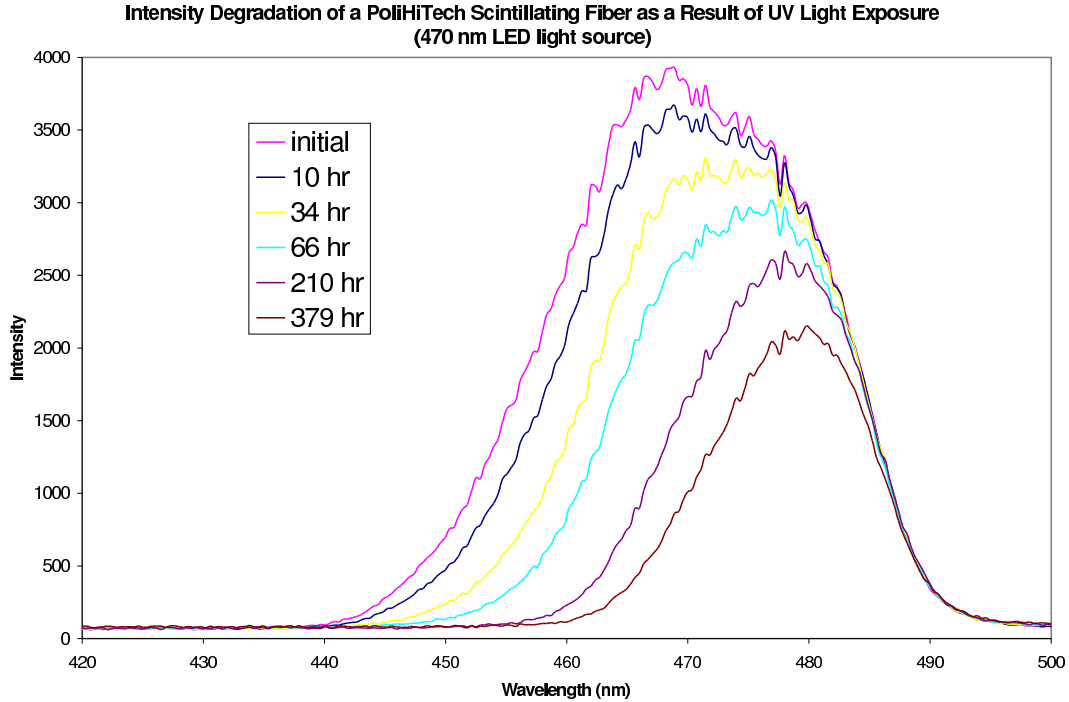


Figure 4.19: Degradation of fiber intensity as a function of UV exposure time. These are the final measurements using the 470 nm LED.

alyzed. Several lessons were learned that will help future measurements of the spectral response of scintillating fibers [58]. In the future, the long term effects of cosmic rays on scintillating fibers should be studied to give an idea of the longevity of the Barrel Calorimeter. This can be achieved by placing a select group of fibers into a tube made of UV filter and measuring the spectra every few months. Due to the extreme length of this investigation, it is not feasible to study one fiber at a time. In this case, plenty of care must be given to ensuring consistent coupling between the fibers and the OOI system.

Silicon Photomultiplier Tests

Although single-pixel Geiger mode devices (Avalanche Photo Diodes - APDs) were developed in the mid sixties, the SIPM is a novel type of APD [59]. It is a promising device for our application in GlueX, since it is insensitive to magnetic fields, has a high gain ($\sim 10^6$), good quantum efficiency, provides excellent timing resolution (~ 120 ns for single photo electron detection) and a fast risetime (sub-ns), achieves good dynamic range ($\sim 10^3/\text{mm}^2$), and does not suffer from nuclear counter effects when operated in Geiger mode. Finally, it has a solid performance at room temperature (in contrast to VLPCs) and does not exhibit any serious radiation damage effects, other than perhaps from neutrons [60].

The SIPM is a multi-pixel photo diode with a large number of micro pixels (500-1500 each with a typical size of 20–30 μm) joined together on a common substrate and under a common load. The total number of pixels defines the dynamic range of the photodetector. The photodiode has a multi-layer structure with different doping levels. As a result, within the thin depletion region between p^+ and n^+ layers, a very high electric field of about 5×10^5 V/cm is created, with the right conditions for a Geiger discharge mode to take place. The operational bias voltage is 10–20% higher than breakdown voltage, with typical supplied bias voltage of 50–60 V.

The single pixel gain is approximately 10^6 , roughly the same order of magnitude as that of a traditional PMT. While each pixel operates digitally as a binary device – because all SIPM pixels work together on a common load and there is a large number of pixels – the output signal is a

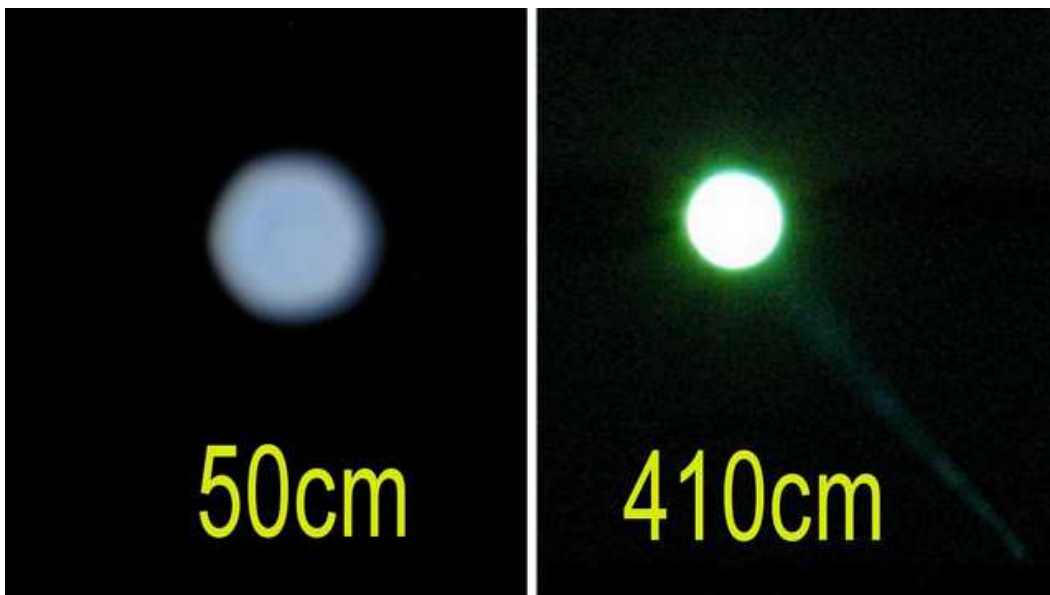
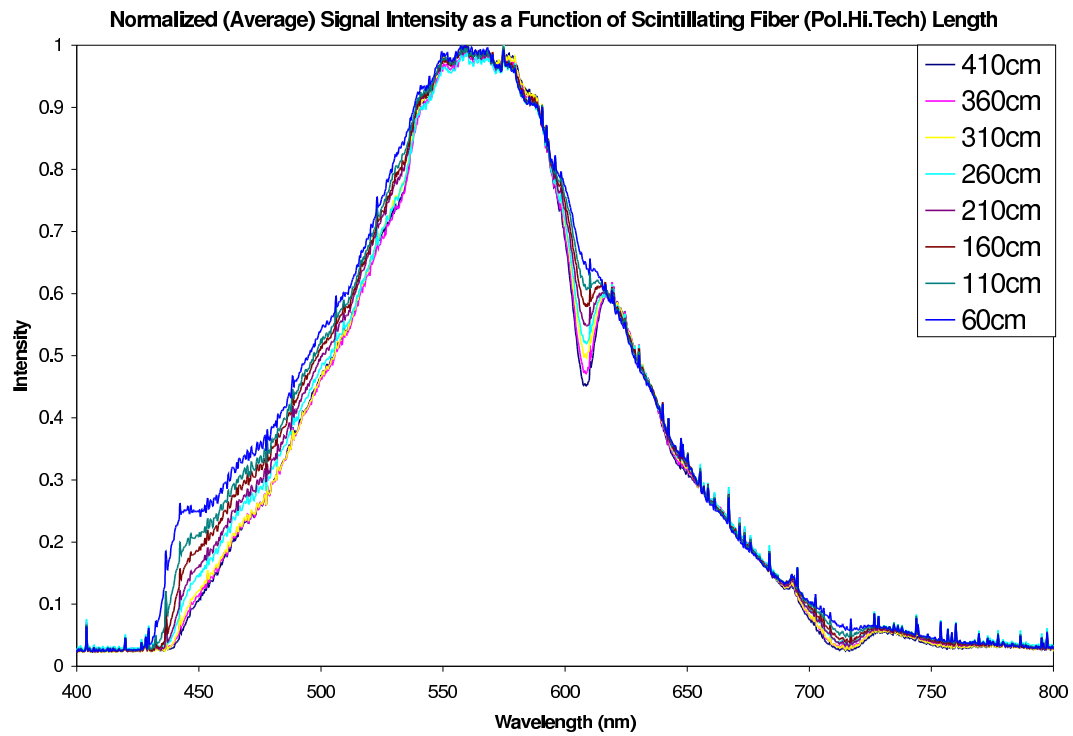


Figure 4.20: Fiber intensity as a function fiber length. These are the final measurements using the 470 nm LED. The shift in color from blue to green is evident even visually.

sum of the signals from all pixels registering a “hit”. Thus, the SiPM, as whole, is an analogue detector that can measure the incident light intensity. The distribution of the voltage across the depletion depth of 4–6 μm is such that for only a fraction of the depth ($\sim 1\text{--}2 \mu\text{m}$) the former exceeds a value sufficient for Geiger discharge creation, and therefore, the Geiger discharge is contained within this limited region. As a result, its duration is very short, a few hundreds of ps, resulting in typical rise times of 1 ns.

The SiPM’s photon detection efficiency, η , is given by $\eta = QE \cdot \varepsilon$, where η is the photon detection efficiency, QE is the quantum efficiency and ε is a geometrical factor. The latter is a ratio of the sensitive area (as defined by the total active pixel area) to the total area. This value does not depend on wavelength and is a constant for each SiPM. The devices used in our particular tests had geometrical factors of 0.3/1.0 for all SiPM’s/PMT’s investigated, respectively.

The SiPM’s used in our tests were developed and produced by the Moscow Engineering and Physics Institute (MEPHI) in cooperation with a state enterprise (PULSAR). The specific SiPM’s had 1000 pixels in each detector covering the 1 mm^2 sensitive area and the supplied bias voltage was 50–60 V. Although the geometrical factor for these SiPM’s was 0.3, efforts are underway at MEPHI/PULSAR to increase this to as much as 0.7. Competitors at the University of Obninsk in cooperation with a private firm (CPTA) [61] claim that their device has 50% higher photon detection efficiency in the green region and fewer constraints on mechanical performance. Moreover, the Obninsk/CPTA is investigating the construction of larger areas by connecting SiPM’s in a matrix configuration [61]. We have recently obtained 60 1 mm^2 CPTA units and these are currently undergoing evaluation at Regina. In addition, negotiations are underway with experts at CERN and DESY to allow for future testing of these devices with sophisticated setups and for testing with beam.

Tests of the MEPHI SiPM’s were conducted in order to investigate their use as front-end detectors for the Barrel Calorimeter readout system. The results of this work have been accepted for publication in Nuclear Instruments and Methods. Specifically the SiPM’s were investigated under the following two conditions: a) detection of incident light of high flux intensity, where about 200–500 SiPM pixels registered a hit but the signal was not saturated, and b) Detection of light of lower photon flux intensity in which case only few pixels registered a hit. This regime corresponds to a few-photon-counting condition.

An Optitron nanosecond broad spectrum optical pulse radiator (Model NR-1A) with a Nitrogen Plasma Discharge Tube⁶ was used as a source of light for the SiPM investigation under high photon flux conditions. The light pulses had a 1 ns rise time and a few ns pulse duration, and were measured with the SiPM as well as with a 2” Burle PMT (model 8575). A clear, pure fused silica fiber of 5 m length was used to transport the light from the Optitron plasma discharge tube to the sensitive surface of the SiPM. The light intensity emitted from was monitored by the PMT.

Pulses from the SiPM and the PMT were measured with a Tektronix TDS-5104 digital oscilloscope. The detected signal amplitude for the SiPM was ~ 300 mV, corresponding to $\sim 200\text{--}300$ pixels registering a hit. Whereas the timing distributions have a similar structure with risetimes of 1 ns and 4 ns for the SiPM and PMT, respectively, the former has a σ that is less than half of the latter’s: $\sigma = 140$ ps vs. 375 ps.

In order to investigate the energy resolution of the SiPM, we measured the pulse amplitude distribution under low photon flux conditions employing the Optitron unit and a neutral-density attenuation filter that reduced the light to 1% of its initial value. The amplitude of the signals in the SiPM, in this case, was 5–10 mV, and this necessitated the use of a fast amplifier (LeCroy 612A). Under such conditions it was not possible to eliminate completely the noise pick-up from electronic equipment present in the area. Nevertheless, the pulse amplitude distribution shown in Fig. 4.21 exhibits five well separated peaks corresponding to single photon detection and good separation for emission of up to five photoelectrons.

Next, we evaluated the performance of the SiPM used as a front-end detector for light signals produced by minimum ionization particles traversing a 4-m-long Kuraray SCSF-81 single-clad

⁶Optitron Inc. 23206 Normandie Ave. #8, Torrance, CA 90502, USA.

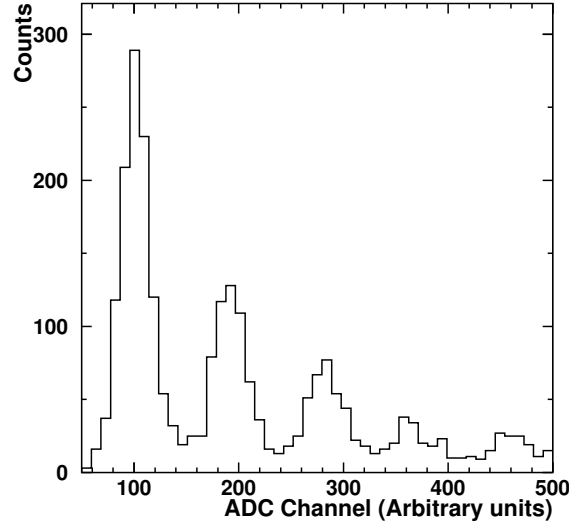


Figure 4.21: SIPM pulse height spectrum for low intensity light pulses.

SciFi. Fibers with similar parameters will be used in the Barrel Calorimeter for GLUEX detector system.

Kuraray SCSF-81 SciFi's have an emission spectrum range of 400–550 nm, peaking at 437 nm, with a 2.4 ns scintillation decay time and an attenuation length of ~ 3.5 m. The fiber was in direct contact with the surface of the PMT window, while it had a 0.3–0.5 mm air gap between the end of the fiber and the sensitive surface of the SIPM in order to prevent damage to the SIPM. It should be noted that the Burle 8575 PMT has a 25% efficiency at the peak of the Kuraray emission wavelength while the SIPM's efficiency for that region is about 15%. As a result, for the the same light intensity from the scintillating fiber, the SIPM exhibits a photon detection efficiency that is 60% of the PMT's. The comparison in efficiency between the two devices is summarized in Table 4.3.

λ	Device	ϵ	QE	η
550 nm	SIPM	0.3	60%	20%
	PMT	1.0	5%	5%
437 nm	SIPM	0.3	45%	15%
	PMT	1.0	25%	25%

Table 4.3: Detection efficiency, $\eta = QE \cdot \epsilon$, for the SIPM's and PMT's.

The scintillating fiber was excited using a $^{90}\text{Sr}(^{90}\text{Y})$ beta source that has a 2280 keV maximal and 935 keV average energy of beta particles. The difference in the distributions of ionization energy loss in the scintillating-fiber core, as calculated by a Monte-Carlo simulation for the triggering beta particles and compared to the minimum ionization particles, is only a few percent on average [62]. The TDC and ADC spectra were accumulated and analyzed to extract the dependence of the detected light and timing resolution as a function of distance of the source from the respective readout end of the fiber. The mean values of the distributions were used in the calculation of the attenuation length.

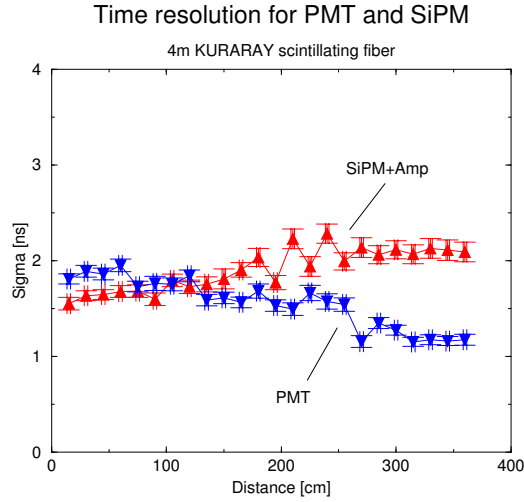


Figure 4.22: The timing resolution as a function of the distance from the ν detector.

The experimental data were fit with an exponential curve, $y = I \cdot \exp(-x/L)$, where I is the amount of light produced at the interaction point, L is the attenuation length and x is the distance to the ionization source. The ratios of the mean values for the two identical positions of an ionization source are larger for the PMT in comparison with the SiPM. As a result, two different attenuation lengths were obtained for the same fiber, $L_{SiPM} = 251$ cm and $L_{PMT} = 146$ cm for the SiPM and the PMT data, respectively, stemming from the difference in the spectral sensitivity of these two devices. The SiPM is more sensitive to longer values of λ where the transmission loss for the Kuraray fiber is lower. Therefore, the SiPM “realizes” a longer attenuation length compared to the PMT. Obviously, the SiPM-fiber combination provides a clear advantage over the PMT-fiber one, in applications where long fibers must be used.

The TDC peak location (the mean value of the Gaussian fit) was plotted versus the distance from the front-end detector. The slopes of the linear fits for the SiPM and the PMT agree with each other within the error of measurement, and are equal to 1.32 ± 0.01 ch/cm and 1.33 ± 0.01 ch/cm for the ν and the PMT experimental data, respectively. The TDC conversion factor was 47 ps/ch. The calculation of the velocity of light propagation gives $v = (1.60 \pm 0.03) \times 10^8$ m/s, a value that agrees with the Kuraray SciFi specifications sheet.

The timing resolution is presented in Fig. 4.22 as a function of the distance of the ionization source from each front-end detector. The data presented in Fig. 4.22 have not been corrected for the time jitter of the trigger detector or the jitter connected with the LeCroy 612 amplifier. The smallest values of sigma were 1.5 ns and 1.1 ns for the SiPM and the PMT, respectively, corresponding to the minimal distance between the ionization source and the front-end detector. Finally, the timing resolution depends on the number of detected photoelectrons. The average number of photoelectrons detected for the closest position of the ionization source from each front-end detector was ~ 3 – 5 for the SiPM and ~ 5 – 8 for the PMT. The resultant timing resolutions for the SiPM and for the PMT were comparable.

The properties of a SiPM working in Geiger limited mode have been measured and compared with a standard 2” vacuum PMT. The measurement with the nitrogen plasma discharge unit shows that the SiPM can achieve better time and energy resolutions under high photon flux. To evaluate the possibility of using the SiPM as a front-end detector for an electromagnetic calorimeter readout system, we measured the ADC/TDC spectra from the SiPM for 4 m scintillating fiber irradiated by ^{90}Sr beta source. Coupled to the performance attributes of SiPM’s, the results of these investigations demonstrated that SiPM’s satisfy the basic requirements for such an application.

Although SiPM’s appear to satisfy all the performance criteria of timing and energy resolu-

tions - and they also eliminate the need for high voltage supplies and associated cabling - one serious issue remains, namely their small active areas. Conventional coupling methods between the polished area of the fiber-lead composite and the SIPM's are not possible. Embedded wave shifting fibers in plexiglas light-guides or tiles will not suffice either, due to the loss scintillation light of low λ . One solution under investigation is the use of small light guides to collect the light from an area of the read-out face of the modules, a Winston cone to increase the light density and embedded clear fibers viewed head-on to collect the light to a number of SIPM's. Preliminary calculations indicate an adequate amount of light collected by each SIPM and a matrix of a number of them will combine into one output. We expect to have the first matrix of 16 SIPM's with common voltage supply and output within a few months and testing to begin.

4.3.4 Upstream Photon Veto

Studies of the photon angular distribution for the GLUEX experiment have shown the need for photon detection in the backward or upstream direction [46]. Several exclusive reactions, listed below, contain photons in the final state originating from both the meson and baryon decay vertexes, and were simulated to study the emission angles of the decay particles within the HALL D detector. These reactions were simulated using the GENR8 [63] phase space event generator assuming a photon beam energy of 9 GeV and a t dependence of $e^{-5|t|}$. The Monte Carlo events were then tracked through a simulation of the detector assuming the production and decay vertex coincided with the center of the target region, and analyzed for three different detector regions: the lead glass detector, barrel calorimeter, and the backward region upstream of the target (see Figure 4.23).

$$\begin{aligned} \gamma p &\rightarrow N^*(1500)\pi^+ \rightarrow (n\eta)\pi^+ \rightarrow n\pi^+\gamma\gamma \\ \gamma p &\rightarrow X^+(1600)\Delta^0 \rightarrow (\pi^+\pi^+\pi^-)(n\pi^0) \rightarrow \pi^+\pi^+\pi^-n\gamma\gamma \\ \gamma p &\rightarrow X^+(1600)n \rightarrow (\eta\pi^+)n \rightarrow n\pi^+\gamma\gamma \\ \gamma p &\rightarrow X(1600)p \rightarrow (\pi^+\pi^-\pi^0)p \rightarrow p\pi^+\pi^-\gamma\gamma \end{aligned}$$

In addition to the importance of keeping the energy threshold of the barrel calorimeter and the lead glass as low as possible, it was found that the reactions with photons emanating from the baryon decay vertex have shown that approximately 10% of the photons miss detection by either the barrel calorimeter or the lead glass detector. These photons go undetected by escaping out the upstream hole, which corresponds to emission angles greater than 117° .

Figure 4.24 displays where these lost photons hit the plane at the upstream end of the solenoid. The ring at 117° is the current barrel calorimeter limit. Several rings are shown at other angles, indicating the geometrical losses from each. In order to detect the escaping backward photons and provide nearly hermetic photon coverage it is necessary to implement an Upstream Photon Veto counter (UPV).

Design Considerations

The UPV is a lead scintillator sampling veto calorimeter located directly upstream of the CDC and in place of the solenoid's original field-shaping mirror plate. In the current GLUEX design, this mirror plate is modified by removing all of the soft iron within the inner solenoid radius. This modification effectively removes the upstream mirror plate leaving only a soft iron annulus the size of the magnet coils. This modification has several benefits. First, it allows for upstream access to the target region, cylindrical drift chamber, and the upstream end of the barrel calorimeter. More importantly, it allows for the addition of an upstream photon veto.

The UPV is designed to detect soft photons of energy 20 MeV and greater emerging from the target region. The counter is able to detect multiple photons with fast detection and with timing information that may be utilized at the trigger level.

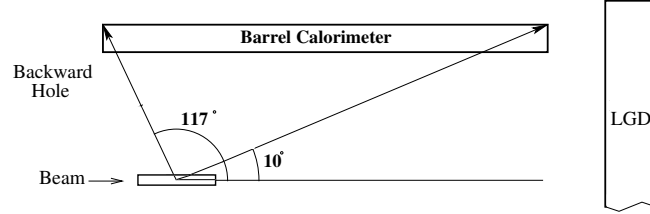


Figure 4.23: Angular distribution, in degrees, from the center of the target to various reference points, for various simulated reaction channels. Tracks more forward than 10° miss the barrel calorimeter and will hit the LGD. Between 10° and 117° the photons will enter the barrel calorimeter. Photons produced at angles larger than 117° miss both calorimeter detectors, and necessitate the construction of an upstream veto detector to achieve near hermeticity.

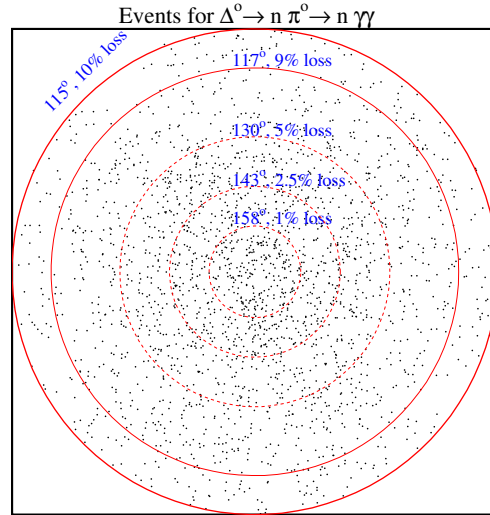


Figure 4.24: The tracked photon intersections on the x-y plane at the upstream end of the barrel calorimeter. The 117° circle is the end of the barrel calorimeter. Various other photon-loss percentages, and their corresponding angles are plotted as well.

As shown in Figure 4.25, the UPV consists of 18 layers of 1 cm thick scintillator alternating with first 12 layers 0.185 cm thick lead sheets ($0.36X_0$ each) then 6 layers of 0.370 cm thick lead sheets ($0.72X_0$ each). This design was simulated using the GEANT 4 package to study the expected performance of the UPV calorimeter. The study uses a photon beam of various energies incident normal to the detector face. The results, summarized in Figure 4.26, ignore quantum fluctuations and express an optimal resolution of $\frac{\sigma}{E} = 5\% + \frac{8\%}{\sqrt{E(\text{GeV})}}$.

Each scintillator layer consists of seven $34\text{ cm} \times 238\text{ cm}$ paddles forming a plane. The central paddle has a 10 cm hole to allow for the passage of the beam. The effective area of each plane is approximately $238\text{ cm} \times 238\text{ cm}$. The total counter thickness is 22.4 cm or $8.91X_0$. The layers are arranged into three alternating orientations: x , u , and v ($\pm 45^\circ$, respectively) as shown in

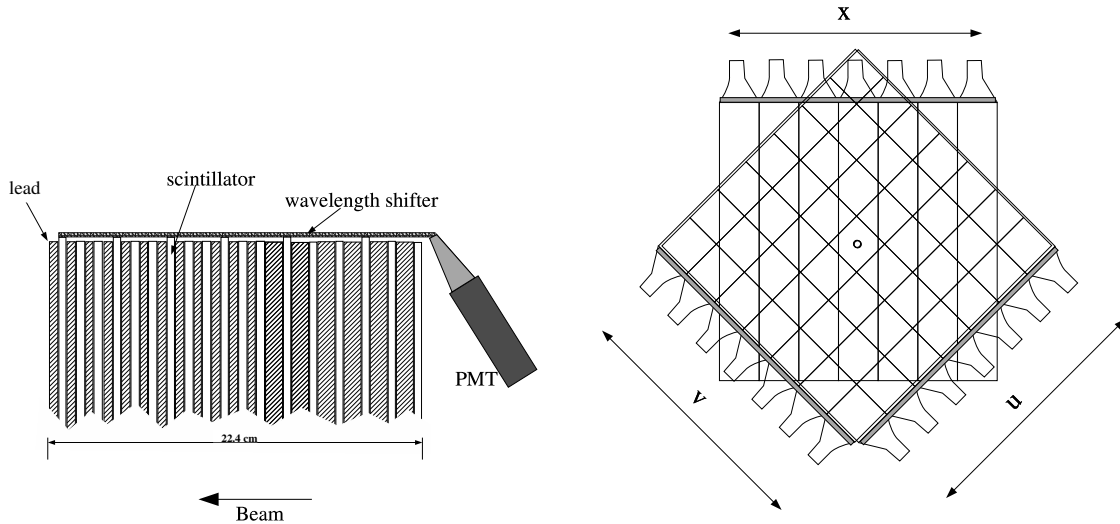


Figure 4.25: The left-hand figure is a sketch of a UPV segment. The 18 scintillator layers are arranged into 3 alternating orientations: x , u , and v . Shown is the light collection for one such orientation. The light-collecting ends of the scintillators are joined together via a wavelength shifter which is oriented perpendicular to the scintillators. The wavelength shifter is used to redirect the light through 90° and out the upstream end of the solenoid to PMTs. The right-hand figure is a sketch of an upstream photon veto counter orientation. The layers are arranged into three alternating orientations: x vertical, $u +45^\circ$ and $v -45^\circ$ layers.

Figure 4.25.

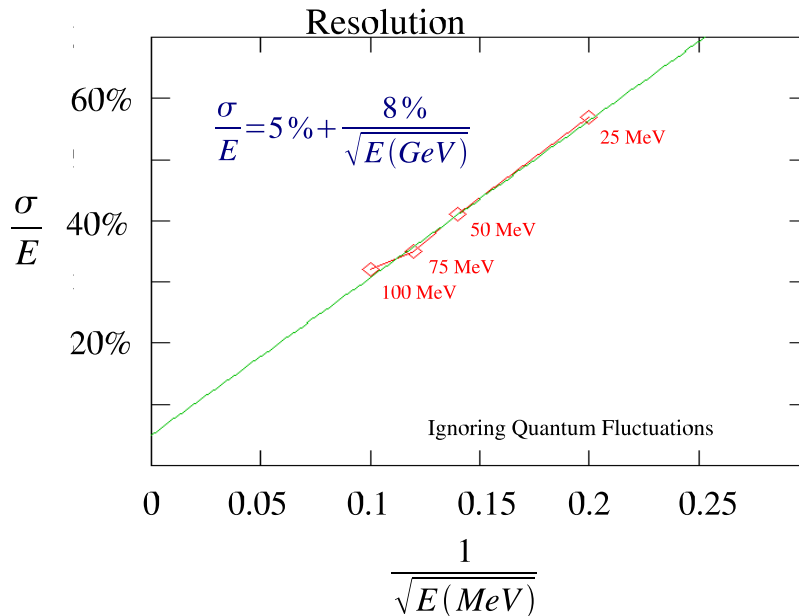


Figure 4.26: Simulation using the GEANT 4 package to study the expected performance of the UPV calorimeter. The study uses a photon beam of various energies incident normal to the detector face. The results, ignoring quantum fluctuations, express an optimal resolution of $\frac{\sigma}{E} = 5\% + \frac{8\%}{\sqrt{E(\text{GeV})}}$.

The scintillation light collection is realized at one end of each paddle only. The opposite end is coated with an opaque material to eliminate reflections. For each orientation, the light collecting ends of the scintillators are joined together via a wavelength shifter which is oriented perpendicular to the scintillators. The wavelength shifter is used to redirect the light through 90° and out the upstream end of the solenoid to photo-multiplier tubes (PMT). Each PMT is protected from any fringe magnetic field with soft steel casing and mu-metal shield.

4.4 Charged Particle Tracking

The system of tracking chambers in the GLUEX detector must cover as close to a 4π solid angle as possible over a wide range of particle momenta and must have sufficient momentum resolution to be able to identify missing particles. All tracking devices are located inside the barrel calorimeter which is in turn inside the $2.24 T$ solenoid. The barrel calorimeter defines a maximum keep-out radius of about $65 cm$. The physical radius of all chambers has been limited to $59 cm$. This provides $6 cm$ of space for support and installation rails, and cables and gas feeds for the forward chamber packages. In the forward region, the chambers need to extend as close to the beam line as possible. In the initial detector design, there is no vertex chamber around the liquid hydrogen target. A possible upgrade to the system would be the addition of a device which could achieve sub- $100 \mu m$ resolution. Very accurate vertex information from such a device could be important in identifying secondary vertexes from decaying particles (e.g. K_S , Λ , Σ , ...). In the forward region, it is important to be able to reconstruct fast, small-angle particles (down to nearly 0°). Finally, there is a small hole in the particle identification for particles that spiral and do not reach the barrel calorimeter. It is necessary that in the central region, the tracking should have sufficient dE/dx information to aid in the separation of π 's, K 's and p 's up to momenta of about $0.45 GeV/c$ — a regime where dE/dx measurements work extremely well.

4.4.1 Design Considerations

In order to achieve the desired goals in the GLUEX tracking, the LASS detector [26] design was used as our starting point. This device used several different tracking elements each optimized for a particular region in the detector. Figure 4.27 shows the GLUEX tracking regions. Surrounding the target is a cylindrical straw-tube drift chamber (CDC) which provides very good $r - \phi$ and good z resolution. In addition, it is necessary for this detector to provide some dE/dx information. In the forward region, round planar drift chambers (FDC) will be arranged in four identical tracking packages. There are still background studies underway to determine exactly how to handle the beam-line region. One option is to have the chambers physically fill the space, but to deaden the active elements that are in the beam line. This could be accomplished by placing Styrofoam around them. An alternative would be to add small support structures around the beam hole and physically remove all material. The final decision will be based on the results of background studies. A summary of the tracking chamber parameters are given in Table 4.4.

System	Radius		Length		Resolution	
	r_{\min}	r_{\max}	z_{\min}	z_{\max}	$\sigma_{r-\phi}$	σ_z
CDC	13.0 cm	59.0 cm	10 cm	210 cm	150 μm	1.5 mm
FDC	3.5 cm	59.0 cm	230 cm	400 cm	150 μm	fixed

Table 4.4: A summary of the tracking chamber parameters. The z values under *Length* indicate the smallest and largest z of the combined system. The z origin is at the upstream end of the magnet. The z resolution for the CDC comes from $\pm 6^\circ$ stereo layers. The z resolution of the planar chambers is assumed to be given by their position in space.

The charged-particle system within the solenoid must be optimized for both overall ac-

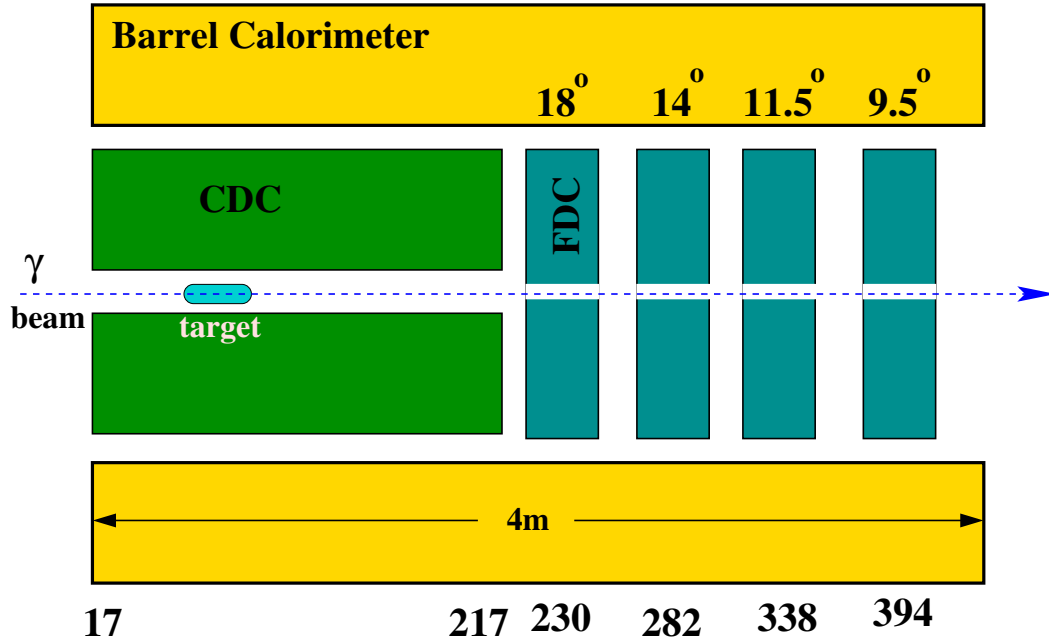


Figure 4.27: The GLUEX detector. The tracking is composed of two elements: a straw-tube chamber called the cylindrical drift chamber (CDC) and circularly-shaped planar chambers designated as the forward drift chambers (FDC). The small gap indicated in the middle of the FDCs is due to wires that will not be instrumented. If background studies merit, we could also consider a physical hole. The distances labeled along the bottom of the figure are the z coordinate of the upstream and downstream ends of the CDC, and the center of each FDC package. The angles labeled above the FDC packages are from the center of the target to the center of the outer edge of the chamber.

ceptance and momentum resolution. A detailed study using the *HDFast* framework has been performed to examine this [64]. The results of this study indicate that the above combination of the straw-tube chamber and planar drift chambers with typical $r - \phi$ position resolutions of $150 \mu\text{m}$ will satisfy our requirements. A plot of resolution as a function of angle is shown in Fig 4.28 where we have zoomed in on the forward angles in the left panel of the figure. Note that the current Monte Carlo does not fully deal with the degradation in resolution as the tracks become parallel to the CDC wires. A couple of features of these plots are worth commenting on. The rapid degradation in resolution as one goes to very forward angles is driven by the distance (in z) between the first and fourth FDC packages. The most forward numbers can be decreased by about 0.01 for each additional 25 cm of length. Unfortunately, moving the fourth FDC package further down-stream moves it into a non-uniform field region. This tends to cancel the improved resolution due to the larger length. The degradation in resolution from about 10° to 20° corresponds to the transition region from mixed FDC-CDC tracks to all CDC tracks. It is due to the successive loss of FDC packages being linked to the tracks. It is possible to somewhat shorten the CDC and move the first FDC package upstream. However, if the CDC is shortened by as much as 50 cm , then the transition region degrades significantly. An optimum length for the CDC is between 170 and 200 cm and is currently understudy. Such a small perturbation in length has little effect on construction of the chamber.

The 22.4 kG solenoid field determines the physically measurable quantities, and hence, the momentum resolution. The transverse momentum, p_\perp and the dip-angle, λ , ($\lambda = \frac{\pi}{2} - \theta$) are measured from the curvature of the tracks and their initial direction. The total momentum and the longitudinal momentum are then obtained from these as $p_{\text{total}} = p_\perp \sec \lambda$ and $p_\parallel = p_\perp \tan \lambda$. The accuracy of the p_\perp measurement is completely dominated by the $r - \phi$ resolution of the

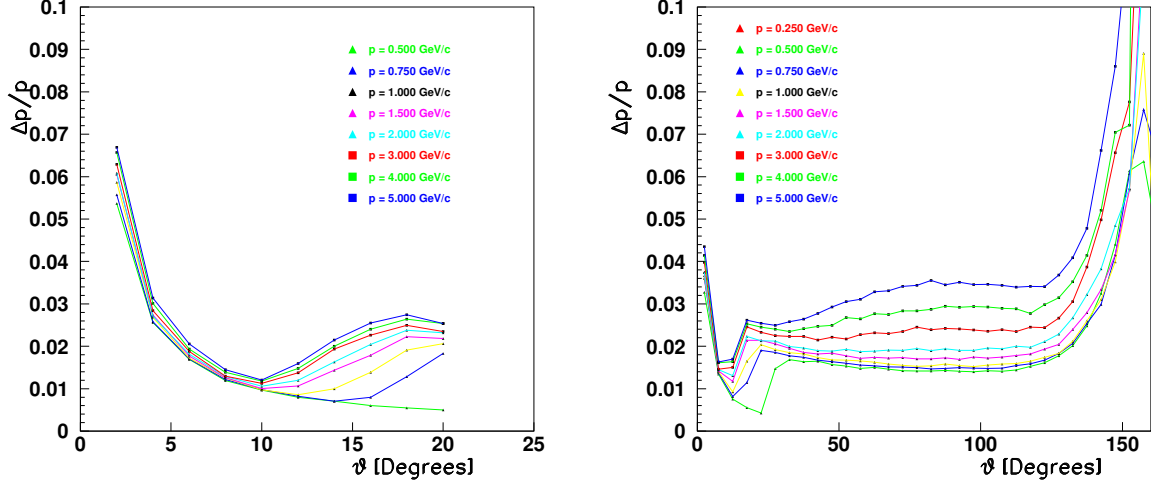


Figure 4.28: The resolution as a function of angle is plotted for several total momenta. The plots correspond to the detector design shown in Figure 4.27. For polar angles larger than 70° , the maximum detected momentum will be well under $1\text{GeV}/c$ so even though the resolution for high-momentum tracks is poor in this large-angle region, it will not affect the overall tracking of physics events.

tracking chambers, while the λ measurement relies on an accurate measurement of both z and the distance traveled.

4.4.2 Track Reconstruction

Track reconstruction effects play a very important role in the design of the combined system. In particular, track matching between different detectors and the associated inter-calibration problems often limit the ultimate resolution. In addition, the high magnetic field strength of 22.4 kG means that tracks may spiral significant distances between measurement planes in the forward direction. This means that one would like as much information as possible from each measured hit in the detector. Other complicating issues are that the magnetic field is non-uniform near the ends of the magnet, and in the region between the end of the solenoid and the forward calorimeter. However, particle identification will require projecting charged tracks forward through this non-uniform field region. Tracking near the end of the solenoid needs to be as good as possible.

An example showing the typical charged particle momentum that needs to be measured comes from reaction 4.9. This final state consisting entirely of charged particles is fairly typical of the typical exotic-hybrid channel that will be studied.

$$\gamma p \rightarrow \eta_1(1800)p \rightarrow \pi^+\pi^-\pi^+\pi^-p \quad (4.9)$$

The exotic spin-one $\eta_1(1800)$ is produced with a mass of $1.8\text{ GeV}/c^2$ and a typical t distribution. The incident photon energy is $9\text{ GeV}/c^2$. Figure 4.29 shows the transverse and longitudinal components of momentum from the π 's in this reaction while Figure 4.30 shows the same distributions for the protons.

From the two sets of plots, several important features can be seen. The charged pions from the decay of the meson system are fairly forward peaked. Once θ_π is larger than about 40° , there are almost no pions with a momentum larger than about $1\text{ GeV}/c$. Additionally, there are almost no pions with θ larger than 100° . The protons almost all fall within the angular

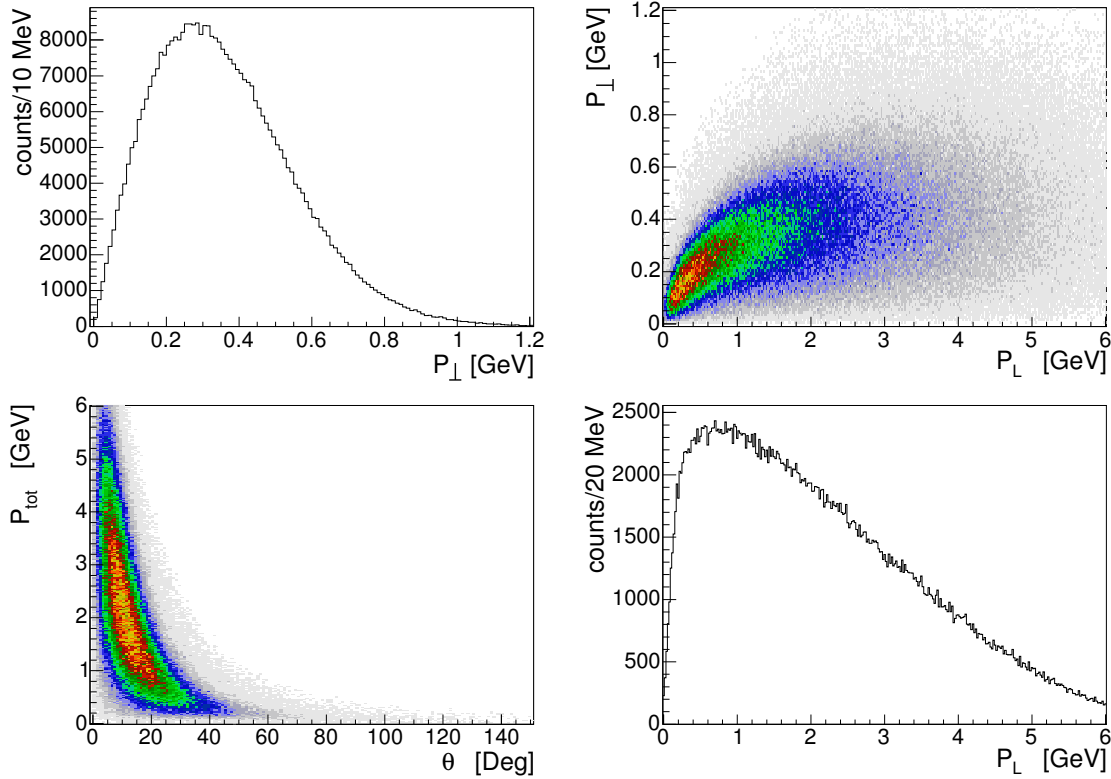


Figure 4.29: The momentum distribution of charged pions from the reaction $\gamma p \rightarrow \eta_1(1800)p \rightarrow 2\pi^+2\pi^-p$. The upper left-hand figure shows the momentum perpendicular to the beam direction. The upper right-hand figure shows the perpendicular versus the longitudinal momentum. The lower left-hand figure shows the total momentum versus the polar angle θ and the lower right-hand figure shows the momentum along the beam direction.

range of 20° to 60° degrees. This is almost entirely covered by the CDC. Many of these protons will need to be identified by either time-of-flight for the BCAL or using dE/dx in the CDC. Good tracking resolution for high-momentum particles in the backward angle region is not required, so the rapid degradation of momentum resolution for these large angles as seen in Figure 4.28 is not a real issue for the detector's overall performance. In addition, most events have at least one particle moving in the forward direction at high momentum. The momentum versus angle for all particles in each event is displayed in Figure 4.29. Good tracking will be needed as close to the beam line as possible, hopefully extending down to 2° .

Another tracking issue is that many of the charged particles in GLUEX will produce spiraling tracks in the solenoid. Figure 4.31 shows the p versus θ plane for tracks in the solenoid. Tracks which fall above the hyperbolic curve cannot spiral in the 59 cm radius region containing the tracking chambers. Below the hyperbola are a series of approximately horizontal lines. Tracks below these lines spiral the number of times indicated. Based on the p versus θ distributions in Figures 4.29 and 4.30, it is clear that most tracks at angles larger than 50° will always spiral at least once in the detector.

Pattern recognition is an important part of track reconstruction as well. This process requires finding local clusters of hits and associating them into small track segments that can be combined into larger tracks. In order for this procedure to work well, it is desirable to have sufficient hits in close proximity such that they will be easily associated. One useful comment on this issue is when the LASS experiment ran in similar conditions, they had severe pattern recognition issues due to the large magnetic field. They resolved it by building chambers with both anodes and cathodes which were read out, with the cathodes and anodes being arranged such that together

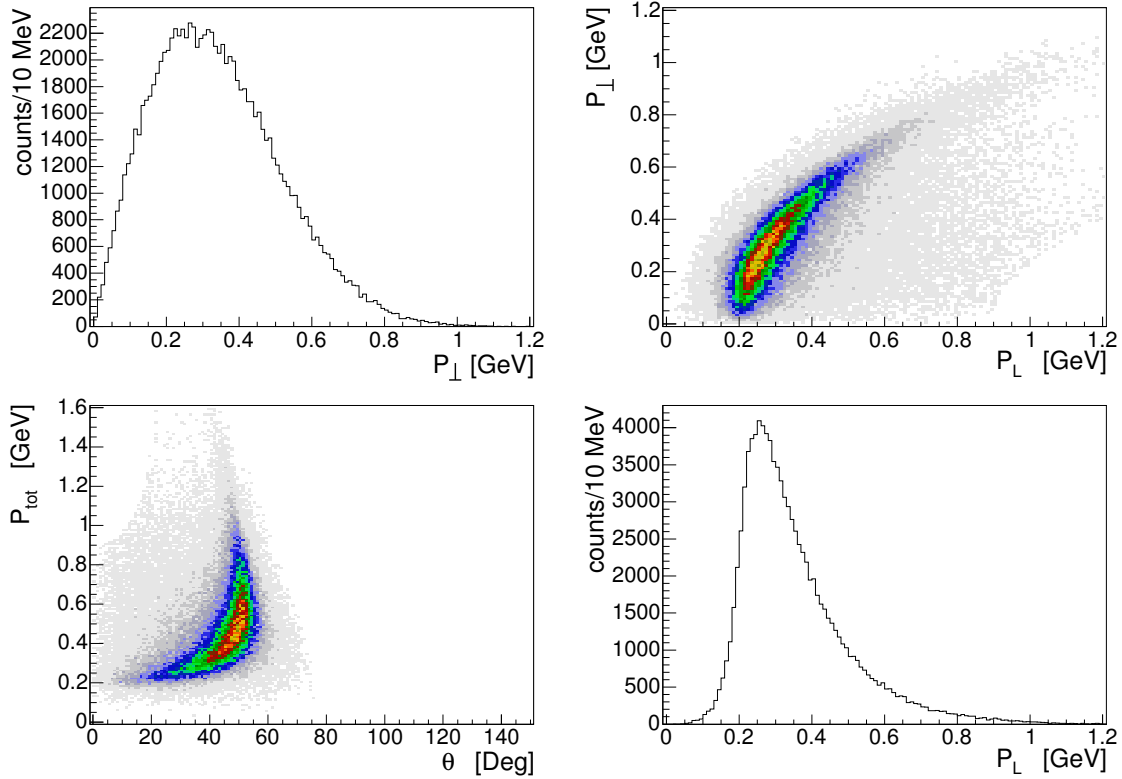
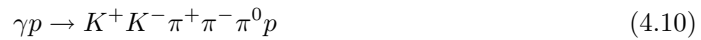


Figure 4.30: The momentum distribution of protons from the reaction $\gamma p \rightarrow \eta_1(1800)p \rightarrow 2\pi^+2\pi^-p$. The upper left-hand figure shows the momentum perpendicular to the beam direction. The upper right-hand figure shows the perpendicular versus the longitudinal momentum. The lower left-hand figure shows the total momentum versus the polar angle θ and the lower right-hand figure shows the momentum along the beam direction.

they provided a 3-dimensional point. The GLUEX detector is trying to build on this experience by reading out both cathodes and anodes in the forward direction. We are also planning packages that consist of six closely spaced planes. Such packages will allow local identification of track segments with a reasonable measure of curvature. This has then been repeated four times to provide sufficient segments for high efficiency track-segment linking. In the CDC, the pattern recognition issue is dealt with by creating three sections containing several adjacent straight tube. These are then interleaved with two sets of crossed stereo layers.

The resolution necessary in the photon beam energy has been matched to the expected momentum resolution in the tracking elements of the GLUEX detector. This has been done by looking at the missing mass resolution. As an example, consider reaction 4.10.



It is also assumed that the π^0 in 4.10 is not detected. Using the reconstructed charged tracks, the known beam energy, and the assumption that the reaction took place on a proton target, the square of the missing mass is computed and shown in Figure 4.32(a) for a nominal 0.1% beam energy resolution. The distribution is centered at the square of the π mass, but it has a non-negligible width. In Figure 4.32(b) the width of the peak in (a) is plotted as a function of the beam energy resolution. For this particular reaction with a missing π^0 , a beam energy resolution of 0.1 to 0.2% is well matched to the 200 μm resolution of the tracking system.

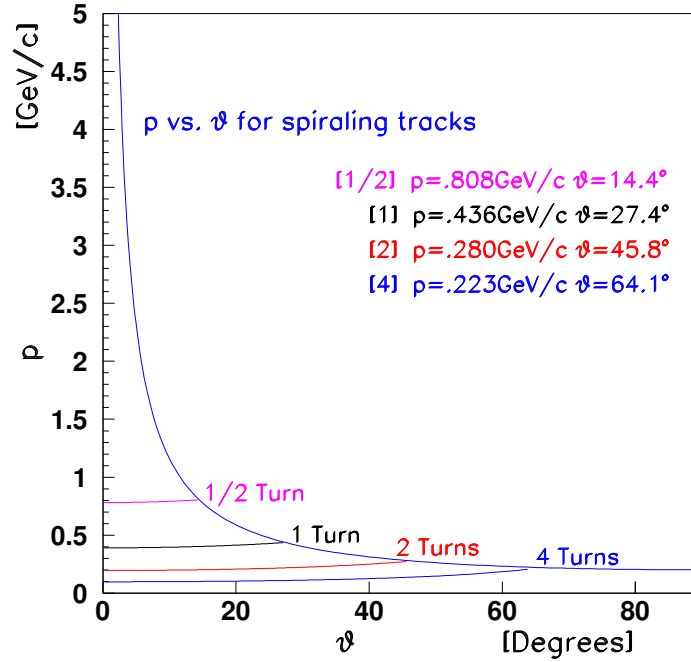


Figure 4.31: This figure shows the number of full circles made by charged particles in the magnetic field. The limit line corresponds to $p_{\perp} = 0.2 \text{ GeV}/c$ tracks. The approximately horizontal lines indicate when the particle can make the indicated number of turns without leaving the magnet.

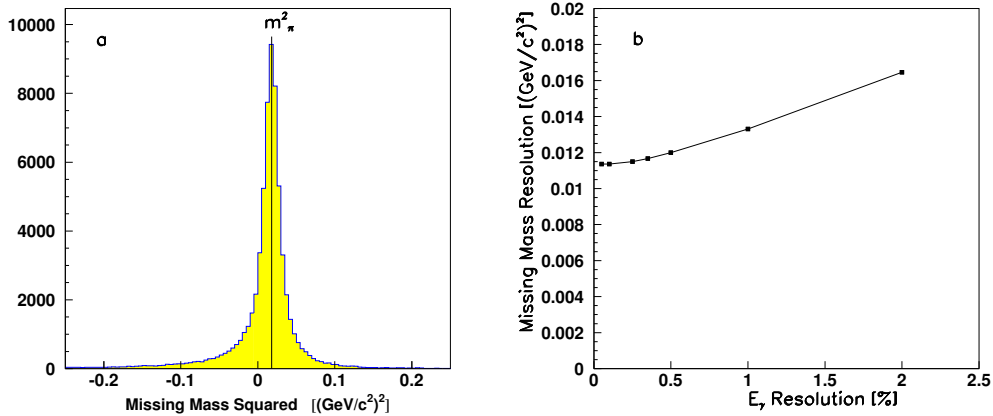


Figure 4.32: Missing mass squared from the reaction 4.10 where the π^0 is assumed missing. (a) is for 0.1% beam energy resolution, while (b) is a plot of the missing mass resolution as a function of the beam energy resolution.

4.4.3 Straw-tube Drift Chamber

The straw-tube drift chamber (CDC) is used to track particles coming from the GLUEX target with polar angles between 6° and 155° with optimal coverage from about 20° to 140° , (see

Figure 4.33). Tracks moving more forward than about 20° will be tracked by both the CDC and the FDC systems. These tracks will need to travel through the downstream end plates of the CDC, so minimizing the material in these plates is extremely desirable. The use of a straw-tube chamber in this region allows us to accomplish this goal as the straws can easily support the $\sim 50\text{ g}$ of tension on each of the 3240 anode wires in the chamber. If one were to go with a wire-cage geometry using field wires, one would need to support about 3000 kg of tension between the end plates. This would require thick end plates as well as thick shell material at both the inner and outer radius of the chamber. In addition to minimizing material, the straw-tube designs also allows for an extremely well defined electric field through which the ionization drifts. This is especially important given the 2.24 T magnetic field. With straw-tubes, the time-to-radius relation is extremely simple, (see Figure 4.36). In the case of field wires, there are always regions between the field wires where the field is poorly defined. This in turn leads to a significant deterioration in resolution for tracks passing near the edge of such cells.

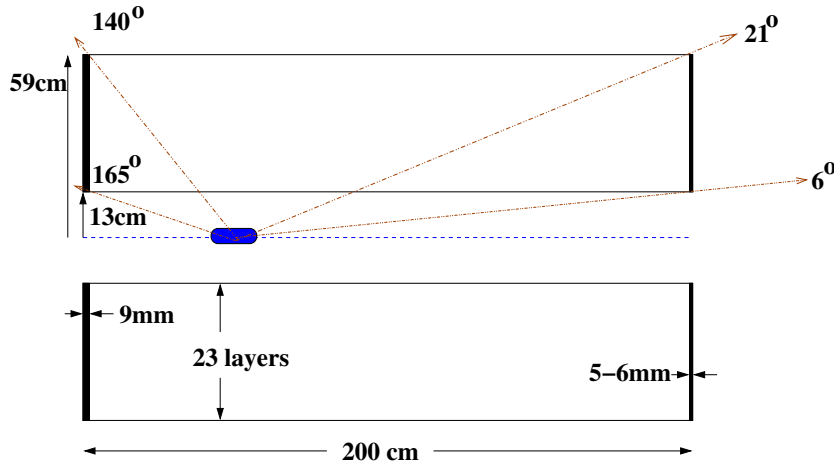


Figure 4.33: A side view sketch of the CDC.

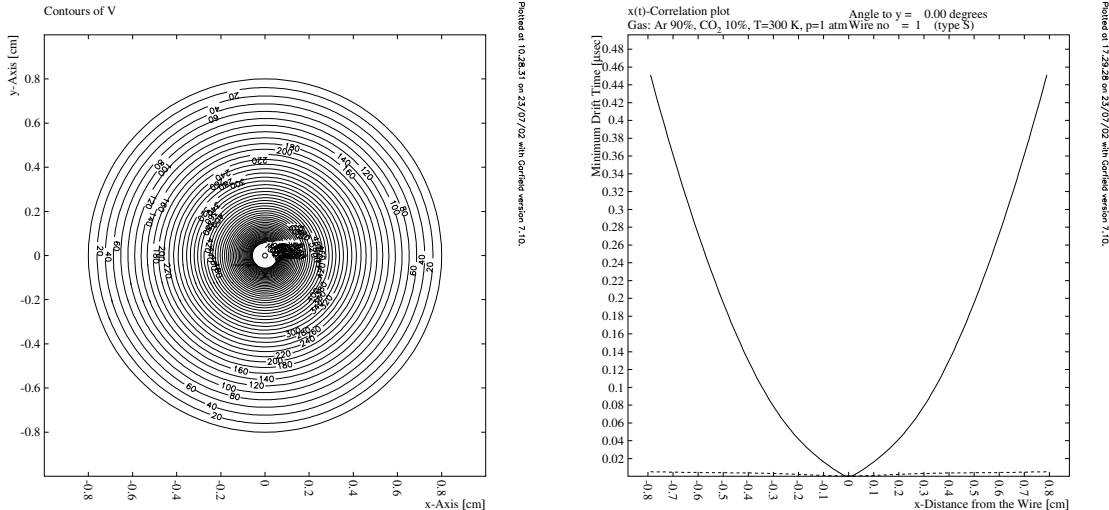


Figure 4.34: The left-hand plot shows a GARFIELD [65] calculation of the electric field in the straw tube. The right-hand figure shows a typical time-to-distance plot calculated for the straw-tube geometry in the 2.24 T magnetic field.

The major disadvantage of a straw-tube design is that it adds additional material in the tracking region. However, by careful use of thin straws, this material can be minimized. An additional concern is the measurement of dE/dx using straw-tube chambers. This has been done once [66], but is typically not something that straw-tube chambers are asked to do. In order to do this, one has to be able to accurately compute the tracks path length within the ionization volume. Fortunately, the particles for which the dE/dx measurements are to separate π s, Ks and ps whose total momentum is under $0.45 \text{ GeV}/c$. A region where dE/dx does not need to be particularly good to have a big impact.

Table 4.5 lists the material type and approximate thickness of all materials used in the CDC. The upstream end plate is about 9 mm thick aluminum. However, the down stream will be either $5 - 6 \text{ mm}$ thick aluminum or 9 mm thick G10. The minimum thickness of the downstream end plate is controlled by machining that needs to be done to support the stereo layers. However, in addition to the end plate themselves, the feed throughs in the down stream end do not need to be conductive. The use of plastic (DELRIN) will help to minimize the material. The exact choice between aluminum and G10 will be based of structural studies that are currently underway. It is anticipated that in the CDC, the amount of material in the down-stream end plate will be between $\frac{1}{3}$ and $\frac{1}{2}$ of that in the up-stream plate.

Part	Material	Thickness	
		r	z
Upstream End plate	Al		9 mm
Downstream End plate	Al		$5-6 \text{ mm}$
	G10		9 mm
Inner Shell	Carbon Fiber	0.7 mm	
Outer Shell	Fiberglass	6 mm	
Upstream Feed Through	Al		1.5 cm
Downstream Feed Through	Delrin		1.0 cm
Wire	Au-W	$20 \text{ }\mu\text{m}$	
Straw Tubes	Kapton	$100 \text{ }\mu\text{m}$	
	Al	$15 \text{ }\mu\text{m}$	
Upstream Gas Plenum	Lucite		5 mm
Downstream Gas Penum	Lucite		3 mm

Table 4.5: The anticipated material to be used to build the CDC. See the text for discussion.

The CDC will contain 3240 straws, each of which is 1.6 cm in diameter and 2 m long. The straws are arranged in 23 layers (see table 4.6). Eight of the 23 layers will be stereo, tilted by $\pm 6^\circ$ from the straight tubes. The tubes are assumed to have an $r - \phi$ resolution of $150 \text{ }\mu\text{m}$, while resolution along the wire length will be obtained using the 8 stereo layers. This will yield a resolution along the length of the wire of about $150 \text{ }\mu\text{m}/\sin(6^\circ)$ or about 1.4 mm . The straws will be at ground potential, while the $20 \text{ }\mu\text{m}$ diameter gold-plated tungsten wire will be at a positive high voltage between 1.5 and 2.5 kV such that they provide a gain of about 10^4 . The exact voltage will depend on the final choice of gas mixture. The wires will be read out only at the upstream end of the detector. This will also minimize material between the CDC and FDC chambers and improve the overall momentum resolution.

We are also considering the possibility of of connecting pairs of wires together on the down stream end and using the effective two-ended readout to provide a charge division measurement. While the resulting z -resolution would be on order of 10 cm , this may be useful in pattern recognition. It would also provide a hardware measurement of the transit time correction in the anode wire. A final decision awaits both completion of the prototype and initial work on pattern recognition software. However, the only impact in chamber design is in the choice of anode wires. A second small design change that may also improve pattern recognition is the arrangement of stereo layers. Table 4.6 shows the two stereo super-layers containing both $+6^\circ$ and -6° layers. Changing them so that all of one super layer of $+6^\circ$ and the other -6° is likely to make track

finding in these groups easier. The major concern with this is the mechanical torques extorted by the stereo layers will no longer be completely balanced. A careful engineering study needs to be done to determine how to prevent an induced twist in the chamber.

Layer	No. of Tubes	Radius <i>cm</i>		Stereo Radians
		Center	Plate	
1	58	14.777	14.777	0.000
2	65	16.559	16.559	0.000
3	72	18.340	18.340	0.000
4	79	20.122	20.122	0.000
5	86	21.905	24.295	0.105
6	93	23.687	25.913	0.105
7	100	25.469	27.552	-0.105
8	107	27.251	29.207	-0.105
9	121	30.816	30.816	0.000
10	128	32.598	32.598	0.000
11	135	34.381	34.381	0.000
12	142	36.163	36.163	0.000
13	149	37.945	37.945	0.000
14	156	39.728	41.094	0.105
15	163	41.510	42.820	0.105
16	170	43.293	44.550	-0.105
17	177	45.075	46.284	-0.105
18	189	48.131	48.131	0.000
19	196	49.913	49.913	0.000
20	203	51.696	51.696	0.000
21	210	53.478	53.478	0.000
22	217	55.261	55.261	0.000
23	224	57.043	57.043	0.000

Table 4.6: Geometrical data about the CDC. There are a total of 3240 straw tubes in the CDC. The listed radii are at the center (length-wise) of the chamber and at the end plates. It should be noted that the stereo wires have a smaller radius at the center than at the end plates.

The choice of gas also plays a significant role in the chamber's performance due to the 2.24 T magnetic field. In order to study this, the GARFIELD program [65] has been used to compute electrostatic properties of the straw tubes, both with and without the magnetic field. The results of this work can be summarized in reference [67]. Figure 4.34 shows an electrostatic calculation for a tube with the wire well-centered in it. Figure 4.35 shows GARFIELD calculations for two tracks going through a straw tube in three different gas mixtures. The three gas mixtures are Ar(30%)-C₂H₅(20%)-CO₂(50%), Ar(90%)-CO₂(10%) and Ar(50%)-C₂H₅(50%). While in all three cases the time-to-distance relationship is well defined, the longer drift distances of the spiraling tracks introduce a large diffusion contribution to the total resolution. The diffusion resolution, σ_L is also dependent on the gas. Pure argon has an extremely poor resolution, while pure carbon dioxide has a very good resolution. Finally, it is desirable to collect the electrons as quickly as possible. A slow gas, or a very long drift distance can easily push the collection time over a micro second. For this reason, the Argon-Ethane mixture shown in the lower two plots of Figure 4.35 is an inappropriate mixture. Investigations are ongoing to identify mixtures that will satisfy the all of the requirements. To indicate the advantage of good electrostatics, Figure 4.36 shows what happens to the time-to-distance relation as one goes from zero magnetic field to full magnetic field.

In order to achieve the desired 150 μm resolution in the CDC, we need to account for all possible contributions to the resolution. Table 4.7 summarizes these. Clearly the most important is the diffusion term, which depends on the gas. In order to achieve this, a gas mixture that

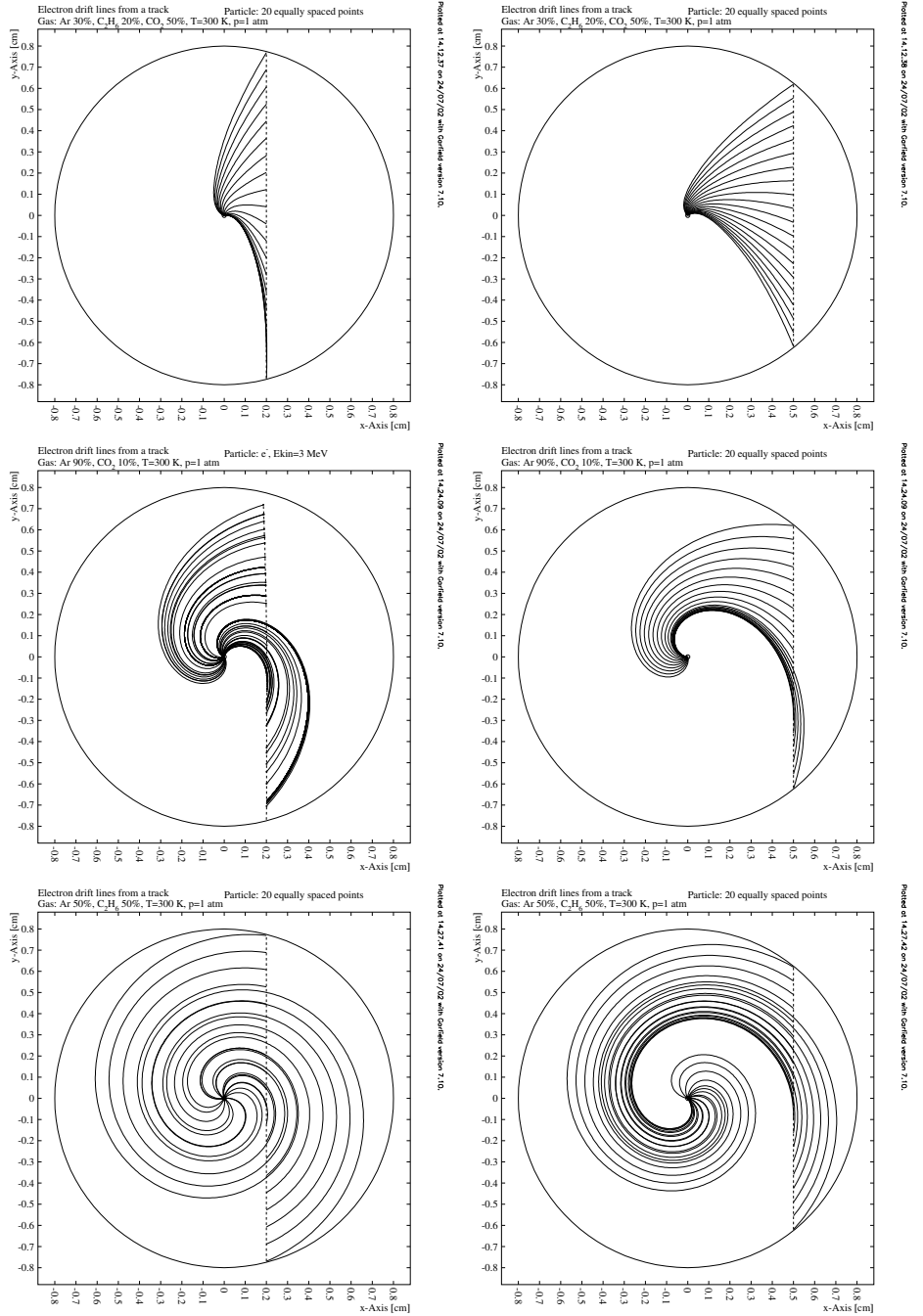


Figure 4.35: Garfield simulations of electrons drifting through a straw tube in the CDC. The curved shape of the tracks is due to the Lorentz angle induced by the 2.25 T magnetic field.

contributes about $120 \mu\text{m}$ for an average 5 mm drift in a $\sim 2.5 \text{ kV/cm}$ electric field needs to be used. Many gas mixtures satisfy this requirement. The next largest contribution is the gravitational sag. This scales with the length squared, and will go down if the chamber is shorter than 2 m. The timing resolution of $45 \mu\text{m}$ assumes that the signal is digitized using 125 MHz flash ADCs and that a timing algorithm that yields times to about $\frac{1}{3}$ of the digitization are used. Time fitting algorithms that are matched to the pulse shape in chambers usually yield intrinsic time resolutions around 20% of the time bin width.

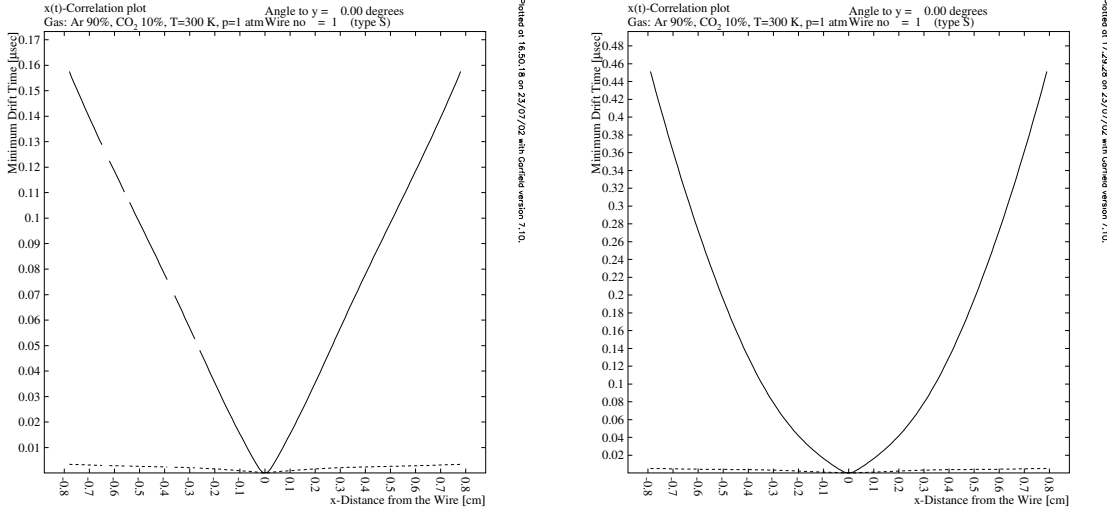


Figure 4.36: Calculated time versus distance in 90% Argon, 10% Carbon Dioxide mixture. **left:** No magnetic field, **right:** full magnetic field.

Effect	Resolution μm
Diffusion σ_L	50 to 200 μm
Geometrical Precision	40 μm
Gravitational Sag	56 μm
Electrostatic Deflection	10 μm
Timing Resolution	45 μm
Quadrature Total	96 to 216 μm
Design Resolution	150 μm

Table 4.7: The estimated contributions to the ultimate chamber resolution from various known effects. These numbers are based on 2 m long, 20 μm diameter, Au-W wires under 50 g tension.

In the construction of the straw-tube chamber, the most technically difficult part involves the stereo layers. Several aspects contribute to this. The holes for these layers need to be drilled at a layer-dependent compound angle. The outside of the tube inserts need to rest flush against the end plates as shown in Figure 4.37 for both the straight-through and the stereo tubes. Such work either requires a multi-axis CNC machine, or a rotary table stacked on top of three sine plates. This machining also limits the minimum thickness of a plate.

There are also difficulties in mounting the straw tubes for the stereo layers. In the final chamber, the tubes are glued to adjacent tubes in the same layer, and adjacent layers are glued together. In order to do this gluing, clam-shell holders need to be built that match the spacing in each layer and hold the tubes in position while they are glued. For the stereo layer, these clam shells need to be built with the same compound angles as the end plates.

In order to understand the issues involved in the building and operating the straw-tube chamber, the Carnegie Mellon (CMU) group has gone through several steps in prototyping the chamber. They are currently completing a full-scale prototype of $\frac{1}{4}$ of the chamber.

To study the behavior of straw tube chambers, a 2 m long chamber with 2 cm diameter tubes has been acquired from the EVA experiment at Brookhaven [68]. A setup which reads out four tubes in the chamber using a 4-channel digital oscilloscope, and then transfers the data to a local computer for analysis has been built. Signals are produced from a $^{44}Ru_{106}$ source, (see Figure 4.38). The β 's from the source are collimated through a 1 mm diameter, 1 cm long tube. The source is placed about 30 cm below the chamber and aligned as shown in the figure. The

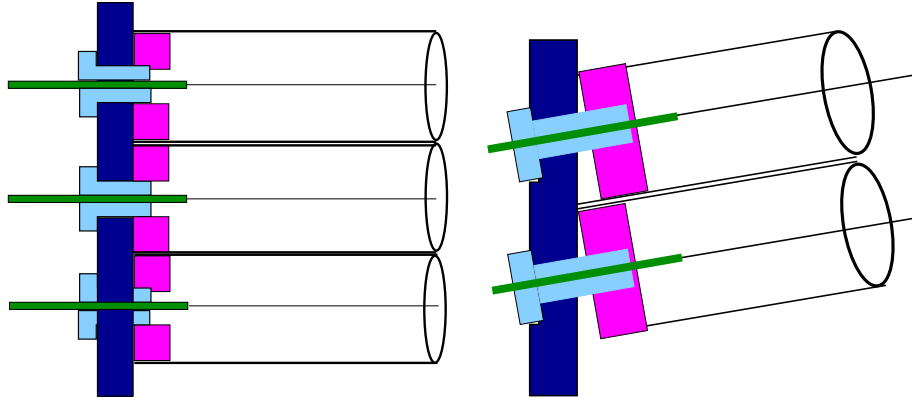


Figure 4.37: Schematic drawings of the feed throughs for both the normal (**left**) and stereo (**right**) wires.

system is triggered on a signal in the upper tube, and events with signals in all four tubes are read out. Gas mixtures can be varied using a locally built three-component gas-mixing system. This allows for detailed studies of the chamber performance in different gas mixtures [69].

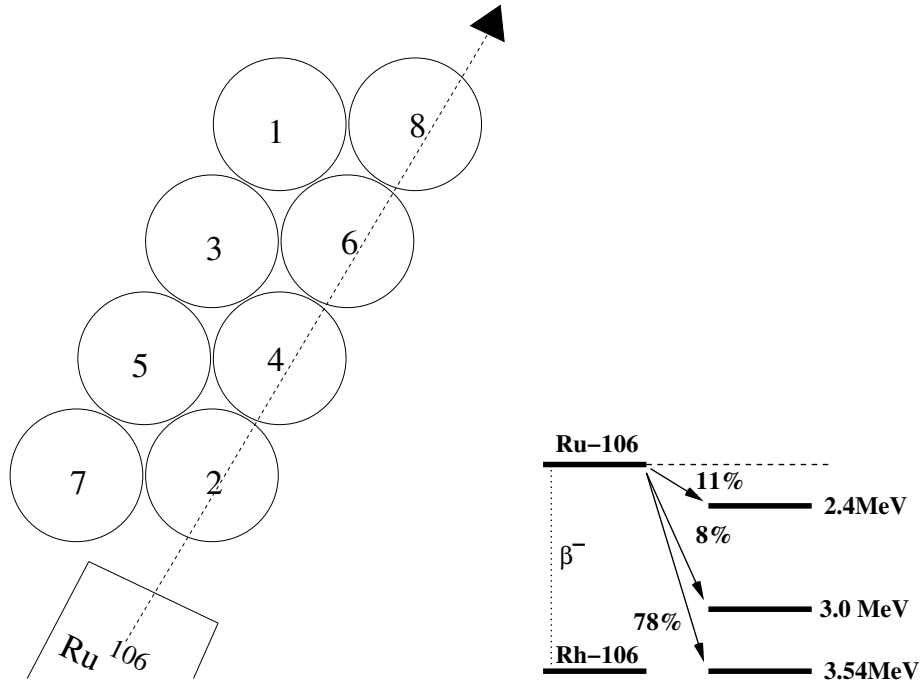


Figure 4.38: Setup of the straw-tube prototype chamber used in studying signals and gas properties. Note the ^{106}Ru source emits primarily 3.54 MeV electrons but there are also up to 1.14 MeV photons.

Figure 4.39 shows signals measured in two different gas mixtures. Currently, there is no way of applying a large magnetic field to the straw tubes. This makes detailed studies of the Lorentz angle only possible through simulation which is currently underway using the GARFIELD [65] program.

In order to build the full-scale prototype, software was written that computes the necessary compound angles at each end plates, and then turns them into machining instructions. An example of the visual output of this program is shown in Figure 4.40 which shows the drilling

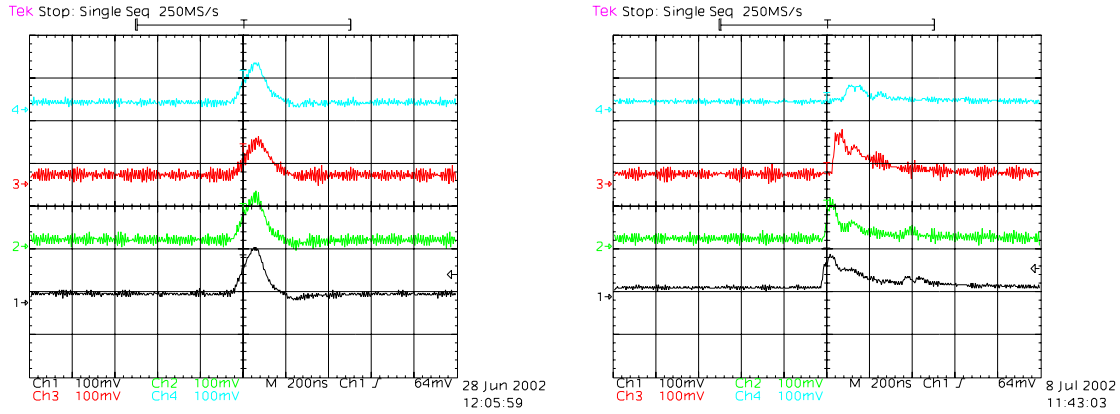


Figure 4.39: Signals observed in the straw-tube chamber for two different gas mixtures. **left:** 50% Argon, 50% Ethane at 2050 V **right:** 90% Argon, 10% Carbondioxide at 1800 V.

pattern for the down-stream end plate. Due to the mills available at CMU, two end plate sections each representing $\frac{1}{8}$ of the chamber were made. These were then connected together and the resulting quarter-end-plate sections were sent to JLab to be measured [70]. While this process led to a number of improvements in the construction technique, it was finally concluded that maintaining sufficient accuracy over eight sections that needed to be connected together would probably not be possible, and it would make more sense to contract out the end plate fabrication to industry.

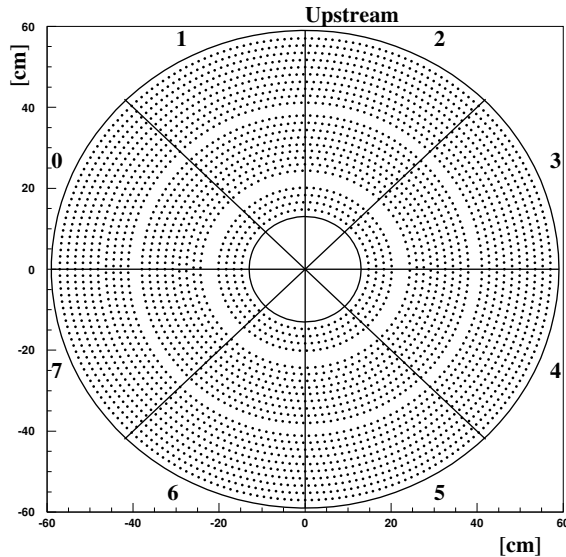


Figure 4.40: The position of the 3240 holes that need to be drilled in the downstream end plate of the CDC. The gaps in radius after layers 4 and 13 are due to the layers just beyond these being stereo wires.

An problematic issue that is common with straw-tube chambers is the conductive glue joints that both hold the straws to the feed throughs as well as the feed throughs to the chamber end plates. Careful examination of an existing straw tube chamber from the Brookhaven EVA experiment showed that all of these joints tend to develop leaks over time. In order to try to alleviate this leak problem, a detailed study of many conducting and non-conducting epoxies

was carried out to see if a good glue could be found. The conclusion of this work was that the particular choice of glue did not matter. Instead, the act of inserting one part of a feed through into another part tended to scrape much of the epoxy off the contact surface. This led to a joint with many weak spots that over a short period of time, developed leaks.

Upon careful study of this, it was decided that the only way to guarantee a good glue connection was to develop a system in which one is certain the the glue is actually making solid contact with both surfaces. The result of this is a feed through system as shown in Figure 4.41. The *donut* is a small tube with a small *glue trough* machined into its perimeter. From one end of the donut, a small *glue port* is drilled from the outside to the *glue trough*. Once the donut has been inserted into the straw tube, a known amount of conducting epoxy can be injected through the *glue port* into the *glue trough*. The strength of the resulting glue joint is solid, independent of the tested epoxies. In fact several test sells have maintained several psi overpressure for nearly nine months without leaking.

Into the donut, it is necessary to glue the insert that both holds the straw tube the chamber end plate and holds the crimp pin. In order to guarantee a good glue joint between the donut and the insert, a small *glue lip* has been machined on the tip of the insert. If a uniform coat of glue is applied to the outside of the *insert*, then when it is inserted into the donut, the epoxy tends to collect in both the *glue lip* and between the *insert* and the chamber end plate. Exactly where we need it to guarantee a good epoxy seal. Using these specially designed feed through systems, we are able to obtain a conducting gas-tight joint with all conducting epoxies that we have tried.

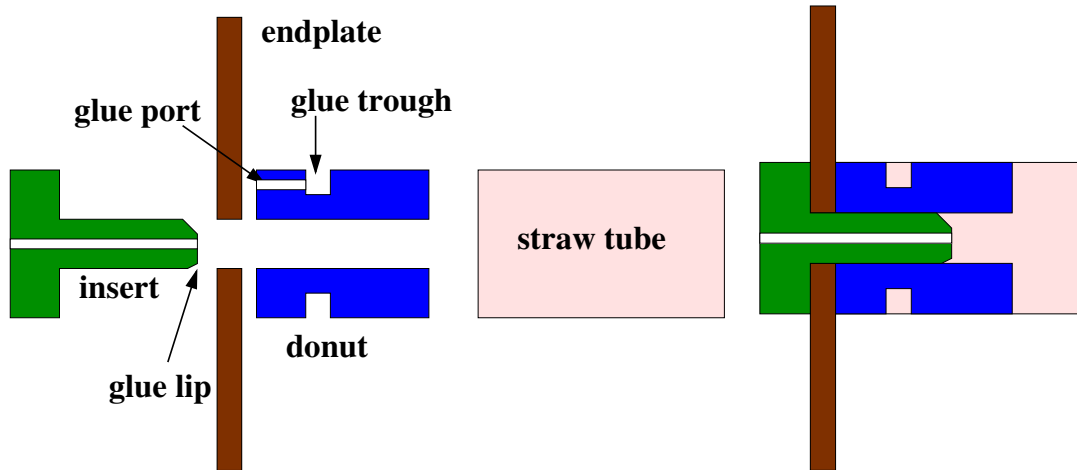


Figure 4.41: The CMU designed feed throughs which provide a solid glue joint between the straw-tube and the end plate. The left-hand figure shows an expanded view, while the right-hand shows the feed throughs in the chamber end plates.

Figure 4.42 shows several photographs of the prototype straw-tube chamber being built at CMU. Four tubes per layer are being put into this chamber, with particular emphasis on making sure that we have both the transition from straight to stereo and from stereo back to straight layers. During construction, wire tension has been carefully monitored. Summaries of tests that have been performed during the construction of the CDC can be found in reference [71].

4.4.4 Forward Drift Chambers

The Forward Drift Chamber system (FDC) is used to track charged particles coming from the GLUEX target with polar angles up to 30° . Tracks at angles greater than 10° also pass through the CDC detector and its associated downstream endplate. Due to the spiraling trajectories of the charged particles and the high multiplicity of charged tracks passing through the FDC, it is crucial for this system to be able to provide a sufficient number of measurements with

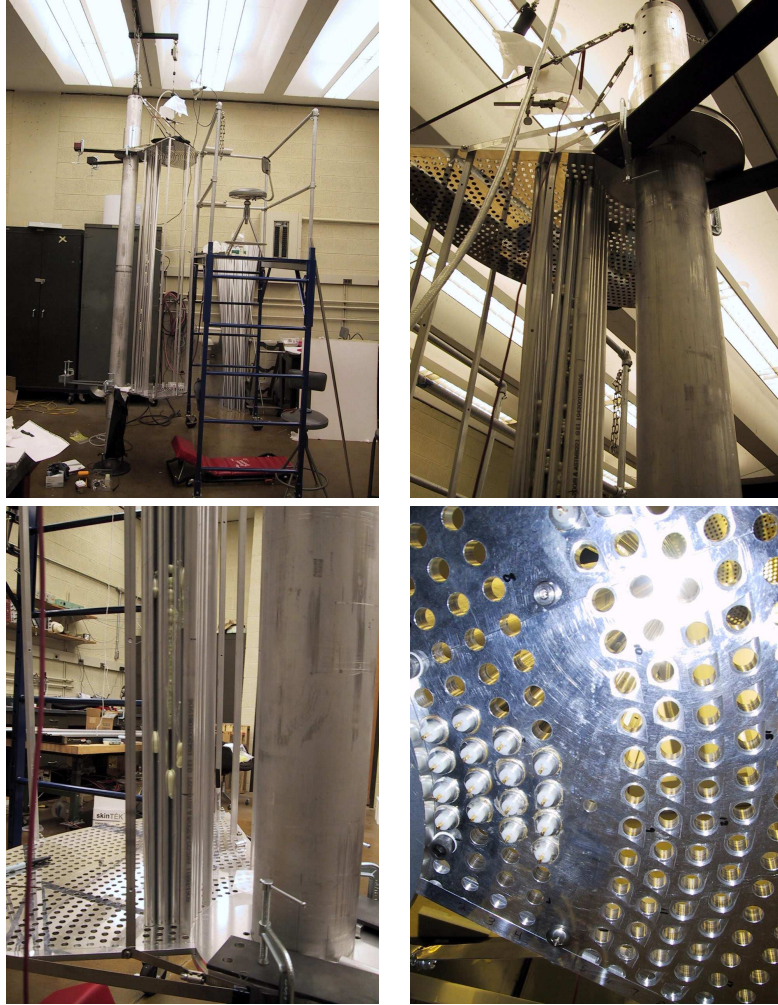


Figure 4.42: The upper-left picture shows the prototype chamber suspended and in position to string wires. The upper-right picture shows several partial layers of tubes glued into the prototype CDC. The lower-left picture shows the same tubes at the lower plate. The lower-right picture is taken from under the lower plate showing several crimped wires in the chamber.

appropriate redundancy to enable linking of the hits from the different tracks with high accuracy, while providing good spatial resolution with reasonable direction information. Current studies with the *HDFast* Monte Carlo program indicate that track hit coordinates should be measured to an accuracy of $150\ \mu\text{m}$ in order to achieve the desired momentum resolution for the charged tracks in the final state.

In the current detector design, the FDCs include four separate but identical disk-shaped planar drift chambers (MWDC's) as shown in Fig. 4.27. Each package will include six layers of alternating anode and field-shaping wires sandwiched between planes of cathode strips. The total thickness of each package is estimated to be roughly $0.15\ \text{gm}/\text{cm}^2$. Neighboring wire planes will be rotated by 60° with respect to each other in order to improve track reconstruction decisions on the corresponding anode wire left/right ambiguities, hence improving the overall resolution. By charge interpolation of the electron avalanche image charge in the cathode strip readout, spatial resolutions at the cathode planes are expected of better than $150\ \mu\text{m}$.

The orientation of the cathode strips on either side of the wires has yet to be decided. The optimal resolution of the hit coordinate along the wire direction is obtained when the cathode strips are perpendicular to the anode wires. In this configuration there is no quantization of the

position measurement resulting from the discrete nature of the anode wires (i.e. the cathode measurement in the coordinate perpendicular to the wires simply locates the wire position). The issue of the optimal electrode configuration for the FDC chambers will ultimately be answered for GLUEX from studies of a prototype cathode readout chamber that is currently being tested at Jefferson Laboratory (discussed later in this section). In the current FDC system design, the cathode strips on either side of the anode plane are arranged in a U and V geometry at $\pm 45^\circ$ with respect to the wires. This technique of employing a stereo angle may prove valuable in separating and assigning multiple hits within a chamber to the different tracks.

The basic chamber element is a disk of outer radius 60 cm, where the wires are strung as cords across the chamber as shown in Fig. 4.43. With a wire-to-wire spacing of 5.0 mm, each chamber plane will contain 119 anode wires. In addition, there will be double this number of cathode strips on each cathode plane. This amounts to 595 channels per FDC chamber element and 3570 channels per FDC chamber package.

The cathode readout as presently planned will employ 125 ps F1 TDCs for the anode wire drift time readout and 125 MHz FADCs for the cathode readout. This would enable commonality with the readout electronics planned for the other GLUEX detector subsystems. Note that with a clock rate of 125 MHz on the FADCs, time fitting algorithms matched to the chamber pulse shape can be employed to provide a time resolution of ~ 2 ns (amounting to $\sim 40\%$ of the time bin width). This timing information from the cathode signals would aid in pattern recognition of multiple tracks passing through the chamber volume. We are also exploring options with FADCs with slower clock rates. This could in principle reduce the electronics costs significantly if we can accept the poorer time resolution.

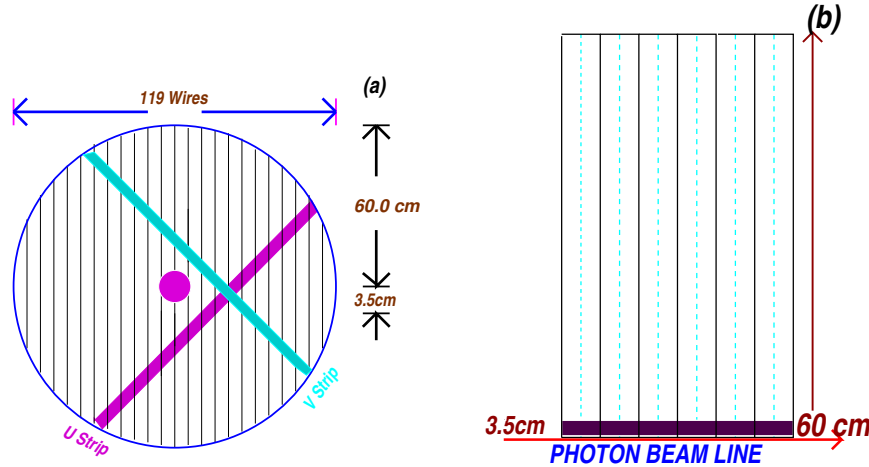


Figure 4.43: A front (a) and side (b) sketch of an FDC package. In (a) the wires are schematically indicated as the vertical lines. The U cathode strips are in front of the wires and the V cathode strips are behind the wires. The field-shaping wires are not shown. In (b) a side view of the upper half of a six-chamber package is shown. The wire planes are shown as the dashed lines, while the cathode planes are shown as the solid line. Ground planes between adjacent chambers are not shown.

The wires that cross through the beam line require special treatment to handle the otherwise unmanageable rates. Several possibilities are currently being considered. The first is to deaden the wires out to a radius of ~ 3.5 cm by placing a material such as Styrofoam around them or to include support structures around the beam line to remove the wires entirely from this vicinity. The final decision will be based on background and design studies.

The primary development issues associated with the FDCs that must be addressed are factors affecting the intrinsic resolution of the chambers, along with the mechanical and electronics

layout. The goal is to construct a tracking detector that meets the required design specifications and has a long life time, a uniform and predictable response, a high efficiency, and is serviceable in case of component failure.

FDC Monte Carlo Studies

The initial specifications for the layout of the FDC system have been studied within the framework of the *HDFast* Monte Carlo. The goals of these studies were to consider the basic number of FDC chamber packages within the solenoid and to consider the number of wire planes per package.

For these studies, pions with momenta between 0.25 and 4.0 GeV and angles from 5-10° were generated and the momentum uncertainty in the form of $\delta P/P$ was studied as a function of momentum. Fig. 4.44(a) shows results comparing a 3-package vs. a 4-package configuration (with packages equally spaced along the beam line). Here the preliminary results make it apparent that the single track resolution, if all cathode and anode positions can be resolved to 150 μm , is improved by roughly a factor of 2 (for pion momenta above 2 GeV/c) with the 4-package configuration. Although the resolution decreases with increasing momentum, it worsens at a noticeably slower rate for the 4-package configuration. The tracking system design parameters can be met with such a 4-package configuration. However, it is the redundancy that the fourth package provides that will be crucial in disentangling multiple charge particle hits and background within the readout time window.

Fig. 4.44(b) shows results for a 4-package FDC system with each package containing either 4, 5, or 6 wire planes. Here the 4-layer design yields a resolution about 20% worse than for the 5 and 6-layer designs. Although the resolution of the 5 and 6-layer packages are about the same, the 6-layer design has been shown to improve pattern recognition for multiple hits within a chamber.

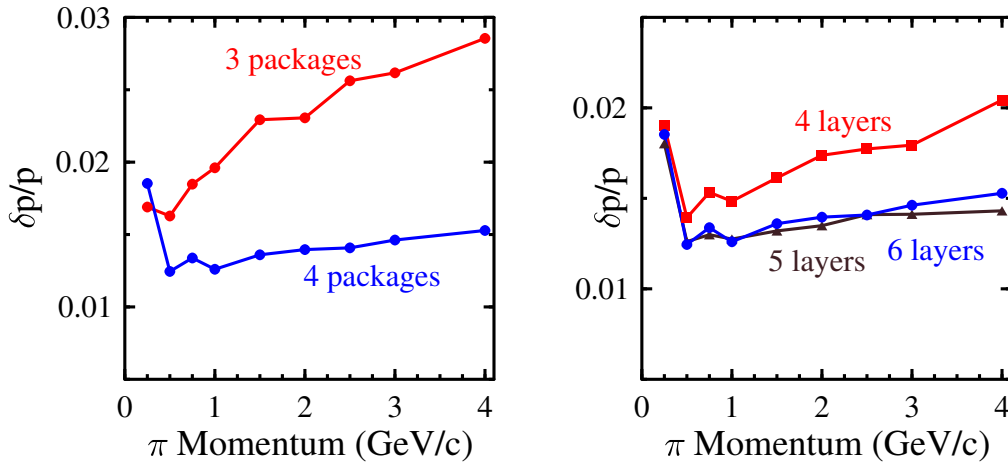


Figure 4.44: Monte Carlo studies comparing the FDC resolution in (a) a configuration with three packages vs. four packages and (b) a 4-package configuration with 4, 5, and 6 wire planes per package.

At the present time the Monte Carlo work is proceeding in earnest to perform detailed systematic studies of the FDC design with realistic backgrounds in the chambers. This will enable final decisions to be made regarding the number of chamber packages, the number of wire planes, the optimal rotation between neighboring planes, the number of cathode strips and their segmentation, and the optimal z -positions of the chambers. Also note that as discussed in Section 4.4.1 for the CDC, the final z -extent of the straw tube chamber has not been finalized. In this case and others, the design of the CDC and FDC systems must be considered in concert. Of course the final resolution for charged tracks is firmly connected to the design and performance of *both* the CDC and the FDC tracking packages.

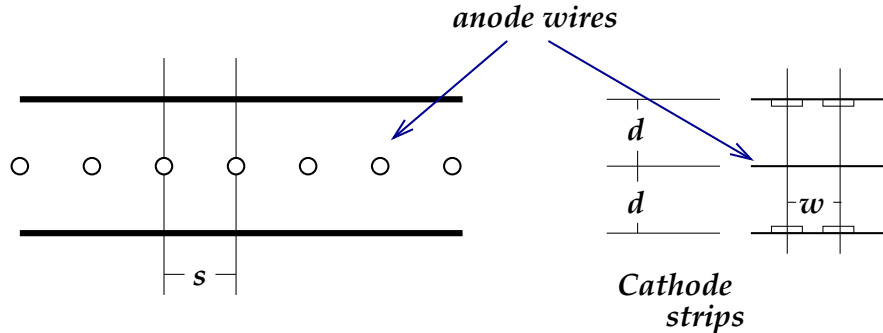


Figure 4.45: Schematic diagram of a typical cathode strip chamber.

Cathode Strip Chambers

Cathode strip chambers (CSC) are typically multiwire proportional chambers (MWPCs) with a symmetric drift cell in which the anode-cathode spacing d is equal to the anode wire pitch s (see Fig. 4.45). In these chambers the spatial resolution of the anode readout is limited to roughly $s/\sqrt{12}$ (RMS). In a CSC the precision coordinate is obtained by measuring the charge induced on a segmented cathode by the electron avalanche formed on the anode wire as shown in Fig. 4.46(a). For the case of multiple tracks, a second segmented cathode rotated at an angle with respect to the first cathode can also help to reduce multi-hit ambiguities as shown in Fig. 4.46(b). The stereo technique is superior to the alternative of reading out only one cathode plane and a hit wire number in that multiple hits on a single wire may be resolved.

The optimum cathode readout pitch w is determined by the width of the induced charge distribution. It has been shown by several groups that minimal differential non-linearity ($\sim 1\%$) is achieved when $w/d \approx 1$ (e.g. [72]). This ratio is employed in the current FDC design, although optimization studies are underway with our prototype cathode chamber. Other groups [73] have been able to construct cathode chambers with larger w/d ratios while maintaining acceptable resolution and minimal differential non-linearity by using intermediate strips between cathode readout nodes that are capacitively coupled to their adjacent readout strips as shown in Fig. 4.47. This option, which can significantly reduce the associated readout costs, is also being considered in the FDC design studies.

Simulations from Ref. [72] have shown that resolutions of $25 \mu\text{m}$ for the precision coordinate in a CSC could be achieved for minimum-ionizing tracks if the electronics and readout could be provided with noise and inter-channel gain variations of less than 0.5% of the nominal pulse height. The primary factor limiting the spatial resolution of a cathode chamber is the electronic noise of the preamplifier. Other factors such as the uncertainty in the gain calibrations and cathode plane distortions should also be considered as well. The precision in the determination of the position of the induced charge depends linearly on the signal-to-noise ratio. Note that preamplifier noise is dominated by the input capacitance and that optimal capacitive coupling requires that the inter-strip capacitance be much larger than the capacitance of a strip to ground [73]. Operation within a realistic experimental environment will result in resolutions much closer to our design goal of $150 \mu\text{m}$.

An interesting question regarding cathode chambers is the change in system resolution when they are also employed as drift chambers (MWDCs), specifically horizontal drift chambers. The principles of operation of a MWDC are such that the best position resolution is achieved when the first electrons that reach the anode wire drift along field lines in the plane of the wires. If we consider a GARFIELD calculation [65] of the field lines for such a chamber (see Fig. 4.48(a)), the first electrons to reach the anode wire will most certainly arise from other locations within the drift cell. This gives rise to non-linearities in the space-time correlation that strongly degrade the position resolution. In order to improve the field configuration for the MWDC operation, field-shaping wires can be included within the anode plane between each anode wire. This can

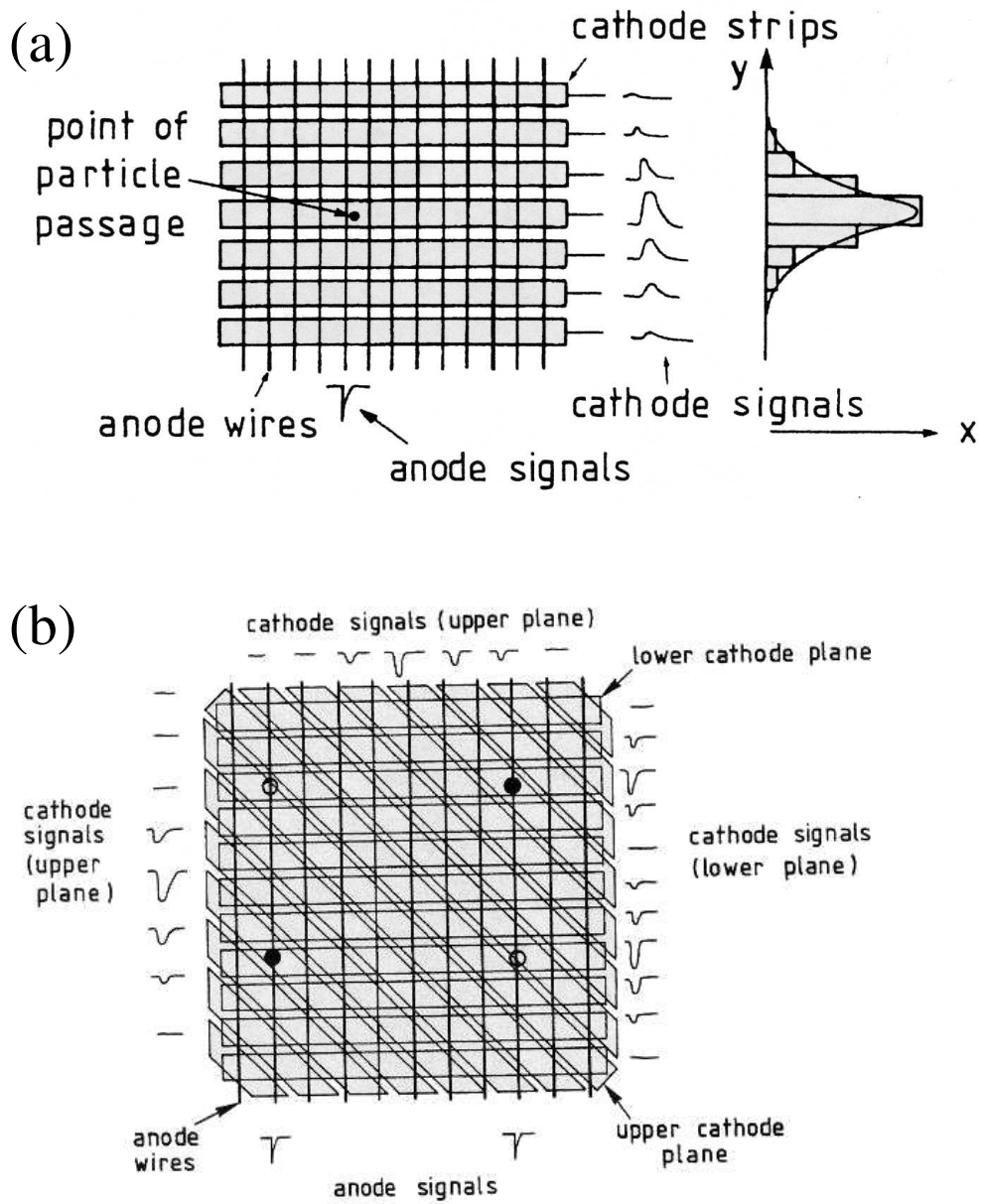


Figure 4.46: Illustration within a typical MWPC of (a) the cathode readout and (b) the resolution of ambiguities within a CSC for two particle hits.

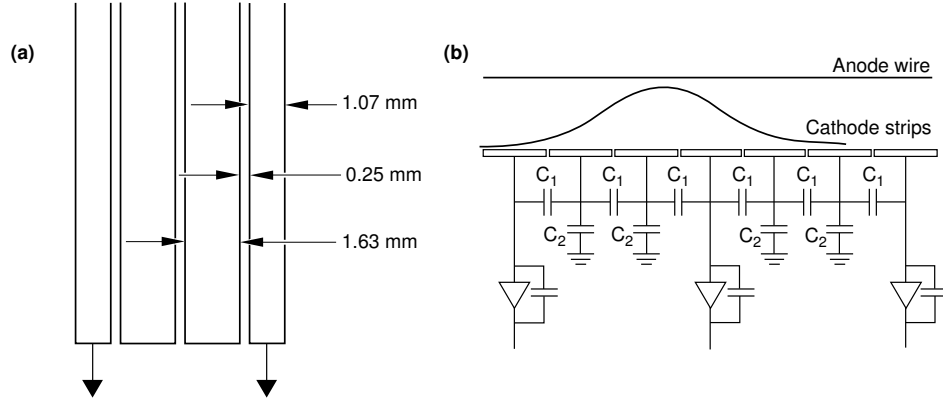


Figure 4.47: (a). CSC layout with a modified cathode strip layout using readout and intermediate strips (from the ATLAS detector). (b) The equivalent circuit highlighting the capacitive interpolation using the two intermediate strips.

clearly improve the field configuration as shown in Fig. 4.48(b).

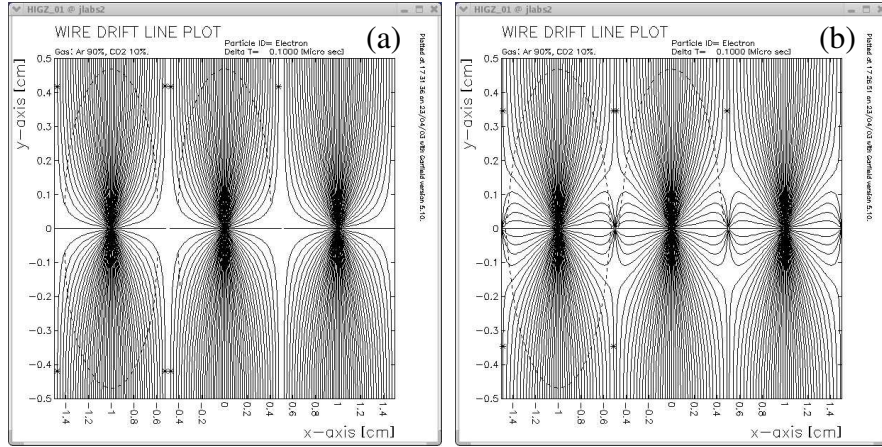


Figure 4.48: GARFIELD calculations of electric field lines (for a $B = 0$ field configuration) within a square drift cell for a 90% argon - 10% CO_2 gas mixture for electrode configurations without (a) and with (b) field-shaping wires.

It is not known at the current time how inclusion of field-shaping wires will affect the cathode position resolution. One of the central questions that we are investigating through our R&D program for the FDC system regards the optimal electrode structure in our cathode chambers. Specifically we are seeking to fully understand the trade-offs between timing resolution from the wire planes and spatial resolution from the cathode planes. However, with inclusion of the field-shaping wires and maintaining a square drift cell, in order to achieve optimal resolution, the number of cathode strips on each cathode plane increases by a factor of two relative to an anode wire only plane design.

The basic algorithm to determine the cathode position of the charged track is to fit the charge distribution across the cathode plane. This amounts to determining the position of the center of gravity using the ratio of the first and second moments of the charge distribution on the plane of the strips from [73]:

$$x_{c.g.} = \frac{\sum_{i=1}^N x_i q_i}{\sum_{i=1}^N q_i}, \quad (4.11)$$

where N is the number of strips involved, $x_i=iw$ is the strip coordinate, and w is the pitch of the cathode readout. If the charges q_i on each strip are measured with an RMS error of σ , then with $Q = \sum_i q_i$, the uncertainty in $x_{c.g.}$ is given by:

$$\sigma_{c.g.} = \frac{\sigma}{Q} \sqrt{2 \sum_i x_i^2} \quad (4.12)$$

or

$$\sigma_{c.g.} = \frac{\sigma}{Q} \sqrt{2w^2 + 2(4w^2) + 2(9w^2) + \dots} \quad (4.13)$$

Therefore the resolution depends on the number of strips used. Monte Carlo simulations and operational experience from different groups have shown that the optimum number lies between three and five strips. The position resolution is poor when only one or two strips are present as there is not enough information, while it increases slowly when more than five strips are used. The resolution function in this case also includes the additional electronic noise from each strip. Here there must be an optimization of chamber resolution factoring in the desire to minimize the number of readout channels to contain costs.

Resolution Effects

Resolution degradation of cathode chambers comes primarily from two sources, tracks inclined from the normal to the face of the chamber and Lorentz angle effects. In both cases the spatial resolution is degraded because the avalanche charge is distributed non-uniformly along the anode wire due to the energy loss fluctuations in the gas. The cathode position resolution is optimum when the avalanche is formed at a single point along the wire. A finite spatial extent of the anode charge results in a resolution degradation \mathcal{D} . Studies of the PHENIX cathode chamber [74] have shown that \mathcal{D} goes as:

$$\mathcal{D} = 0.16d \tan \theta, \quad (4.14)$$

where d is the anode-to-cathode spacing and θ is the angle from the normal to the face of the chamber.

Skewed or non-local charge distributions along the anode wire can also be caused by a Lorentz force along the anode wire from the presence of magnetic field components that are not collinear with the electric field of the chambers. The Lorentz effect itself does not result in a systematic shift of the measured coordinate in the cathode plane. It simply results in a degradation of the resolution because of the spread of the charge along the wire.

Gas Considerations

There are several basic requirements that need to be met by the chamber gas that will be used for the FDC system. These include a high drift velocity (50-60 $\mu\text{m}/\text{ns}$), low Lorentz angle ($< 10^\circ$), and for safety, we much prefer a non-flammable mixture. It is important to understand that the performance of a cathode chamber in terms of cathode position resolution is reasonably insensitive to the exact values of the gas parameters. Here variations of the drift velocity or non-uniform drift velocities as a function of E/p (i.e. electric field/pressure) are relatively unimportant. For the same reason, the cathode readout operation is immune to modest variations of temperature and pressure. Variations in gas gain on the order of 20% do not strongly affect the cathode resolution since a relative charge measurement in adjacent strips is involved.

However, the gas mixture and its control are essential to consider carefully for the operation of the MWDC. In order to enable accurate calibrations of the drift times, it is essential that the gas mixture is stable, which amounts to constructing a gas handling system that carefully controls the gas mixture, as well as hall controls to fix the temperature and relative humidity as much as possible.

Detailed studies of chamber performance will be performed with our prototype cathode chamber employing various gas mixtures. A number of gas mixtures have been studied by various groups that have proven suitable for cathode chambers. Most of these gases contain CF_4 in combination with isobutane (C_4H_{10}) or CO_2 . The Lorentz angle is similar for each gas and is about 5° at 0.5 T magnetic field. One chamber-safe gas mixture that has worked well with the PHENIX cathode chambers consists of 30% argon, 50% CO_2 , and 20% CF_4 [74].

Readout Electronics

The primary design issue for the front-end electronics for the FDC system is to maintain a signal-to-noise ratio of better than 100:1 in the presence of a large detector capacitance. Capacitance measurements in detectors are very important because they serve to determine the performance of the detector in terms of the charges induced on the cathodes, gain variations, detector efficiency, etc. They also play an important role in determining the characteristics of the readout electronics. For the FDC chambers the dominant contribution to the capacitance seen by the preamplifiers will be the strip-to-strip capacitance. The capacitance between adjacent strips is given approximately by [74]:

$$C(\text{pF}/\text{cm}) = 0.12t/w + 0.09(1+k)\log_{10}(1 + 2w/s + w^2/s^2), \quad (4.15)$$

where t is the strip thickness, w is the strip width, s is the strip separation, and k is the dielectric constant of the backing material (here it is envisioned to be kapton). For the FDC design that is presently considered, this capacitance is roughly 1 pF/cm. Accounting for the total capacitance of the system then forms a basic requirement for the input capacitance for the front-end electronics performance. An additional concern for this design is the coupling of the signals between adjacent strips. Studies of the PHENIX CSCs have shown that appropriate setting of the integration times of the electronics is important to decrease sensitivity to distortions in the induced charge distribution due to inter-strip coupling.

The chamber-mounted electronics for the cathode strip readout will consist of a charge-sensitive preamplifier that drives a pulse-shaping amplifier. The pulse shape will be chosen as a compromise between noise and pileup, both of which degrade the resolution. The electronics must also be designed to minimize cross-talk, particularly to non-adjacent channels. R&D efforts related to selection of the preamplifier and pulse-shaper are just now beginning. However we expect to develop contacts with outside groups who have more experience. We will also work with the Fast Electronics group at Jefferson Laboratory to explore potential options. The preamplifier circuits employed for the prototype cathode chamber employ the same preamplifiers used with the CLAS drift chambers. This choice was made mainly for convenience, and their performance will provide a benchmark for comparison.

FDC Cathode Chamber Prototype

The FDC prototype cathode chamber has been designed primarily to provide us experience with cathode strip chambers. Through detailed study of this prototype we hope to be able to better understand which electrode structure and layout will fulfill the design requirements for the final FDC chambers. The prototype will also provide important insights into the mechanical design, tolerances, construction and assembly techniques, noise immunity, and calibrations that will be important for the final FDC detector design. Some of the elements of the FDC prototype design have descended from the cathode chambers employed in the original LASS spectrometer [75].

A schematic of the FDC prototype chamber is shown in an exploded view in Fig. 4.49. The basic chamber layout consists of two cathode planes with strips oriented at $\pm 45^\circ$ sandwiching a single wire plane. The gas volume is defined by two outer aluminum frames that each include an aluminized mylar window. The active area of the prototype chamber is roughly 20 cm \times 20 cm, and the chamber is about 8 cm thick.

The test chamber has purposefully been designed to act as a test bed for any number of electrode configurations. So far we have wound wire planes consisting only of anode wires

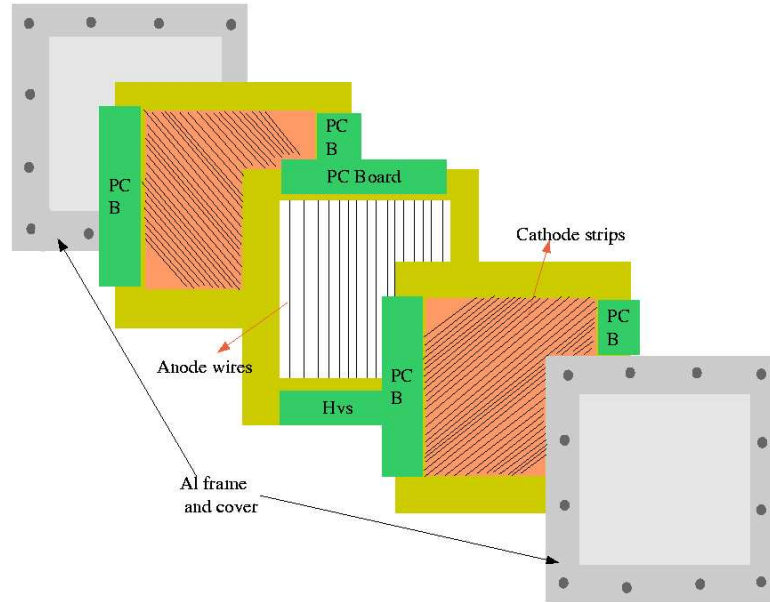


Figure 4.49: Schematic representation of the FDC prototype chamber in an exploded view showing the wire plane, two cathode planes, and the two aluminum window frames.

and planes consisting of alternating anode and field-shaping wires. We have also designed cathode planes of varying rotation angle, varying cathode strip pitch, and varying cathode strip separations. Ultimately each configuration will be studied in order to come to an understanding of the optimal electrode structure for our purposes.

The U and V cathode planes are mirror symmetric with respect to each other. The cathode planes are copper-clad kapton sheets (~ 2 mil thickness) mounted onto 5-mm thick G10 frames. The chamber is designed to operate with the anode wires at positive high voltage, the field wires at negative high voltage, and the cathode strips at ground.

The printed circuit board for the wires was designed to capacitively decouple high voltage from the signals and to route the signals to the output connector. The printed circuit board for the cathodes routes the signals directly to the output connector. The basic circuits on the boards are shown in Fig. 4.50. Small signal routing circuit boards attach to the output connectors on the wire and cathode circuit boards and contain the preamplifiers for each readout channel. The output connects to a shielded twisted-pair line that routes the signals to the readout electronics (FASTBUS 1877 TDCs and 1881 ADCs). The signal readout boards used for the cathodes are essentially the same as those used for the anode wire readout. The only difference in the design is a polarity switch of the cathode signals before sending the signals to the amplifier and the ADC.

Each readout channel has its own associated “SIP” preamplifier. These single-channel transimpedance preamplifiers were originally designed for the Hall B CLAS detector. They have complementary outputs designed to amplify signals by a factor of $2.25 \text{ mV}/\mu\text{A}$. Besides high gain, characteristics of the SIPs include: fast rise and fall times (3 to 4 ns), wide frequency bandwidth, wide dynamic range, and low noise and power dissipation (65 mW).

In total the prototype chamber includes 16 $20\text{-}\mu\text{m}$ diameter sense wires alternated with $80\text{-}\mu\text{m}$ diameter field wires, with a wire-to-wire separation of 5 mm and a strip-to-strip separation of 1 mm. The cathode planes are located 5 mm away from the wire plane. They each include 32 copper strips with a pitch of 5 mm. Three different sets of U and V cathode planes have been designed with strip separations of 0.25 mm, 0.50 mm, and 1.0 mm to allow for the optimal configuration to be determined. Presently the chamber is operating with a 90% argon - 10% CO_2 gas mixture. Photographs of the prototype cathode chamber and the cathode plane itself

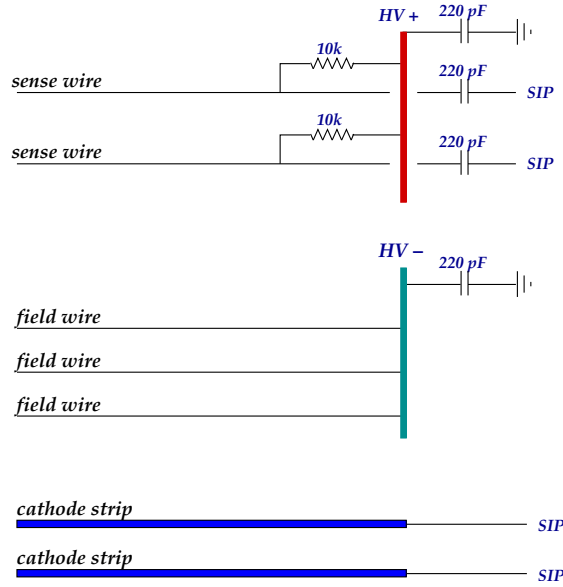


Figure 4.50: Circuit board electronics for the sense and field wires, along with the cathode strips.

are shown in Fig. 4.51.

A set of 19 wire chambers have been borrowed from IUCF in order to assemble a cosmic ray test stand at Jefferson Laboratory. This test stand is being used to define tracks through the FDC prototype chamber. A schematic drawing of the layout of the cosmic ray test stand is shown in Fig. 4.52. This system employs multiple layers of drift chambers above and below the FDC prototype chamber to precisely define the trajectory of an incident charged particle track that can be used to compare against the position measured in the FDC prototype. The configuration of the test stand includes two X layers and two Y layers above the FDC prototype and a matching set of four layers below. This system, once properly calibrated, should be capable of defining a track to roughly $200 \mu\text{m}$ at the location of the FDC prototype. A photograph of the test setup is shown in Fig. 4.53.

At the present time the cosmic ray test stand has been crudely calibrated and we have succeeded in getting readout of the cathode chamber. A look at the first anode and cathode signals from this chamber is shown in Fig. 4.54. So far the detector is operating quite nicely and an initial characterization of its performance and resolution is in progress.

Based on the results of studies of the first cathode chamber prototype, as well as continued Monte Carlo studies of both the detector and the physics, we will begin working on the design for a second prototype for the FDC system. One of the primary purposes of the second prototype chamber will be to test mechanical support designs for the full-scale chamber and wire planes. This is necessary to avoid electrostatic instabilities and non-uniformities that are known to affect resolution. To illustrate the issue at hand, the gain \mathcal{G} in a proportional counter is given in general by:

$$\mathcal{G} = Ke^{CV}. \quad (4.16)$$

For an operational voltage V , the gain is dependent on the capacitance of the detector C . Thus any variation on the flatness of the cathode plane changes the capacitance of the detector and hence the gain. It also creates field non-uniformities that affect the cathode position resolution. For gain variations of less than 5%, a rough calculation shows that the cathode plane must have less than a ± 5 mil flatness variation.

Various schemes have been employed by different groups to provide mechanical support for the cathode planes in large area chambers. For example, in the so-called *Plug Chambers* used

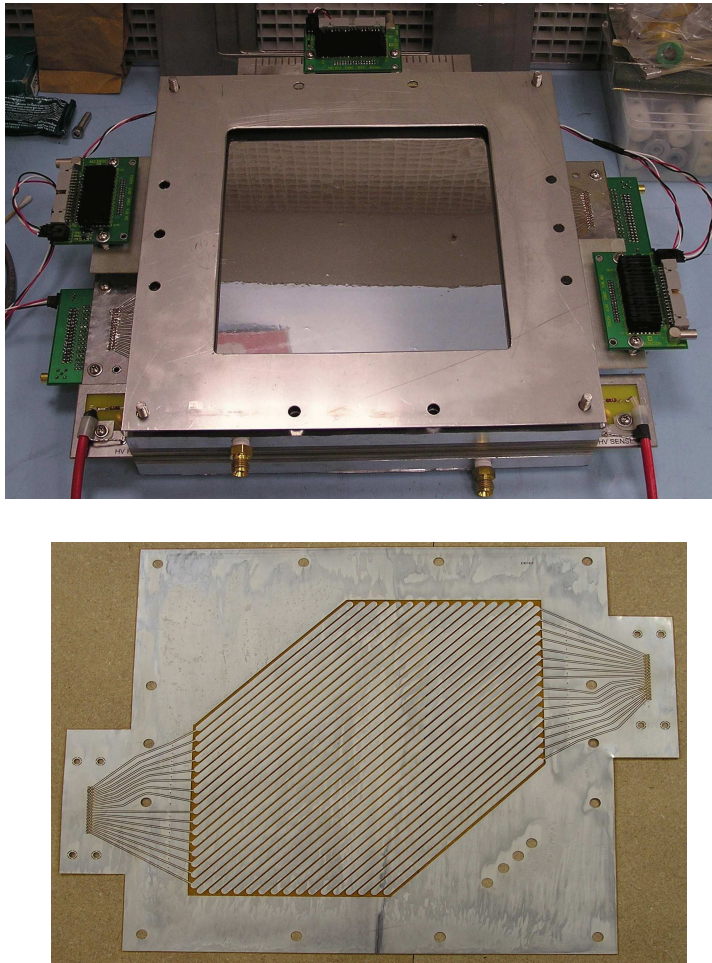


Figure 4.51: (Top) Photograph of the prototype FDC cathode chamber constructed to optimize chamber electrode structures. (Bottom) Photograph of a cathode plane showing the cathode strips.

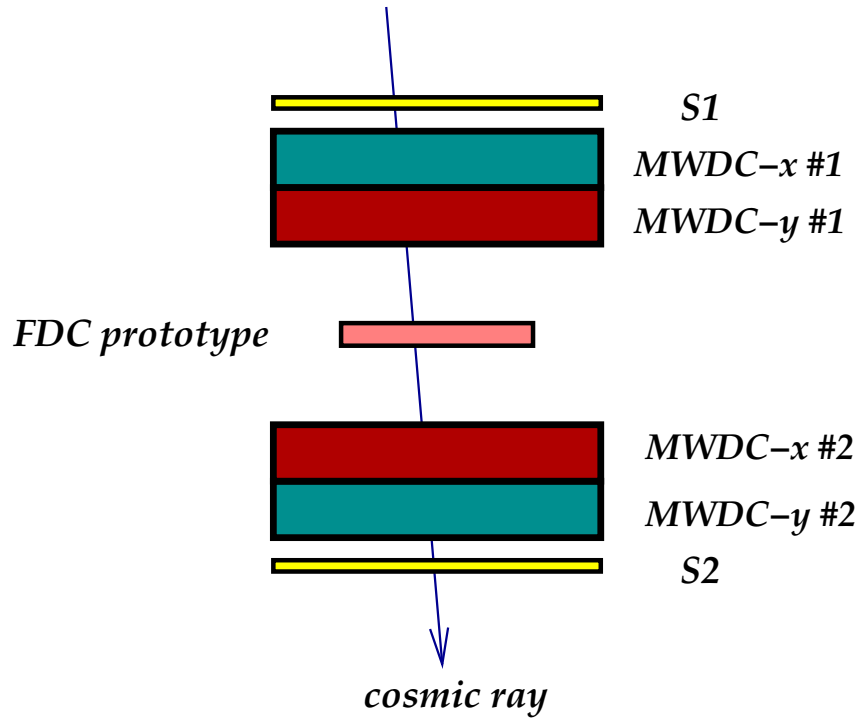


Figure 4.52: Schematic drawing of the cosmic-ray telescope used for FDC prototype resolution studies.



Figure 4.53: Photograph of the cosmic ray test stand set up at Jefferson Laboratory to study resolution characteristics of the cathode strip chambers.

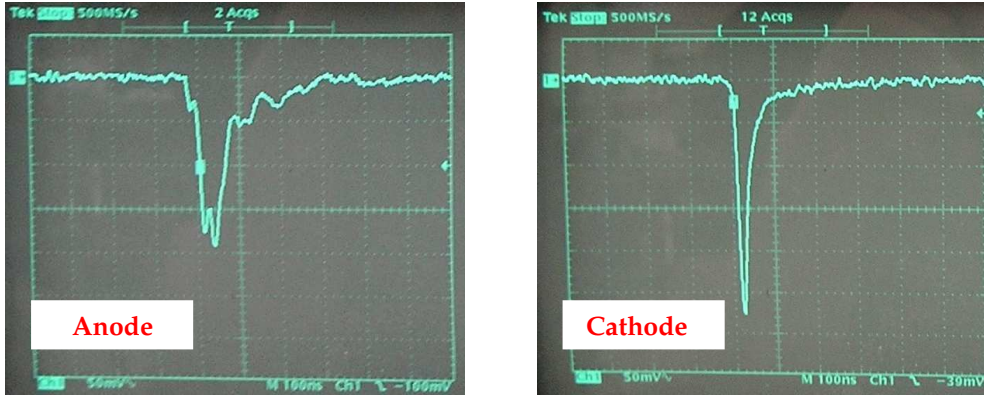


Figure 4.54: Anode (left) and cathode (right) signals from our prototype cathode strip chamber. The electrode structure and layout of this prototype is expected to be very similar to the final FDC design.

in the LASS experiment [75], polyurethane spacers were epoxied onto the cathodes to fix the anode-cathode gap spacing. This and other options are currently being explored.

Another important role for the second prototype chamber is to give us a design test bed for the circuit boards associated with both the cathode and wire planes. We will again seek out contacts with other groups who have constructed chambers of similar design as well as work with the Fast Electronics Group at Jefferson Laboratory in order to minimize R&D lead times.

4.4.5 The Start Counter

The START counter will provide a fast signal which is used in the level-1 trigger of the experiment. For this purpose the time resolution cannot be worse than 4 - 5 ns. As an element of the level-1 trigger, this detector needs an excellent solid angle coverage and a high degree of segmentation for background rejection. Using tracking information the start counter will be able to provide a time resolution of better than 0.5 ns thus allowing us to identify the electron beam pulse associated with the event.

The start counter will consist of a cylindrical array of 40 scintillator paddles (see figure 4.55). The scintillators have a thickness of 5 mm. This will provide a good light output and therefore a good timing signal. The downstream side of the scintillators will be bent toward the beam line in order to increase the solid angle coverage while minimizing multiple scattering.

Each paddle will be coupled at the upstream end to a light guide leading out of the very high magnetic field region. Photo-tubes which can be operated in magnet fields of the order of one to two kilo gauss will be used for readout. Tests with the Hamamatsu system H6614 have shown that the required time resolution can be achieved routinely. As scintillation material we plan to use Eljen Technology EJ200 which is fast and has a large absorption length. The time resolution (σ) for a EL204 scintillator bar, directly coupled to a H6614-01 system, is shown in figure 4.56 as a function of distance from the PMT. This detector is similar to the start detector currently used in CLAS in HALL B at Jefferson Lab.

4.5 Particle Identification

4.5.1 Overview

Particle identification in the GLUEX detector (i.e., the separation of pions, kaons, and protons) will incorporate information from at least four different subsystems – two subsystems in the central region and two in the forward region.

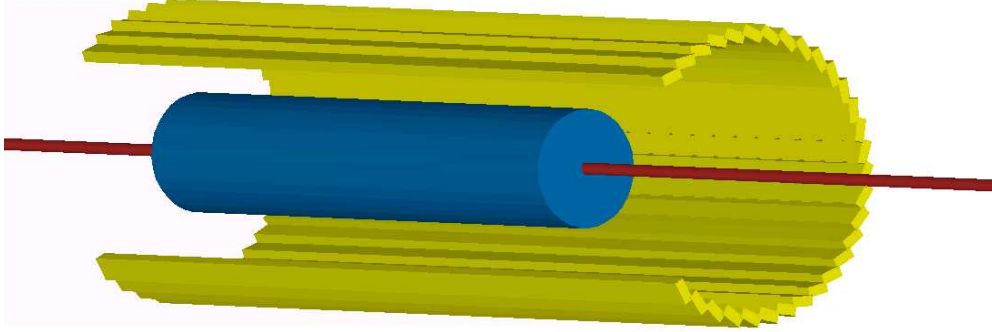


Figure 4.55: Cerenkov detector barrel geometry. The central blue cylinder is the drift chamber and the yellow layers are the cylindrical array of scintillator.

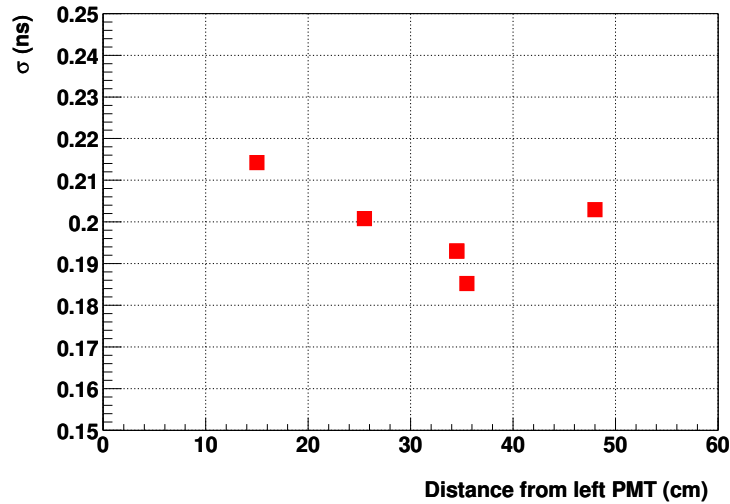


Figure 4.56: The Start Counter time resolution (σ) as a function particle trajectory position along a EJ204 bar with the dimensions $0.5 \times 3 \times 70 \text{cm}^3$.

1. Low momentum central tracks will be identified using dE/dx measurements from the Central Drift Chamber (CDC).
2. A time of flight measurement from the barrel calorimeter (BCAL) will also provide identification information for central tracks. The CDC and the BCAL working in conjunction will provide an excellent means for identifying recoiling protons from the target.
3. Higher momentum forward-going kaons and pions will be distinguished using a Cerenkov detector. Two possibilities for this detector exist – a threshold gas option (CKOV) using C_4F_{10} , and a Quartz-based DIRC option; each will be discussed in detail in a later section.
4. Time of Flight (TOF) information for forward-going tracks with momenta less than around $2.5 \text{ GeV}/c$ will be provided by a scintillator wall 500 cm downstream of the target.

Once information is gathered from each of these four elements, the information will be combined into likelihoods in order to provide a unified way of making a particle identification decision. The likelihood method will be discussed in section 4.5.4.

To illustrate the overall features of the particle identification, consider the reaction $\gamma p \rightarrow K^* \bar{K}^* p$. This reaction has kinematics that are typical of the reactions to be studied by the GlueX experiment. The $K^* \bar{K}^*$ system is produced peripherally with a t dependence of e^{-10t} . The proton recoils predominantly in the central region with a momentum below $2 \text{ GeV}/c$. The central kaons from the K^* decays range in momentum up to $5 \text{ GeV}/c$; central pions range up to $3.5 \text{ GeV}/c$. Forward kaons and pions have higher momenta, in general, than those in the central region, kaons ranging up to $7 \text{ GeV}/c$, and pions up to $5 \text{ GeV}/c$.

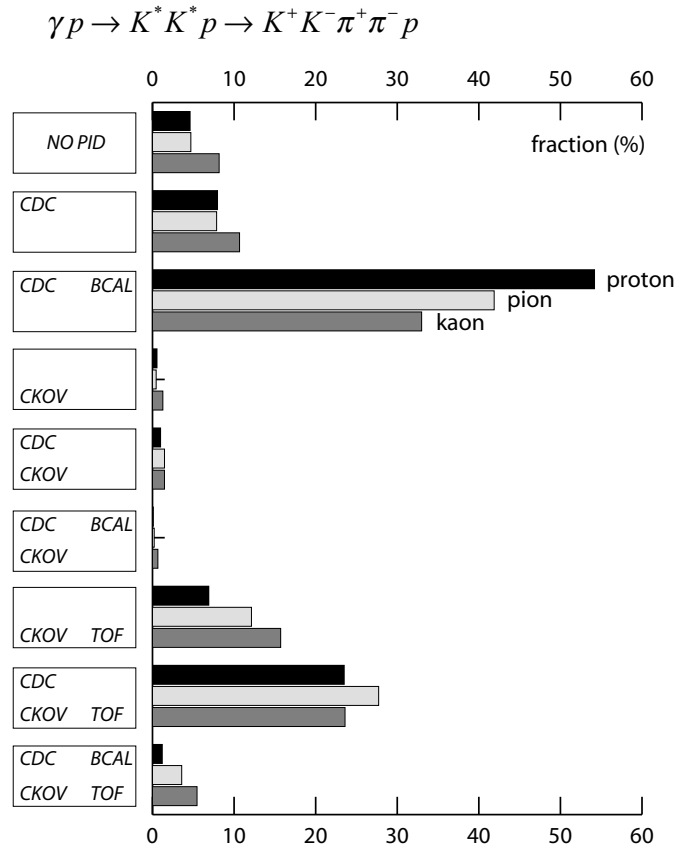


Figure 4.57: The fraction of tracks from the reaction $\gamma p \rightarrow K^* \bar{K}^* p$ detected by different combinations of particle identification elements.

Each of the five tracks in the final state can be categorized according to the particle identification elements it encounters. Figure 4.57 shows the percentage of tracks from $\gamma p \rightarrow K^* \bar{K}^* p$ encountering each of the eight possible combinations of PID detectors. Cases 1 (CDC) and 2 (CDC,BCAL) are purely central tracks; cases 6 (CKOV,TOF) and 7 (CDC,CKOV,TOF) are the dominantly forward tracks. Notice that the proton usually lands in the central region, and larger fractions of the pions and kaons go forward.

In the central region, the CDC and BCAL effectively work together to identify the recoiling proton. Figure 4.58 shows the momentum spectrum of the central protons from $\gamma p \rightarrow K^* \bar{K}^* p$ overlaid with K/p and π/p separations from the CDC and BCAL. For the dE/dx measurements from the CDC, an Argon-based gas was assumed and the resolution was estimated to be 10%. A 250 ps time resolution was assumed for the BCAL, and a typical path length of 2 m was used for the figure. The entire range of the central proton momentum spectrum is well covered. Protons in the forward region also have low momenta and are easily identified by the TOF wall.

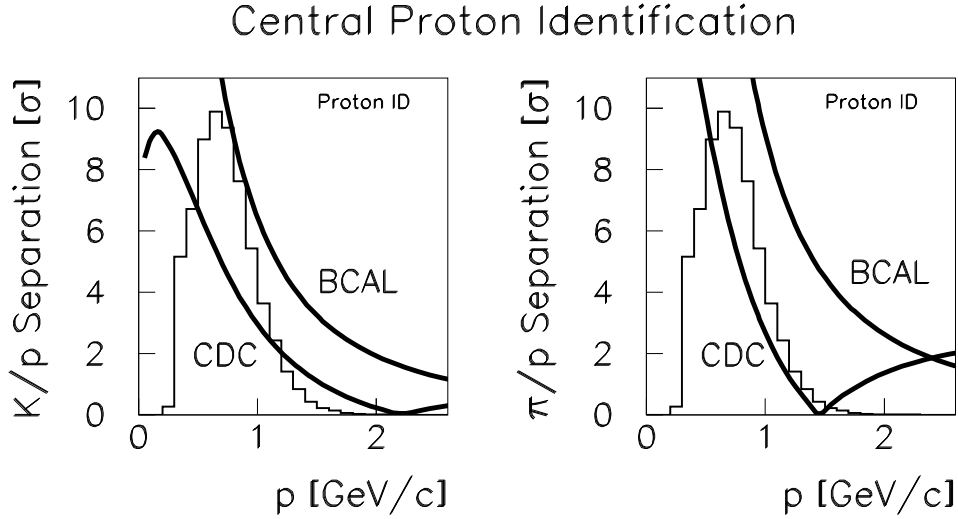


Figure 4.58: Identifying protons in the central region of the detector. The left plot shows K/p separation; the right shows π/p . The histogram in each is the momentum distribution for central protons from the reaction $\gamma p \rightarrow K^* \bar{K}^* p$. The curves are estimates of the separating power (in numbers of sigma) of the CDC dE/dx and the BCAL time of flight measurements.

Central Pion/Kaon Identification

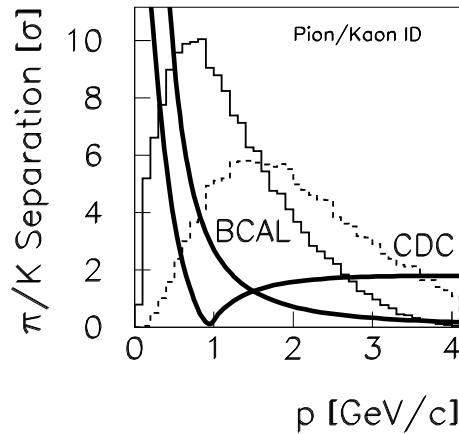


Figure 4.59: Identifying pions and kaons in the central region of the detector. The solid histogram is the central pion momentum spectrum; the dashed histogram is the momentum spectrum of central kaons. The curves are estimates of the separating power (in numbers of sigma) of the CDC dE/dx and the BCAL time of flight measurements.

In addition to the recoiling proton, however, a fraction of the pions and kaons in the reaction $\gamma p \rightarrow K^* \bar{K}^* p$ end up in the central region. Figure 4.59 shows estimated π/K separation curves (using the same detector parameters as above) overlaid on the pion and kaon momentum

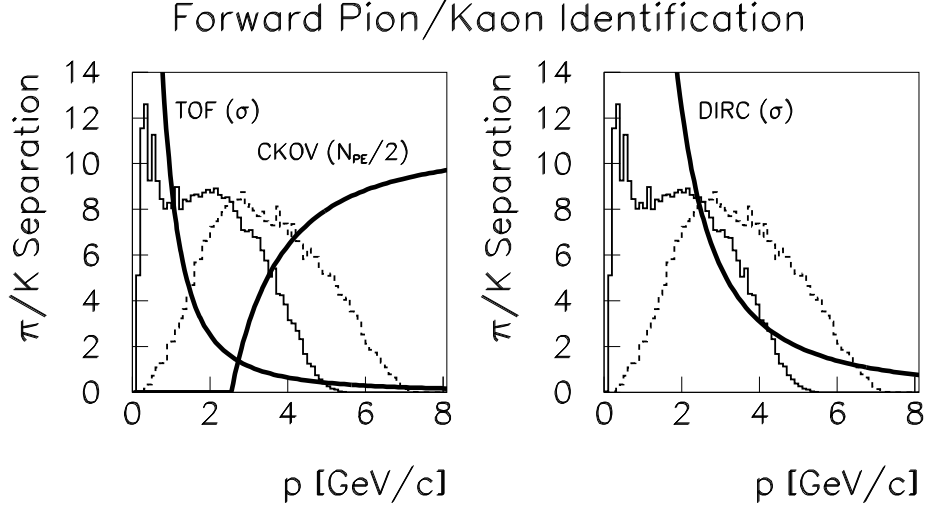


Figure 4.60: Identifying pions and kaons in the forward region of the detector. The left plot shows the gas Cerenkov option; the right plot is for the DIRC option. In each case, the solid histogram is the forward pion momentum distribution; the dashed is the forward kaon distribution. The curves of the left plot are the estimated π/K separations of the TOF and CKOV systems. The TOF π/K separation is expressed in numbers of sigma; the CKOV performance is plotted as the number of expected photoelectrons divided by two. The right plot shows the DIRC π/K separation in numbers of sigma. (Note the TOF will be used in conjunction with either option but is shown only in the left plot.)

distributions. Some fraction of the higher momentum tracks cannot be identified, but the strong separations in the forward region compensate.

The momentum spectra of forward-going pions and kaons from the $\gamma p \rightarrow K^* \bar{K}^* p$ reaction are shown in Figure 4.60. These will be identified by a time of flight measurement from the forward TOF wall in conjunction with either a gas Cerenkov system (CKOV) or a DIRC. The expected π/K separations from each option are overlayed on the momentum spectra. Typical TOF parameters were used in generating the time separation: a detector time resolution of 70 ps, a typical flight length of 5.0 m, and a conservative momentum resolution of 1% and length resolution of 1% added on when projecting different particle hypotheses to the wall.

The performance of the gas Cerenkov system is expressed in terms of the average number of photoelectrons, N_{pe} , for π mesons traversing 80 cm of C_4F_{10} gas with index of refraction $n = 1.0015$. The momentum threshold for π and K mesons are 2.5 and 9.0 GeV/c respectively and the light yield per radiator length is given by:

$$\frac{dN_{pe}}{dx} = N_o \cdot \sin^2 \theta_c = N_o \cdot \left(1 - \frac{1}{\beta^2 n^2}\right) \quad (4.17)$$

and since $n \approx 1$, in the relativistic limit $\beta \rightarrow 1$:

$$\frac{dN_{pe}}{dx} \approx N_o \cdot 2(n - 1) \quad (4.18)$$

N_o is the figure of merit of a Čerenkov counter taking into account all efficiencies in the system and for a counter of reasonably good design $N_o \approx 90 \text{ cm}^{-1}$. Based on this, the average photoelectron yield for the Čerenkov counter will be about 21 in the relativistic limit.

The gas Cerenkov option leaves a significant gap in momentum where the π/K separation is restricted. The TOF separating power falls below 3 σ at a momentum near 2 GeV/c , while the pion threshold in the C_4F_{10} gas is 2.5 GeV/c .

The DIRC option, on the other hand, will use a higher index of refraction (Quartz) to make a measurement of the Čerenkov opening angle:

$$\cos\theta = \frac{1}{\beta n} \quad (4.19)$$

The estimated π/K separation of figure 4.60 assumed a resolution on the opening angle measurement of 2.1 mrad. More details on the DIRC will be given in a later section.

Required Design Parameters For the Čerenkov counter, assuming that the inefficiency for detection is given by $e^{-N_{pe}}$, then the efficiency for detecting pions exceeds 95% when the π momentum is above 3 GeV/c . At this momentum the TOF difference is about 210 ps . For 95% (3σ) efficiency to separate pions and kaons with the TOF at this momentum, the time resolution, σ_t should be less than about 70 ps .

dE/dx in the chambers

As described above, there is a subset of the low momentum charged particles which will not reach a time of flight counter, or will reach them after spiraling so many times in the magnet that the TOF information will be very difficult to use. For these particles, dE/dx information from the CDC chamber will be the primary source of identification. Fortunately, these particles all have momenta smaller than about 450 MeV , which is exactly where dE/dx will work the best. This detector has been discussed in an earlier section.

4.5.2 The Time-of-flight System

Barrel Time-of-flight Measurement

The design of the barrel calorimeter is dictated primarily by the available space inside the magnet and the method chosen for photon conversion. Charged particles emitted at large angles to the beam often have low velocity so even moderate time resolution is sufficient to distinguish pions from kaons. The lead/fiber design of the barrel calorimeter provides a large number of scintillator samples as a particle traverses the individual fibers. The KLOE collaboration has demonstrated [76] an RMS time resolution of 252 ps for minimum ionizing particles traversing 19 layers of lead and fiber. This value will be used as an estimate of the performance that can be achieved in the TOF measurement from the calorimeter in HALL D. This detector has been discussed in an earlier section of this report.

The Lead Glass Forward Calorimeter

Located just upstream of the forward electromagnetic calorimeter, the LGD, and downstream of the Čerenkov counter will be the forward time-of-flight system, the TOF. The goal of the forward TOF is to separate K^\pm from π^\pm among forward-going charged particles. The TOF will also provide a forward multiplicity count to be used in the level-one trigger.

Assuming a momentum resolution of about 1% and a particle path length resolution of 1% an overall TOF time resolution of 80 ps should allow for K/π separation at the 3σ level up to a momentum of 2.5 GeV/c . The TOF will consist of two planes of scintillation counters, each 2.5 m long, 6 cm wide and 1.25 cm thick. Each counter will be read out at both ends. The counters in one wall will be oriented perpendicular to the other wall. The total module count is 84 modules and the total channel count is 168 for the number of FADC's, constant fraction discriminators and TDC's.

The scintillator bars need to be 2.5 m long to cover the active regions of the Čerenkov counter. The 6 cm width of the bars is set by the requirement that the overlap of charged particles from the same event at the TOF in any one bar be acceptably small ($< 2\%$). From Monte Carlo simulations of $\gamma p \rightarrow K^* \bar{K}^* p$ it was found that a 6 cm width satisfies the occupancy requirement. (We studied four reactions, but are most vulnerable to this one because of its low

Q value.) Specifically we find a probability of 0.22% that two charged particles go through just one bar in both the front and back planes. The thickness of the scintillation bars, the dimension along the beam direction, is set by the requirement that sufficient light be produced to meet the time resolution requirements, while at the same time minimizing the amount of material in front of the LGD.

Prototype Studies

Extensive prototype studies have been carried out to optimize the TOF system design. Data using scintillation bars of various dimensions and manufacture and various phototubes were collected using a cosmic ray test facility at Indiana University. Data were collected in several data runs with hadron beams at the Institute for High Energy Physics (IHEP) in Protvino, Russia. During the data runs we also explored the possibility of using Čerenkov light in Plexiglas (non-scintillating) bars to exploit prompt Čerenkov light to build a TOF system. Results of the IHEP tests have been presented at various instrumentation conferences and publications [77, 78, 79, 80]. Further beam tests at IHEP are planned using 2.5 m scintillator bars with four elements in each of two walls in early 2005.

Cosmic Ray Test Facility Figure 4.61 shows part of the cosmic ray test facility. A large light-tight box was prepared to accommodate a 2-m long scintillator bar and a cosmic ray telescope consisting of two small scintillation counters that can be positioned along the bar. The scintillation bar under test is read out at both ends with Phillips XP2020 PMT's and their signals are read into separate channels of a TDC and ADC. Trigger electronics use signals from the telescope to define the passage of a cosmic ray particle and define the start signal for the TDC and gate for the ADC.



Figure 4.61: Part of the cosmic ray test facility showing a light-tight box inside of which is a 2-m long scintillator bar, read out at both ends, as well a trigger telescope with two small scintillation counters that can be positioned along the bar.

Measurements Made in a Hadron Beam at IHEP Several data runs testing TOF prototype modules were made at the IHEP accelerator. The setup for these runs is shown in Figure 4.62. The two bars under test were coupled to PMTs T1 through T4 at their ends. The bars could be moved transverse to the beam. We define x as the position of the center of the long scintillator relative to the beam with $x=0$ at the center of the bar.

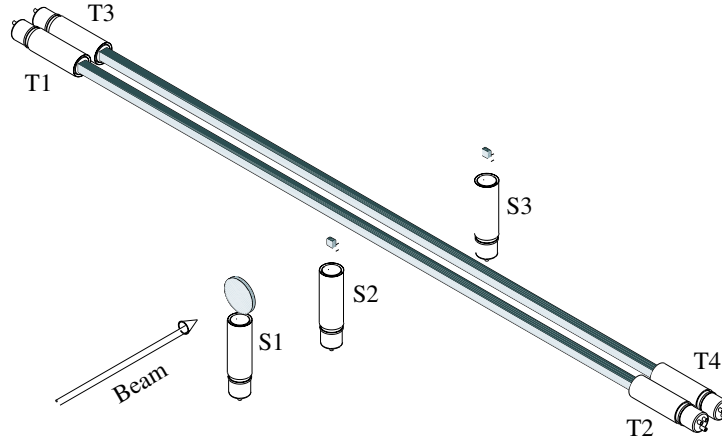


Figure 4.62: The setup for the beam tests at IHEP at Serpukhov.

Table 4.8: Time resolution for various phototubes.

Phototube	T_{av} Time Resolution (ps)
2.5 cm Bar	
XP2020	102
FEU 115	172
Hamamatsu R5506	167
Hamamatsu R5946	102
5.0 cm Bar	
XP2020	89
XP2020/UR	82

The beam defining counters shown in Figure 4.62 are S1, S2, and S3. The cross sectional size of the beam was large compared to the 2 cm by 2 cm size of S2 and S3. S2 and S3 were each 1.25 cm thick and both coupled to an XP2020 phototube with a 5 cm air gap. S1 was not used for timing purposes, nor to define the effective size of the beam.

The first data run at IHEP was used to test 2-m long counters with square cross sections of $2.5 \times 2.5 \text{ cm}^2$ and $5.0 \times 5.0 \text{ cm}^2$. The scintillator is type EJ-200, produced by the Eljen Corporation. This scintillator has a decay time of 2.1 ns, a bulk attenuation length of 4 m, an index of refraction of 1.58, a peak in the emission spectrum at 425 nm, and a light output equal to 64% of that of Anthracene. The surfaces of two of the four long sides of each bar were in contact with the casting form and had no other preparation. The other two long sides and the two ends of each bar were diamond fly-cut in order to minimize losses due to surface imperfections. A phototube was placed on each end of each bar. The two bars, with their phototubes, were placed in a light-tight box. The beam was a 3 to 40 GeV/c positive beam with variable energy.

Table 4.5.2 shows the results for average time resolution measured for various combinations of scintillation bars and PMTs. Figure 4.63 shows the variation of time resolution as a function of position of the beam along the bar ($x=0$ at the center) for the two types of bars.

In a later data run 2 m-long bars of cross sections $2.5 \times 6.0 \text{ cm}^2$ were tested using a 5 GeV/c beam. A typical PMT pulse observed after a 40 m cable is shown in Figure 4.64. These

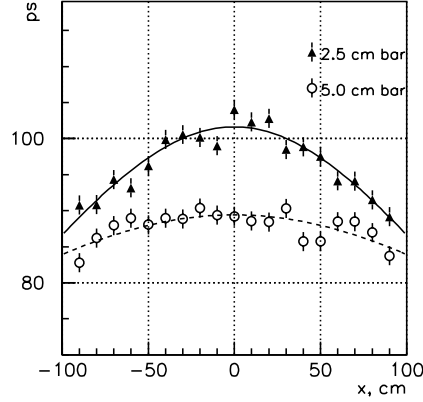


Figure 4.63: The average time resolution for a 2 m-long scintillation counter read out at both ends with Phillips XP2020 PMTs as a function of position of a charged particle beam along the bar ($x=0$ at the center of the bar). Bars of square cross section $2.5 \times 2.5 \text{ cm}^2$ and $5.0 \times 5.0 \text{ cm}^2$ were tested.

signals went to constant fraction discriminators (CFD) to eliminate time corrections associated with variations of signal amplitude. Measurements using leading edge discriminators (LED) and Analog to Digital Converters (ADC) were also made. In this case a time vs. amplitude correction was made using measured signal pulse heights. Custom made Time to Digital Converters (TDC) with 26.5 ps least count were used for time measurements. The S3 signal was used as the common start and signals from the other beam counters and the bars under test were used as stop signals. The intrinsic time resolution of the electronics was 18 ps (r.m.s.) as measured by using the S3 signal to both to start and to stop the TDC. The measured time resolution of S2 and S3 was 70 ps.

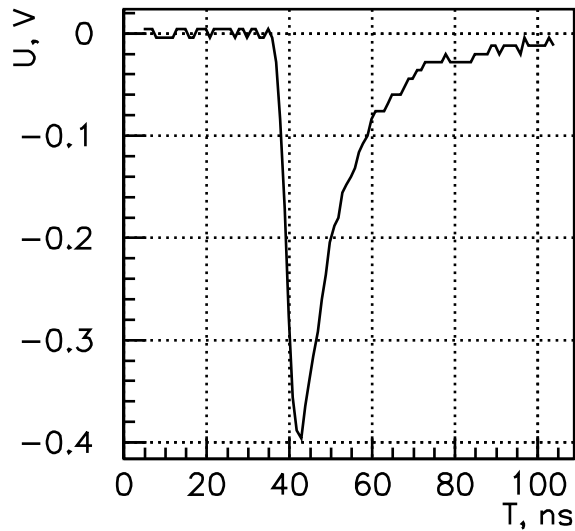


Figure 4.64: A typical pulse a Phillips XP2020 PMT attached to a 2 m long scintillation bar after the signal passed through a 40 m delay cable.

Figure 4.65 shows the average time resolution as a function of the position of the beam along the 2 m-long scintillator bar ($x=0$ at the center of the bar). In Figure 4.65a and figure 4.65b the open circles show resolution using a single bar and the closed circles show resolution using

information from both bars. In (a) the beam passed through 2.5 cm of scintillator and in (b) through 6.0 cm of scintillator. In (a) and (b) a constant fraction discriminator was used and in (c) pulse height information was used to do the time-walk correction for the case when the beam passed through 2.5 cm of scintillator.

Using constant fraction discriminators the time resolution for two bars was measured to be less than 40 and 60 ps when particle cross 6.0 cm and 2.5 cm of scintillator respectively. The results obtained with leading edge discriminators and corrected for time walk effect were similar to those measured with CFDs.

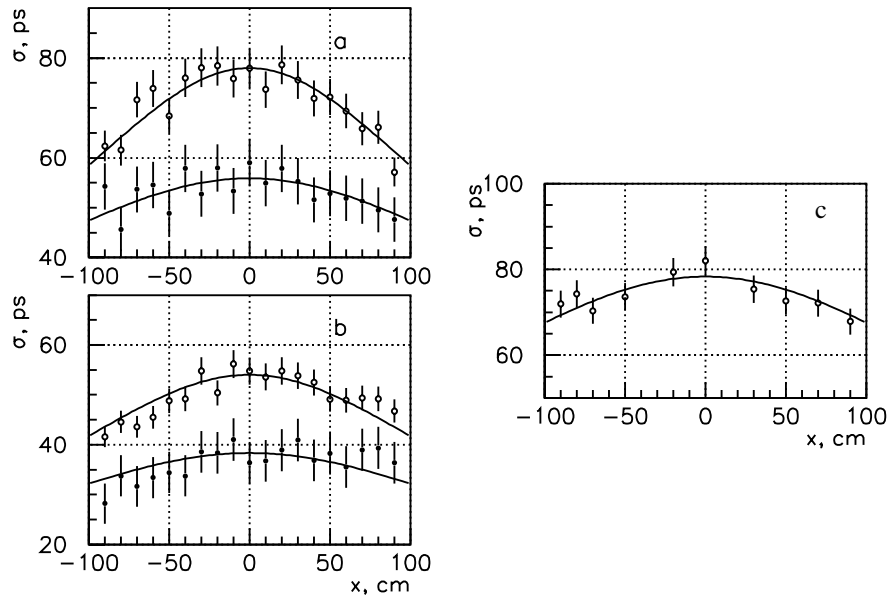


Figure 4.65: Average time resolution as a function of the position of the beam along the 2 m-long scintillator bar ($x=0$ at the center of the bar). In (a) and (b) the open circles show resolution using a single bar and the closed circles show resolution using information from both bars. In (a) the beam passed through 2.5 cm of scintillator and in (b) through 6.0 cm of scintillator. In (a) and (b) a constant fraction discriminator was used and in (c) pulse height information was used to do the time-walk correction for the case when the beam passed through 2.5 cm of scintillator.

The tests described above in the hadron beam are described in more detail in references [77, 78]. In order to minimize the amount of material in front of the LGD bars of 1.25 cm thickness were tested and compared and those measurements were reported in reference [79].

Comparison of timing properties for the $1.25 \times 6.0 \text{ cm}^2$ and $2.5 \times 6.0 \text{ cm}^2$ bars shows that the time resolutions at the center of the bar are better by factor of ≈ 1.4 for the $2.5 \times 6.0 \text{ cm}^2$ bar. But the time resolutions at the bar edges are the same in both cases indicating that near the PMT's the time resolution does not depend on photoelectron statistics.

Conclusions and remaining issues

Based on the results presented above, therefore, we have chosen the 1.25 cm thick, 6 cm wide bar for the TOF wall. As shown in Figure 4.65a, the time resolution for two bars of this size is 80 ps or less at all point on the bar – satisfying our design criterion.

In addition to optimizing the time resolution, a practical consideration in the choice of bar geometry is the ability to accommodate magnetic shielding for the approximately 200 G magnetic field in the vicinity of the XP2020s. For a 6 cm wide bar the phototubes can simply be attached

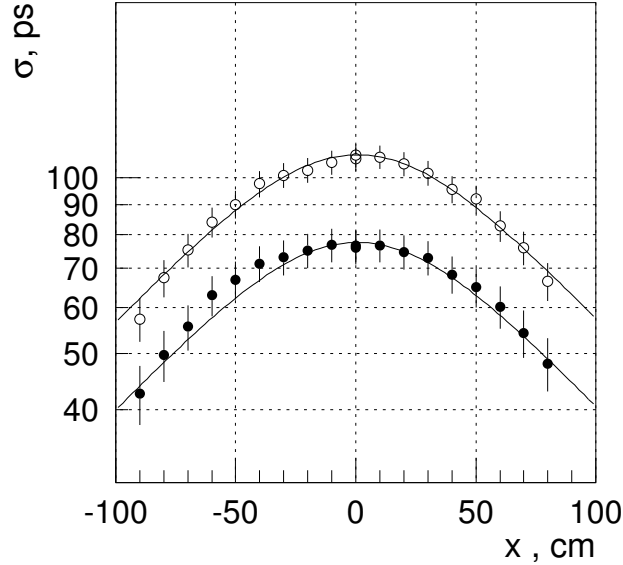


Figure 4.66: The time resolution for one (\circ) and two (\bullet) $1.25 \times 6.0 \text{ cm}^2$ bars viewed by XP2020 PMT's.

to scintillator snouts and then surrounded by magnetic shielding; this cannot be done for bars less than 6 cm wide.

4.5.3 Čerenkov Counter

The Čerenkov detector for GLUEX is unfortunately not as well defined as the rest of the equipment. This is due to the fact that the first group to express interest in this detector pulled out of GLUEX because of the long time scales involved and detector became an *orphan* for several years. After the granting of CD0 to the JLab upgrade and GLUEX in the spring of 2004, a pair of groups from Tennessee approached the collaboration about joining GLUEX and taking on a large detector responsibility. The natural piece of hardware was the orphaned Čerenkov system.

Based on this interest, it was felt that a completely fresh look should be taken at the system. This should consider both the physics of GLUEX and technological developments that have occurred over the last several years. The result of this effort is a proposal to build a DIRC detector rather than the gas Čerenkov system that had been proposed earlier. Because this proposal is so new, and the collaboration is still evaluating its implications, we have presented both the newer DIRC material and the older gas Čerenkov material here. A final decision on this clearly depends on many factors including physics, manpower, costs and timescales. The collaboration is currently evaluating these.

In the case of both Čerenkov designs, it is possible for the GLUEX experiment to start taking quality data without this system in place. There is a very solid physics program with pions that does not need the Čerenkov. However, as the collaboration begins to study final states with both hidden and open strangeness, the Čerenkov system will be crucial. What follows are first a discussion of the DIRC option followed by the earlier work on the gas Čerenkov detector.

A DIRC Čerenkov Detector

The Čerenkov detector, DIRC, of the BABAR experiment at the PEP-II asymmetric B -factory of SLAC has proven to be a successful novel technique for pion and kaon identification [81] [82][83].

The DIRC (acronym for **D**etection of **I**nternally **R**elected **C**herenkov (light)) is a ring imaging Cherenkov detector. It provides the identification of pions, kaons, and protons for momenta up to $4.5 \text{ GeV}/c$ with high efficiency. This is needed to reconstruct CP violating B -decays and to provide B -meson flavor tagging for time-dependent asymmetry measurements. The DIRC radiators consist of long rectangular bars made of synthetic fused silica and the photon detector is a water tank equipped with an array of 10,752 conventional photo-multiplier tubes (PMT). By the summer 2004, BABAR had recorded about 227 million $\bar{B}B$ pairs, exceeding the design luminosity of $3 \cdot 10^{33}/\text{cm}^2\text{s}$. The observation of direct CP violation with more than 4 standard deviations in the decay $B^0 \rightarrow K^+\pi^-$ [84], which has to be distinguished from B^0 decays into $\pi^+\pi^-$ and K^+K^- , is a successful demonstration of the DIRC's capabilities.

Similar to the physics program of BABAR, the spectroscopy program of GlueX depends on the capability to identify charged kaons. We discuss the possibility to adapt the DIRC concept for the GlueX detector to complement the particle identification information of the tracking chambers and the time-of-flight (TOF) detector for momenta above $1.5 \text{ GeV}/c$.

The BABAR DIRC

The physics program of the BABAR [85] detector is to observe CP violation and to probe the Standard Model of Particle Physics by collecting enough B -meson decay channels to over-constrain predictions. The source of B mesons is the PEP-II asymmetric e^+e^- collider [86][87][88], where 9 GeV electrons strike 3.1 GeV positrons producing $\Upsilon(4S)$ resonances with a boost of $\gamma\beta \simeq 0.56$. The $\Upsilon(4S)$ resonance decays nearly exclusively in a pair of B and anti- B mesons. This allows precise measurements of time-dependent asymmetries in B meson decays which can be related to the CP violation phase in the Cabbibo-Kobayashi-Maskawa (CKM) matrix [89].

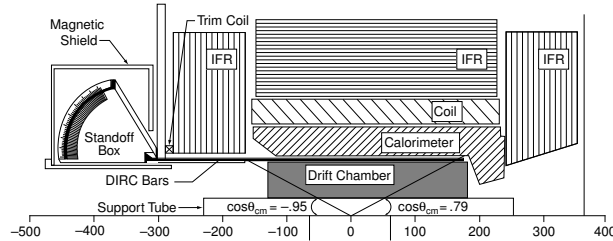


Figure 4.67: The side-view of the BABAR detector with the components of the DIRC indicated (units in cm).

BABAR is a typical collider detector but asymmetrically placed around the interaction point to ensure nearly full solid angle coverage in boost (forward) direction (see Fig. 4.67). The location of the particle identification system is radially between the drift chamber and a CsI(Tl) crystal calorimeter. Therefore, a small radiation length is preferred to avoid deterioration of the excellent energy resolution of the calorimeter. The DIRC minimizes the radial dimension and keeps the amount of required calorimeter material (cost) small. Up to a momentum of $700 \text{ MeV}/c$, the drift chamber can provide pion-kaon separation based on the dE/dX measurement. Only if pion-kaon separation up to $4.5 \text{ GeV}/c$ particle momentum is available can one distinguish the channels $B^0 \rightarrow \pi^+\pi^-$ from $B^0 \rightarrow K^+\pi^-$ or $B^\pm \rightarrow \phi\pi^\pm$ from $B^\pm \rightarrow \phi K^\pm$, interesting for the measurement of indirect or direct CP violation. Moreover, the flavor content of the recoil $B(\bar{B})$ needs to be tagged by identifying kaons in its successive decays with momenta below $4 \text{ GeV}/c$. In addition, τ , charm-, and light-quark meson spectroscopy profit from kaon identification.

The difference in the Cherenkov angle between a pion and a kaon at $4.0 \text{ GeV}/c$ momentum is 6.5 mrad . Therefore, a 3 standard deviation π/K separation requires resolution of the Cherenkov angle for given a track of 2.2 mrad or better (see Fig. 4.68). Finally, to operate successfully in the high-luminosity environment of PEP-II, the Cherenkov detector has to be radiation hard,

fast, and tolerant of background.

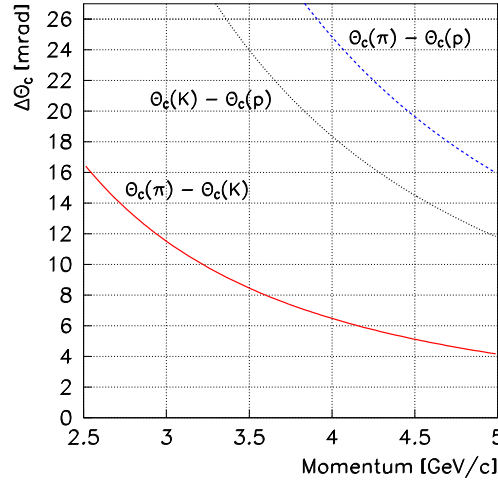


Figure 4.68: The difference in the Cherenkov angles between pions, kaons, and protons in synthetic quartz.

Principle of the BABAR DIRC

The DIRC uses thin, long rectangular bars made of synthetic fused silica (quartz) [90] ($H \times W \times L = 17 \text{ mm} \times 35 \text{ mm} \times 4900 \text{ mm}$) both as Cherenkov radiators and light guides (refractive index $n_1 \approx 1.47$). Bars are glued together from four pieces, each 1225 mm long. All together, 144 bars are arranged in a 12-sided polygonal barrel with a radius of about 84 cm around the beam axis. The DIRC bars extend 178 cm forward from the interaction point of BABAR covering 87% of the polar solid angle in the center-of-mass frame. The azimuthal coverage is 93%, since there are gaps between the bars at the 12 sides of the radiator polygon. Every 12 bars are housed in a bar-box surrounded by nitrogen at STP (index $n_2 \approx 1$). The box is built mostly of aluminum honeycomb material. The radiation length (X_0) of the bars is 14%, and 19% for the full assembly at perpendicular incidence. A schematic view is presented in Fig. 4.69.

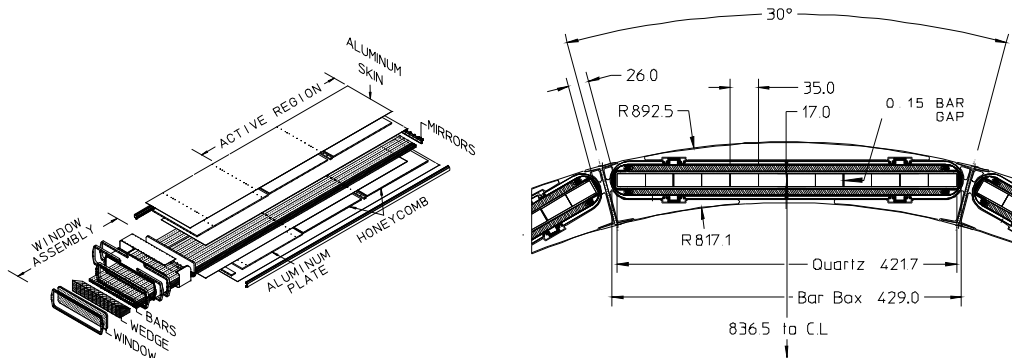


Figure 4.69: Left: View of a bar-box assembly. 12 bar-boxes surround the drift chamber. Right: Placement of the bar-box in the BABAR detector above the cylindrical drift chamber.

The principle of the DIRC is shown in Fig. 4.70. The DIRC imaging works like a pinhole focus camera with the bar cross section small compared to the imaging plane.

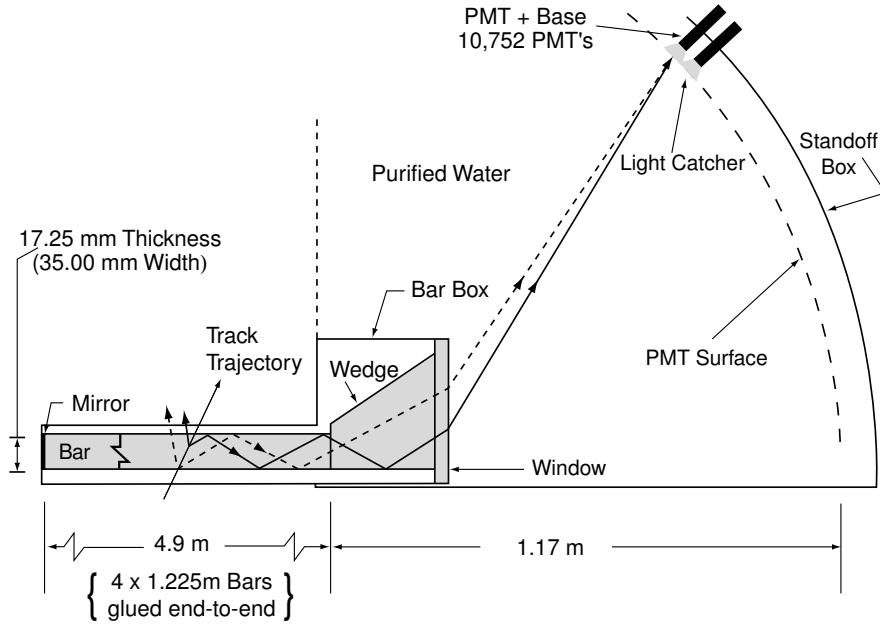


Figure 4.70: The principle of the BABAR DIRC.

Since the refractive index of the radiator bar n_1 is larger than $\sqrt{2}$, a certain fraction of the Cherenkov photons produced by a relativistic charged particle traversing the quartz bar will be totally internally reflected, regardless of the incidence angle of the track, and propagate along the length of the bar. Only one side is viewed by the PMT array and a mirror (reflectivity $\approx 92\%$) is placed perpendicular to the bar axis on the other end, where positrons enter the BABAR detector. Due to the boost of the $\Upsilon(4S)$ there is a higher density of charged tracks towards the mirror side and hence it is less preferable for the readout. Since the rectangular bar is of high optical precision (mean surface reflectivity $\approx 99.96\%$ per bounce at 442 nm photon wavelength), the initial direction of the photon is preserved throughout its propagation, modulo left/right, up/down and forward/backward ambiguities. The latter is resolved by the measurement of the photon arrival time. The bars have very high light transmission (99.9% at 442 nm photon wavelength) required for the typical photons path-lengths of 6 to 20 m.

Photons exiting the bar in the downward direction, or with large exit angles with respect to the bar length axis, are partly recovered into the instrumented area by a prism (wedge). This optical element is 91 mm long and the top side has a 30° opening angle. The bottom side is slightly tilted upwards by 6 mrad. It reduces the required photon-sensitive area by more than a factor of two.

A thin (9 mm) quartz window separates the prism from the so called standoff box (SOB), a water tank filled with 6000 liters of purified water ($n_3 \approx 1.33$) in a toroidal shape. The backplane of the SOB is divided into 12 sectors, each equipped with 896 conventional photo-multiplier tubes [91] ($\approx 25\%$ quantum efficiency at 400 nm wavelength, 250 nm – 650 nm spectral range), facing the wedge of a corresponding bar box. Hexagonal reflectors (light catchers) with water-resistant rhodium surfaces surround the PMT cathodes improving the detection efficiency by about 20%. The ratio of refractive indices n_1/n_3 is nearly wavelength independent. It reduces internal reflection at the bar-box wedge. Furthermore, the exit angle is magnified by this ratio, increasing the position resolution of the photons.

The detector provides a three dimensional measurement of the photon in the variables (α_x, α_y) , the photon exit angles with respect to the bar axis, and the arrival time of the photon t_a . The spatial position of the bar through which the track passed and the particular PMT hit

within a certain readout time interval is used to reconstruct the photon vector pointing from the center of the bar end to the center of the tube. This vector is then extrapolated back into the quartz bar using Snell's law, where the photon exit angles (ϕ_C, θ_c) with respect to the track are calculated. Most of the photon phase space $(\alpha_x, \alpha_y, t_a)$ is mapped onto the Cherenkov angles (ϕ_C, θ_c) with less than a three-fold average ambiguity.

The timing information apart from the resolution of the forward-backward propagating photons, is not competitive with the position information, but it is crucial for suppression of beam background. The expected arrival time of the Cherenkov photon is a sum of the time-of-flight of the charged particle from its origin to the quartz bar (typically 2-3 ns), the photon propagation time in the quartz bar and the wedge along its reconstructed path, and the traveling time through the water before reaching the surface of the PMT. Applying the reconstructed mean arrival time of the photons in an event as correction for the uncertainty in the bunch-crossing time yields a precision of about 1.5 ns in the time between photon creation and photon arrival, which is close to the intrinsic time resolution of the PMTs. This allows restriction of the event time interval to 8 ns.

Particle identification uses likelihood ratios for different particle hypotheses based on the number of photons above and below threshold and the Cherenkov angle. Another way to use the information is to compare the ring pattern in the PMT plane with expected patterns for the different particle hypotheses.

Imaging with Synthetic Fused Silica

The Cherenkov angle separation between particle types is the Cherenkov angle difference in Fig. 4.68 divided by the Cherenkov angle resolution σ_C . This resolution, in turn, depends primarily on the precision of the track angle of incidence as provided by the tracking detectors, σ_t , and the single photon Cherenkov angle resolution in the DIRC, $\sigma_{C,\gamma}$, and the number of photo-electrons contributing to the measurement, N_γ , as follows:

$$\sigma_C = \sqrt{\sigma_t^2 + \sigma_{C,\gamma}^2 / N_\gamma}. \quad (4.20)$$

The dominant contributions to the error of the single photon measurement are

chromatic	5.4 mr
imaging (bar size) and detection (PMT size)	7.5 mr
transport (through the bar)	1.0 mr .

These add in quadrature to $\sigma_{C,\gamma} = 9.3$ mr. The number of Cherenkov photons per track for di-muon events versus the track polar angle with respect to normal incidence is shown in Fig. 4.71 b). The number varies between 25 and 60 photons. Therefore, with negligible tracking resolution, σ_C decreases from 1.9 mr to 1.2 mr in the extreme forward direction where tracks have the highest momenta in BABAR due to the boost. The imaging and detection error can be improved by extending the distance between bar end and PMT plane. For instance, with a distance of 1.4 m we obtain a single photon angle resolution of about 8.3 mr. With a slightly increased bar thickness and shorter bars the minimum number of photons per track can be increased to 25 or higher.

Features of the BABAR DIRC

Here we summarize the main advantages of the BABAR DIRC type Cherenkov detector:

- The BABAR DIRC separates kaons from pions to better than 3 standard deviations below 4 GeV/c. It is an imaging device in the required momentum range with high photo-electron yield (25 or more). It also works as a threshold detector for different particle types with momenta below 0.92 times the particle's mass.
- Compact: The total thickness between tracking and calorimeter is less than 5 cm. The total radiation length (X_0) for a full assembly is 19%.

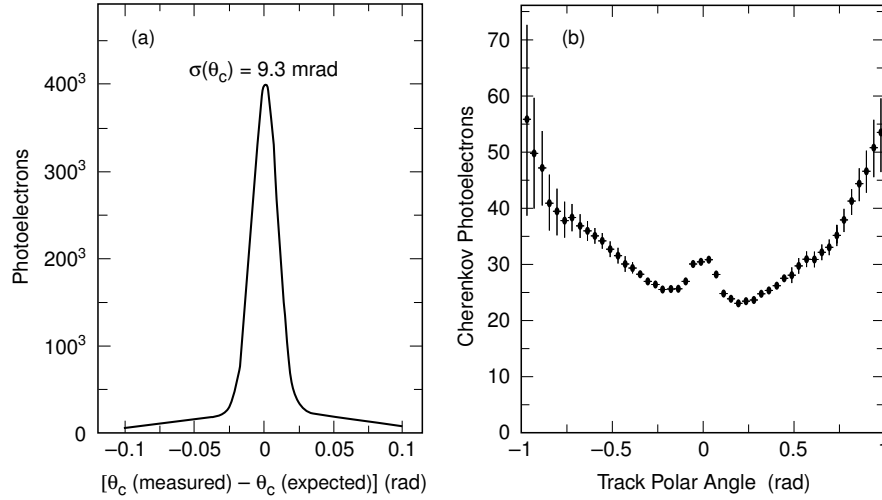


Figure 4.71: (a) The Cherenkov angle resolution for single photons associated with a particle track. (b) The number of Cherenkov photons per track versus the track polar angle with respect to normal incidence. The slightly lower efficiency in forward direction is due to the reflection in the mirror and the increased photon path-length in the bar.

- Radiation robust: It has been demonstrated that there is no efficiency loss in the wavelength regime above 280 nm after irradiation with 250 krad [92].
- Fast device: The photon collection time is less than 100 ns.
- Insensitive to background: The BABAR DIRC is a 3-dimensional device; the photon arrival time and the location of the PMT are correlated, allowing reconstruction of the true arrival time of the Cherenkov photons originating from the same track with a precision of 1.5 ns. Therefore, the event time interval can be smaller than 10 ns.
- Robust device: The radiator is passive and needs only to be kept in a dry atmosphere. Conventional photo-multiplier tubes are used which can be easily accessed. The DIRC is the subsystem within BABAR that requires the least maintenance.

Requirements for GlueX

In the previous design a gas-Cherenkov detector is placed behind 4 layers of FDCs and before the TOF system. It extends into the inner cylinder of the solenoid and has an effective length along the beam axis (z -axis) of 1.4 m. Instead of this detector a DIRC system can be positioned at some short distance behind the solenoid opening. To evaluate the situation with GEANT simulations [93] we place a virtual (xy) plane perpendicular to the beam direction at $z = 450$ cm, which is about 10 cm behind the solenoid opening. Without modification of the bar-imaging concept of the DIRC detector, the bars would line up along one axis in that plane and leave a gap for the beam to pass through.

Particle Momenta and Angle of Incidence In a typical reaction $\gamma p \rightarrow (\text{mesons}) p$ with strangeness production, 50% of the pions and kaons (somewhat fewer protons) produced with momenta between 1 GeV/c and 5 GeV/c arrive at the Cherenkov detector plane. In many cases strangeness conservation can be used to recover the final state if the remaining particles are identified with high efficiency. Highly efficient and redundant kaon identification is required to access a large variety of final states and to reduce combinatorial background in the search for new signals. A particle identification coverage with constant efficiency and low mis-identification rate over the full momentum range is essential to perform angular analysis of their decays.

Figure 4.72 shows the momentum spectra for the pions, kaons, and protons which arrive at the Cherenkov-detector plane for the two reactions:

$$\begin{aligned} \gamma p &\rightarrow K^{*0}(892)K^{*0}(892)p & (4.21) \\ &\rightarrow K^+\pi^-K^-\pi^+p \end{aligned}$$

$$\begin{aligned} \gamma p &\rightarrow K_1(1270)K^-p & (4.22) \\ &\rightarrow K^{*-}\pi^+K^-p \\ &\rightarrow K^-\pi^0\pi^+K^-p. \end{aligned}$$

These are typical reactions with more than two final state pions and kaons. In these final states kaon-pion separation is required up to a momentum of 5 GeV/c . Based on dE/dX and TOF a 3 standard deviation separation is obtained up to 1.5 GeV/c momentum, while with the kaon threshold in a DIRC at 0.45 GeV/c enough photo-electrons are created for efficient Cherenkov imaging. The proton spectrum extends to 2 GeV/c and below 1 GeV/c a DIRC detector acts as a threshold Cherenkov detector for this particle type.

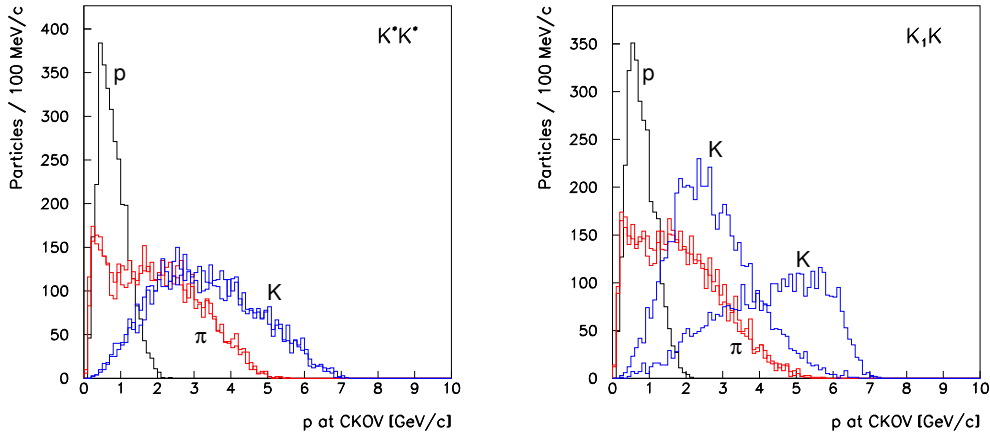


Figure 4.72: The particle momenta at the Cherenkov detector plane ($z = 450$ cm) for the two reactions described in the text (π :pions, K :kaons, p :protons).

Figure 4.73 shows the polar angle with respect to the z -axis for the charged final state particles in the reactions Eq. 4.21. This angle typically does not exceed 15 degrees. Pions with polar angles greater than 15 degrees typically have momenta below 1 GeV/c .

Beam Background We assume an electron beam current of 3 μA . This is the high-luminosity scenario for the Hall-D project. We use a full GEANT simulation of the GlueX detector [93] to track primary and secondary particles. The charged particle background which can create Cherenkov light consists mostly of electrons and positrons coming from upstream or from photon conversions in the Cherenkov detector.

Figure 4.74 shows the combined electron-positron rate along the y -axis in our virtual detector plane at $z = 450$ cm. We obtain rates below 100 kHz per cm (200 kHz per 2 cm) at distances of about 6 cm from the beam axis. The total rate integrated over all of x and from ± 6 cm to ± 65 cm (the hole radius) of y is at the most 900 kHz. The integration from ± 10 cm to ± 65 cm of y yields a total rate of 580 kHz.

Figure 4.75 shows the photon rate per cm along the y -axis integrated over all of x in the virtual detector plane at $z = 450$ cm. We expect 600 kHz/cm photons at distances near $y = 6$ cm. The total rate integrated over all of x and from ± 6 cm to ± 65 cm of y is 29.6 MHz; from ± 10 cm to ± 65 cm of y it is 24 MHz.

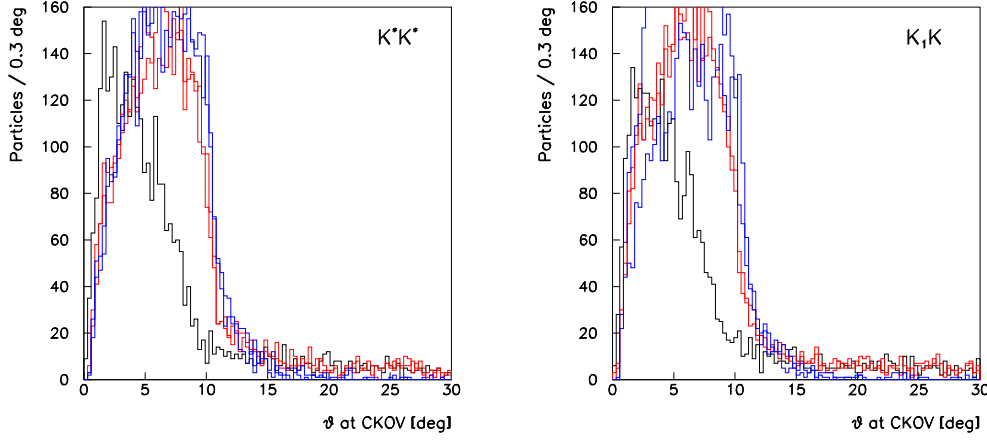


Figure 4.73: The polar angle with respect to the normal incidence at the Cherenkov detector plane ($z = 450$ cm) for pions, kaons, and protons in the two reactions described in the text.

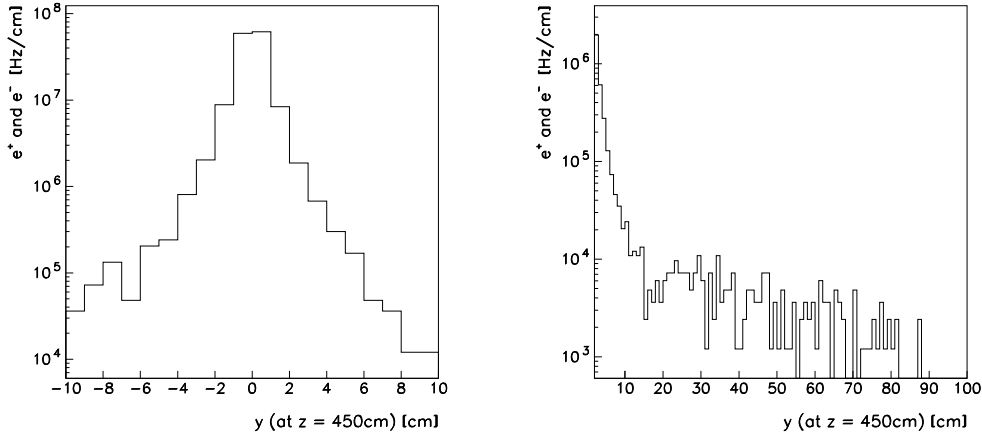


Figure 4.74: The rate of electrons and positrons per cm along the y -axis integrated over all of x at the location $z = 450$ cm. Left: rate/cm below ± 10 cm in y . Right: rate/cm versus y . The innermost 3 cm are omitted.

Each electron or positron potentially creates 30 detected photons in the struck bar. A beam photon converts with a probability of about 15% into an electron-positron pair somewhere inside the DIRC generating an average of 20 photons per lepton track. We estimate, that a DIRC placed at a distance of ± 6 cm away from the beam axis produces Cherenkov light into the readout tank at a rate of 210 MHz. If the DIRC has a central gap of ± 10 cm the total rate is 160 MHz. The time to collect photons out of the bars is less than the 100 ns for the long BABAR DIRC bars. We estimate the number of beam-background related Cherenkov-photons within 100 ns for a gap in the plane along the y -axis of ± 6 cm (± 10 cm) to be 21 (16). After reconstruction we can reduce the time window for the photon arrival to less than 10 ns, which reduces the background photons to 2, while we expect 25 or more signal Cherenkov photons in a limited region of the readout plane.

The hit rate in a single PMT depends also on the optics at the bar end (opening angle of the wedge) and the profile of the background shown in Fig. 4.74 and Fig. 4.75. Assuming that

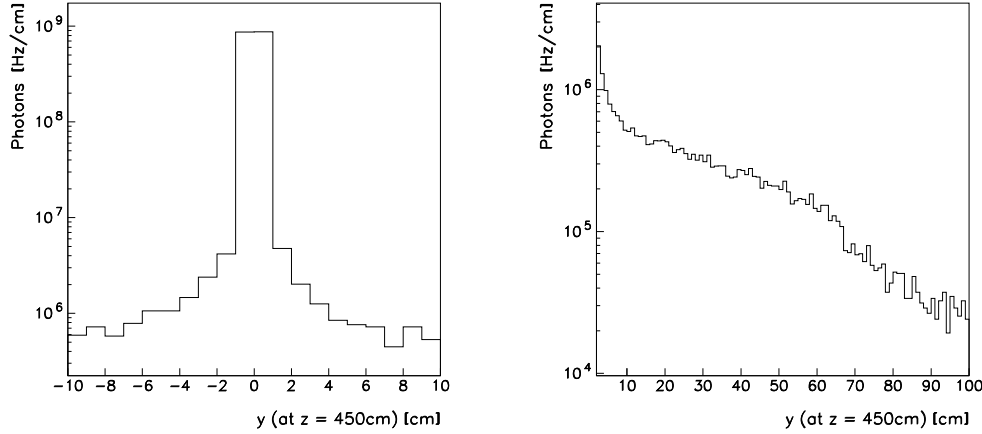


Figure 4.75: The rate of photons per cm along the y axis integrated over all of x at the location $z = 450$ cm. Left: rate/cm below ± 10 cm; Right: rate/cm versus y . The innermost 3 cm are omitted.

typically 1000 PMTs are randomly hit, the rate per tube is 210 kHz. This is the average rate encountered by PMTs in the BABAR DIRC which tolerates up to 1 MHz.

Magnetic Field The solenoid has strong fringe fields. We simulate the situation with the TOSCA program [94]. At a distance of about 3 m left or right of the solenoid center the field strengths are below 100 Gauss. Efficient operation of conventional photo-multiplier tubes requires shielding. In BABAR a magnetic field strength transverse to the PMTs of less than 0.2 Gauss is achieved with metal shielding and bucking coils.

Irradiation From the penetration rate with charged particles we estimate the radiation dose per year. We assume that the dominant component is secondary electrons and positrons created upstream or in the bars by photon conversions. The flux versus radius is shown in Fig. 4.76. It stays below 100 kHz/cm² for radii greater than 3 cm. For a flux of 100 kHz/cm² and a minimum ionizing $dE/dx = 1.6$ MeVcm²/g we estimate a yearly dose of 51 krad. This rate is well below the negligible dose of 250 krad tested with a ⁶⁰Co source [92].

Conceptual Design

At this point we discuss a geometry and imaging concept similar to that in the BABAR DIRC. In fact, we can even envision the use of four of the DIRC bar-boxes which would only need the design of a new support and a new shielded readout tank.

However, for a new design the bar dimensions can be optimized. Because azimuthal and polar angles of incidence are comparable and we expect a higher background rate per bar closer to the beam compared to BABAR, a width of 2 cm is more appropriate than 3.5 cm. The thickness can be increased from 1.7 cm to 2 cm to increase the photon yield and the structural stability. The modularity should be kept, with say, 14 bars in a box. Altogether four boxes provide a geometrical match. In principle, the bars could follow the circular boundary of the magnet opening. Also, the gap can be partly covered from the readout side. This would result in bars with different lengths.

The water tank should be placed on the side of the magnet, shielded, and away from secondary tracks which are produced in the forward direction in the central calorimeter or in the magnet yoke. This may also require that the bars be somewhat farther downstream (greater z). Hence, the length of the bars and their z position is a matter of further optimization. We

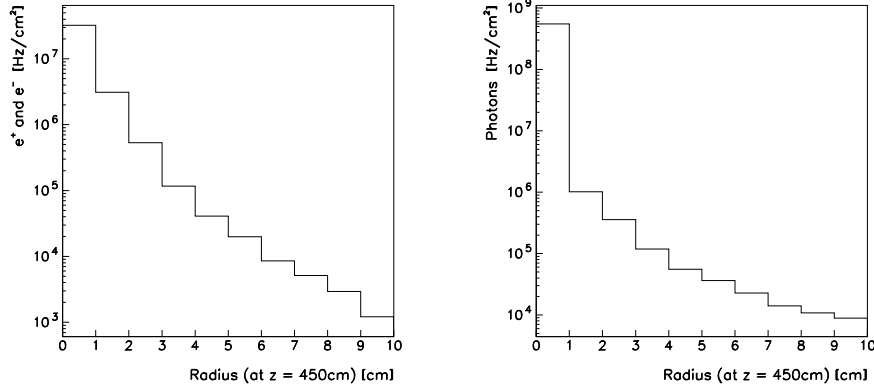


Figure 4.76: Left: The rate of electrons and positrons together per cm^2 versus radial distance from the beam axis in the virtual plane at $z = 450$ cm. Right: The same for photons.

explore the possibility that the purified water can be kept sealed in the tank for several years without maintenance.

In our first approach we allow the bars to extend into a region where there are no spatial restrictions and the transverse magnetic field [94] at the location of the PMTs is about 10 Gauss, while the longitudinal field drops below 45 Gauss. This corresponds to about 3 lengths of BABAR DIRC bars. Figure 4.77 shows the technical drawing of a first draft design of the bar arrangement with bars of 1.225 m length and a front area of $2 \times 2 \text{ cm}^2$. We have not optimized the bar length to follow the circular shape of the hole. Each 14 bars are housed in a separate bar-box. Two bar-boxes are placed below and two above the center leaving a gap for the beam to pass through. The readout side is shown in Figure 4.78. The maximum upward opening angle at the readout is 52 degrees. The sides open up with an angle of 30 degrees. Each tube covers an angle of 2 degrees. In this scenario the number of photo-tubes is 1512. A three-dimensional view of the half open bar-boxes and the readout tank is presented in Fig. 4.79.

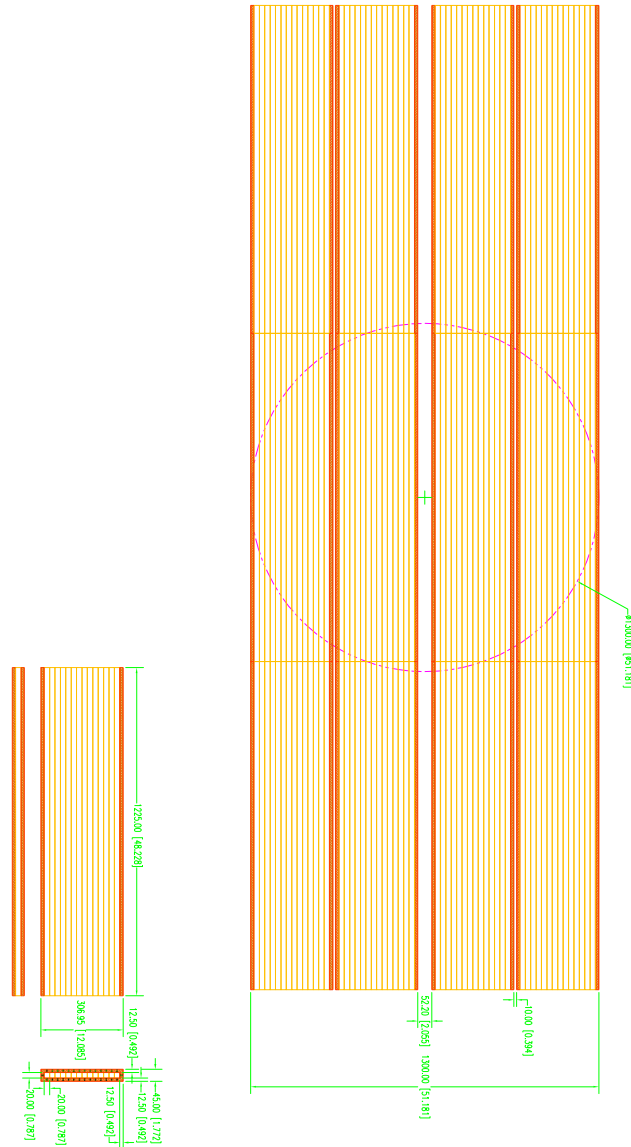


Figure 4.77: Arrangement of the bar-boxes in front of the solenoid. The circle indicates the size of the inner radius of the cylindrical calorimeter inside the solenoid. The bar-boxes will be placed asymmetrically with respect to that hole.

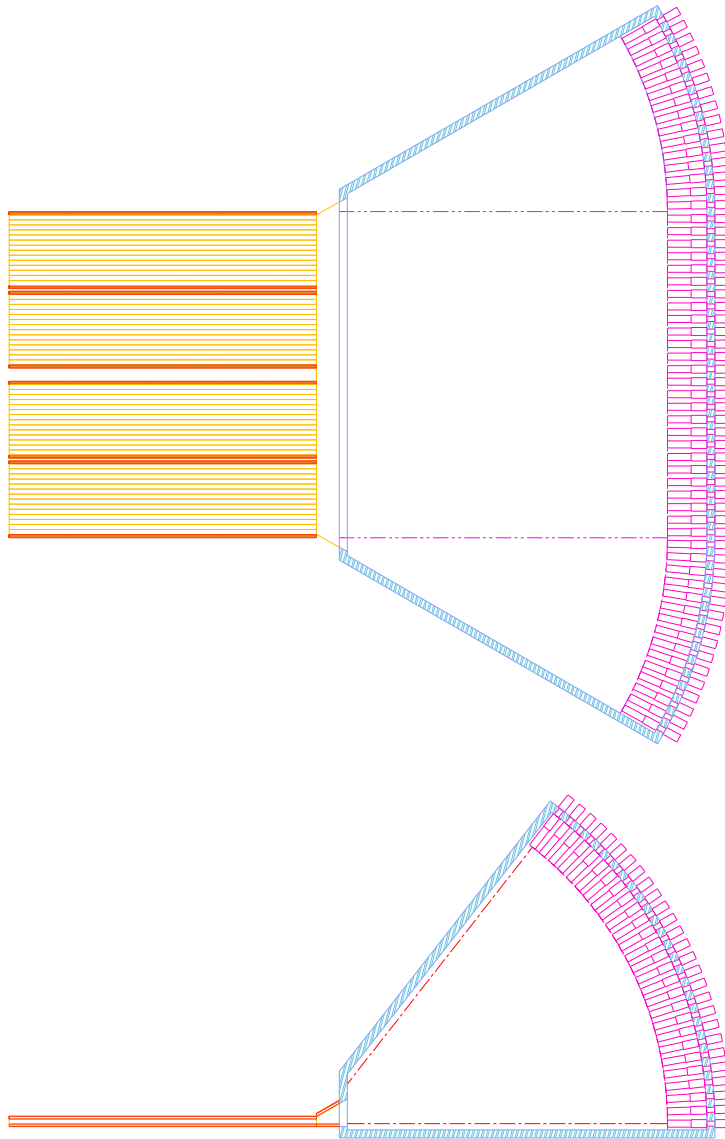


Figure 4.78: The readout side of the bars. The volume will be filled with water and the photomultiplier tubes will be immersed in the water as in the BABAR DIRC.

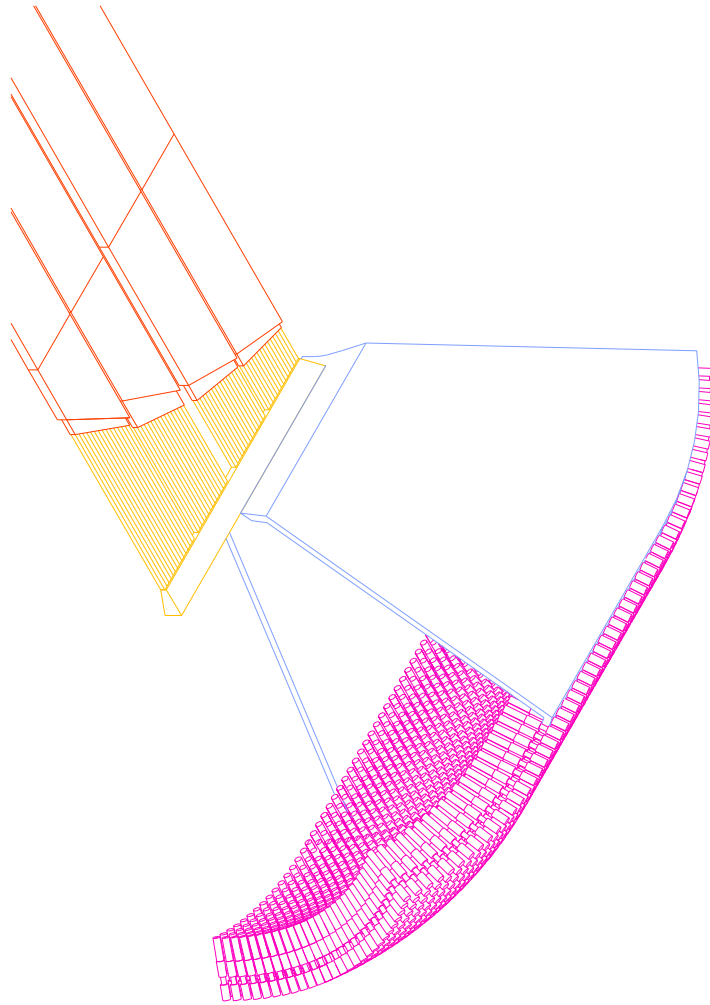


Figure 4.79: A 3-D view into the four half open bar-boxes and the readout tank.

The Gas Čerenkov Counter System

TOF measurements alone will not provide particle identification above $3 \text{ GeV}/c$, and thus TOF does not suffice for typical reactions of interest. Therefore a threshold Čerenkov detector has been included in the HALL D design. The primary function of this detector is to signal the presence of pions over a large part of the expected momentum range (see Figure 4.80).

Several radiator materials have been considered for the design. A pressurized gas radiator has the advantage of allowing one to match the index of refraction to the desired momentum range. A prototype of such a detector was developed for CLEO-III [95]. However this method requires the use of thick gas containers in the downstream detector region. This results in unwanted photon conversions and hadronic interactions, as well as safety concerns. Two atmospheric-pressure radiators were found to produce high acceptance rates: aerogel ($n = 1.008$), and C_4F_{10} gas ($n = 1.00153$). The C_4F_{10} gas radiator has been chosen for HALL D because it has a threshold momentum of $2 \text{ GeV}/c$ for pions, which complements the TOF system's useful range of $3 \text{ GeV}/c$ and below. The kaon threshold of $9 \text{ GeV}/c$ in this gas is nicely above the momenta that will be encountered in the experiment, overlapping less with the TOF system.

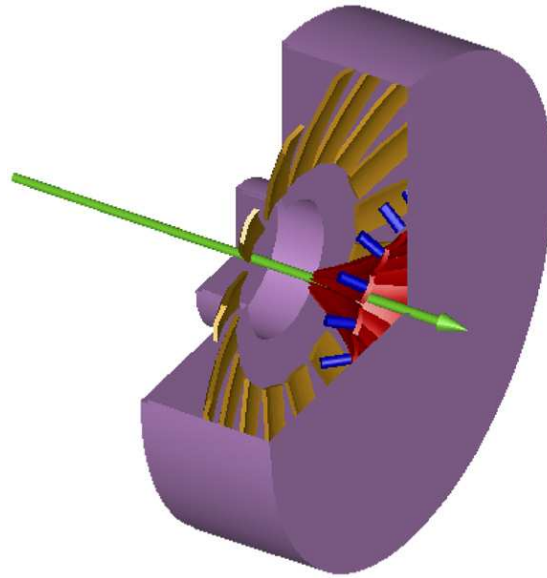


Figure 4.80: A schematic drawing of the HALL D Čerenkov detector system. The particles enter from the left into the gas volume in the center. The Čerenkov light is then reflected off the mirrors in the center (shown in dark) into the phototubes at the outer rim (shown as dark cylinders).

Gas-filled Čerenkov detectors have been used in many particle physics experiments. The original LASS spectrometer [26] used a freon radiator in a design similar to the one in HALL D. The primary changes we will make in the LASS design are the use of an environmentally friendly gas (freon is no longer available) and mirrors made of low-density carbon-fiber composite materials. The gas handling system will be patterned after a similar system now in use on the JLab CLAS spectrometer. The detector will be segmented into sixteen azimuthal regions, each housing a single mirror that focuses light onto its own photomultiplier tube. Light emitted into the region within 10 cm of the beam axis will not be collected in order to suppress accidental coincidences in the detector. A sketch of the optical design is shown in Figure 4.80. The minimum radiator thickness encountered by a particle traversing the detector is approximately 90 cm . The measured performance of the JLab CLAS Čerenkov detector was used to estimate the photoelectron yield of the HALL D design, adjusting for radiator length and the number of mirror reflections. This results in an expected average yield of 5.0 (3.3) photoelectrons for 5.0 (2.9) GeV/c pions.

Particles that traverse thicker regions of the detector will register proportionately larger signals.

The optical design of the detector (two ellipsoidal mirrors) was chosen to produce a strong focus at the photomultiplier tubes. This produces small linear magnification and allows good light collection from the wide range of particle trajectories exiting the solenoid. Prototype mirrors were constructed and tested for their focal properties. These were found to be mechanically and optically stable after cutting to shape. Having two mirrors in the design also offers flexibility as to the placement of the photomultipliers. This freedom was used to place the axis of the tubes perpendicular to the ambient magnetic field. This was done to optimize the effectiveness of the passive magnetic shields surrounding the photomultipliers.

A finite-element analysis of the shielding requirements was performed with the FLUX-3D computer code. A four-layer shield with axial symmetry was found to produce adequate reduction in the magnetic field. The predicted transverse field at the photocathode is less than 0.1 gauss. Burle 8854 photomultipliers were chosen for their high detection efficiency and low noise level.

A Monte Carlo simulation of the Čerenkov detector efficiency was made for the events in the following reaction:

$$\gamma p \rightarrow X p \rightarrow K^* \bar{K}^* p \rightarrow K^+ \pi^- K^- \pi^+ p \quad (4.23)$$

The geometry, mirror reflectivity, kinematics and photomultiplier response were modeled in the simulation, which yielded the detector efficiency as a function of pion momentum (see Figure 4.81).

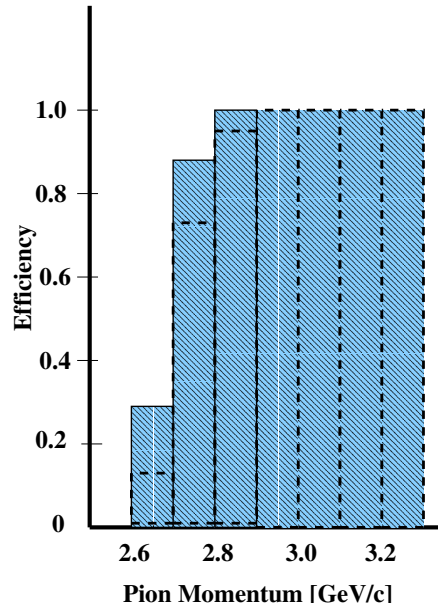


Figure 4.81: Predicted pion detection efficiency as a function of average pion momentum. The solid histogram is for a one-photoelectron detection threshold and the dashed line is for a two-photoelectron threshold.

4.5.4 Acceptance of The Particle Identification System

Since each of the particle identification subsystems works most effectively in different regions of momentum and different regions of particle production, and since no subsystem alone can provide particle identification for all the events necessary for GLUEX analyses, it is crucial to integrate the information from the different subsystems in the most effective way possible. An algorithm based on assigning likelihoods to different particle hypotheses using information from all the relevant subsystems is one natural and straightforward way to proceed.

Given a track with a measured momentum, the basic idea is to use information from the different particle identification elements (dE/dx from the CDC, times from the BCAL and forward TOF, and Cerenkov photoelectrons or Cerenkov opening angle) to assign this track a set of likelihoods, each likelihood corresponding to a different particle hypothesis. For example, $L(\pi)$ and $L(K)$ are the likelihoods a given track is a pion or a kaon, respectively. Once these likelihoods are known, a statistical test can be performed to discriminate between hypotheses. One of the most convenient tests, the likelihood ratio test, works by forming the χ^2 statistic $R(i)$ for each particle hypothesis i ($i = \pi, K, p$):

$$R(i) = -2 \ln \frac{L(i)}{L(\pi) + L(K) + L(p)}. \quad (4.24)$$

Making the requirement

$$R(i) > 2.7 \quad (4.25)$$

rejects hypothesis i at the 90% confidence level.

This method lends itself well to the GlueX environment since separate likelihoods can be calculated for each subdetector individually and then combined into overall likelihoods. For example, the likelihood a given track is a kaon is computed from individual detector likelihoods as:

$$L(K) = L^{CDC}(K)L^{BCAL}(K)L^{CKOV}(K)L^{TOF}(K). \quad (4.26)$$

To illustrate how likelihoods are calculated for specific detector elements, consider the forward TOF system. Start with a track with measured momentum p . The expected time required for this particle to traverse a distance L from the target to the TOF wall can be calculated under different assumptions for the particle mass:

$$t_i = \frac{L}{c} \left(\frac{m_i^2}{p^2} + 1 \right)^{\frac{1}{2}}, \quad (4.27)$$

where $i = \pi, K, p$. This time will have an associated error σ_i , which can be obtained by combining the inherent resolution of the scintillator and electronics (≈ 70 ps) with the effects of momentum resolution and the uncertainty in the path length. Assuming the time measurement follows a gaussian distribution, the likelihood for hypothesis i is then:

$$L^{TOF}(i) = \frac{1}{\sigma_i \sqrt{2\pi}} \exp \frac{-(t - t_i)^2}{2\sigma_i^2}, \quad (4.28)$$

where t is the measured time the particle spent between the target and the TOF wall. The closer the measured time t is to a calculated expected value t_i the more likely the particle being considered is of type i . Likelihoods for the other detectors are calculated in a similar way, using predicted and measured dE/dx for the CDC, predicted and measured time at the BCAL, and the expected and observed numbers of photoelectrons in the gas Cerenkov (or the predicted and measured Cerenkov angle in a DIRC detector).

A simulation of the integrated GlueX particle identification system using the likelihood methodology was carried out for $\gamma p \rightarrow K^* \bar{K}^* p$ events. The properties of these events have already been described at the beginning of this chapter (see figures 4.57 to 4.60). The generated events were sent through a full GEANT simulation and hits were recorded at each of the subdetectors associated with particle identification.

Relevant track measurements were smeared at each subdetector according to their expected resolutions. The dE/dx measurement of the CDC was smeared by 10%; the time of flight at the BCAL by 250 ps; and the time of flight at the forward TOF wall by 70 ps. In addition, the momentum and path length of each track was perturbed randomly by 1% to simulate uncertainties in the tracking. For the simulation using the Gas Cerenkov option (CKOV), the generated number of photoelectrons were distributed according to a Poisson distribution with an 80 cm C₄F₁₀ radiator length with index of refraction $n = 1.0015$ and efficiency $N_0 = 90 \text{cm}^{-1}$ (see equation 4.17). The Cerenkov opening angle of the DIRC option was smeared by its estimated

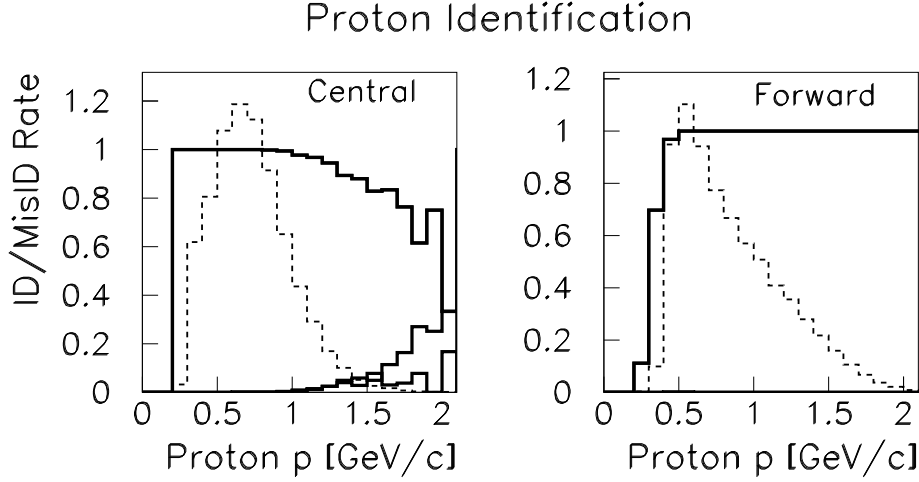


Figure 4.82: The acceptance of proton tracks in the reaction $\gamma p \rightarrow K^* \bar{K}^* p$. The left plot shows central tracks and the right plot shows forward tracks. The top curve is the correct identification rate; the bottom is the misID rate. The starting momentum spectra for proton tracks in the central or forward regions are shown in the background.

resolution, 2.1 mrad. The particle separations in numbers of sigma versus momentum using these parameters were shown previously (figures 4.58 to 4.60).

Likelihoods were then calculated for each track at each detector and combined into total likelihoods according to the method described above. Particles were identified by rejecting hypotheses at the 90% confidence level, as prescribed in equation 4.24. A particle is called a pion if the kaon hypothesis is rejected and the pion hypothesis is not rejected:

$$R(K) > 2.7, R(\pi) < 2.7.$$

Similarly, a particle is identified as a kaon if:

$$R(\pi) > 2.7, R(K) < 2.7.$$

Finally, to find protons, both the pion and kaon hypotheses must be rejected, but the proton hypothesis is not rejected:

$$R(\pi) > 2.7, R(K) > 2.7, R(p) < 2.7.$$

This is perhaps the most basic algorithm possible for this situation. Certainly improvements could be made, such as incorporating strangeness conservation.

The results of this exercise can now be studied in several different pieces. Case 1(CDC) and case 2(CDC,BCAL) tracks are referred to as “central” (see figure 4.57); case 6(CKOV,TOF) and case 7(CDC,CKOV,TOF) tracks are “forward.”

First consider proton identification. Figure 4.82 shows a nearly perfect proton identification rate for both the central region and the forward region; there is a drop in efficiency for central tracks above 1 GeV/c, but it has little effect on the overall identification rate. In addition, only a small fraction of tracks are misidentified.

Next, pion and kaon identification rates in the central region of the deceptor are shown in figure 4.83. Tracks less than 1 GeV/c are identified reliably; above that the efficiency drops to around 60%. Higher momentum central tracks are relying entirely on dE/dx information from the CDC in the relativistic rise region. With a dE/dx resolution of 10% this should be achievable

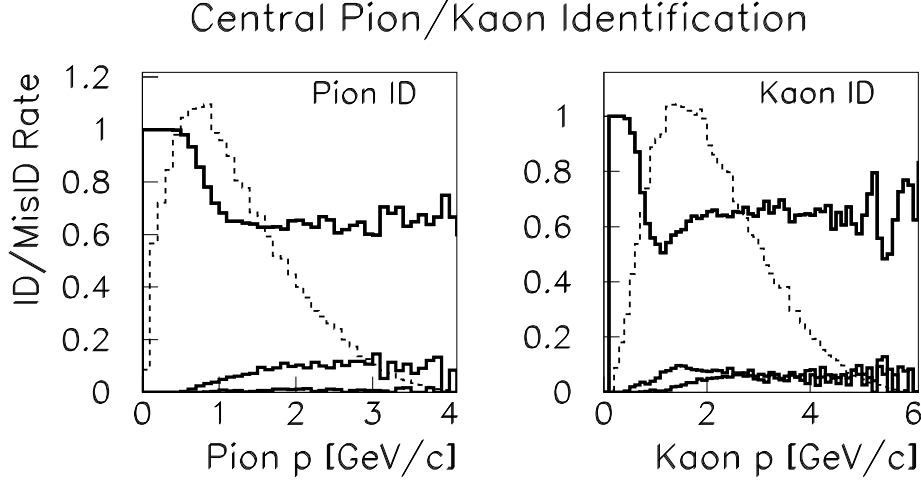


Figure 4.83: The acceptance of pions and kaons in the central region of the detector. The left plot is for pions; the right for kaons. The histograms in the background are the starting momentum spectra for pions and kaons in the central region. Each plot shows the identification and misidentification rates.

	π	K	p
Starting Number	50368	43665	62581
ID Rate	76.4%	64.0%	99.2%
MisID Rate	5.6%	10.1%	0.6%

Table 4.9: Particle identification in the central region for $\gamma p \rightarrow K^* \bar{K}^* p$ events. The statistics are for case 1(CDC) and case 2(CDC,BCAL) tracks. The starting number is the number of π , K , or p in the central region out of 100,000 total events generated.

at the 2σ level (also see figure 4.59). Table 4.9 tabulates all the particle id results for central tracks.

Results for tracks in the forward region of the detector are shown in figure 4.84. The top two plots use the gas Cerenkov option. Notice the drop in efficiency between 2 and 3 GeV/c where the momentum is too high for the TOF wall to be effective, but still not high enough to reliably measure photoelectrons from pions in the Cerenkov detector. The DIRC option solves this problem; its results are shown in the bottom two plots. Table 4.10 summarizes the efficiency numbers of forward tracks under the two different Cerenkov options. Finally, the central and forward cases are combined into overall pion and kaon identification rates in figure 4.85. The overall rates are tabulated in table 4.11.

	Gas Option			DIRC Option		
	π	K	p	π	K	p
Starting Number	38793	38789	30267	38793	38789	30267
ID Rate	94.4%	91.4%	99.1%	98.6%	90.3%	99.2%
MisID Rate	1.5%	4.8%	0.02%	0.3%	2.0%	0.8%

Table 4.10: Particle identification in the forward region for $\gamma p \rightarrow K^* \bar{K}^* p$ events. The statistics are for case 6(CKOV,TOF) and case 7(CDC,CKOV,TOF) tracks. The starting number is the number of π , K , or p in the forward region out of 100,000 total events generated.

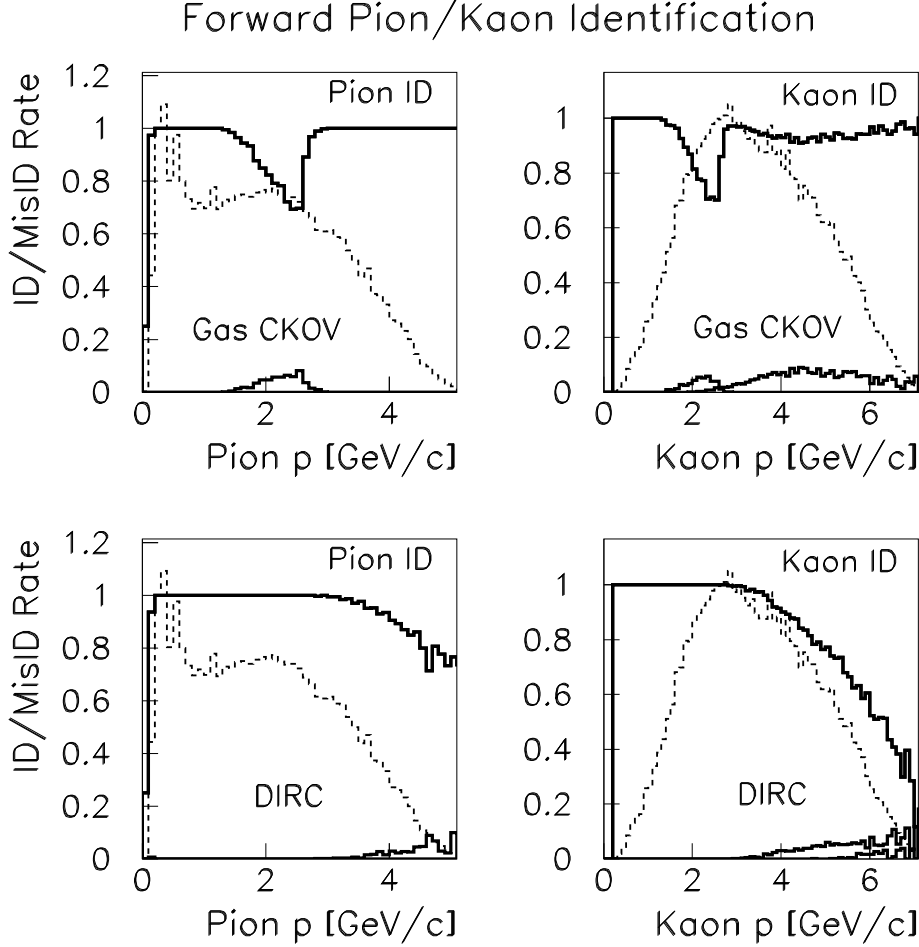


Figure 4.84: The acceptance of pions and kaons in the forward region of the detector. The top two plots are for the gas Cerenkov option; the bottom two are for the DIRC option. The left plots show pions; the right kaons. The histograms in the background are the starting momentum spectra for pions and kaons in the forward region. The curves in each plot represent the identification and misidentification rates.

	Gas Option			DIRC Option		
	π	K	p	π	K	p
Starting Number	100000	100000	100000	100000	100000	100000
ID Rate	80.4%	71.2%	94.3%	82.9%	71.9%	94.7%
MisID Rate	3.5%	6.8%	0.4%	2.9%	5.3%	0.8%

Table 4.11: Overall particle identification for the reaction $\gamma p \rightarrow K^* \bar{K}^* p$. The statistics are for all track cases.

It should be remembered that one of the crucial design parameters of the GLUEX experiment – in addition to, and perhaps more important than, the total efficiency numbers – is the uniformity of acceptances in the angles that will be used in Partial Wave Analyses. Efficiencies based on identification rates for the Gottfried-Jackson $\cos\theta$ angle of the $K^* \bar{K}^*$ system are shown in figure 4.86. This acceptance rises at $\cos\theta \approx \pm 1$ and falls at $\cos\theta \approx 0$ for the gas Cerenkov

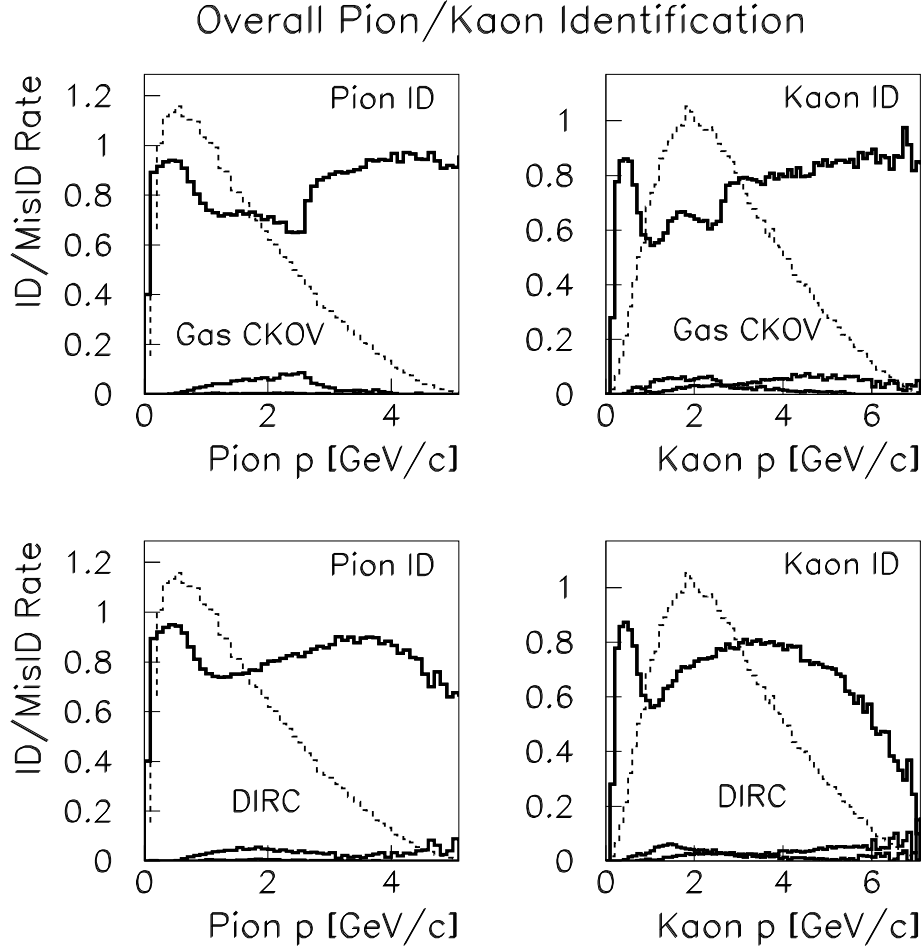


Figure 4.85: The overall acceptance of pions and kaons in all regions of the detector in the reaction $\gamma p \rightarrow K^* \bar{K}^* p$. The top two plots are for the gas Cerenkov option; the bottom two are for the DIRC option. The left plots show pions; the right kaons. The histograms in the background are the overall starting momentum spectra for pions and kaons. Each plot shows the identification and misidentification rates.

option for the following reason. When $\cos\theta$ is near its extremes, the final state particles are typically divided into high momentum (along the decaying resonance direction) and low momentum (against the decaying resonance direction) cases. The high momentum tracks are above pion threshold and are identified by the gas Cerenkov system; the low momentum tracks are effectively identified by the TOF wall. On the other hand, when $\cos\theta$ is near zero, final state tracks tend to fall in the momentum region where neither the TOF nor the gas Cerenkov is effective.

The DIRC option avoids this problem. Consequently, the $\cos\theta$ acceptance of the second plot of figure 4.86 is significantly more uniform.

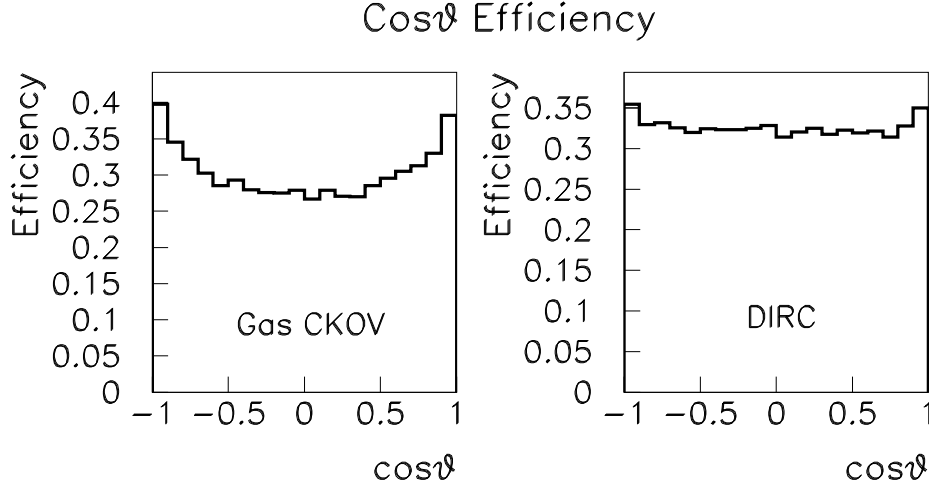


Figure 4.86: Angular efficiencies for $\cos\theta$ in the Gottfried-Jackson coordinate system for $\gamma p \rightarrow K^* \bar{K}^* p$ events. The left plot is for the Cerenkov option, the right for the DIRC option.

4.6 Detector Integration

The assembly and integration of each of the detector subsystems into the GLUEX detector requires careful coordination and attention to many diverse issues. The magnetic field configuration outside the magnet dictates the location and orientation of standard PMTs and/or use of high field devices such as HPMTs and SiPMs. The field distribution can be affected by magnetic materials used for support structures such as iron and, therefore, care must be taken in choosing common materials for the various support systems. The magnetic field in the vicinity of the Čerenkov counter is estimated to be approximately over 1 kG at the location of the readout devices and between 0.300 kG and 0.160 kG at the position of the PMTs for the forward LGD. The mounting and assembly of detectors must allow for the delivery of services required for their

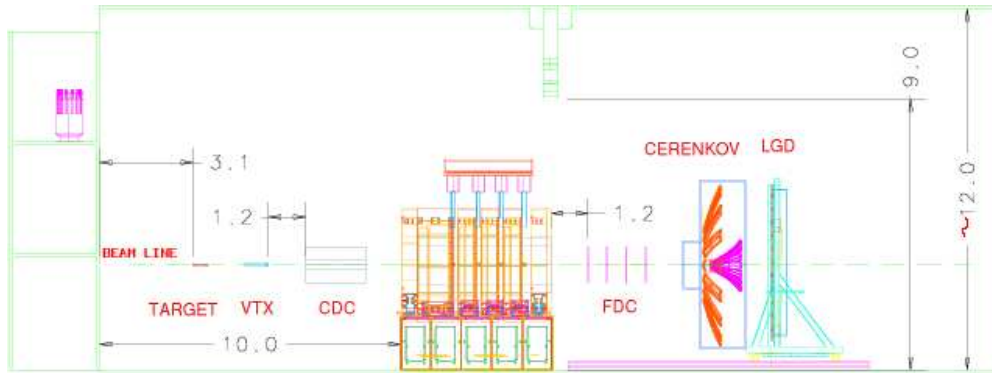


Figure 4.87: Exploded view of detector showing the detector subsystems in their extracted positions. The magnet does not move and detectors are inserted both from upstream and downstream into their nominal positions for normal operation.

operation, including cryogenics, cooling, electrical power, ventilation, gas connections, high voltage and signal and monitoring cables for all detectors. Moreover, access to each sub-system must be facilitated for purposes of maintenance or repair.

The detector sub-systems are shown in Figure 4.1 while the general layout of HALL D with all detectors extracted is shown in Figure 4.87. As the detector will need to be in its extracted position for both installation and servicing, it is important that its layout in the HALL D building accommodate access to the detector. Figure 4.88 shows a sketch of the detector in HALL D. The cryogenic connections to the solenoidal magnet are brought in from the north-west corner of the building, opposite the ramp used for truck access. This permits a large staging area in front of the door and minimal blocking of crane movement by the cryogenic lines. These lines can also be used to feed other cryogenic systems such as the liquid hydrogen target and potentially VLPCs used in the start counter. Gas lines from external mixing systems can also be run along this common path to minimize obstructions for crane and assembly operations.

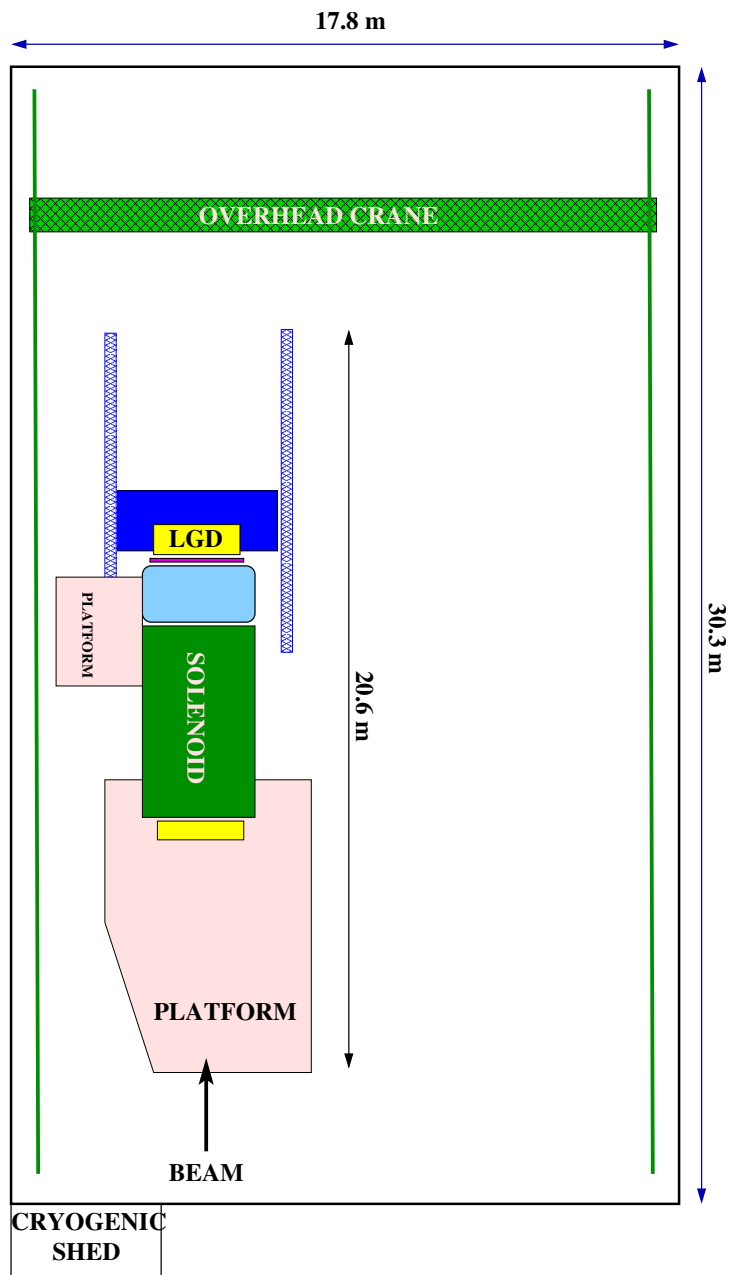


Figure 4.88: Plan view of the GLUEX experiment in HALL D.

Electrical power will be most likely delivered in trenches in the floor from breaker panels located on the north wall of the building. Clean power will be provided to detector electronics using isolation transformers as close to the detector as possible. As an example, the estimated power consumption of the forward calorimeter is 30 KW. All detector frames will be connected to the building ground network both for safety and to minimize electrical noise.

In terms of installation, most of the detector is fairly open and can be quickly accessed with minimal disruption of operations. However, the limited space inside the solenoidal magnet deserves special attention. This space contains the BCAL and its support structure, the Straw-tube Chamber, CDC, the Forward Drift Chambers, FDC, and the structures which both align and support these chambers as well as the mechanisms for extracting them. Finally, inside the CDC is space for the liquid hydrogen target, the beam pipe and the Start counter. Space allocation also needs to be made to assure that signals cables can be brought out from the detectors, while voltage and monitoring cables as well as gas, cryogenics and cooling lines can be brought to the appropriate detectors. Table 4.12 shows the radial space allocation inside the solenoid. The spaces labeled *keep out* are reserved for support, installation structures, signal and power cables, and other necessary services to the detectors such as gas and cooling.

Detector Name	r_{min}	r_{max}
Solenoid	92.7 cm	
Keep Out	90 cm	92.7 cm
Barrel Calorimeter	65 cm	90 cm
Keep Out	59 cm	65 cm
Straw Tube Chamber	13 cm	59 cm
Forward Drift Chambers		59 cm
Keep Out		12 cm

Table 4.12: A radial space allocation map for the space inside the GLUEX solenoid.

4.6.1 Assembly and Mounting

As much of the GLUEX detector will need to be assembled in HALL D, the construction of the building is critical to any time line of the experiment. It is absolutely necessary that JLab do everything possible to guarantee early construction of this building. Once the building can be occupied, the assembly of the detector can begin. The first item will be the solenoidal magnet. It is transported in sections and will need to be re-assembled inside HALL D. It is also expected that both the BCAL and the LGD calorimeters will be assembled in HALL D. The assembled LGD will not fit through the door. It is also possible that parts of other detectors would be assembled in the HALL D building as well.

Of all the in-hall assemblies, the BCAL is likely to be another time line bottle neck. The time from start of construction until delivery at JLab is estimated at three years, but it is likely that the detector would arrive in several shipments spread out over the 3-year time frame. There are currently two possible assembly scenarios. The first follows what was done with the KLOE detector. This would have the BCAL being assembled inside the solenoid. The draw back to this plan is that the assembly of th BCAL cannot begin until the solenoid is fully installed. A second scenario would be to assemble the BCAL in a vertical orientation outside the solenoid, and then rotate it to horizontal and roll it into the solenoid as a single unit. This latter scenario both allows assembly to proceed in parallel with the solenoid and requires less service space between the outside of the BCAL and the inside of the solenoid. In both scenarios, the BCAL would be held in place with bolts that come through ring girders in the gaps between the magnet coils. These would connect to the 2.5 cm thick Aluminum backing plates on the BCAL modules as shown in Figure 4.89. In both installation scenarios, an assembly and installation jig will need to be designed and built. These options are currently under study by the engineering staff at JLab.

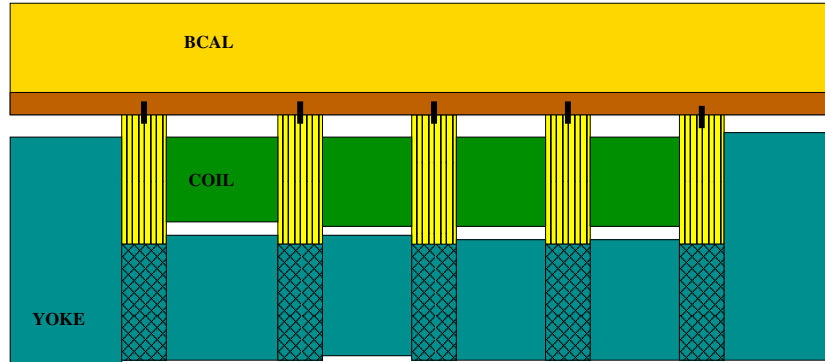


Figure 4.89: The Barrel Calorimeter bolted to the inside of the solenoid.

Once the BCAL has been mounted on the inside of the magnet, only the readout electronics will be accessible. Because of its design, it is anticipated that once it has been installed, it will not be removed. If for some reason it became crucial to replace a module, a fairly extensive down time would need to be scheduled. However, given that there is nothing that can be serviced except for the readout electronics, such an event is considered highly unlikely over the lifetime of the experiment. Finally, to facilitate the installation of the tracking devices inside the solenoid, we anticipate placing a protective cover over the inner face of the BCAL. This will both protect the calorimeter and provide a surface to which the chamber supports can be mounted.

After the BCAL has been mounted in the solenoid, it will be necessary to install a pair of rails along the length of the detector. These rails will be used to support the CDC and FDC packages. Extensions can be added to allow for installation and extraction of the chambers. There is some possibility of the lead in the barrel calorimeter settling slightly over time. While we are currently investigating this, we also recognize that the rails will need to be fitted with bearings that have some play to prevent things from locking up due to small shifts in the *bed rock*. Both because of the difficulty of maintaining precision alignment between two rails over the 4 m length of the magnet and the possibility of settling in the BCAL, we anticipate no more than one precision rail, with the 2nd rail being used for load bearing.

The CDC will be inserted from the up-stream end of the magnet, while FDC will be inserted from down-stream end. On the down-stream end, the Čerenkov, TOF and LGD detectors will be rolled back to make room for the FDC packages. On the up-stream end, the UPV will need to be put in place after the CDC has been installed. Then the START counter and target will be inserted into the CDC from the upstream end. They will be mounted on an independent cantilever system.

The Čerenkov counter and forward calorimeter will be mounted on independently movable support frames which can be moved in and out of their nominal location for access to the FDC. The TOF detectors will be mounted on the frame for the forward calorimeter. Each support structure will be self-contained, including electrical power and the appropriate readout electronics. Access platforms will be provided to allow easy access to the PMTs and readout electronics.

4.6.2 Survey and Alignment

In order to achieve the physics goals of the experiment, a system must be devised that can measure and maintain at least $100\ \mu\text{m}$ relative alignment of all of the tracking packages inserted into the magnet. The locations of the drift chamber wires relative to each other and the magnetic field are the most critical alignment tasks for the experiment. In addition, for ease of maintenance, the positions of the chambers should be either reproducible at that level, or a system needs to be established that can easily survey them into position at this accuracy. It will also be important to have an on-line monitoring system in place to dynamically correct for time dependent shifts in alignment. Such shifts might arise due to settling of the BCAL, thermal expansion and contracting of the chambers themselves, or accidental moving of the chambers when other detectors are being serviced. The collaboration is currently exploring the use of a system used by ATLAS for maintaining alignment.

As the CDC and FDC are inserted from opposite ends of the magnet, the mating and initial alignment are blind. The z positions of these chambers can be accurately registered at a single point by surveying in stops along the guide rail. We will also need a remote adjustment system that allows for correction of possible *pitch*, *roll* and *yaw* of the chamber packages.

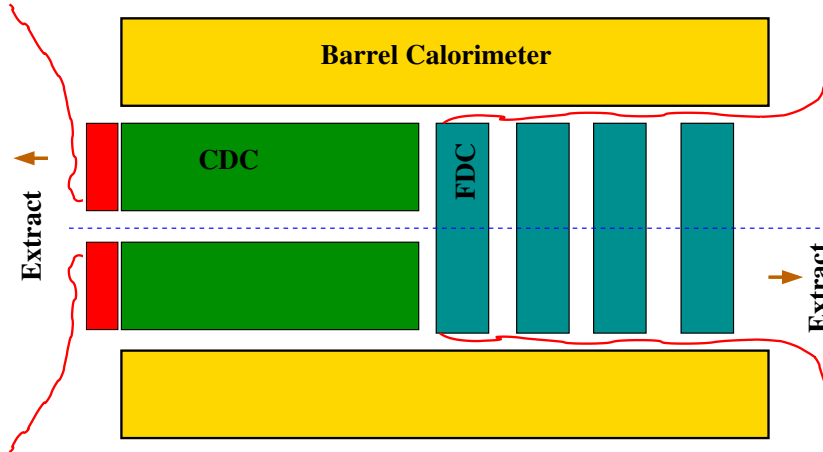


Figure 4.90: The insertion of the Central and Forward Tracking chambers inside the Barrel Calorimeter.

4.6.3 Access

Ease of access to the detector for maintenance ensures short commissioning and debugging times. Our goal is to allow maintenance of all detector components in less than one day. In order to maintain or check the upstream BCAL readout, the UPV will have to be removed and the service platform must be designed in a way to allow access to readout both above and below the horizontal scattering plane of the detector. To service the CDC, the UPV, the target and START detectors must be moved out of the way. All serviceable elements are located on the up-stream end of the CDC. To access the FDC and/or the downstream BCAL readout, the Čerenkov and forward calorimeter must be moved on their rail systems, as shown in the exploded view in Figure 4.87. Service to the FDC is likely to be the most involved operation. Once the downstream detector packages are moved out of the way, a support structure will need to be craned in, and the chambers extracted from the solenoid.

The readout electronics for all the systems will be accessible without having to move any detector component. The PMTs for the Čerenkov, TOF and LGD will be accessible by at most moving the forward calorimeter carriage. Access to the LGD enclosure will in principle be easy, but radiation levels must be measured and deemed to be at a safe level prior to any access.

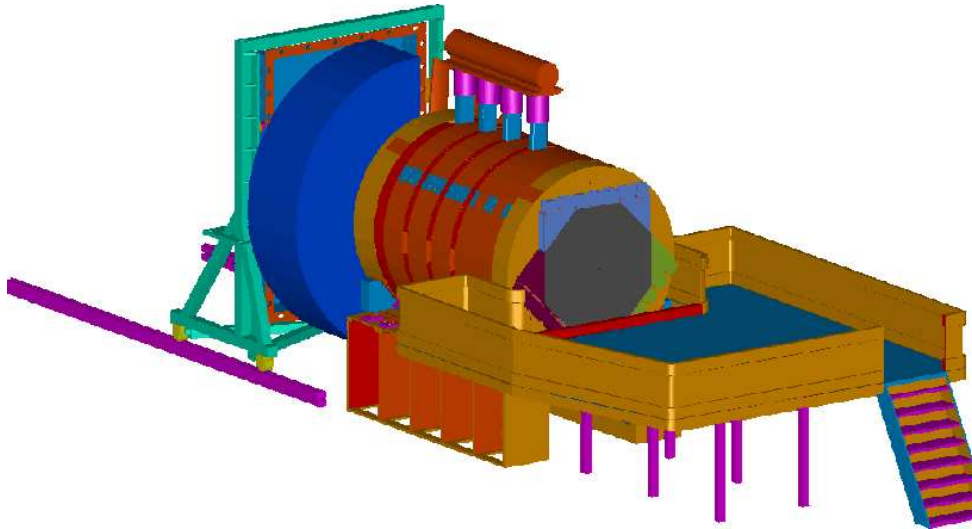


Figure 4.91: Detector and upstream platform for service of the inner detector packages.

4.6.4 Interaction Between Subsystems

The detectors in the forward direction (Čerenkov, TOF and LGD) are relatively isolated mechanically and operate independently of other systems. The detectors inside the magnet, however, are in close proximity and mounted on the same mechanical frames that are anchored on the BCAL and/or the solenoid. Therefore, cabling, power consumption, and access for maintenance must be coordinated carefully.

4.6.5 Cabling

All detector electronics will be located near the detector itself. This will minimize cable lengths and eliminate the need for large cable runs from the detector to electronic racks far from the detector. The racks of electronics servicing the inner detectors will be located on a platform upstream of the magnet with ample space for access. A possible *Access Platform* is shown in Fig.4.91 with the primary aim being that detectors can be operated both inside and outside the solenoid without making any disconnections. This implies that either the cabling for START detector, CDC and FDC will have enough slack so that they can be moved in or out of the magnet without any disconnections, or that the electronics will themselves move along with the detector elements. It is crucial that the detectors can be operated in the extracted position for testing and the installed position during normal operation without wiring changes.

Chapter 5

Readout Electronics

5.1 Overview

The goal of the GLUEX readout electronics system is to digitize and read out the detector signals for level 1 trigger rates of up to 200 kHz without incurring deadtime. A pipelined approach is required. The digitized information will be stored for several μs while the level 1 trigger is formed. Multiple events must be buffered within the digitizer modules and read out while the front ends continue to acquire new events.

A summary of the GLUEX detector subsystems from an electronics viewpoint is shown in figure 5.1.

Two basic types of readout electronics will be used in GLUEX, FADCs and TDCs. Detectors which measure energy will be continuously sampled with flash ADCs while detectors which require precise time measurements will use a multi-hit TDC. No currently available commercial solutions exist. These boards will be designed by our collaboration. Prototypes have been constructed, and are being tested.

The number of channels in the GLUEX detector is not large enough to justify the financially risky development of custom integrated circuits. ICs developed for other experiments will be used as well as commercially available chips. Programmable logic devices will be extensively used for data path, memory, and control functions.

Technology is constantly evolving, and the optimum solution for the GLUEX detector depends on when funding becomes available and the construction schedule. Presented here is a preliminary design which could be implemented with currently available components.

5.2 FADCs for Calorimetry

The calorimeters will be read out with 8-bit, 250 MHz FADCs. The 250 MHz sampling clock will be derived from the 1499 MHz accelerator clock. This sampling rate and bit depth is well matched to the FEU84-3 PMTs used in the Forward Calorimeter, and is adequate for the silicon PMTs used in the Barrel Calorimeter. Additional FADC channels will read out the Photon Tagger, Backwards Veto, Start Counter, Čerenkov Detector, and time-of-flight PMTs.

Figure 5.2 shows an FEU84-3 PMT pulse digitized by the prototype FADC described in section 5.2.1. Note that the sum of the samples from 120 to 180 ns is 1429; for this PMT the 8-bit FADC is equivalent to a 10 or 11-bit conventional charge-integrating ADC. To address resolution concerns, simulations were performed to show that the proposed FADC provides an adequate measurement. Pulses measured with a digital oscilloscope were fitted to determine their functional form. The response of the FADC was simulated using this functional form and the time integral of the function was compared to the summed output of the simulated FADC for many pulses. Since the relationship between deposited energy and pulse height in this type of calorimeter is known, direct comparison of the resolution due to the FADC and the resolution of

Summary of GlueX Detector Subsystems

Detector	Photon tagger	Upstream Photon veto	Start counter	Central drift	Forward drifts	Cerenkov	Time-of-flight	Barrel calorimeter	Forward calorimeter
Type	Scintillator	Scintillator	Scintillator	Straw tube	Planar chamber	Gas	Scintillator	Sci fibers	Lead glass
Energy resolution	0.1% (segmentation)	10%/√E	N/A	20%	N/A	N/A.	N/A	10% @ 1 GeV	3.6% + 7.1%/√E
Channel count	192	20	40	3240	2900 anode 11,400 cathode	40	168	960	2500
Signal source	PMT	PMT	PMT	Straw tube	anode wires cathode strips	PMT	PMT	SIPMT	PMT
Physics signal	100 pe	100 pe	100 pe	25 e	25 e	5 pe	500 pe	100 pe/GeV	250 pe/GeV.
Gain in detector	10 ⁶	10 ⁶	10 ³	10 ⁴	10 ⁴	10 ⁵	10 ⁶	10 ⁵	10 ⁶
Typical charge	16 pC	16 pC	16 pC	40 fC	40 fC anodes 4 fC cathodes	1 pC	80 pC	16 pC/GeV	40 pC/GeV
Preamp gain	no	no	no	10 ³	10 ³ anodes 10 ⁴ cathodes	10 ²	no	no	no
Discrimination	constant fraction	no	constant fraction	no	yes (anode) no (cathode)	no	constant fraction	constant fraction	no
Time resolution	100 ps	1 ns	350 ps	1 ns	1 ns	3 ns	80 ps	200 ps	400 ps
Dynamic range	5	100	100	1000	100 anodes 1000 cathodes	10	10	1000	1000
FADC	8 bits 250 Msps	8 bits 250 Msps	8 bits 250 Msps	10 - 12 bits 125 Msps	Cathodes: 10 - 12 bits 62.5 Msps Anodes: 125 ps	8 bits 250 Msps	8 bits 250 MSPS	8 bits 250 Msps	8 bits 250 Msps
TDC	62 ps	no	62 ps	no	no	no	31 ps	62 ps	no
Level 1 trigger	yes (low rate runs)	no	track count	no	no	no	track count	track count	energy sum

Figure 5.1: Detector subsystems

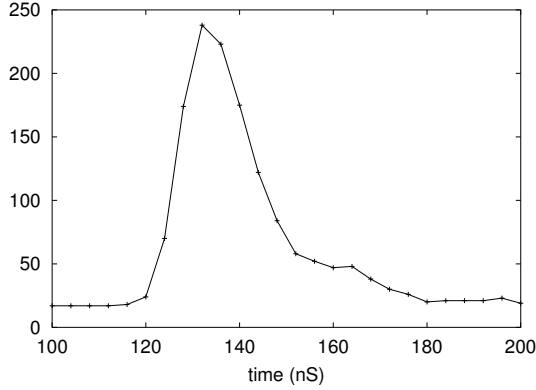


Figure 5.2: Digitized FEU84-3 pulse.

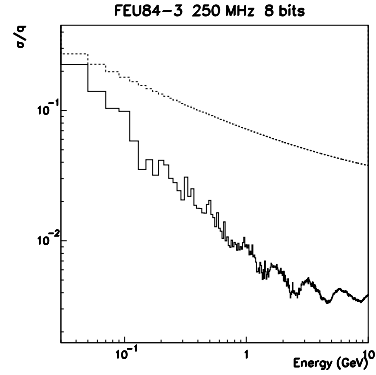


Figure 5.3: Dashed - calorimeter resolution, Solid - FADC resolution.

the calorimeter is possible. Figure 5.3 shows the result of this comparison. Clearly, above 0.15 GeV the resolution of the FADC is small compared to the intrinsic resolution of the calorimeter.

The FADCS will also give a measurement of the time a photon arrived at the calorimeter. Previous work [96, 97] indicates that a time resolution better than the FADC sampling interval can be achieved by fitting the FADC waveform. To study how well this time could be determined a “library” of pulses from phototubes of the type to be used was created using a digital oscilloscope with a 2.5 GHz sampling frequency. The leading edge of these sampled pulses were fitted to a 9th order polynomial to determine the location of various “features” of the pulses. The features considered were the time the pulse achieved 10, 25, 50, 75, 90 and 100% of its maximum value. These features carry the arrival time information of the pulses and were used as reference times.

To determine how well the FADC could determine the pulse arrival time, the samples from the digital oscilloscope (2.5 GHz) were averaged over 10 samples (to 250 MHz) and quantized to 8 bits. These transformed samples are what would be expected from the FADC system proposed here. Using only the bin containing the pulse maximum and the two samples preceding it and a simple algorithm, it was found that the 50% crossing time could be determined with a resolution of 160 ps compared to the time determined by the detailed fitting described above. This resolution is sufficient to determine if a pulse is in time with an event (rejecting background) or to determine the time of the event sufficiently well to select the beam “bucket” that initiated the event.

5.2.1 Prototype

A single channel prototype of the calorimeter FADC has been designed and built at Indiana University. A block diagram is shown in Fig. 5.4 and a photo in Fig. 5.5.

A differential amplifier inverts the negative PMT signal and shifts the voltage levels to match the input range of the digitizer integrated circuit. The digitization is performed by an SPT7721 integrated circuit manufactured by Fairchild Semiconductor [98]. This IC costs about US\$20. An 8-bit value is produced internally every 4 ns ; two samples are output every 8 ns (125 MHz).

All digital functions are performed in a Xilinx [99] XC2S50 programmable gate array. This IC costs about US\$10. A dual port RAM configured as a circular buffer stores the data for 8 microseconds. Upon receipt of a trigger signal the data from the time window of interest is copied to an output FIFO which can buffer the data from multiple events. This FIFO is interfaced to a 32 bit, 33 MHz PCI bus. More information on this prototype is available [100].

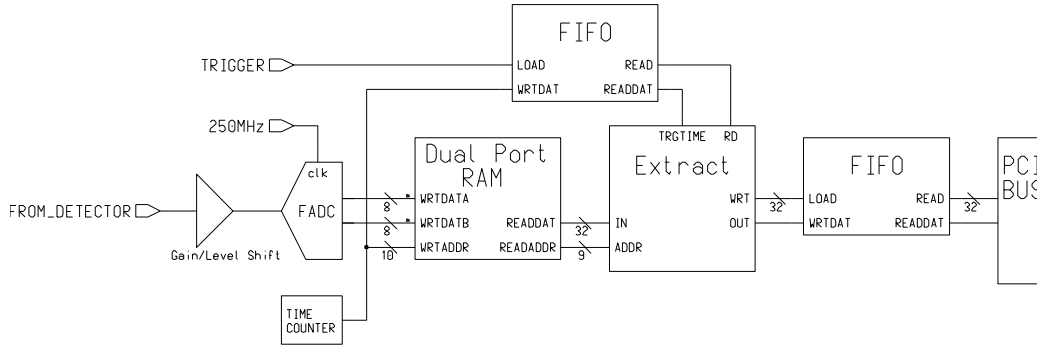


Figure 5.4: Block diagram of prototype FADC board.

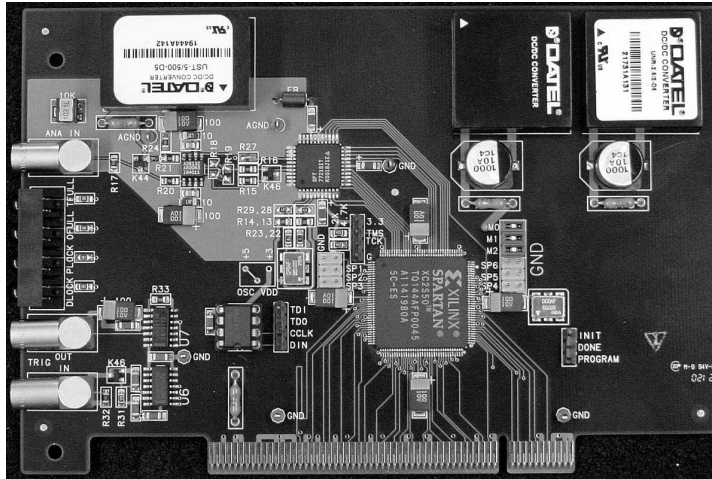


Figure 5.5: Photograph of prototype FADC board.

5.2.2 Additional requirements for final version

The final version of the calorimeter FADC board will include pipelined adders operating at the 125 MHz digitizer output clock which continuously sum the digitized information from all channels on a board. Additional pipelined adders will sum the information from all boards in a crate, and then sum the information from all the crates associated with a detector. The sum of all channels will be passed through a shift register giving a time history. Successive samples within a programmable time window will be summed, analogous to the gate in a conventional charge sensitive ADC. Energy sums from the Forward and Barrel Calorimeters will be used in the level 1 trigger. A block diagram is shown in Fig. 5.6.

Assuming a 100 ns time window, each FADC channel will produce 25 bytes of data per level 1 trigger. In the final version of the FADC we will want to suppress the readout of channels with no data. The FADC data will be processed in real time to provide an energy and time measurement. We believe that the raw FADC data can be reduced to about 10 bytes per channel. This zero suppression and pulse shape processing may be done at the channel level in the gate array, at the board level, the crate level, the detector system level, or in some combination of these levels.

5.3 FADCs for Tracking

The Central Tracking Drift Chamber anodes will be read out with 10 or 12-bit, 125 MHz FADCs. The additional dynamic range is required for the dE/dx measurement. The Forward Tracking

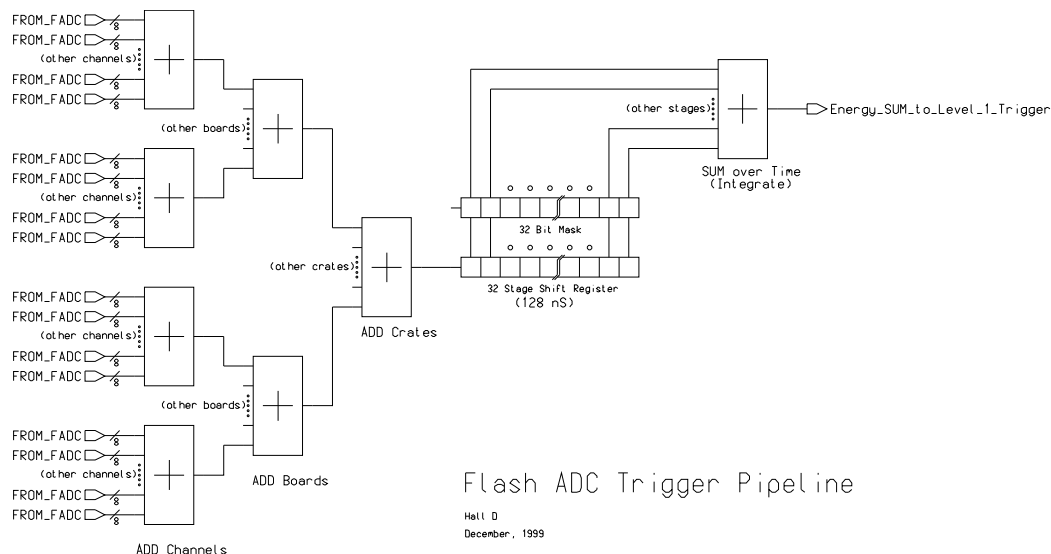


Figure 5.6: Block diagram of energy sum.

Drift Chamber cathodes will be read out with 10 or 12-bit 62.5 *MHz* FADCs. The exact read out electronics requirements for these detectors is the subject of ongoing R&D efforts.

5.4 TDCs

The Photon Tagger, Start Counter, Forward Drift Chamber anodes, Čerenkov Detector, Barrel Calorimeter, and Time of Flight detectors will be read out by multi-hit TDCs.

5.4.1 Jefferson Lab TDC

A high resolution pipeline TDC module has been developed for use at Jefferson Lab. The design is targeted to meet the requirements of current experiments, as well as to serve as a prototype for future experiments at Jefferson Lab, including Hall D. The design is implemented as a VME-64x module. This bus standard was chosen because it is already in use at Jefferson Lab, has good (and evolving) data transfer capabilities, and reasonable channel densities are possible.

The module is built around the TDC-F1 integrated circuit from acam- messelectronic gmbh [6]. The TDC-F1 chip was designed for the COMPASS experiment at CERN [7], and costs about \$130 each in small quantities. The chip utilizes purely digital delay techniques to measure time. In normal mode the TDC-F1 chip provides 8 input channels with resolution of 120 ps (LSB). In high resolution mode channels are combined in pairs to yield a resolution of 60 ps for 4 input channels. The dynamic range for measurement is 16 bits. The resolution of the chip is tunable about its nominal value. A PLL circuit adjusts the core voltage of the chip to compensate for temperature and supply voltage variation, assuring stability of the resolution value. On-chip buffering for input channels, triggers, and output data allows for multihit operation with nearly zero deadtime. The chip also has a complex trigger matching unit that can filter out hits unrelated to the input trigger. When enabled, only hits that are within a programmed timing window and latency from the trigger time are kept. The trigger matching feature is used in common start and synchronous measurement modes. In common start mode, an external start signal resets the internal measurement counter and a delayed trigger signal sets the measurement window. In synchronous mode, an external 'sync reset' signal is used to reset the internal measurement counter and clear internal buffers. Internal start signals are then automatically generated at a programmable rate.

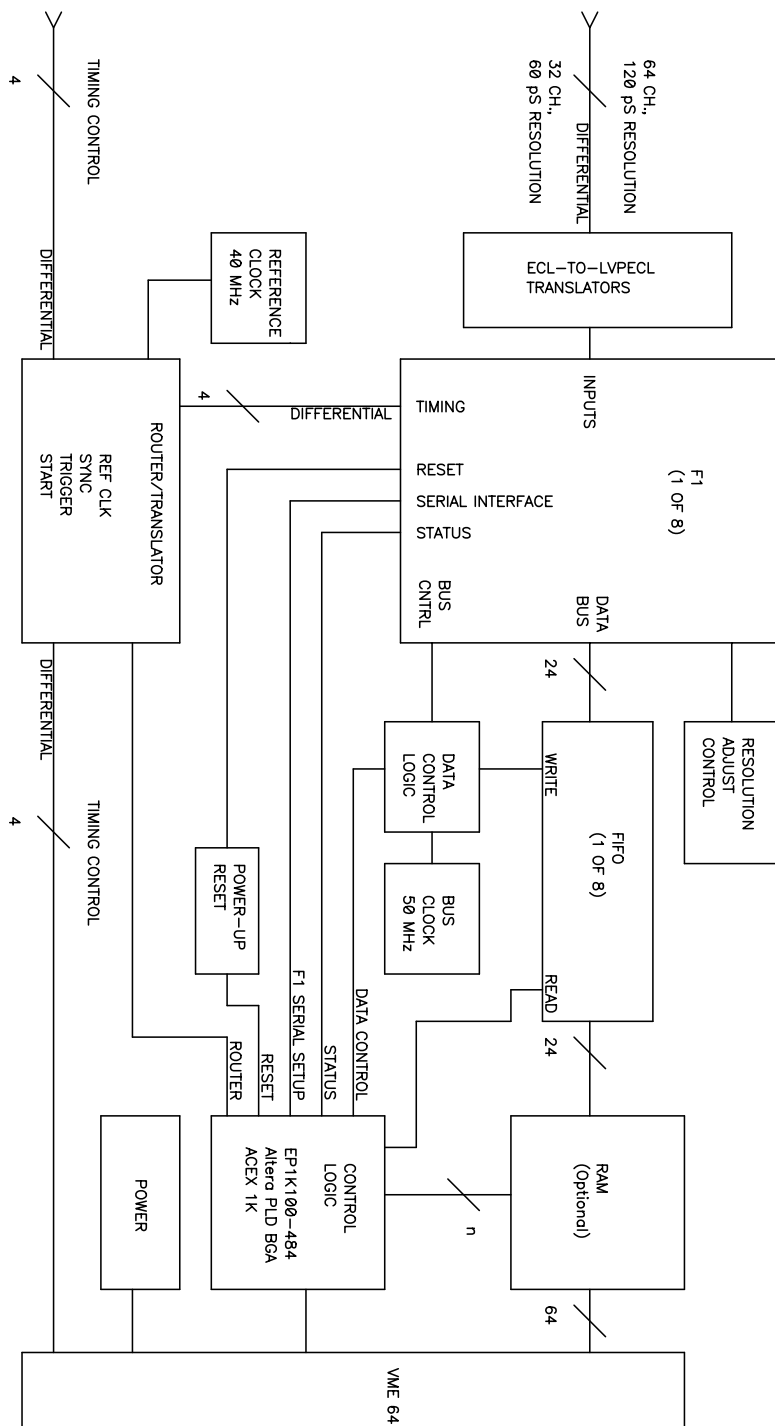


Figure 5.7: Block diagram of TDC board.

Figure 5.7 shows a block diagram of the TDC module. The 8 TDC-F1 chips on the module provide 64 channels in normal mode, or 32 channels in high resolution mode. Front panel input signal levels are differential ECL to be compatible with existing systems a Jefferson Lab. Timing control signals are also available through backplane connections for ease of system integration. A 128K word deep FIFO is attached to each TDC-F1 chip to buffer its output data. In addition, a global 1K word FIFO buffer is implemented within the single FPGA that controls the module.

The external RAM shown in the figure is not present on this version. The module can be set up to interrupt the crate controller after a programmable number of triggers have been received. During read out the module will provide a block of data associated with a programmed number of triggers, and then terminate the transaction. To enhance system performance a set of TDC modules may be read out as a single logical read using a multiblock read protocol. This involves passing a token between modules along a private daisy-chain line. In this setup, only the first module in the chain will generate the interrupt, and only the last module in the chain will terminate the transaction. Configuration parameters for the 8 TDC-F1 chips are stored in non-volatile memory on the module and may be updated by the user. The configuration process is automatic at power up.

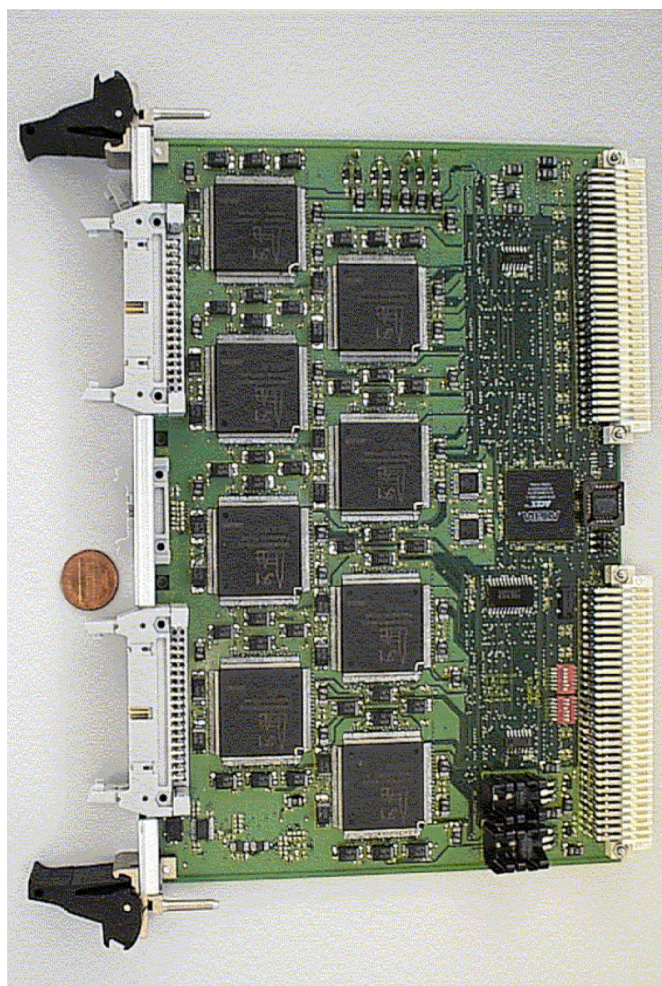


Figure 5.8: Photograph of TDC board.

A photograph of the module is shown in Figure 5.8. Fifty TDC modules have been produced and are currently being installed into Jefferson Lab experiments in Halls B and C.

5.4.2 TDC Performance

Figure 5.9 shows the timing distribution for an input signal that has a fixed time relationship to the start signal. The TDC was operated in high resolution mode. Unfolding the uncertainty of the input signal (33 ps) from the measured distribution yields a TDC resolution (RMS) of 61.2 ps. Figure 5.10 shows the equivalent distribution for a TDC operated in normal resolution mode. The resolution is 86.2 ps. These resolutions were confirmed across the entire dynamic

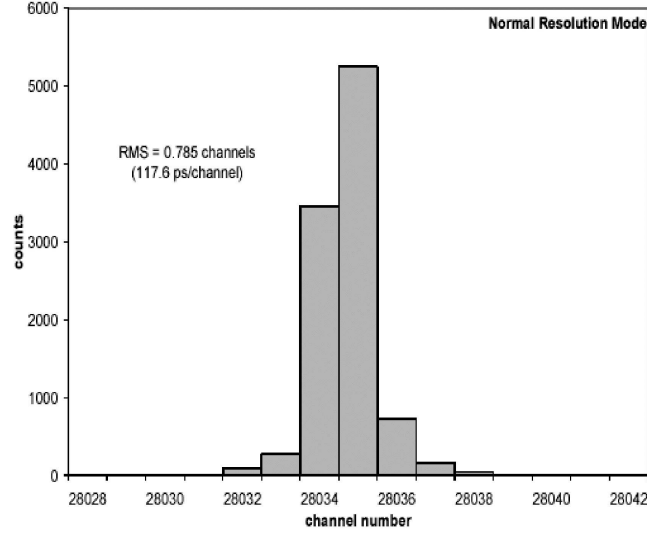


Figure 5.9: TDC performance in low resolution. (resolution=86.2ps)

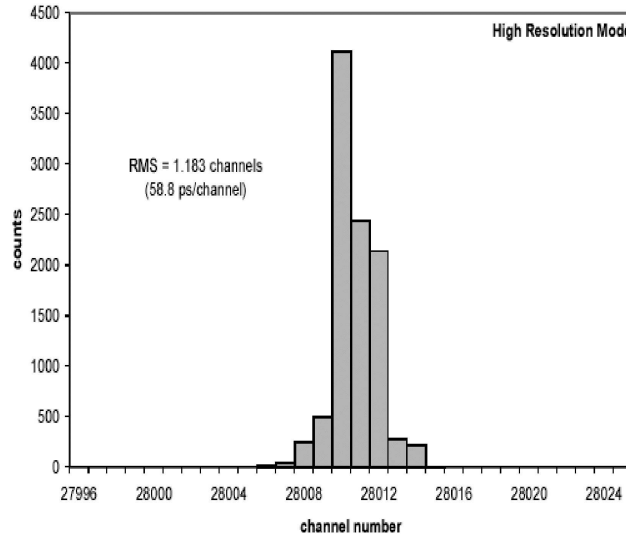


Figure 5.10: TDC performance in high resolution. (resolution=61.2ps)

range of the TDC, and for trigger rates up to 200 KHz. Full crate tests have been performed using the multiblock readout protocol. Sustained data transfer rates of 40 Mbytes/s over the VME bus have been achieved.

5.4.3 Additional requirements for final version

A 62.5 MHz clock phase-locked to the accelerator will be distributed to all TDC modules so that every channel has the same time calibration. With this clock frequency, LSB resolutions will be 125 ps for the standard version and 62.5 ps for the high resolution version.

A commercial TDC module, the CAEN[101]v1290, based on the HPTDC chip developed at CERN, is being evaluated by Jefferson Lab. It might be possible to use this type of TDC to provide 31 ps LSB resolution for the time-of-flight counters.

5.5 Track Count

The Start Counter, Barrel Calorimeter, and Time of Flight detectors will require pipelined adders to implement a track count for use in the level 1 trigger.

5.6 Clock Distribution and Pipeline Synchronization

A 62.5 MHz global front end clock will be phase-locked to the 1499 MHz accelerator clock. This global clock will be distributed to all readout electronics crates and used directly by the TDCs and Forward Drift chamber cathode FADCs. The Calorimeter and Central Drift chamber FADCs will phase-lock their higher frequency clocks to the global front end 62.5 MHz clock. A global reset will be distributed to synchronize all pipelines. The level 1 trigger as well as calibration and other special triggers will also be distributed globally.

5.7 Discriminators and Amplifiers

Detectors which provide precise timing (Photon Tagger, Start Counter, Barrel Calorimeter, and Time of Flight counters) will require “constant fraction” discriminators. The Forward Drift Chamber anodes require leading-edge discriminators mounted on the chambers inside the solenoid. The Central Drift Chamber anodes and Forward Drift Chamber cathodes will need an amplifier to drive their FADC inputs. These amplifiers should be located on the chambers. ICs developed for the Atlas [102] detector are being considered for all chamber mounted electronics.

5.8 High Voltage

The Forward Calorimeter PMTs will be powered by Cockcroft-Walton voltage multipliers [28] which will be built at Indiana University. This type of base provides for the very low power consumption necessary for such a tightly packed array and is controlled over a CAN communication link. One hundred prototypes of these bases have been built at Indiana University and are being tested. The other GLUEX PMTs will likely use conventional resistive divider bases powered by commercial HV power supplies. The Tracking Chambers will use commercial HV power supplies with sensitive current monitoring.

5.9 Packaging

The calorimeter FADC circuit requires about 50 cm² of board space and adjacent channels will need to be about 2 - 3 cm apart. This implies a density of about 8 channels on a 6U board or possibly 16 channels on a 9U board.

The tracking FADCs will be designed at Jefferson Lab. Sixteen channels of 125 MHz FADC for the Central Drift chamber should fit on a 9U board. The exact requirements for the Forward Drift cathode FADCs have not been determined; it should be possible to put 64 channels of 62.5 MHz FADC on a 9U or possibly even a 6U board.

In the low resolution (125 ps) version of the TDC 64 channels fit on a 6U board. This version of the TDC is used for the Forward Drift Chamber anodes.

The Photon Tagger, Start Counter, Barrel Calorimeter, and Time of Flight counters require the high resolution (62.5 ps) version of the TDC; the density is 32 channels per 6U board.

Assuming a maximum of 18 boards in a crate, and 3 9U or 4 6U crates in a 7 foot tall rack, figure 5.11 summarizes the space required for the readout electronics. Estimated counts for high voltage, gas handling, level 1 trigger, and other necessary racks are also included.

The readout electronics will be located as close to the detector as possible to minimize signal cable runs. Note that the Tagger electronics will be located in a separate building 80 m upstream of the main detector. The Time of Flight and Forward Calorimeter electronics will

Summary of GlueX Rack Space

Detector	Type	Channels	Modules	Crates	Racks
Photon Tagger	6U, 8 channel, 8 bit, 250 Msps FADC	192	24	2	
	6U, 32 channel, 62 ps TDC	192	6	1	
	High voltage	192		1	1
Upstream Photon Veto	6U, 8 channel, 8 bit, 250 Msps FADC	20	3		
Start Counter	6U, 8 channel, 8 bit, 250 Msps FADC	40	5		
	6U, 32 channel, 62 ps TDC	40	2	1	
	High voltage (includes UPV)	60		1	1
Central Drift	9U, 16 channel, 125 Msps FADC	3240	203	12	4
	High voltage			1	1
	Gas				2
Forward Drift anodes	6U, 64 channel, 125 ps TDC	2900	46	3	1
Forward Drift cathodes	9U, 64 channel, 10 bit, 62.5 Msps FADC	11,400	179	10	4
	High voltage			1	1
	Gas				2
Time of Flight	6U, 8 channel, 8 bit, 250 Msps FADC	168	21	2	
	6U, 16 channel, 31 ps TDC	168	11		
	6U, 8 channel, 8 bit, 250 Msps FADC	40	5	1	1
Cerenkov	High voltage (includes TOF)	208		1	1
	Gas				2
	6U, 8 channel, 8 bit, 250 Msps FADC	960	120	7	
Barrel Calorimeter	6U, 32 channel, 62 ps TDC	960	30	2	3
	6U, 8 channel, 8 bit, 250 Msps FADC	2500	313	18	5
Forward Calorimeter	Cockcroft Walton control, misc				1
Level 1 Trigger				4	1
Totals				68	31

Figure 5.11: Rack space

be downstream of these detectors. Cabling from detectors inside the solenoid will exit at the upstream and downstream ends of the magnet and connect to nearby electronics. Fiber optic cables will transport the data from the crate readout processors to the level 3 trigger processor farm in the GLUEX counting house.

5.10 Readout Bus

FASTBUS crates are no longer being manufactured, and FASTBUS is not being considered for GLUEX. CAMAC crates are fairly slow and have limited board space and power available. Some legacy devices like discriminators, trigger logic or HV supplies which are not part of the data readout may be packaged in CAMAC, but not the bulk of the readout electronics.

VME is popular at Jefferson Lab and the TDC prototype is constructed on a VME64x card. Compact PCI is used extensively in the telecommunications industry and can be driven directly by typical FPGA ICs without the need for bus interface ICs. Predefined PCI interface “cores” are available, minimizing design time. One disadvantage of cPCI is that bridges are required for a system with more than 8 slots, although commercial bridges which consume no slots are available. VXI and PXI are “instrumentation” extensions to VME and cPCI. Shielding, triggering, clock distribution, and additional power are added to the basic bus standard.

The FADCs require a low skew fanout of the 250 MHz clock, a synchronization signal, and the level 1 trigger. The need to form a digital global energy sum for the level 1 trigger will probably drive the choice of packaging for the calorimeter FADCs. Some sort of custom backplane will be required to support the trees of adders which form the energy sum and track counts.

The telecommunications industry is moving towards “Switched Serial Fabrics.” This adds a high speed serial connector to the backplane which can support Ethernet and other high speed serial technologies. For VME the applicable standard is VXS (VITA 41) and for cPCI the standard is cPSB (PICMG 2.16). For a 16 channel FADC module producing 25 bytes per channel per level 1 trigger; a level 1 trigger rate of 200 kHz; and a 2% occupancy the data readout bandwidth required for a module is 16 Megabits per second, well within the capability of a 100baseT Ethernet connection.

5.11 Construction

Indiana University has experience building large electronic systems for experiments at Fermilab, Brookhaven, and Jefferson Lab. The GLUEX experiment is larger and more complex than past experiments and will require the development of new techniques. High reliability is crucial to the success of the GLUEX experiment. We plan to begin long term tests of GLUEX electronics as soon as they are produced giving early identification of problems and failure modes.

A robotic electronic assembly machine[103] shown in figure 5.12 was purchased and used to construct 100 prototype Forward calorimeter Cockcroft-Walton PMTbases. This device dispenses solder paste, picks and places components, and uses infrared lasers to selectively solder components without disturbing nearby devices. This facilitates building a board in stages and testing partial assemblies, a technique especially useful in producing the Cockcroft-Walton PMT bases. The infrared lasers are particularly useful for removing and replacing defective components.

Producing electronics assemblies in house has several advantages over having a commercial firm doing the assembly. To achieve the lowest cost, a commercial service would assemble a large batch all at once. This risks learning about problems after it’s too late to change anything. Assembling smaller batches in house allows immediate feedback to the assembly process.

The lifetime of the GLUEX experiment will be long enough that we must plan for maintenance and repair of the custom electronics. Sufficient spare parts must be purchased at construction time to avoid the risk of a component manufacturer discontinuing some crucial part. Spreading the purchase of components over too long a time also risks some components becoming unavailable.



Figure 5.12: Selective assembly robot.

Jefferson Lab used a commercial board assembly contractor to build the 50 TDC boards used in Hall C. No major problems were associated with this contract assembly, although it was necessary to quickly test the first few units before committing to assembling the remainder.

5.12 Review

The GLUEX electronics were reviewed by one internal and two outside reviewers in July of 2003. The report of this review is attached as an appendix. The review was scheduled at an early stage in the development of GLUEX so that their recommendations could be incorporated into final designs. The guidance of the committee has been extremely useful in the continued prototyping and design of the system.

The present design for the GLUEX electronics differs in a few ways from the reviewers recommendations:

At the time of the review it was believed that a single FADC module could be used for all detectors. The detector characteristics have been further defined since the review and it seems unlikely that one type of FADC is optimal for all detectors. The channel count for the Forward drift cathodes has grown substantially; the overall system cost will likely be lowered by designing a module specifically for this detector. The different types of FADC will be as similar as possible; it may be possible to use a common printed circuit board stuffed with different components.

The reviewers recommended locating the readout electronics in a radiation free area. The collaboration believes the advantages of shorter signal cables outweigh the access considerations and is planning to locate the electronics in crates adjacent to the detector. Access to the above ground GLUEX detector should be easier than access to the existing underground experiments at Jefferson lab.

Appendix A

Report of the Hall D Electronics Review Committee

Review Committee:

Andrew Lankford
Glenn Young
John Domingo

University of California - Irvine
Oak Ridge National Laboratory
Jefferson Laboratory

Date: July 23-24 2003

We have organized the report as a response to the questions posed in the charge to the committee.

Is the GlueX electronic design sound?

Although the GlueX electronics design has many features that differ from present JLab experiments, the design is fairly conventional relative to many other recent nuclear and high energy physics experiments. The GlueX electronics design is characterized by:

- Detector-mounted analog front-end electronics
- Pipelined data acquisition
- Crate-based TDC and Flash ADC modules
- Two stage trigger, with a hardware-based first level followed by software-based second level
- Parallel event building

All of these characteristics are sound and appropriate choices for GlueX (where “appropriate” assumes adequate human and fiscal resources). Although the GlueX electronics design parameters (e.g. data rates) exceed current JLab experiments, they do not exceed the performance of other contemporary experiments.

The committee notes that although its members are comfortable with the choice of pipelined electronics and data-acquisition systems, development of a compact justification for this choice might be advisable in preparation for a Lehman review of GlueX

The decision to standardize all detector readout on a single TDC module design and a single Flash ADC module design is good, and will help simplify the overall electronics system design in a constructive way and conserve valuable engineering resources. The Committee feels that it is desirable to locate these modules in a radiation-free area if possible, in order to improve access. Such a location is also likely to provide a cleaner and better cooled environment, which will also improve reliability. The Committee does not feel that there is a compelling reason not to use a crate and bus based system for the electronic modules.

Are there any special areas of concern that deserve special study?

More manpower will be needed in order to fully realize the GlueX electronics system. Considerable special (technical) expertise will also be required.

The requirements and specifications of the analog front-end electronics are not yet adequately defined. This is coupled to the tentative status of some detector designs. The lack of full definition of detector designs may soon limit progress on electronics design, although there are other issues on which progress can presently be made. Some issues deserving attention now are listed under the “Milestones” section.

Does the collaboration have a sensible plan for management?

Rudiments of a plan for management of the electronics system exist, although the plan needs further development. The Committee suggests creating a single organization covering front-end electronics of all detector subsystems, trigger, data acquisition, and online software.

The electronics organization should be put in place during the development of the CDR, and the electronics management plan included in that document

Are their estimates of manpower needs realistic?

The manpower resources shown during the review will be inadequate for developing an electronics system of the scope required by GlueX. A bottoms-up estimate of the necessary manpower should be derived from the manpower requirements for development of the electronics chain for each electronics subsystem, including packaging, grounding, shielding, and power issues.

The committee anticipates that the GlueX collaboration will need to discuss support for additional electronics and computing manpower with Jefferson Lab and the funding agencies.

Do they have a realistic milestones as we prepare for the Lehmann review and beyond to construction?

The Committee estimates that a project of the overall scale of GlueX will require about 6 years to complete after CD-3 is achieved. Approximately two years are available between obtaining CD-0 and CD-3, during which the CDR must be developed and all groups involved in the construction of GlueX be put in place. This requires that by FY2006, all major R&D issues should have been addressed.

The current good work on the flash TDC and ADC should continue. A multichannel FADC needs to be designed, fabricated, and tested. The Committee takes note that multichannel testing has started on the FTDC, with encouraging results on cross-talk and time-slewing due to hits in neighboring channels which overlap in time. The collaboration is developing strategies to record all needed data online to correct such dependencies during offline analysis. High-speed, densely populated pipelined systems are known to have such coupling issues, and a strategy should be developed to address them for all electronics and detectors.

Analog front-end requirements deriving from the detector should be settled; a good first summary of this was exhibited to the Committee. The resulting specifications for the electronics should be settled and used to drive further R&D work. Prototype work on the needed front-ends will require about one year once these specifications are settled. This suggests a review of progress in this area by Jefferson Lab management around the beginning of FY2005, covering the status of analog designs and prototypes.

The collaboration has experience with the needed fast discriminators and has started to explore options for tracking chamber front-ends. A program to develop the tracking chamber front-ends, either from a new design or by adapting an existing design, for example from among the family of ASD-8 ASICs developed at U. Pennsylvania, needs to be mapped out soon by the collaboration.

There is a concept for a pipelined LVL-1 trigger as an integral part of the pipelined online system. The link work shown should be completed. The general concept of local sums at the

front-end board level, followed by crate-level sums and subsequent transfer to a central Global LVL-1 processing area, is sound. A concept and proof-of-principle for crate backplane operation at the required high rate needs to be developed for the CDR. If high-speed serial operation proves challenging, the collaboration should explore possible parallel concepts to lower the bus-speed requirements. The global design concept for LVL-1 also needs to be developed for the CDR.

A concept for the timing system and trigger distribution system, as well as their synchronization (pipelined operation, exception injection), needs to be developed for the CDR. This should address establishing, maintaining and diagnosing the synchronization of the various pipelines. Similarly, a concept for the calibration system, and how it integrates with both the timing/trigger system as well as the analog front-ends and FADC/FTDC, needs to be prepared for the CDR.

The collaboration should start prototyping of the parallel event builder. Manpower needs to be identified at Jefferson Lab and elsewhere to carry this concept through to its execution. The LVL-3 concept is sound and the Committee applauds the opportunistic tests of it using CLAS. A concept for the software framework for algorithms needs to be established for the CDR as well as a method to test this using simulated events.

Finally, power management, grounding and shielding concepts need to be established for the CDR. These must address overall issues as well as those specific for each detector type. The Committee was pleased to hear the report about existing efforts in these areas at Jefferson Lab. GlueX is a large and complicated apparatus employing a demanding readout architecture, which in turn requires proper grounding and shielding be incorporated from the outset.

Are there any major items missing in their list of R&D tasks? Is the priority given to each appropriate at this stage?

The R&D tasks judged to be most pressing are noted above. It is critical that the choices made in readout architecture reflect requirements imposed by the physics and detector choices. We recommend that Jefferson Lab review the status of detector prototypes, with a key aspect of this review being the ability of each detector group to define their electronics needs. It is important to insure that the requirements on the electronics derive from the physics. For instance, momentum resolution requirements drive position resolution requirements, which drive time resolution requirements. Similarly, energy resolution and trigger sum selectivity requirements for the calorimeter drive choices about the number of bits in flash circuits. It must always be kept in mind that requirements are distinct from achievable performance and specifications. The review suggested above should examine these points so that design time and construction cost may be minimized while needed physics performance is preserved.

One example of an area of concern is the choice of barrel calorimeter photosensors. Familiarity with the chosen sensor and its implications for electronics requirements should be demonstrated. The Committee notes that CMS and ALICE have chosen to use custom Hamamatsu avalanche photodiodes to read out both crystal and lead-scintillator calorimeters and have developed appropriately matched preamplifiers and shapers. These APDs have moderate gain, around 50, are fast, and operate at modest voltages of less than 100 volts. These devices need to be studied by the collaboration to see if they would match the proposed barrel calorimeter light output levels. The CMS and ALICE groups use over 200,000 of these photodiodes and CLAS has several hundred of them and can probably supply samples.

Another area of some concern is the technology choice for the vertex tracker, particularly since its physics requirements seem to be undergoing some reconsideration. Present ideas center on tracking fibers and dense arrays of photosensors, such as the VLPC sensor array developed at FNAL. There are issues of VLPC suitability and availability which must be addressed in a timely manner if the collaboration is to pursue this option. Further remarks concerning the VLPC system are given below. If only vertex finding is needed and the fiber solution proves overly challenging, the Committee asks whether a modest silicon-strip array would serve the purpose. Various electronics designs exist, notably at SLAC and FNAL for Tevatron and LHC use.

In many of the above remarks we have stressed the relative priorities between design and prototyping for various items. The collaboration may choose to be more ambitious than sug-

gested, but the Committee feels the items noted should reach the state suggested before the CDR is deemed complete. Some of these efforts will likely require directed funding beyond present resources of the collaboration; thus a prioritized R&D program should be developed in consultation with Jefferson Lab and the funding agencies as soon as possible.

Are there technologies or developments which we have overlooked that may allow cost savings and/or improved technical performance?

The Collaboration should perform a systematic search for existing developments performed by other experiments that will facilitate the development of the GlueX analog front-end electronics. Some examples of interesting developments include:

- For anode wire readout in drift chambers, the family of amplifier/shapers and amplifier/shaper/discriminators developed at the University of Pennsylvania. These are generally referred to as the ASD-8 family and have been used successfully in experiments (ATLAS and PHENIX) in which two of the Committee members currently participate. If the ASD-Q, presented at the meeting, is chosen, then a pipelined TDC capable of recording pulse width is a must. The TMC chip developed by Y. Arai of KEK, also used in different manners by ATLAS and PHENIX, should be investigated.
- The Fermilab design for VLPC readout should be investigated for use in the vertex trackers fiber readout. The collaboration should consider the availability of VLPCs and whether elements of the Fermilab readout system are applicable within the context of the system design of the GlueX electronics. These considerations should be addressed soon, because significant development work may be required for this subsystem.
- For the forward drift chambers, the amplifier/shapers developed for the ATLAS, CMS, and PHENIX cathode strip chambers might provide a solution for the analog front-end. These ASICs are designed for strips up to over 200 pF in one case. The speed and packaging requirements differ among these experiments, thus the collaboration would need to study their suitability for the GlueX chambers, once the parameters are sufficiently well determined.

Bibliography

- [1] G. S. Bali *et al.* [SESAM/TCL Collaboration]. *Phys. Rev.*, D62:054503, 2000.
- [2] Y. Nambu. Univ. of Chicago report No. 70-70, 1970.
- [3] N. Isgur and J. Paton. Flux-tube model for hadrons in QCD. *Phys. Rev.*, D31:2910, 1985.
- [4] C. Bernard *et al.* [MILC Collaboration]. *Phys. Rev.*, D56:7093, 1997.
- [5] National computational infrastructure for lattice gauge theory. <http://www.lqcd.org>.
- [6] G. S. Adams *et al.* (E852 Collaboration). *Phys. Rev. Lett.*, 81:5760, 1998.
- [7] A. Afanasev and P. R. Page. Photoproduction and Electroproduction of $J^{PC} = 1^{-+}$ exotics. *Phys. Rev.*, D57:6771, 1998.
- [8] A. P. Szczepaniak and M. Swat. *Phys. Lett.*, B516:72, 2001.
- [9] GlueX websites. <http://www.gluex.org> and <http://portal.gluex.org>.
- [10] A. P. Szczepaniak and A. Afanasev. 1999. hep-ph/9910268.
- [11] The Science Driving the 12 GeV Upgrade of CEBAF. Technical report, Jefferson Lab., 2001.
- [12] A. R. Dzierba, C. A. Meyer and E. S. Swanson. The Search for QCD Exotics. *American Scientist*, 88:406, 2000.
- [13] A. R. Dzierba and N. Isgur. Mapping quark confinement by exotic particles. *CERN Courier*, 40 No. 7:23, 2000.
- [14] DOE/NSF Nuclear Science Advisory Committee. Opportunities in Nuclear Science - A Long Range Plan for the Next Decade. Technical report, 2002.
- [15] C. Keppel. Development of a Compton-backscattered photon source for Hall B at Jefferson Lab. In Alex Dzierba, editor, *Physics with 8+ GeV Photons Workshop*, 1997. Workshop in Bloomington IN, July 14-16 1997, proceedings available from Jefferson lab.
- [16] W. Kaune, G. Miller, W. Oliver, R.W. Williams, and K.K. Young. Inclusive cross sections for pion and proton production by photons using collimated coherent bremsstrahlung. *Phys. Rev.*, D11(3):478-494, 1975.
- [17] H. Bilokon, G. Bologna, F. Celani, B. D’Ettorre Piazzoli, R. Falcioni, G. Mannocchi, and P. Picchi. Coherent bremsstrahlung in crystals as a tool for producing high energy photon beams to be used in photoproduction experiments at CERN SPS. *Nuclear Inst. and Meth.*, 204:299-310, 1983.
- [18] G. Diambrini-Palazzi. *Revs. Mod. Phys.*, 40:611, 1968.
- [19] U. Timm. *Fortschr. Phys.*, 17:765, 1969.

- [20] J. Kellie. Private Communication.
- [21] C. Sinclair. Private Communication.
- [22] J. Benesch. HallD Preliminary Optics Design. Technical Report JLab TN 00-011, Jefferson Lab., 2000.
- [23] L. Keller. Muon calculation results. Technical Report GlueX-doc-**33**, SLAC, 2000. <http://portal.gluex.org/>.
- [24] Anthony, *et al.* *Nuclear Inst. and Meth.*, **A301**:230, 1991.
- [25] J. Hall, *et al.* *Nuclear Inst. and Meth.*, **A368**:689, 1996.
- [26] D. Aston *et al.* The LASS spectrometer. Technical Report SLAC-Report-298, 1987. Copies available from the SLAC publications office, at <http://www.slac.stanford.edu/pubs/>.
- [27] J. S. Alcorn, H.O. Peterson, and S. St. Lorent. In *Applied Superconductivity Conference*, page 273, 1972.
- [28] A. Brunner *et al.* A Cockcroft-Walton base for the FEU84-3 photomultiplier tube. *Nuclear Inst. and Meth.*, **A414**:446, 1998.
- [29] B. B. Brabson *et al.* A study of two prototype lead glass electromagnetic calorimeters. *Nuclear Inst. and Meth.*, **A332**:419–443, 1993.
- [30] R. R. Crittenden *et al.* A 3000 element lead-glass calorimeter. *Nuclear Inst. and Meth.*, **A387**:377–394, 1997.
- [31] R. Jones *et al.* The Radphi detector. *submitted to Nucl. Instrum. Meth.*, 2004.
- [32] C. P. Steffen. PhD thesis, Indiana University, 2001.
- [33] J. Gunter. An analysis of the reaction $\pi^- p \rightarrow \pi^0 \pi^0 n$ at 18 GeV/c. Ph. D. Thesis - Indiana University, 1997.
- [34] J. Gunter *et al.* A partial wave analysis of the $\pi^0 \pi^0$ system produced in $\pi^- p$ charge exchange collisions. *Phys. Rev.*, **D64**:072003, 2001. hep-ex/0001038.
- [35] R. Lindenbusch. *An analysis of the reaction $\pi^- p \rightarrow \eta \pi^0 n$ at 18 GeV/c.* PhD thesis, Indiana University, 1997.
- [36] M. Swat. *Analysis of the $\eta \pi$ system.* PhD thesis, Indiana University, 2003.
- [37] A.R. Dzierba *et al.* A study of the $\eta \pi^0$ spectrum and search for a $J^{PC} = 1^{-+}$ exotic meson. *Phys. Rev.*, **D67**, 2003. hep-ex/0304002.
- [38] S. Teige *et al.* *Phys. Rev.*, **D59**:012001, 1999.
- [39] J. Manak *et al.* *Phys. Rev.*, **D62**:012003, 2000.
- [40] P. Eugenio *et al.* *Phys. Lett.*, **B497**:190, 2001.
- [41] M. Nozer *et al.* *Phys. Lett.*, **B541**:35, 2002.
- [42] J. Kuhn *et al.* *Phys. Lett.*, **B595**:109, 2004.
- [43] R. Fruhwirth *et al.* *Data Analysis Techniques for High-Energy Physics.* Cambridge University Press, 2000.
- [44] R. Wingman. *International Series of Monographs on Physics*, volume 107. Oxford University Press, 2000.

- [45] R. T. Jones and M. Kornicer. LGD Shower resolution. Technical report, 2003.
- [46] Graham McNicoll. A study of photon sensitivity in the Hall D detector. Technical Report GlueX-doc-**36**, Carnegie Mellon University, 2000. <http://portal.gluex.org/>.
- [47] Joachim Kuhn and Curtis A. Meyer. Acceptance Study for the GlueX detector system. Technical Report GlueX-doc-**264**, 2004. <http://portal.gluex.org/>.
- [48] C. A. Meyer. A study of timing resolutions on particle identification in the HALL D detector at jefferson lab. Technical Report GlueX-doc-**14**, Carnegie Mellon University, 1999. <http://portal.gluex.org/>.
- [49] C. A. Meyer and P. Eugenio. A Study of Compined $K-\pi$ Separation using Time-of-Flight Counters and a Gas Čerenkov Detector. Technical Report GlueX-doc-**15**, Carnegie Mellon University, 1998. <http://portal.gluex.org/>.
- [50] The GlueX Collaboration. Hall D Design Report, Version 4. Technical Report GlueX-doc-**58**, 2002. <http://portal.gluex.org/>.
- [51] D.W. Hertzog *et al.* *Nuclear Inst. and Meth.*, **A294**:446, 1990.
- [52] A. Antonelli *et al.* *Nuclear Inst. and Meth.*, **A370**:367, 1996.
- [53] M. Adinolfi *et al.* *Nuclear Inst. and Meth.*, **A494**:326, 2002.
- [54] Brian Klein *et. al.* B-CAL Progress and Construction Report. Technical Report GlueX Technical Note **333**, 2004. <http://portal.gluex.org/>.
- [55] Brian Klein *et. al.* B-CAL Progress and Construction Report. Technical Report GlueX Technical Note **333**, 2004. <http://portal.gluex.org/>.
- [56] Z. Papandreou, E.J. Brash, G.M. Huber, V.D. Kovaltchouk, S. Li, G.J. Lolos, L. Snook and S. Vidakovic. Attenuation Length and Timing Resolution of Scintillating Fibers for Hall D. Technical Report GlueX-doc-**50**, University of Regina, October 2001. <http://portal.gluex.org/>.
- [57] A. Antonelli *et al.* *Nuclear Inst. and Meth.*, **A354**:352, 1995.
- [58] B. Jasper and R. Filby. Degradation of Fibers with UV Exposure and Construction Aspects of the 4m Calorimeter Module. Technical Report GlueX-doc-**331**, University of Regina, April 2004. <http://portal.gluex.org/>.
- [59] B. Dolgoshein. *Nuclear Inst. and Meth.*, **494**:48, 2003.
- [60] D. Renker. Avalanche photodiodes now and possible developments. In *Vienna Conference on Instrumentation*, 2004. February 16-21 2004, conference web site: <http://vci.oeaw.ac.at/>.
- [61] V. Saliev. Private Communication.
- [62] T. Okusawa. *Nuclear Inst. and Meth.*, **459**:440, 2001.
- [63] P. Eugenio. *Genr8*: A general monte carlo event generator. Technical report, Carnegie Mellon University, 1998.
- [64] C. A. Meyer. Tracking Resolution Requirements in the Meson Spectroscopy Facility at Jefferson Lab. Technical Report GlueX-doc-**7**, Carnegie Mellon University, 1998. <http://portal.gluex.org/>.
- [65] Rob Veenhof. *The GARFIELD Program, Simulation of Gaseous Detectors*. CERN, 1984. <http://garfield.web.cern.ch/garfield/>.

- [66] H. Wirth. Particle Identification with the JETSET Straw Chambers. *Nuclear Inst. and Meth.*, **A367**:248–251, 1995. Prepared for 7th International Wire Chamber Conference (WCC 95): Recent Trends and Alternative Techniques, Vienna, Austria, 13-17 Feb 1995.
- [67] Zebulun Krahn and Mike Williams. Gas Composition Study for the Straw Tube Chamber in the GlueX Detector at Jefferson Lab. Technical Report GlueX-doc-**62**, 2003. <http://portal.gluex.org/>.
- [68] D. Barton, *et al.* (The EVA Collaboration). Color Transparency with EVA, October 1994. BNL-PROPOSAL-850.
- [69] Mike Williams, Zebulun Krahn and Curtis A. Meyer. A Study of the Straw Tube Detector for the GlueX Detector at Jefferson Lab. Technical Report GlueX-doc-**54**, Carnegie Mellon University, July 2002. <http://portal.gluex.org/>.
- [70] Curtis A. Meyer. Accuracy Measurements of the straw-tube chamber end plates. Technical Report GlueX-doc-**61**, 2003. <http://portal.gluex.org/>.
- [71] Curtis A. Meyer and Zebulun Krahn. A Summary of Straw-tube Chamber Tests. Technical Report GlueX-doc-**280**, 2004. <http://portal.gluex.org/>.
- [72] H. Fenker *et al.* *Nuclear Inst. and Meth.*, **A367**:285, 1999.
- [73] *ATLAS Collaboration*. ATLAS Technical Design Report, Chapter 6, June 1997.
- [74] *PHENIX Collaboration*. PHENIX Internal Note PN125.
- [75] D. Aston *et al.* (*The LASS Collaboration*). SLAC Internal Note SLAC-298.
- [76] A. Antonelli *et al.* A Pb SciFi EM calorimeter for an experiment on CP violation at DAPHNE. Technical Report LNF-91-073-P, Frascati, 1991.
- [77] S. Denisov *et al.* Timing characteristics of scintillation counters. *Nuclear Inst. and Meth.*, **A478**:440–443, 2002.
- [78] S. Denisov *et al.* Characteristics of the TOF Counters for the GlueX Experiment. *Nuclear Inst. and Meth.*, **A494**:495–499, 2002.
- [79] S. Denisov *et al.* Systematic studies of timing characteristics for 2-m long scintillation counters. *Nuclear Inst. and Meth.*, **A525**:183, 2004.
- [80] S. Denisov *et al.* Studies of magnetic shielding for phototubes. *Nuclear Inst. and Meth.*, article in press, 2004.
- [81] I. Adam *et al.* The DIRC Particle Identification System for the BaBar Experiment. 2004. accepted for publication.
- [82] P. Coyle *et al.* *Nuclear Inst. and Meth.*, **A343**, 1994.
- [83] B. Ratcliff. Technical report, 1992 and 1993. SLAC-PUB-5946 and SLAC-PUB-6047.
- [84] B. Aubert *et al.* Observation of Direct CP Violation in $B^0 \rightarrow K^+ \pi^-$ Decays. 2004. hep-ex/0407057.
- [85] B. Aubert *et al.* The BABAR Detector. *Nuclear Inst. and Meth.*, **A479**, 2002.
- [86] *Status of the PEP-II B Factory*. talk given at the 14th Advanced ICFA Beam Dynamics Workshop: Beam Dynamics Issues for e^+e^- Factories “ (ICFA 97), Frascati, Italy, 1997.
- [87] E. Bloom *et al.* The PEP-II Asymmetric B Factory: Design Details and R&D Results. Technical Report SLAC-PUB-6564, 1994.

- [88] E. Bloom *et al.* PEP-II: An Asymmetric B Factory. Conceptual Design Report. Technical Report SLAC-R-418, 1993.
- [89] The BABAR Collaboration. The BABAR Physics Book. Technical Report SLAC Report 504, 1998.
- [90] The provider of fused silica: TSL Group PCL,
P.O. Box 6, Wallsend, Tyne & Wear, NE28 6DG, England.
Quartz Products Co., 1600 W. Lee St., Louisville, Kentucky 40201.
Manufacturer of quartz bars: Boeing, Rockeddyne Division, 2511 C Broadbent Parkway
NE, Albuquerque, New Mexico 87107.
- [91] Manufacturer of photo-tubes: Electron Tubes Limited, (formerly: Thorn EMI Electron Tubes), Bury Street, Ruislip, Middlesex HA47TA, U.K.
- [92] J. Cohen-Tanugi *et al.* *Nuclear Inst. and Meth.*, **A515**, 2003.
- [93] R. Brun *et al.*, 1986. GEANT3, CERN-DD/EE/84-1.
- [94] TOSCA 3D, software for electromagnetic design, Vector Fields Inc., Aurora, IL 60505, USA.
- [95] M. Sivertz *et al.* A compact gas Čerenkov detector with novel optics. *Nuclear Inst. and Meth.*, **A385**:37, 1997. hep-ex/9607013.
- [96] J. Va'Vra. *Nuclear Inst. and Meth.*, **A244**:391–415, 1986.
- [97] D.G.Cussans. *Nuclear Inst. and Meth.*, **A244**:277, 1995.
- [98] Signal Processing Technologies: <http://www.spt.com>.
- [99] Xilinx: <http://www.xilinx.com>.
- [100] More information on the FADC prototype can be found at
<http://dustbunny.physics.indiana.edu/~paul/hallDrd>.
- [101] CAEN: <http://www.caen.it>.
- [102] ATLAS ASD chip: http://bmc.bu.edu/bmc/asd/asd_chip.html.
- [103] Beamworks Spark 400: <http://www.beamworks.com>.